

Doctoral theses at NTNU, 2023:129

Shaoquan Wang

Integration and performance of distributed optical fibre sensors in thermoplastics and thermoplastic composites

Doctoral thesis

NTNU
Norwegian University of Science and Technology
Thesis for the Degree of
Philosophiae Doctor
Faculty of Engineering
Department of Mechanical and Industrial
Engineering



Norwegian University of
Science and Technology

Shaoquan Wang

Integration and performance of distributed optical fibre sensors in thermoplastics and thermoplastic composites



Thesis for the Degree of Philosophiae Doctor

Trondheim, April 2023

Norwegian University of Science and Technology
Faculty of Engineering
Department of Mechanical and Industrial Engineering



Norwegian University of
Science and Technology

NTNU

Norwegian University of Science and Technology

Thesis for the Degree of Philosophiae Doctor

Faculty of Engineering

Department of Mechanical and Industrial Engineering

© Shaoquan Wang

ISBN 978-82-326-5864-0 (printed ver.)

ISBN 978-82-326-6284-5 (electronic ver.)

ISSN 1503-8181 (printed ver.)

ISSN 2703-8084 (online ver.)

Doctoral theses at NTNU, 2023:129

Printed by NTNU Grafisk senter



To Gang Wang & Chunxiang Jin, my parents, forever friends and dearest in life.

So grateful that you fill my life with happiness and love.

Preface

This thesis has been submitted to the Norwegian University of Science and Technology (NTNU) for the degree of Philosophiae Doctor (PhD). The work has been carried out at the Department of Mechanical and Industrial Engineering (MTP) at NTNU under the supervision of Associate Professor Kaspar Lasn and co-supervision of Professor Andreas Echtermeyer. Parts of this PhD work have been developed in collaboration with an EU project THOR (Grant No. 826262).

Trondheim, June 2022

Abstract

Today, thermoplastics and fibre reinforced thermoplastic composites, are increasingly being used in all fields of commerce and industry, for their improved performance with respect to impact resistance, recyclability, and the manufacturing cost. However, the damage and performance of thermoplastics and their composite structures is difficult to predict due to viscoelastic mechanical behavior and complicated failure mechanisms. Structural health monitoring (SHM) systems provide effective tools to detect and characterize how material degradation occurs and develops with time, assuring the safety of engineering structures. Optical fibre (OF) sensors are often considered for future SHM systems, because they enable both massive data acquisition and miniaturization of sensors in size and in power consumption. The performance of optical fibres depends to a large extent on how they are integrated into the host structure. For thermoplastics and their composite, OF sensor attachments typically use similar methods than have been used for traditional structural materials. The integration technology is still mostly manual work thereby producing inconsistent sensor measurements. The OF integration has three major issues; 1) lack of well-controlled OF integration methods; 2) lack of assessment methods for the OF attachment quality; 3) coupled sensitivity for thermal and mechanical effects on the OF. This research aims to improve upon these three aspects.

The lack of automated, well-controlled OF integration methods induces inconsistent bonding which causes a non-uniform strain transfer from the host structure to the OF sensors. In this work, a novel method has been developed to integrate OF sensors into thermoplastics and thermoplastic composite materials by utilizing the material extrusion 3-D printing process. A procedure for OF in-situ integration during the printing process with a fused deposition modeling (FDM) 3-D printer was proposed. The material behavior during and after the integration process have been investigated. Tensile testing and creep experiments were carried out to investigate the OF/thermoplastic interface bonding and the mechanical response of the substrate-OF system. Residual strains were measured on the integrated OF after 3-D printing and the residual strain creation mechanisms have been discussed. The measurement accuracy of the novel OF based method is compared with traditional methods.

Quality and consistency of the OF bonding layer affects the measurement accuracy of the OF sensor directly. A good practical non-destructive method to

test and evaluate the OF integration quality is currently missing. In this work, residual strains created by the integration process were used to assess the integration quality of both the novel OF integration by 3-D printing and a selection of traditional methods. Residual strains and their fluctuations along the OF are shown to be correlated to the specific OF integration method and it appears to be a useful quantitative metric for evaluating the attachment quality of the integrated OF.

The coupled sensitivity of temperature and strain is one of the most significant limitations for using Fibre Bragg Gratings (FBGs) as well as Rayleigh backscattering OFDR (adopted in this work) based optical fibre measurements. This coupled sensitivity can introduce large errors for signal interpretation. The relationship between strain and the temperature effects under coupled mechanical-thermal loadings is studied in detail and a mechanical-thermal loading superposition model is confirmed for decoupling strain and temperature effects. A polynomial formula is deduced from physics-based temperature effect models to overcome the poor accuracy of widely used linear calculation principle. This more accurate calculation model is realized and tested in practice to distinguish pure mechanical strains from pure thermal loading on the OF.

Acknowledgements

First and foremost, I wish to express my sincere gratitude to Assoc. Prof. Kaspar Lasn and Prof. Andreas Thorsten Echtermeyer for affording me the opportunity to pursue a PhD degree and become a member of our research team. They not only granted me access to the academic world but also imparted an immense wealth of knowledge and offered unwavering support. Their open-mindedness, eagerness to help, and gentle demeanors have been invaluable in guiding me through both academic and personal challenges in life.

Over the past four years, Kaspar Lasn has provided me with an abundance of aid. He has permitted me to pursue my own interests, encouraged me to explore innovative fields, and mentored me to think independently. Whenever I faced difficulties, I knew I could count on his advice. Despite his busy schedule, he made time for me, holding meetings on weekdays, weekends, and even during his vacation. I am profoundly grateful for his sacrifices and apologize for disrupting his personal time. I cherish the discussions we have had on science, culture, and society and value the knowledge he has imparted, which extends beyond just answering specific research questions but also equips me with problem-solving tools that are applicable in both my work and personal life.

Prof. Andreas Thorsten Echtermeyer has also left an indelible impression on me with his attitude towards students. During my first year, I was fortunate enough to have his lectures. He demonstrated immense patience in the classroom and could simplify even the most complex theories with ease. His office was always open to questions, and his breadth of knowledge in various fields proved invaluable in providing me with useful guidance in my research. Thank you, Prof. Echtermeyer, for the enjoyable times during lectures and research.

Specially, I am particularly grateful to my friend Sondre Østre Rokvam, who was the first person I met in Norway. Starting life in a foreign country is not easy, but I consider myself fortunate to have met him on my first day here. I am even more grateful to have worked with him during my PhD days and to continue our collaboration in the career. I have a great deal of respect and admiration for him because he has always been there for me and provided invaluable support in both my studies and research. His guidance has been instrumental in my successful adjustment to life in Norway, and he has helped me navigate the social rules and customs here with ease. Not only has he been a great mentor, but he has also been a wonderful friend who has made my transition to Norway a seamless one. Indeed, it is the people in a place who make it truly lovable, and

Norway holds a special place in my heart because of you. Sondre, you are my brother in Trondheim.

I express my gratitude to all my dear close friends, namely Anni Cao, Fan Gao, Di Wan, Dong Wan, Jun Ma and Xu Lu, for their invaluable support and companionship during my stay in Norway over the years. Anni Cao, a ray of sunshine and optimism, and I am grateful for the many lessons she has taught me in music, Matlab, and sports, and for reminding me of what truly matters in life. Our travels and explorations of different countries have been some of the most memorable experiences of my life, and I thank God for granting me the opportunity to spend time with her skiing in France. I will never forget how she took care of me when I was sick and needed rest. Thank for your food, they are as delicious as Michelin-3 star. Her kind words and support were a great comfort during that difficult time, and I appreciate how she helped me relieve my stress through our conversations. Spending time with her, both inside and outside the university, has been a true blessing. Fan Gao, I am fortunate to have her as a delightful friend. I am grateful for the companionship she has provided me, which has brought diversity and relaxation to my life. Spending time with her has been truly enjoyable, and I cherish those happy moments. Her cooking skills are outstanding, and the food she prepares reminds me of the tastes of my hometown. I want to express my genuine gratitude to Di Wan for being an altruistic friend. In addition to being a great companion, Di Wan is also a scientist, and our discussions have been incredibly valuable. As a good friend, we have provided each other with unwavering support during difficult times. He is also a skilled driver. The road trips we embarked on in Europe were truly unforgettable, and those memories hold a special place in my heart. He is my best teammate in Fencing, and we share a passion for food as well. Jun Ma, I am incredibly thankful for his unwavering support and companionship during a difficult time when I suspected I had COVID-19. Not only is he a warm-hearted friend, but also an exceptional young scientist whose knowledge and insights have been a great inspiration to me. His eagerness to help and his willingness have been a great source of comfort, and I cherish our conversations that have enriched my understanding of different subjects. With his impressive knowledge and work ethic, I have no doubt that Jun Ma will become a major leader in his research field. Dong Wang and Xu Lu, a charming couple and talented researchers with a long-term vision, you have been successful in both your academic and personal lives. I appreciate your assistance, and all the get-togethers we've had are treasured moments from my time in Trondheim.

I would also like to extend my appreciation to our composite team members: Andrey Krauklis, Chiara Zarna, Erik Sæter, Eivind Hugaas, Nils Petter Vedvik and Victor Maneval. Our work in composite research has been exceptional, and we have made significant contributions to the field. Thank you for the help from my colleagues at NTNU, including Agnes Digranes, Børge Holen, Carl-Magnus Midtbø, Christer Westum Elverum, Kari Elise Dahle, Li Liang, Natalia Trotsenko, Qingbo Wang, Xu He, Yu Wang, and Zhuo Xu. Special recognition goes to Kari Elise Dahle and Natalia Trotsenko, who have assisted me on numerous occasions. They have saved me from bureaucratic troubles during application and registration, cared for me during personal issues, and helped me overcome difficulties during sick leave and other matters. Thank you very much.

I am extremely grateful to UBIQ Aerospace for affording the opportunity to continue my research work and pursue innovation beyond my PhD study. The support has been invaluable in my investigations. Kasper T. Borup and Kim L. Sørensen, I would also like to express my sincere gratitude for your understanding and encouragement, which is a pillar of support in every way. I would also like to express my gratitude to the Research Council of Norway, NTNU, and the Department of Mechanical and Industrial Engineering, Trondheim, my spiritual home, you have transformed me into the man I am today.

Finally, I would like to express my gratitude to my family. My parents gave me life, taught me to work hard, dream big, and showed me how to be a gentleman. You gave me the courage to explore the world and persevere through tough times. My aunt Chunfang Jin, you have taken care of me since my birth, and I have received much assistance from you since then. To my brother and sister, I feel lucky to have you as part of my life. Chunxiang Jin, my dearest mother, you mean the world to me, and I want to spend every day of my life with you. Most especially, I thank my dear father, Gang Wang, who will always hold a special place in my heart. I miss you terribly and love you beyond measure. I will never forget you until the day we reunite.

Shaoquan Wang

June 2022, Trondheim, Norway

Abbreviations and symbols

Abbreviations

<i>A</i>	Absolute mode	<i>i.e.</i>	Id est/That is
<i>AS</i>	Anti-stokes	<i>M</i>	Matrix
<i>BOTDR</i>	Brillouin optical time domain reflectometry	<i>MEX</i>	Bound material-based material extrusion
<i>BOTDA</i>	Brillouin optical time domain analyzer	<i>NTNU</i>	Norwegian University of Science and Technology
<i>BFS</i>	Brillouin frequency shift	<i>OBR</i>	Optical backscattering reflectometer
<i>CAD</i>	Computer-aided design	<i>OTDR</i>	Optical time domain reflectometer
<i>CV</i>	Coefficient of variation	<i>OFDR</i>	Optical frequency domain reflectometer
<i>C_A</i>	Absolute difference coefficient	<i>OF</i>	Optical fibre
<i>C_R</i>	Relative difference coefficient	<i>OFS</i>	Optical fibre sensors
<i>CF</i>	Carbon fibre	<i>PA6</i>	Nylon 6
<i>DOFS</i>	Distributed optical fibre sensor	<i>PI</i>	Polyimide
<i>DSC</i>	Differential scanning calorimetry	<i>PLA</i>	Polylactic acid
<i>DMTA</i>	Dynamic mechanical thermal analysis	<i>PC</i>	Personal computer
<i>EL</i>	Embedding length	<i>PhD</i>	Doctor of Philosophy
<i>EXT</i>	Extensometer	<i>R</i>	Relative mode
<i>e.g.</i>	Exempli gratia/For example	<i>ROI</i>	Region of interest
<i>etc</i>	Et cetera/And other similar things	<i>RBS</i>	Rayleigh backscattering spectral
<i>FFT</i>	Fast Fourier Transform	<i>R&D</i>	Research and development
<i>FBG</i>	Fibre Bragg grating	<i>RQ</i>	Research question
<i>FFF</i>	Fused filament fabrication	<i>S</i>	Stokes
<i>FP</i>	Fabry–Perot sensor	<i>SHM</i>	Structural health monitoring
<i>FRP</i>	Fibre reinforced polymer	<i>SG</i>	Strain gauge
<i>FDM</i>	Fused deposition modeling	<i>STL</i>	Stereolithography
<i>FLIR</i>	Forward looking infrared	<i>SS</i>	Sensor spacing
<i>GF</i>	Glass fibre	<i>SMF</i>	Single mode fibre
<i>GL</i>	Gauge length	<i>1-D</i>	One direction
<i>IoT</i>	Internet of things	<i>3-D</i>	Three directions
<i>IR</i>	Infrared		

Symbols*

<i>Acoustic wave velocity</i>	V (mm/s)	<i>Reflectivity</i>	R (%)
<i>Boltzmann constant</i>	k (J/K)	<i>Shear lag dominant parameter</i>	α (-)
<i>Beat frequency of laser</i>	f (GHz)	<i>Strain</i>	ε (-)
<i>Correlation index</i>	S (-)	<i>Sensitivity coefficient</i>	K (1/°C)
<i>Differential value</i>	Δ	<i>Stress</i>	σ (MPa)
<i>Distance</i>	z (m)	<i>Strain transfer coefficient</i>	K_M
<i>Energy</i>	E (J)	<i>Time</i>	T (s)
<i>Euler's number</i>	e (-)	<i>Temperature</i>	T (°C)
		<i>Thickness</i>	T_{thk} (mm)
<i>Goodness-of-Fit</i>	R^2 (-)	<i>Thermal expansion coefficient</i>	α (-)
<i>Index of refraction</i>	n (-)	<i>Temperature Coefficients of</i>	
		<i>Refractive Index</i>	β (1/°C)
<i>Length</i>	L, l (mm)	<i>Time delay</i>	T (s)
<i>Laser frequency sweep rate</i>	A (GHz/s)	<i>Tuning rate of the laser</i>	γ (GHz)
<i>Modulus of elasticity</i>	E (MPa)	<i>Velocity of light</i>	c (m/s)
<i>Optical frequency</i>	ν (GHz) f (GHz)	<i>Wavelength</i>	λ (nm)
<i>Planck's constant</i>	h (J/Hz)		

* Detailed symbols used for equations are defined at these specific equations.

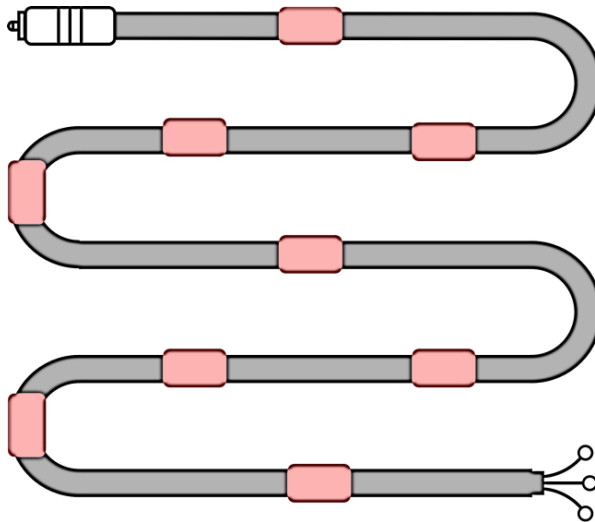
Contents

Preface	ii
Abstract	iii
Acknowledgements	v
Abbreviations and symbols	viii
Chapter 1 Introduction	2
1.1 Motivation and background	2
1.1.1 IoT and SHM	2
1.1.2 Fibre optic based SHM	4
1.2 Optical fibre sensing	7
1.2.1 DOFS	7
1.2.2 Raman scattering	8
1.2.3 Brillouin scattering	8
1.2.4 Rayleigh scattering	9
1.2.5 Optical fibre data processing methods	10
1.3 Sensor integration techniques	16
1.4 Coupled sensitivity of the optical fibre	20
1.5 Technical gaps	21
1.6 Objectives of the PhD project	21
1.7 The structure of appended papers	22
1.8 Structure of the thesis	25
Chapter 2 Experimental methods	26
2.1 Distributed optical fibre measurements	26
2.1.1 OBR-4600 measurement system	26
2.1.2 Measurement theory	27
2.1.3 OBR signal demodulation	33
2.2 Material extrusion 3-D printing	33
2.2.1 Additive manufacturing	33
2.2.2 Fused deposition modeling (FDM)	34
Chapter 3 Main results	36
3.1 Optical fibre integration by material extrusion 3-D printing (RQ1)	36

3.1.1	The embedding procedure	36
3.2	Assessment of the attachment quality (RQ2)	41
3.2.1	In-situ residual strains in blocks of PLA	41
3.2.2	Residual strains from various optical fibre attachment methods.....	43
3.3	An accurate calculation model (RQ3)	47
3.3.1	Mechanical loading effect.....	47
3.3.2	Coupled mechanical and thermal loading.....	48
3.3.3	The novel polynomial formula.....	49
3.4	Creep strain measurements (RQ4)	54
3.4.1	Region of interest (ROI)	54
3.4.2	Comparison of different OF attachment methods.....	55
3.4.3	Bottom interlayer thickness effects.....	58
3.4.4	Shear lag correction.....	61
	Conclusions	63
	Future work	66
	Bibliography	67
	Part 2: Appendices.....	74
	Paper I.....	75
	Paper II	89
	Paper III.....	102
	Paper IV	126

PART 1: INTRODUCTION AND OVERVIEW

OF NOVELTY ASPIRATIONS



CHAPTER 1

INTRODUCTION

'It is a capital mistake to theorize before one has data. Data! Data! Data! ... I can't make bricks without clay!'

-Sir Arthur Conan Doyle

1.1 MOTIVATION AND BACKGROUND

1.1.1 IOT AND SHM

Humans exist in an ever-changing environment, that is increasingly being modified by man-made technologies. Technological revolutions alter the way people live, work, and relate to one another (Figure 1-1). The transition from hunting to agriculture, and later to urbanization, has moved large populations of humans from farms to cities. The modern lifestyle in the Information Age has been shaped by the Internet Revolution since 1983. Now, we are again standing on the brink of a technological revolution, that will fundamentally reshape the way men live, work, and collaborate with one another [1].

Internet of things (IoT) is often defined as a dynamic global network infrastructure, with self-sensing functions, that are based on information and communications technology [2]. IoT introduces and utilizes the next generation of internet, where most of the physical devices and machines are inter-connected and the data is collected, and then processed to help making decisions [3]. The architecture of IoT has been divided into various functional layers, as reported from different perspectives, see Figure 1-2 [3–5]. IoT works through the following flow of information: the data is first obtained in the sensing layer, and then fed into the post-processing layers, where humans and computing systems collaborate to make strategies and decisions based on it. IoT requires a powerful sensing system, and data acquisition and processing capabilities, which bring new opportunities, and great benefits by using many existing and future information analysis techniques. In particular, the advanced processing of information becomes fruitful when the IoT is connected to a structural health monitoring (SHM) system, whose core is data sensing, tracking and analyzing in real-time [6]. SHM systems are a data-driven remedy for the safety of civil/industrial structures [7]. It is a continuous procedure to detect and characterize the degradation and damage of engineering structures. Experience shows that traditional SHM systems are often troubled by the lack of efficiency and high cost, because the data collection, processing and decision-making has mostly been done manually. New automated IoT-SHM systems on the other hand show improved potentials in terms of reliability, efficiency and the low-cost of operation [8].

A crucial requirement for any IoT-SHM system is the need for reliable and timely data. All the data are sensed and received by the sensing layer, also referred to as the ‘Things’ of IoT, essentially anything that is integrated with sensors to sense their status. The more powerful sensors are realized, the more valuable data is captured. Thus far, a lot of the research and R&D work has been focused on the application layer and connectivity. In contrast, the technological development in the hardware of sensors has fallen behind. Key technologies driving the IoT-SHM are the challenges in the miniaturization of sensors, with the corresponding drop in both the size and the power consumption.

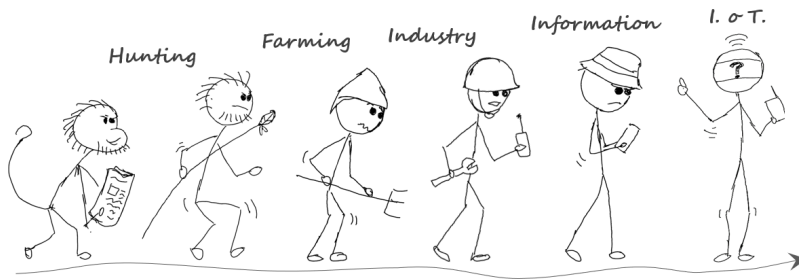


Figure 1-1. Technological revolutions have altered the lifestyles of human beings.

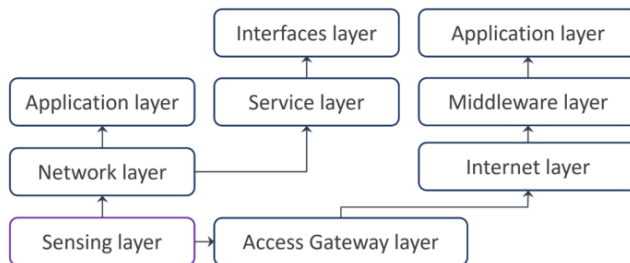


Figure 1-2. Examples of layers in the IoT.

1.1.2 FIBRE OPTIC BASED SHM

Fibre optic sensors provide an excellent solution to many of the technical challenges facing the sensors of new IoT-SHM systems. Compared to conventional electrical sensors, optical fibres (OFs) show several distinguishing advantages for the IoT: (i) they are passive in terms of electrical energy consumption - no need for continuous source of electrical power at the remote location; (ii) optical fibres are small in size and create insignificant disturbances for the integrity of the material when embedded inside a structural component; (iii) glass fibres are immune to electromagnetic interference and environmental corrosion; (iv) and finally, optical fibres have a long lifetime, exceeding 25 years [9,10]. These characteristics of OFs satisfy the crucial needs of IoT-SHM systems and offer advantages over typical electronic/mechanical sensors. Over 60 different optical fibre sensor types have been developed and many of them have already been applied to SHM [8,11–15]. The application of OFs enables IoT-SHM platforms to achieve a reliable and timely source of data in constructions, critical infrastructure and key components of vehicles, as seen from examples in Figure 1-3 [12,16–19].

Optical fibre sensors can be classified into single point-based, and distributed fibre optic sensors (quasi-distributed or truly distributed), as shown in Figure 1-4 (a). On single point OFs, the parameter of interest can only be measured at one specific location. If the OF is sensitive to the environment along its entire length, and able to monitor at various points, it is called a distributed optical fibre sensor (DOFS) [20].

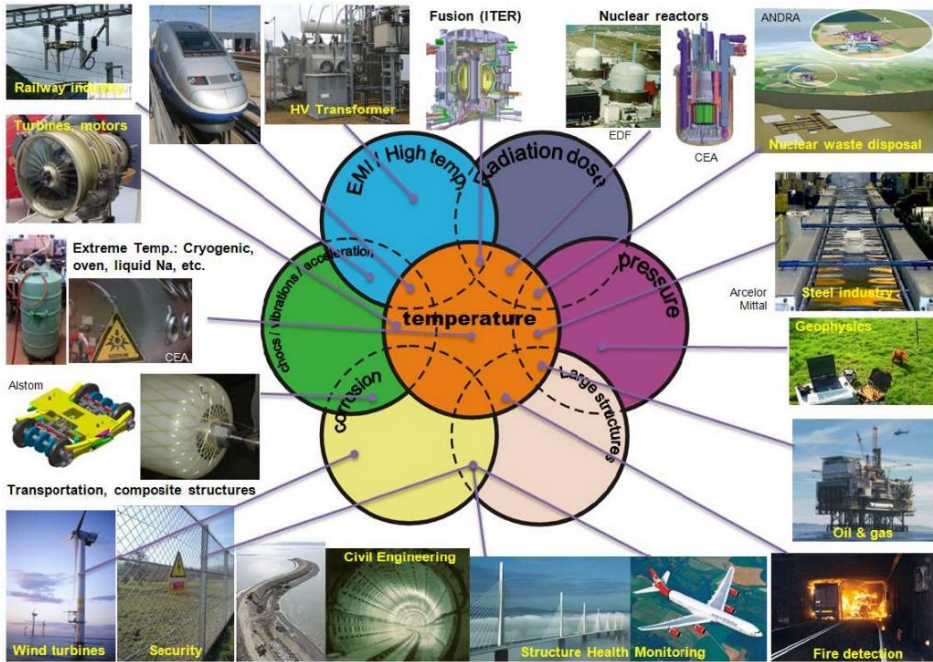


Figure 1-3. Optical fibre sensors based SHM in various industries, reproduced from [12].

DOFS can be achieved by using two strategies: a quasi-distributed sensor array and a true distributed sensor array. As shown in Figure 1-4(b), the quasi-distributed sensor is achieved by placing multiple point sensors, such as Fibre Bragg gratings (FBG) or Fabry–Perot sensors (FP) at certain intervals along the fibre length, typically about 10 sensors/fibre and, if multiplexed by wavelength, up to 1000 sensors per fibre. However, such a multiplexed sensor array is still unable to detect events that happen between any of the two discrete point sensors. In a truly distributed sensing system, the optical fibre works simultaneously to transmit the information and to sense the local external variables [21]. The sensing region is distributed along the entire optical fibre length. When the light passes through the fibre, the intrinsic scattering

phenomena, called Rayleigh scattering, Stokes scattering and anti-Stokes scattering are utilized to measure external perturbations along the length of the OFs (Figure 1-4(b)) [22].

The features of distributed optical fibre sensors make the SHM platform using them serve similarly to the nervous system of the human. As shown in Figure 1-4(c), the DOFS can be used to make distributed measurements of strain and temperature along distributed lines across the whole airplane.

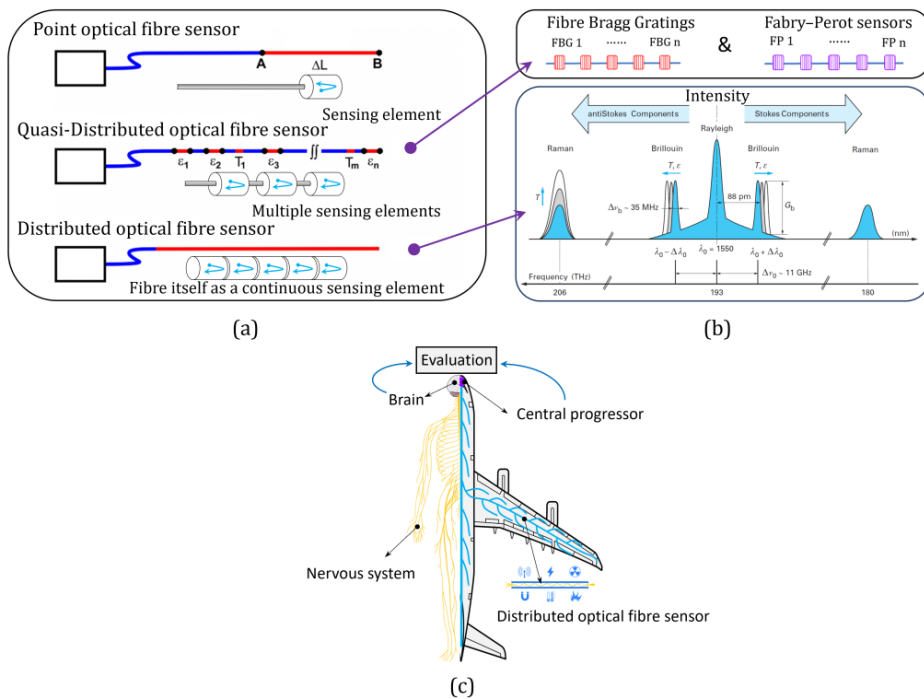


Figure 1-4. Classification of optical fibre sensors (a), the light intensity spectrum and the main working principles of distributed optical fibre sensors (b), DOFS applied for the SHM platform in aviation (c), from [11,23–25].

1.2 OPTICAL FIBRE SENSING

1.2.1 DOFS

The experimental investigations discussed later in the Thesis are carried out by using the Rayleigh backscattering based OFDR (optical frequency domain reflectometry) measurement principle. However, to give a broader context to this specific measurement method, an overview and categorization of optical fibre sensing principles is first presented in this Section.

When a monochromatic laser light (the light from the laser has a single wavelength) propagates through an optical fibre, a small portion of the light becomes scattered by the material [26]. Most of the photons are elastically scattered, and it is called Rayleigh scattering. A smaller fraction of the photons are inelastically scattered, and corresponding phenomena are called Brillouin scattering and Raman scattering. In elastic scattering, the energy of the incident photons remains the same, only its direction becomes changed. In inelastic scattering, both the energy and the direction of the photons are changed by the interaction. As shown in Figure 1-5, Rayleigh scattering occurs when the photons collide with inhomogeneities in the waveguide material; Raman scattering occurs when incident light photons interact with thermally excited molecular vibrations; Brillouin scattering is the result of incident light photons interacting with bulk molecular vibrations. These three scattering phenomena are further detailed in the following sections.

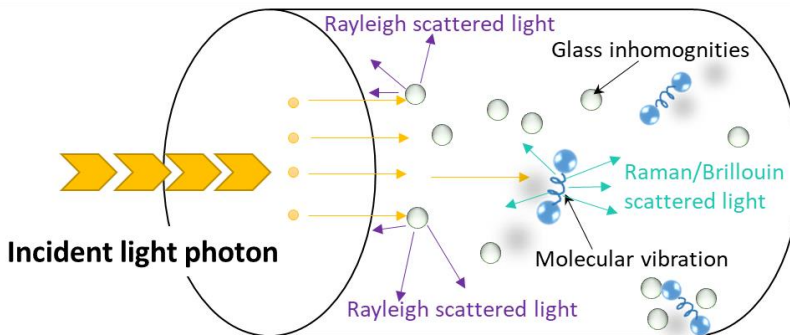


Figure 1-5. Classification of scattering phenomena in the optical fibre sensor.

1.2.2 RAMAN SCATTERING

The details of Raman scattering are discussed for example in [27–29]. As shown in Figure 1-4 (b), the intensity of Raman anti-Stokes scattering depends only on the local temperature of the optical fibre, while its Stokes scattering intensity is not affected by the temperature. This makes Raman scattering suitable for distributed temperature sensing along the DOFS as shown in Figure 1-6(a). The temperature is calculated by evaluating relative intensities $R(z)$ of Raman Stokes I_S and anti-Stokes I_{AS} components as follows [27,28]:

$$R(z) = \frac{I_{AS}}{I_S} = \left(\frac{\lambda_S}{\lambda_{AS}} \right)^4 e^{-\Delta E/k_B T} = \left(\frac{\lambda_S}{\lambda_{AS}} \right)^4 e^{-\hbar\Omega_R/kT} \quad (\text{Equation 1-1})$$

Where λ_S and λ_{AS} are Stokes and anti-Stokes wavelengths respectively. Ω_R is the Raman frequency shift, e is Euler's number, h is Planck's constant and k is the Boltzmann constant. In addition, ΔE is Raman energy shift and T is the temperature of the optical fibre. The temperature resolution of DOFS based on Raman scattering can be ca. 0.1°C, and a spatial resolution of 1 m for the 8 km sensing range and 5 m for up to 40 km sensing range have been reported [29].

1.2.3 BRILLOUIN SCATTERING

The details of Brillouin scattering in the optical fibre are discussed in references such as [22,28,30,31]. Brillouin scattering in the optical fibre is an inelastic interaction process between the photons of the incident laser light and the variation in the glass material. This material variation is due to the bulk pressure wave produced by a traveling acoustic wave (or acoustic phonons) within the optical fibre. The acoustic wave is set off by thermally induced molecular vibrations. Refractive index fluctuations are induced by these acoustic wave pressure variations. The Brillouin frequency shift (BFS) is expressed analogous to FBGs as [30]:

$$\nu_B = \frac{2n_{\text{eff}}V_L}{\lambda_p} \quad (\text{Equation 1-2})$$

where n_{eff} is the refractive index of the waveguide, V_L is the acoustic wave velocity, and λ_p is the wavelength of incident light. The acoustic wave velocity

and the refractive index are both sensitive to the temperature and strain in the optical fibre. When the temperature and strains change, the BFS ν_B is considered to be linearly related to both of them. The DOFS based on Brillouin scattering (Figure 1-6 (b)) are able to have a sensing range up to 50-100 km, with spatial resolutions in the meter range. The finest reported spatial resolution is 2 cm, when the sensing range is reduced to 2 km [31].

1.2.4 RAYLEIGH SCATTERING

Rayleigh scattering is induced by the interaction between the photons of incident light and small-scale inhomogeneities of the optical fibre. The physical structure of the DOFS used in this work consists of a silica core, a silica cladding and a polymer coating (other waveguide and coating materials can also be used). Rayleigh scattering happens when a photon penetrates a medium composed of inhomogeneous regions in the material whose sizes are much smaller than the wavelength of the light. More specifically, in the fibre core which is the waveguide, Rayleigh scattering is caused by impurities with variable refractive index, which are due to glass composition or density fluctuations in small-scale, generated during the fibre fabrication process [32]. When a laser pulse is injected into the optical fibre, this inhomogeneity-induced Rayleigh scattering occurs along the entire optical fibre and the Rayleigh backscattering signal will drop over the fibre length. By measuring Rayleigh scattering loss in the fibre length direction worked with the location information through optical time domain reflectometry (OTDR), Rayleigh backscattering were firstly used to locate fault points in the telecommunication fibre as shown in Figure 1-6 (c) [24]. Today the Rayleigh scattering phenomenon is more used for high resolution distributed strain and temperature monitoring. Based on optical frequency domain reflectometry (OFDR) technology, the measurement system achieves a high resolution of measured perturbations in strain and temperature, and a good spatial resolution (typically a few millimeters), but the maximal length of the sensor is limited to a relatively short distance (70 m) in the case of specific OBR-4600 equipment. The measurement system using the Rayleigh scattering is introduced later in Section 1.2.5 and in Section 2.1.

Introduction

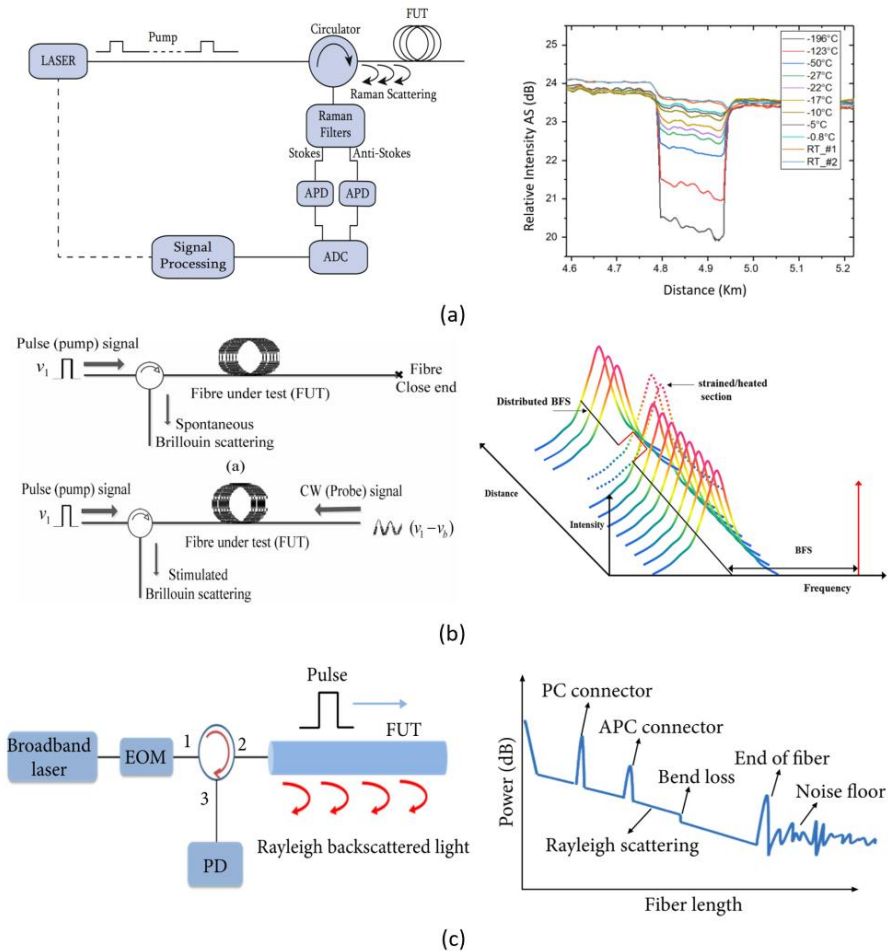


Figure 1-6. Three types of DOFS systems based on optical scattering: (a) Raman, (b) Brillouin, and (c) Rayleigh backscattering with respective light intensities obtained in typical OTDR system, reproduced from [19,24,30,33].

1.2.5 OPTICAL FIBRE DATA PROCESSING METHODS

In the DOFS, the measurement and the signal processing from the backscattering are performed in a reflectometer based on either optical time domain reflectometry (OTDR) or optical frequency domain reflectometry (OFDR) technology.

OTDR

Using the OTDR principle [16], the laser sends incident optical pulses and the location of the perturbation on the optical fibre is determined by measuring it from the arrival time of the backscattered light. As shown in Figure 1-7, the input pulse is launched into the optical fibre, and the light becomes scattered (such as Rayleigh backscatter) when the input pulse travels along the fibre. The backscattered signal from the optical fibre is measured by the photo-detector, and then integrated as a function of time. The location of the specific point of backscattering (D_i) is achieved by using the time delay between the forward incident light pulse and the corresponding backward scattered light as shown in Figure 1-7. By this way, the measured Rayleigh backscattering signal is transferred into a level of attenuation along the optical fibre as a function of position on the fibre, while the attenuation provides information of key features, such as splices, bends and breaks. More detailed, the received optical power (Rayleigh backscattering signal), P_{RS} , at position z is expressed as:

$$P_{RS}(z) = R_t \cdot R_R \cdot P(0) \exp\left[-2 \int_0^z \alpha(x) dx\right] \quad \text{(Equation 1-3)}$$

where $P(0)$ is the input optical peak powder, R_t is the spatial resolution, R_R is the equivalent Rayleigh reflection coefficient, α is the total loss coefficient of the fibre. The return power will decay significantly along the fibre due to the fibre loss as shown by decreasing backscatter signals in Figure 1-7. When there is signal loss in the optical fibre, such as a connector, bend, or break, the received optical power-length pattern displays sudden peaks and dips caused by Fresnel reflections, as shown in Figure 1-6 (c).

For a measurement technique, two of important performance parameters are the sensing range and spatial resolution. Spatial resolution R_t is dominated by the pulse width t as follows:

$$R_t = tc / (2n) \quad \text{(Equation 1-4)}$$

where c is the velocity of light in vacuum, n is the index of refraction and t is the pulse width. The spatial resolution can be improved by decreasing the width of the input pulse. However, the sensing range along the optical fibre will be shortened due to the weaker energy of the incident light as signal-to-noise-ratio decreases. Thus, the sensing range and the spatial resolution in the OTDR have

to be balanced. A measurement technique that provides better spatial resolution while maintaining a sufficient sensing range is always desirable.

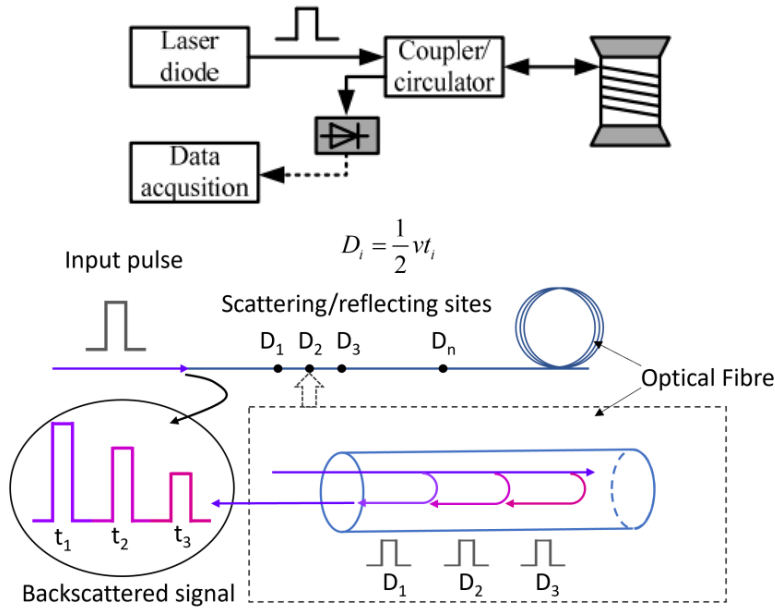


Figure 1-7. Illustration of the optical time domain reflectometry (OTDR) technique, reproduced from [34,35].

OFDR

In order to improve the detection sensitivity and the spatial resolution in the DOFS based on e.g. Rayleigh scattering, a frequency domain reflectometry technique has been proposed and developed [32,35]. This technique can be realized by using two different types of reflectometry: low coherence optical frequency domain reflectometry (OLCR) or optical frequency domain reflectometry (OFDR or C-OFDR). Currently, OFDR is more commonly used than OLCR and is the method utilized in this study. Therefore, OFDR is introduced in the following text. The primary distinctions between these two methods are the type of optical source and reference arm employed. OLCR involves a broad-band source and a reference arm with a moving mirror, whereas OFDR employs a swept laser source and a fixed reference arm. Compared to OTDR, which has

been used for numerous years, OFDR is newer technology and enables some advantages over the OTDR [9,24]: (i) higher spatial resolutions and better sensitivity is achieved; (ii) lower noise levels are reported; (iii) and no dead zones occur in the measurement. The performance of DOFS based on OTDR and OFDR technologies is summarized and compared in Table 1-1 [9,24,36].

Table 1-1. Comparison of DOFS based on OTDR and OFDR technologies [9,24,36].

Sensing principle	Measurement principle	Advantages	Disadvantages	Applications	Suppliers
Rayleigh scattering	OTDR	Long sensing distance	Dead zone, Low spatial resolution	Loss, vibration and breakpoint	LUNA
	OFDR	High spatial resolution (mm range)	Short sensing distance, long measuring time	Loss, vibration and breakpoint, temperature and strain	LUNA
Raman scattering	OTDR	Long sensing distance	Low spatial resolution	Temperature	Halliburton, Sensornet. AP Sensing
	OFDR				
Brillouin scattering	OTDR	Long distance 50 (km), high spatial resolution (meter range)	Long measuring time	Temperature and strain	OZ Optics, Omnisens SA, Neubrex
	OFDR	High spatial resolution (centimeter range)	Long measuring time		

In this work, the OFDR sensing system utilizes a measurement device based on the Mach-Zehnder interferometer [32,35]. Mach-Zehnder interferometer is designed for measuring the phase shift due to the relative length difference of the two arms of the interferometer. The classic Mach-Zehnder interferometer consists of two mirrors, two splitters, and a detector. The incident light is initially split into two beams, which travel through two different paths, referred to as the test arm and the reference arm. Two beams are reflected independently by the mirrors and recombine at the second splitter. The detector records an interference fringe (as shown in Figure 1-8 (a)) that depends on the phase difference caused by the optical path difference between the test arm and the reference arm.

In Figure 1-8(b), it is illustrated that the OFDR system generates incident light through a swept laser source, which linearly scans over the optical frequency range. Directional couplers are utilized to divide the light into a reference arm and a test arm. Backscattered light from the test arm interferes with the reference arm, and the resulting interference fringe is detected by the photo-

detector. The periodic signal observed by the detector possesses a frequency that relies on the location of the fibre point scattering the light back, with the frequency of the interference signal increasing as the point moves further away from the detector. Since the detector receives backscatter signals from all points along the fibre, a frequency domain analysis using the Fourier transform technique is employed to separate the accumulated signal as shown in Figure 1-8 (c). The frequencies produced through this separation correspond to signal locations in the fibre, while the amplitude of each frequency component corresponds to the strength of the respective reflection.

To further elaborate on the application of OFDR in DOFS sensing, it is essential to extract two crucial parameters from the system. These parameters are the interference frequency and the interference amplitude, both of which can provide valuable information. The interference frequency is related to the time delay and can be used to determine the location of an event along the fibre. On the other hand, the interference amplitude is linked to the reflectivity and can be used to quantify the severity of an event, such as strain, temperature variations and chemical environment. These two parameters play a critical role in the functioning of the OFDR for DOFS sensing. To provide more detail, consider the back-reflected light that occurs at a single point located at position L along the fibre in the test arm. The beating signals of intensity $I(t)$ obtained by the detector at time t can be expressed as follows [37,38]:

$$I(t) = 2 \cdot E_1 \cdot E_2 \cos(\alpha \Delta \tau t + \Delta \tau \omega_0), \quad \Delta \tau = \frac{2nL}{c} \quad (\text{Equation 1-5})$$

where c is the speed of light in vacuum, n is index of fibre refraction, E_1 and E_2 are the field intensity of the reference arm and the test arm, $\Delta \tau$ is the time delay (optical path difference) between test signal and reference signal, α is the laser frequency sweep rate and ω_0 is the starting angular frequency.

Position function- Interference Frequency:

According to Equation 1-5, the frequency of the interference fringe f_{OFDR} is expressed as:

$$f_{OFDR} = \tau \frac{\partial \nu}{\partial t} + \nu \frac{\partial \tau}{\partial t} \quad (\text{Equation 1-6})$$

The laser turning rate dv/dt is known to be a constant, so the f_{OFDR} is linearly proportional to the τ , which refers to the distance of the backscatter point along the optical fibre as shown in Figure 1-8 (c) (if the flection delay induced by the event is changing in time, i.e. $d\tau/dt$, the above equation is distorted. For remainder of this discussion, we assume the fibre is stationary and the second term in Equation 1-6 negligible).

Event quantification- Interference amplitude:

As it is well-known that the energy of a wave is proportional to the square of the wave amplitude. In the OFDR system, the resulting optical field intensity E_3 detected by the detector at time t is expressed as [38]:

$$E_3(t) = E_2 \cdot e^{i(k(t) \cdot L_2 - \omega t)} + E_1(t), \quad k(t) = \frac{n}{c} \cdot (\alpha t + \omega_0) \quad (\text{Equation 1-7})$$

where L_2 corresponds to L , E_1 is from the reference arm, which does not change with the disturbance on the test optical fibre, while E_2 is from the test arm, which is determined by the refractive index n that can be affected by environmental factors such as temperature.

Spatial resolution:

$$\Delta Z = \frac{c}{2n\Delta\nu} \quad (\text{Equation 1-8})$$

Where ΔZ is the spatial resolution and $\Delta\nu$ is the frequency range of the laser. Nowadays, the spatial resolution of OFDR can be on the order of millimeters if using a wavelength sweep range of a few tens of nanometers. However, this value is not a physical boundary but rather a limitation imposed by data processing devices[39].

It should be emphasized that the techniques discussed earlier are only effective when the interfering beams' states of polarization are identical. However, the intrinsic birefringence of the fiber under test can lead to a degradation of the interference process in practical applications. To address this challenge, a modified scheme that employs polarization diversity detection is necessary. For example, OBR 4600 device (the device utilized in this study and will be discussed

in detail in section 2.1.2), which comprises two cascaded Mach-Zehnder interferometers, two polarization controllers, and a polarization beam splitter, can accurately identify backscattered events along the optical fiber under test, even in the presence of polarization variations.

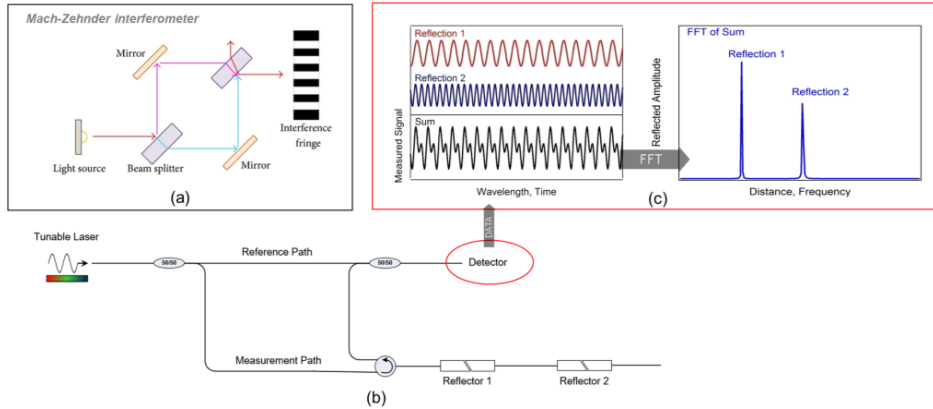


Figure 1-8. (a) classic Mach-Zehnder Interferometer configuration, (b) OFDR basic configuration and (c) typical amplitude and frequency of the signal from the photo detector of the DOFS with different optical path length differences, reproduced from [32, 38].

1.3 SENSOR INTEGRATION TECHNIQUES

When acting as strain sensors, the DOFS need to be integrated into the host structure to assure the sensor fibre deforms together with the substrate material. Thus, the performance of the OF depends to a large extent on the sensor integration technique [40]. Until now, the integration of OFs has not yet been solved satisfactorily for many practical composite material applications [41]. A limited scope literature review was carried out, identifying several basic types of attachment methods typically used for fixing the optical fibres, as summarized in Table 1-2 [42].

Table 1-2. An overview of optical fibre attachments and adhesives used, from [42].

Substrate	Attachment method	Adhesives	Application case
Concrete, steel and timber	Surface mounting	Cyanoacrylate, epoxy, polyester, UV curable polymers	Strain, cracking and vibration [43–47]
	Pre-embedded bar	Epoxy, silicone, rubber	Strain [47–50]
	Specialized optical cables	Epoxy	Creep strains, temperature [51]
Thermosets and thermoset composites	Surface mounting with or without packaging	Cyanoacrylate, epoxy	Strain and stiffness degradation [52–54]
	Embedding	Epoxy resin	Impact damage [55]
Thermoplastics and thermoplastic composites	Surface mounting with or without packaging	Cyanoacrylate, epoxy	Strain [56,57]
	Embedding	Hand lay-up	Residual strains [58]
	Embedding	Partially fixed with epoxy, ultrasonic welding	Relaxation [59,60]
	In-situ embedding (3-D printing)	Inside the polymer	Residual strains and defects [61]

For structural engineering applications practitioners tend to adhere the OFs directly on the surface by using rigid glue [43–47], or pre-embed the OF either in a rigid package [47–50] or by using specialized optical cables [51] before the attachment procedure. Different thermoset-based structural adhesives are used for bonding the fibre on traditional structural materials such as concrete, timber and steel. Fibre reinforced polymer (FRP) composites, where carbon or glass fibres are embedded in a polymer matrix, are increasingly used in aerospace, transportation, infrastructures and sporting goods [62]. The matrix of structural FRPs has typically been a thermosetting polymer. Today, by replacing the thermoset matrix in the composite with a thermoplastic matrix, great improvements for impact resistance, recyclability, manufacturing cost, and environmental performance are reported [63]. The OF integration technology for thermoplastic and thermoset composites remains similar to traditional structural materials. Similar methods are directly adopted, as shown in Table 1-2 and in Figure 1-9. Optical fibres and their packages are either surface-mounted by structural adhesives [52,56,57] or embedded directly inside the composite or polymer structures [55,59,61,64].

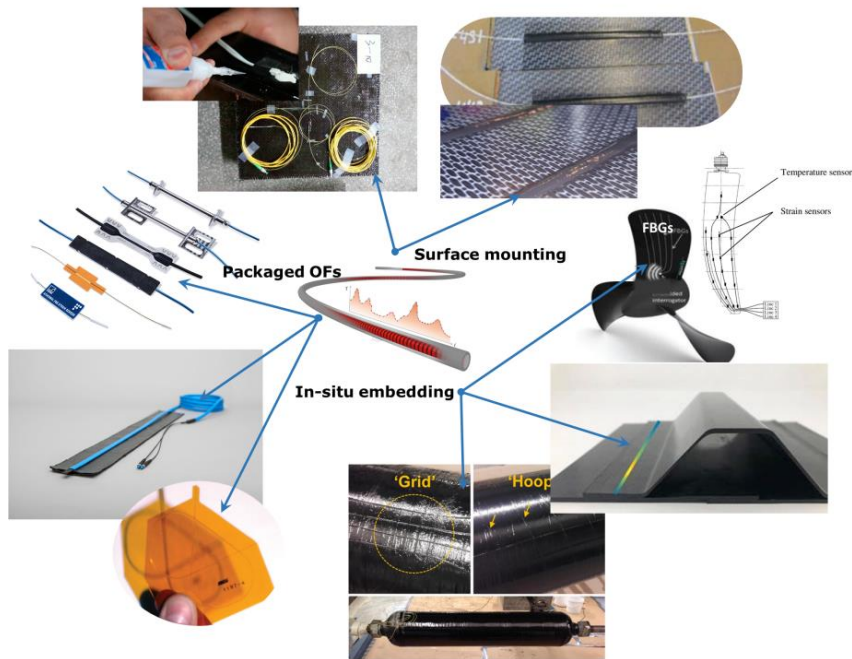


Figure 1-9. OF integration methods for FRP structures, images from [54,55,57,65,66].

For composite structures, the OFs can be embedded directly inside the composite material during the manufacturing process to enable good strain transfer and to protect the sensor better from mechanical and chemical damage. However, this type of OF integration is often hindered due to the following disadvantages: (i) the locations of the OFs can not be chosen with flexibility and the intended OF ingress and egress regions may not be compatible with the manufacturing method; (ii) the OFs can move about with the flow of matrix during manufacturing, changing the location of embedded OFs; (iii) the diameter of the OFs ($\geq 150 \mu\text{m}$) is usually larger than the diameter of glass fibres ($3 \mu\text{m} \dots 20 \mu\text{m}$) or carbon fibres ($5 \mu\text{m} \dots 10 \mu\text{m}$), thus the occurrence of voids, resin pockets or bent structural fibres around the embedded optical fibres can locally affect the strength of the composite; (iv) light attenuation in the OFs can be induced by excessive fibre bending. Bending may occur at the edge of the laminate, where the matrix flows out during curing. The fabric structure of structural fibres can also induce micro-bending effects; (v) high shrinkage of the matrix brings a birefringence effect to the OFs, leading to distortions of the measured signal spectrum instead of peak shifting (Birefringence is a double refraction phenomenon, whereby a ray of incident light is split by polarization into two rays having different paths within the glass).

The surface bonding solution appears less problematic from the manufacturing aspect than the embedding approach. The OFs can be attached on the surface of the composite component after the manufacturing process is completed. Surface bonding allows for more flexibility in the attachment process, and gives better opportunities for replacing any broken OFs. Kuang et al. [67] compares data from the embedded and the surface-bonded OFs fixed on the surface of the same thermoplastic fibre-metal laminate. Experimental results show that strains from the embedded FBGs exhibit good agreement with surface-bonded FBGs. Surface bonding is less practically challenging than embedding, but it also has its own notable disadvantages.

- Thin and rigid bonding is necessary for accurate transfer of strain.
- Some of the structural adhesives need to be cured at elevated temperatures, introducing unwanted heat and residual strains into the host structure.
- In order to improve the handling of fragile OFs, naked fibres are often packaged to make cables or instrumented “patches.” However, this increases the overall sensor size and the fibre sensitivity becomes compromised due to the packaging.
- Optical fibre surface attachments are still mainly done by hand, due to the lack of automated, well-controlled fibre integration methods. Human variability can induce inconsistent bonding that causes a non-uniform strain transfer from the host structure to the sensor.
- In order to minimize creep strains, most structural adhesives in use are thermosetting polymers. It is well known that thermoplastic composites develop a low adhesive bonding strength with thermoset adhesives. Thermoplastic fusion based attachment can therefore be a better solution for thermoplastic composites. Up to very recently, no research work on surface-bonded OFs by using thermoplastic fusion has been reported.

Bonding between the OFs and thermoplastics or thermoplastic composites requires consistency. The lack of automated bonding solutions deserves a deeper research focus to overcome these automation and consistency related practical challenges.

1.4 COUPLED SENSITIVITY OF THE OPTICAL FIBRE

As practical evidence shows, even a perfectly attached optical fibre can sometimes give unreasonable strain values during routine measurements. One significant limitation for using specific types of OFs (e.g., FBGs, Rayleigh backscattering OFDR) is their coupled sensitivity to both strain and temperature. The ability to distinguish between strain and temperature effects is critical for the future large-scale success of OF applications. For Rayleigh backscattering based OFDR, both temperature related changes in the refractive index of glass, and changes in the physical optical fibre length cause the Rayleigh backscattering spectral (RBS) shifts in frequency. Like FBGs, the RBS shift therefore shows a cross-sensitivity to both strain and temperature. Any temperature variation along the sensing fibre, if not accounted for, will introduce errors in the strain measurement. Similarly, any unexpected strain occurrence will introduce errors in the temperature measurement. Different approaches have been proposed to discriminate strain and temperature. An optical fibre sensor system comprising of two parallel OFs which have different temperature and strain sensitivities can be utilized to determine both temperature and strain [69,70]. Although both optical fibres in this system are sensitive to temperature and strain, their sensitivities are different and independent from each other [71,72].

One more significant aspect needs to be highlighted for strain/temperature discrimination methods of OFs based on Rayleigh backscattering. Based on analogy to FBGs, it is typically assumed that both mechanical strain and thermally induced effects have a linear effect on the RBS shifts. As an example, Rayleigh scattering-based DOFS have been successfully used for temperature measurements under thermal conditions [56,73], coupled with irradiation [74], or humidity [75]. In these investigations, RBS shifts were modeled using linear relationships to temperature with fairly good accuracy within the usual temperature ranges from ca. 0 °C to ca. 75 °C. However, trial measurements at NTNU have shown that obvious systematic measurement errors for linear fitting appear at high temperatures (> 80 °C) and at cryogenic low temperatures (< -73 °C). Open literature review indicates that decoupling of strain and temperature induced spectral changes has not been addressed in sufficient rigor thus far, especially for a wider range of thermal conditions, beyond typical inside and outside temperatures. Temperatures higher than 300 °C are not considered in this work, because the optical fibre polymer coating material starts to degrade in such high/temperature environment. When the temperature is above 700 °C in the silica single mode fibre without the polymer coating, significant changes in

the Rayleigh backscattered signal are observed due to the atomic diffusion and defect mobility. For extremely high temperatures (≥ 750 °C) or long-term exposure at 700°C, the Rayleigh backscatter signature can be altered significantly and this optical fibre becomes unfit for temperature sensing [18,45].

1.5 TECHNICAL GAPS

Based on state-of-the-art technical literature, there are gaps in understanding related to DOFS applications in thermoplastic composite structures, affecting the measurement accuracy and long-term measurements with optical fibre based sensor systems. A well-controlled practical OF integration process producing uniform attachment of OFs to thermoplastic components is currently still missing. Furthermore, the coupled strain/temperature sensitivity can introduce large errors for the signal interpretation. A new, more accurate calculation model for signal decoupling is therefore necessary to distinguish pure mechanical strains from pure thermal loading.

1.6 OBJECTIVES OF THE PHD PROJECT

In order to address the aforementioned technical gaps and provide new technical knowledge, improving on the shortcomings in current state-of-the-art, the main objectives of this research are formulated in Figure 1-10.

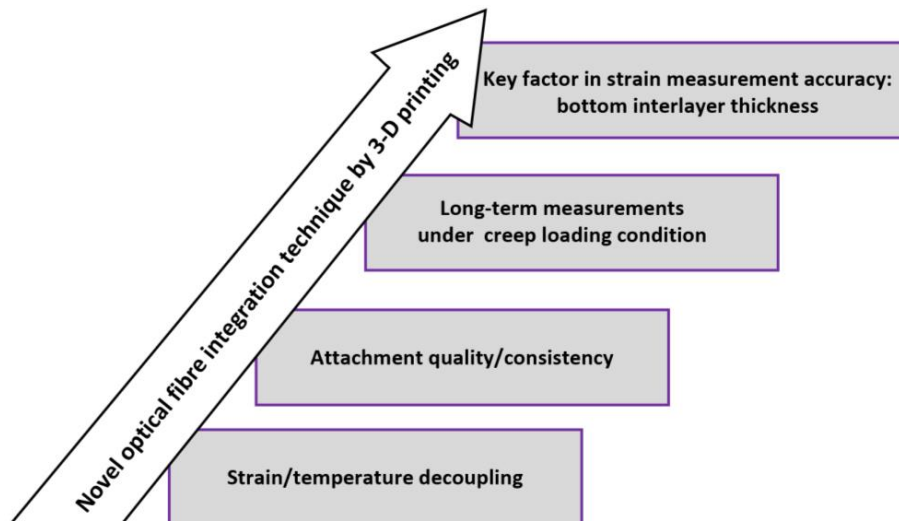


Figure 1-10. Research objectives.

In order to achieve the research goals, the following specific research questions (RQs) were formulated:

- RQ1. How can the OFs be integrated into thermoplastics or thermoplastic composite materials by utilizing the material extrusion 3-D printing process?
- RQ2. How to assess the quality and the consistency of the OF attachment? Comparison of OF strains to results from traditional strain measurement methods (strain gauge, contact extensometer).
- RQ3. Propose a more accurate calculation model for OF strain and temperature decoupling, applicable beyond the usual ca. ± 30 °C range around the room temperature.
- RQ4. How does the optical fibre measurement change under creep loading conditions (if and how does the strain transfer coefficient change)?

The improvements on the state-of-the-art, and the answers to these research questions are provided in the appended four scientific articles. This research proposes and implements a novel OF integration principle by material extrusion 3-D printing and investigates the long-term loading effects affecting the OF strain measurement accuracy.

1.7 THE STRUCTURE OF APPENDED PAPERS

This article collection-based PhD Thesis contains four published papers. The schematic in Figure 1-11 illustrates how the appended papers relate to the overall objectives of research. Each paper contributes to the overall aim and to the research questions posed. However, as independent entities, each of them naturally contains their own individual objectives, methods and findings. Papers are numbered chronologically in the sequence of publishing.

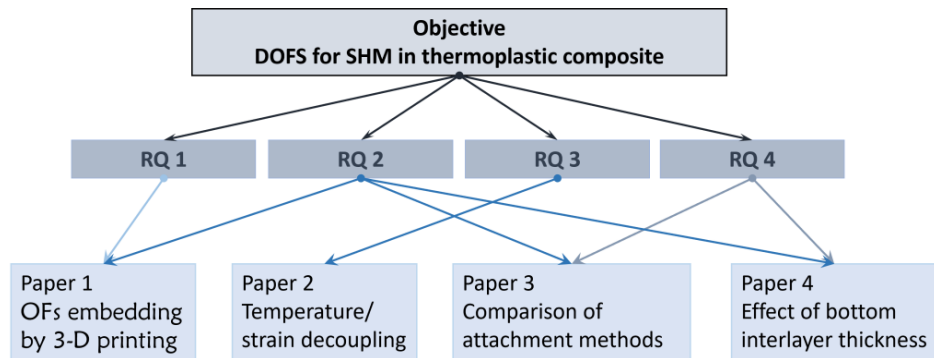


Figure 1-11. Structure of scientific papers related to research questions.

Appended papers:

- *Paper 1 – Novel in-situ residual strain measurements in additive manufacturing specimens by using the Optical Backscatter Reflectometry.*

Wang, Shaoquan; Lasn, Kaspar; Elverum, Christer Westum; Wan, Di; Echtermeyer, Andreas.

Additive Manufacturing, 2020; 32: 101040

The first article proposes and explores a novel OF integration technique by using material extrusion 3-D printing technology. The OFs are embedded inside fairly large blocks of PLA. Optical fibre strains are compared to strain gauge strains. The OF experiments give expected results, such as residual strain distributions and demonstrate how the detection of a large void inside the 3-D printed material can be achieved by using the DOFS.

- *Paper 2 – Accurate non-linear calculation model for decoupling thermal and mechanical loading effects in the OBR measurements.*

Shaoquan Wang and Kaspar Lasn.

Optics Express, 2021; 2: 1532-1544.

An accurate calculation model is proposed to distinguish pure mechanical strains from pure thermal loading based on the RBS shift measurements from distributed optical fibres. A non-linear temperature formula is derived from physics-based refractive index models. This formula enables high precision strain and temperature discrimination and improves the temperature measurement accuracy over an extended temperature range.

- *Paper 3 – Comparison of DOFS attachment methods for time dependent strain sensing.*

Shaoquan Wang, Erik Sæter, and Kaspar Lasn.

Sensors 2021; 21(20): 6879

This investigation clarifies how different optical fibre attachment methods for distributed strain sensing perform under time dependent loading. The OFs are attached on three types of substrates (metal, thermoset composite, and thermoplastic) by a machine-controlled attachment method (in-situ 3-D printing) and several widely used manual attachment methods. The quality of the bondline and its influence on the strain transfer is analyzed. Residual strains and strain fluctuations along the OFs are correlated to the fibre attachment method. The measurement accuracy of time-dependent DOFS strains is assessed by comparing them with contact extensometer strains.

- *Paper 4 – Integration of optical fibre sensors by material extrusion 3-D printing – the effect of bottom interlayer thickness.*

Shaoquan Wang and Kaspar Lasn.

Materials & Design 221 (2022): 110914

In this paper, a number of tensile creep experiments are conducted to test the performance of the optical fibre integration approach by 3-D printing method. OFs were placed inside thermoplastic embedding elements (similar to Paper 3), but at a controlled thickness from the substrate surface. Self-sensing experiments by optical fibres identified a uniform level of residual strains created by the 3-D printing attachment process. Furthermore, tensile creep testing revealed that distributed strain transfer coefficients along the optical

fibre sensors remain constant with time. A simple calculation method that accounts for the shear lag effect between the component strains and the optical fibre strains was derived from previous analytical work, and is validated with experimental data. This method allows to empirically predict the strain transfer coefficient for any optical fibre surface attachment with arbitrary embedding interlayer thickness.

1.8 STRUCTURE OF THE THESIS

The content in the main part of the Thesis is organized into four separate chapters as follows.

- Chapter 2 offers a short description of the materials, methods, and devices used.
- Chapter 3 summarizes the main results and gives answers to each of the research questions (RQs) separately.
- Chapter 4 outlines the conclusions of the Thesis.
- Chapter 5 gives recommendations for further work.

CHAPTER 2

EXPERIMENTAL METHODS

The research within this PhD Project utilizes two recently established methods of experimental work, namely the OBR technology and the material extrusion 3-D printing which were used for building the embedding element as optical fibre attachments. These two methods are central to the understanding of the technical contributions from this research. In addition, other well-established experimental equipment and testing methods such as electrical strain gauges, K-type thermocouples, universal testing machines, DSC and DMTA testing equipment, etc. were used in various experimental set-ups. However, to keep the focus on more novelty-related aspects, only the aforementioned two experimental methods are introduced in detail in this Chapter. The experimental details of other methods can easily be found in the appended full papers.

2.1 DISTRIBUTED OPTICAL FIBRE MEASUREMENTS

In this investigation, the strain/temperature measurements with optical fibres are conducted by using an Optical Backscattered Reflectometry (OBR) system based on OFDR. This distributed sensing system measures Rayleigh backscattering along the optical fibre sensor. By using a single mode fibre as the sensing element, continuously distributed sensing is achieved along the entire optical fibre length. This technology has demonstrated promising results for SHM applications in a wide range of fields due to its high spatial resolution and sensing sensitivity. Currently, spatial resolutions of 20 microns have been achieved, and the longest sensing distance can be 2 km [32].

2.1.1 OBR-4600 MEASUREMENT SYSTEM

As shown in Figure 2-1(a), the distributed optical fibre sensing system consists of a DOFS, a PC, an optical fibre switch, and the OBR-4600 interrogator device. The DOFS was obtained by splicing a data transfer cable to a bare optical fibre sensor. The sensing fibre is a single mode fibre SMB-E1550H from OFS Fitel. with

an operating wavelength of 1550 nm. It has a silica/silica/polyimide structure with a core diameter of 6.5 μm , a cladding diameter of 125 μm , and a coating diameter of 155 μm . The data cable is reinforced with a rubber jacket and ends with a pigtail. The preparation process of the DOFS is shown in Figure 2-1(b). The protective coating and the jacket of the fibres are first stripped out, leaving only the bare fibres. Two bare fibres are terminated by using a fibre cleaver to get as mirror-smooth and perpendicular fibre ends as possible. The two ends are aligned and welded together in the FITELE S178 splicing machine. Finally, a heat shrink tubing is used to protect the fused optical fibre from breakage. All separately prepared DOFS are first connected to an optical fibre switch and then to the optical fibre interrogator OBR-4600 from Luna Innovations.

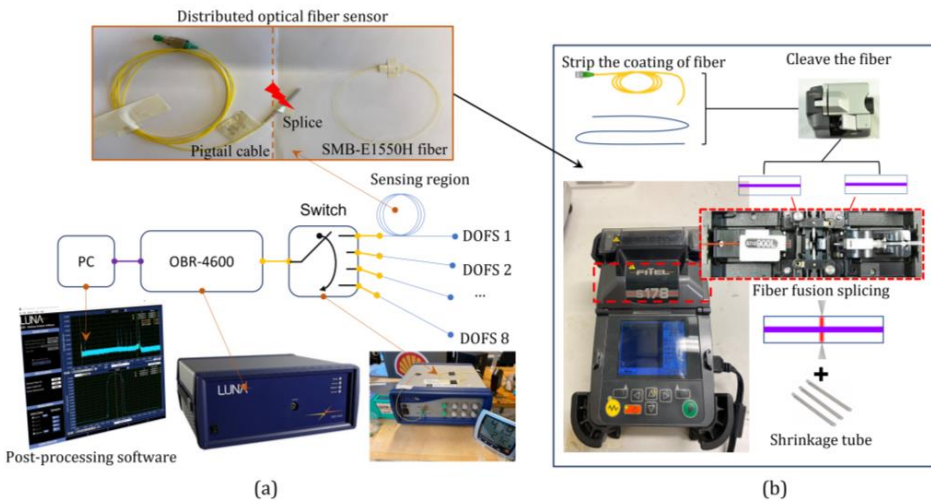


Figure 2-1. Distributed sensing system OBR-4600 (a) and optical fibre preparation process (b).

2.1.2 MEASUREMENT THEORY

The OBR-4600 device is composed of an active laser source and a swept-wavelength interferometer to measure the Rayleigh backscatter amplitude as a function of the optical fibre length [33]. During the measurement procedure, a swept-wavelength laser source emits a continuous wave light with a time-linear sweep of varying frequency. This light is directed into the 3 dB and then divided into two beams which are sent into the reference arm and test arm respectively. As the light passes through the optical fibers (OFs) in both arms, Rayleigh backscattering occurs along the entire length of the fibers. The resulting interference signal between the two arms is detected by a photo detector and stored as the backscatter pattern of the optical fiber under test. This backscatter pattern is then processed using a fast Fourier transform to yield the amplitude

as a function of length along the optical fibre under test, i.e. the fibre 'fingerprint', as shown in Figure 2-2(a). For each glass fibre, this backscattered spectrum has a random pattern, but it remains stable and unique in time. When an external stimulus, such as strain or temperature variation acts on the fibre, the initial 'fingerprint' becomes modified, showing a shift in the backscattered spectra. For example, thermal effects can induce variations to the refractive index due to the thermo-optic coefficient. The optical fibre length also changes simultaneously because of the coefficient of thermal expansion. By using this 'fingerprint' comparison approach from Rayleigh backscattering, an individual OF can provide thousands of measurement points distributed along its length.

The demodulation procedure of RBS shifts in OFDR system is implemented through the following steps [37]:

Step 1: Performing the measurements on the given optical fibre under reference and measurement state. Save the resulting beating signal in the time domain.

Step 2: Convert both the reference and measurement results from the time domain to the frequency domain using a fast Fourier transform (FFT). Then, convert the resulting frequency domain signals to spatial domain signals.

Step 3: A method called sliding window is used to divide the optical fibre virtually into short segments, as shown in Figure 2-2 (c), typically of the order of millimeters or centimeters, using a sliding window with a length that holds a certain numbers of data points of local beating signals.

Step 4: Convert each local spatial domain signals interval back to the time domain using an inverse FFT. The resulting windowed Rayleigh backscattering spectrum (RBS) pattern represent each interval along the optical fibre from the reference and measurement tests.

Step 5: Perform a cross-correlation of the reference and measurement RBS of each interval. The shifts in the correlation peak represent the RBS shifts of each interval along the optical fibre. These shifts can later be converted to changes in sensing parameters, such as temperature or strain.

All these steps are implemented in the post-processing software. In post-processing programme, the OF becomes divided into many virtual sensors, such as strain gauges, along the sensing length of the fibre. All virtual sensors have the same gauge length (GL) and sensor spacing (SS) between them as shown in Figure 2-2(c). In this way, optical fibres can multiplex thousands of virtual

sensors along a single fibre, setting up a distributed optical fibre sensor array. When the sensor spacing is less than the gauge length, it gives overlapping virtual strain gauges. The post-processing configuration of sensor spacing, and gauge length is normally selected as a compromise between high spatial resolution and unwanted noise occurrences. In this work, depending on the task different configuration of GL/SS are adopted such as 10/4, 10/0.5, 5/0.5 and 4/0.15 (mm/mm) [9,32,76]. Compared to other commercial DOFS systems for strain/temperature sensing, the OBR-4600 system has advantages in spatial resolution and accuracy as shown in Table. 2-1 [76].

In the measurement, Rayleigh backscattering spectral shifts (Δf in Figure 2-2 (a)) are first obtained and then scaled to give either distributed temperatures or strains with a high spatial resolution. That is, when distributed strains are being measured, they are actually being calculated from the averaged frequency shifts of each virtual sensor. The strains from the ingress and egress parts of the OF can therefore be artificially smaller than the natural strain of the host material surrounding it (Figure 2-3). Thus, the OBR measured/calculated strains often show gradual tapering of the strain curves in the ingress and egress parts of optical fibre the attachment (two disturbed regions l in Figure 2-3 (b)). The length l is reasonable to be assumed equal to the chosen virtual gauge length value. But the post-processing calculation uses a cross-correlation algorithm to compare the reference and the measurement spectra. It has been noted that when only a small portion of the virtual gauge exceeds the attached part of the OF, the obtained strain will not decrease just yet, due to the nature of cross-correlation algorithm [38,38]. Therefore, l turns out to be slightly smaller than the virtual gauge length [42] often in practical applications, only strains from the central quasi-constant region of the attached fibre (ROI in Figure 2-3(b)) are used to calculate the average OF strains to avoid the inaccuracies present in the strain measurements within ingress/egress regions l .

Experimental methods

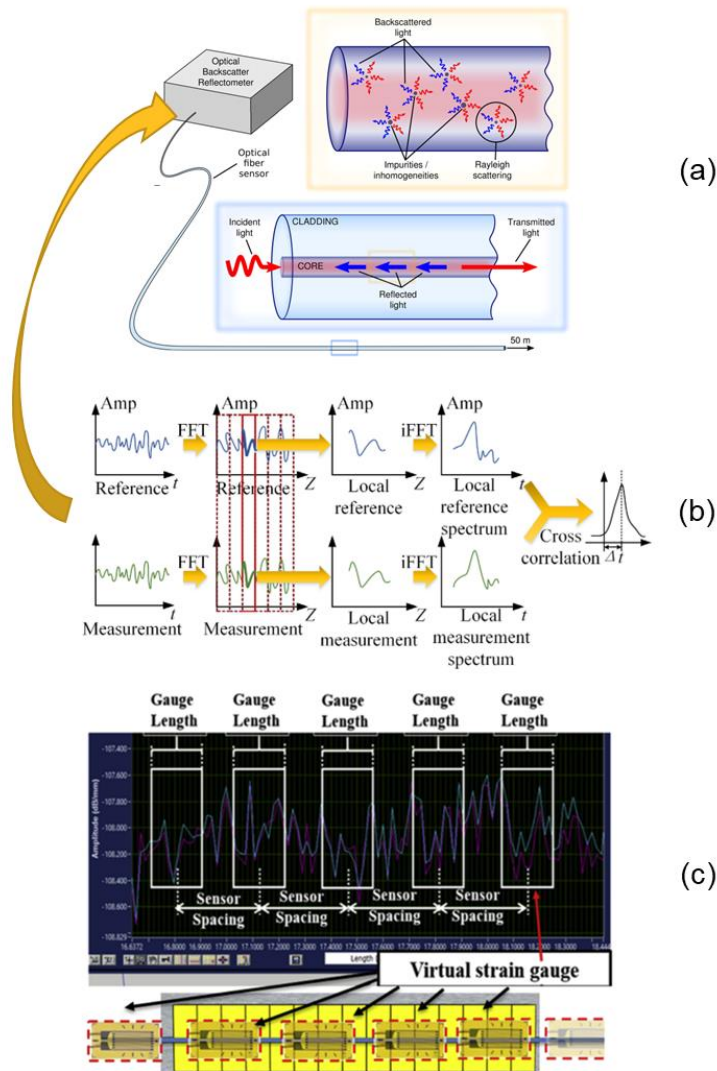


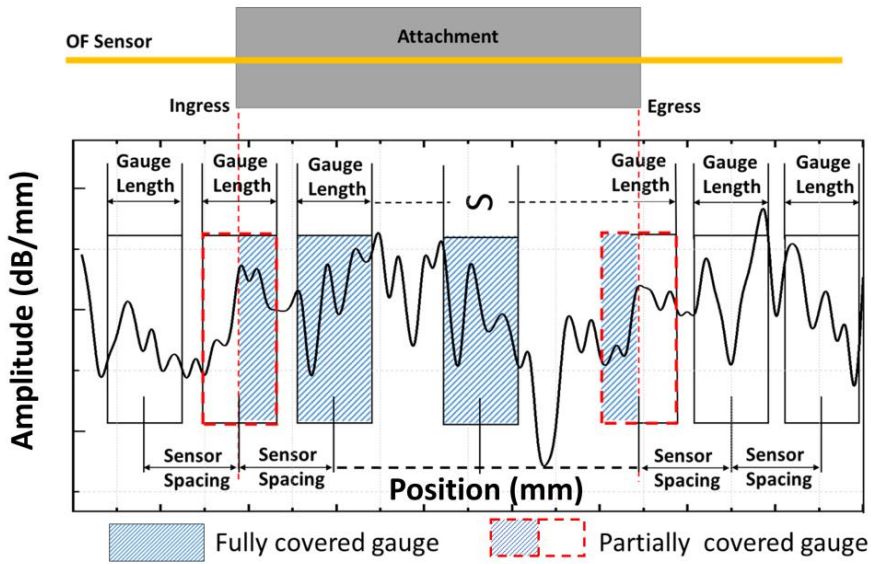
Figure 2-2. The working principle of the OBR 4600 interrogator (a), the demodulation procedure of RBS shifts (b) and the two main post-processing variables GL, SS (c), reproduced from [61,77,78].

Experimental methods

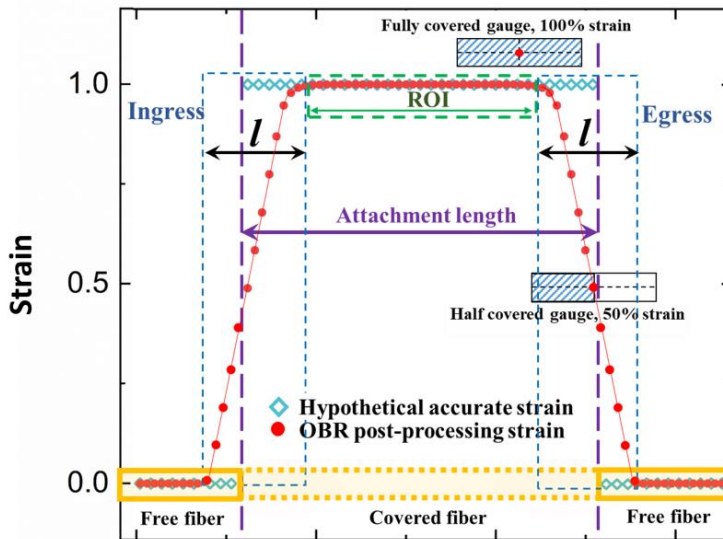
Table 2-1. Comparison of different commercial DOFS strain and temperature sensing systems.

	FBGs	Brillouin Optical Time Domain Reflectometer (BOTDR)	Brillouin Optical Time Domain Analysis (BOTDA)	OBR 4600
Strain accuracy	$\pm 1 \mu\epsilon$	$\pm 30 \mu\epsilon$	$\pm 10 \mu\epsilon$	$\pm 1 \mu\epsilon$
Spatial resolution	Related to grating length	0.1 m	0.1 m	0.001 m
Sensing length	-	100 km	100 km	2 km
Acquisition time	3 kHz	0-20 min.	As low as 5 min.	Related to sensing length (typical 5 to 10 sec for fibre length of less than 30 m)
Temperature accuracy	$\pm 0.1 \text{ }^\circ\text{C}$	N.A.	$\pm 1\text{-}2 \text{ }^\circ\text{C}$	$\pm 0.1 \text{ }^\circ\text{C}$
Equipment manufacturers (2022 status)	MicroOptics, Fibresensing, Insensys.	Yokogawa, NTT, Sensornet	OZ Optics, Omnisens, Neubrex	LUNA
System cost	3,000 - 15,000 €	> 100,000 €	> 200,000 €	> 100,000 €

Experimental methods



(a)



(b)

Figure 2-3. Illustration of OBR virtual sensors over the attachment length (a) and strains of disturbed regions l at the ingress/egress of the OF (b), from [42].

2.1.3 OBR SIGNAL DEMODULATION

The Rayleigh backscattering spectral shift (RBS shift, denoted by $\Delta\nu$ in Equation 2-1 and by Δf in Figure 2-2(a) earlier) between the spectra of the reference scan and the measurement scan are demodulated in the OBR Desktop software. Identical to the response of FBG sensors, the $\Delta\nu$ of the spectrum induced by an environmental perturbation (mechanical strain and/or temperature) is calculated from [18]:

$$-\frac{\Delta\nu}{\nu} = K_T\Delta T + K_\varepsilon\varepsilon \quad \text{(Equation 2-1)}$$

where ν is the mean optical frequency, and K_T and K_ε are the temperature and strain sensitivity coefficients, respectively. Typical values for germanium-doped silica are reported as: $K_\varepsilon = 0.78$, and $K_T = 6.45 \times 10^{-6} \text{ }^\circ\text{C}^{-1}$ [79]. The post-processing principle of the software assumes that either the temperature or the strain remains constant throughout the measurement. If both quantities are varied, post-processing has to be carried out manually by using the RBS shift output from the software.

2.2 MATERIAL EXTRUSION 3-D PRINTING

2.2.1 ADDITIVE MANUFACTURING

Additive manufacturing, also known as 3-D printing, is a fairly new manufacturing technology only recently (within the previous decade) adopted by the industry and the academia. Additive manufacturing methods are often classified into seven basic types, as shown in Figure 2-4. The method adopted in this work is based on small-scale material extrusion, normally called fused deposition modelling (FDM) or fused filament fabrication (FFF). The 3-D printed specimens are hereby built on a PRUSA I3 MK2S 3D printer. The FDM uses thermoplastic filaments or TPE to build layered structures with great geometric flexibility. This process has become very attractive for building small-scale structures for scientific purposes and to companies for rapid prototyping. Large scale printers exist too, but are not as wide-spread as small-scale material extrusion today.

FDM based 3-D printers have good potential for modifications and the low-cost characteristic of tabletop printers is very attractive for a wide set of users. Chopped and continuous glass/carbon fibres can also be mixed with

thermoplastic resin, extending the FDM into thermoplastic composite manufacturing.

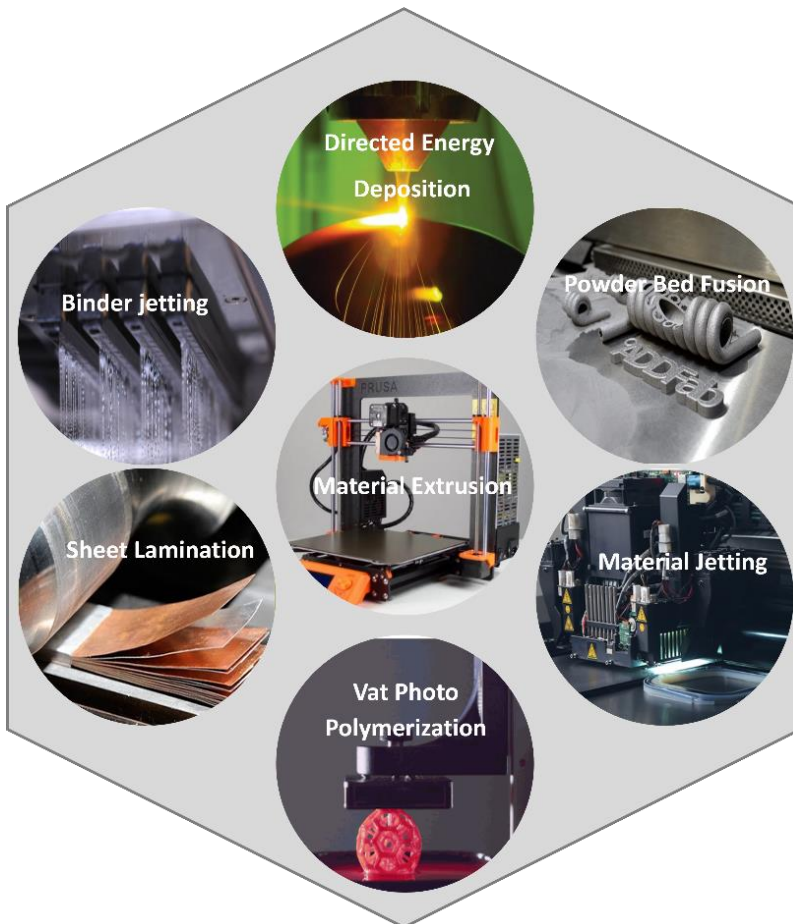


Figure 2-4. Different types of additive manufacturing processes [80,81].

2.2.2 FUSED DEPOSITION MODELING (FDM)

The working principle of FDM is based on layer-by-layer manufacturing, as shown in Figure 2-5(a). Before printing, the specimen design is generated and processed in a CAD program to define the desired geometry of the structure. Besides avoiding very steep over-hange, the choice of geometry is very flexible. The CAD model is first converted into a STL file, which is then processed by the slicer software to achieve the path for adding the material. The path of the nozzle is saved in the G-code language for the printer. In the printing process, a

Experimental methods

thermoplastic filament is uncoiled from the roll and fed into the heating chamber where the polymer is melted and extruded through the nozzle (Figure 2-5(b)). The nozzle moves accurately in the x-y-z directions defined by the G-code to build layer after layer of thermoplastic structure onto the build platform. Through repeating the process i.e. adding the liquid/semi-solid layers of plastic one above the other, the layers are bonded by thermoplastic fusion and the prescribed shape of the CAD model is eventually achieved.

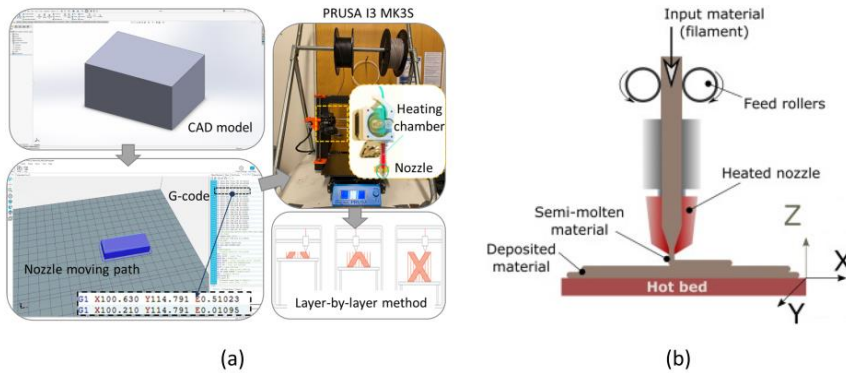


Figure 2-5. Fused Deposition Modeling (FDM) for 3-D printing: (a) workflow of the manufacturing process, (b) illustration of the extrusion system, reproduced from [82].

CHAPTER 3

MAIN RESULTS

3.1 OPTICAL FIBRE INTEGRATION BY MATERIAL EXTRUSION 3-D PRINTING (RQ1)

3.1.1 *THE EMBEDDING PROCEDURE*

A new working procedure had to be developed in order to embed the OF into the plastic specimen during the 3-D printing process. A methodology for optical fibre in-situ integration during the building procedure of the FDM 3-D printer was proposed. A schematic illustration of this embedding procedure is shown in Figure 3-1. There are four steps in the procedure: (1) G-code rewriting; (2) application of the OF alignment system; (3) the OF embedding process; (4) cooling and specimen detachment. This methodology is described in Paper 1 [61] and in Paper 4 [83].

There are two main challenges with embedding of optical fibre sensors during the small-scale material extrusion 3-D printing process.

Challenge 1: the embedding procedure itself. The OF will have to become encapsulated inside the thermoplastic melt extruded off the moving nozzle before it cools down. The moving nozzle however is very close to the substrate surface and may displace the OF, leading to damage on the OF. The viscous flow of the thermoplastic melt may also drag the OF, leading to its mispositioning.

Solution: The OF embedding procedure was first developed in Paper 1 [61] and later put to practice in Paper 3 [42] and in Paper 4 [83]. In order to avoid above mentioned problem, which can damage or displace the OF, the printing layer height was defined as 200 μm , slightly larger than the diameter of the OF ($160\pm 5 \mu\text{m}$). Optical cross-section microscopy was used to investigate the in-situ state of the embedded OFs. As shown in Figure 3-2, the embedding process did not bring any significant disturbances on the geometry and the immediate surroundings

of the optical fibre, i.e, the OF remains straight and properly embedded in the polymer. No visible damage was observed on the embedded OF and no unusual signal loss in the OBR measurements.

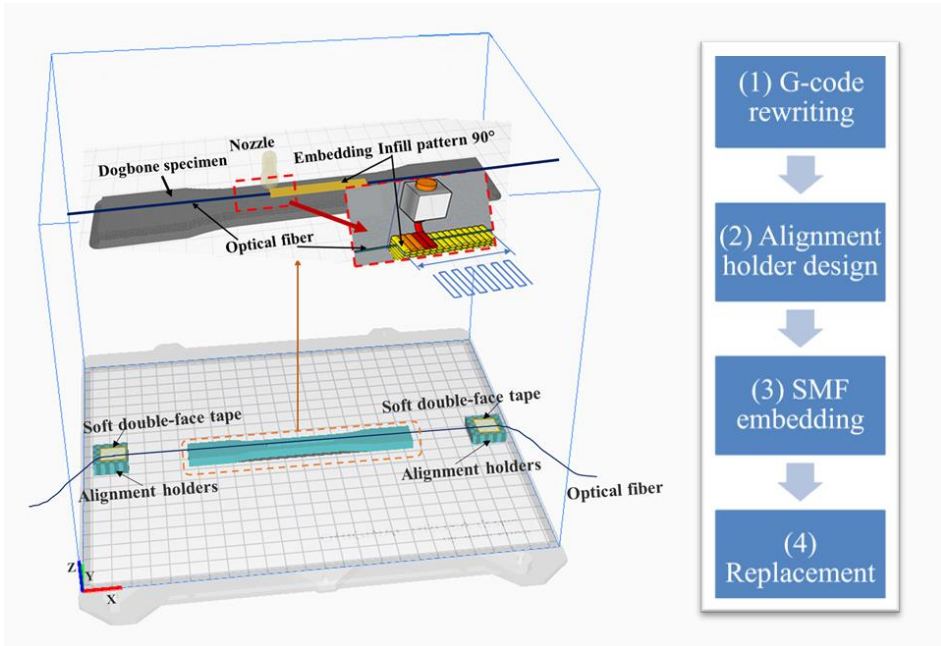
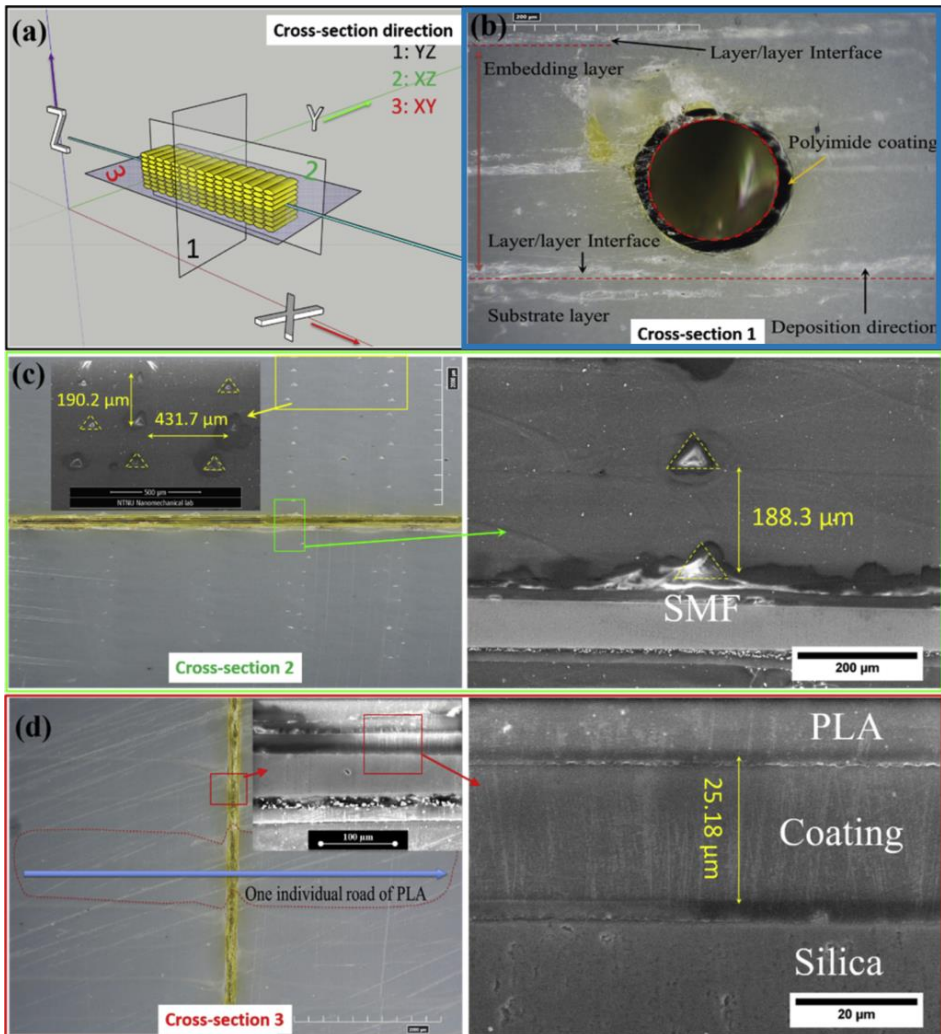


Figure 3-1. A schematic of the OF embedding procedure, from appended paper 1 [61].

Optical fibre integration by material extrusion 3-D printing (RQ1)



8877kiu

Figure 3-2. Example of optical cross-section micrographs taken from the embedded OF, from Paper 1 [61].

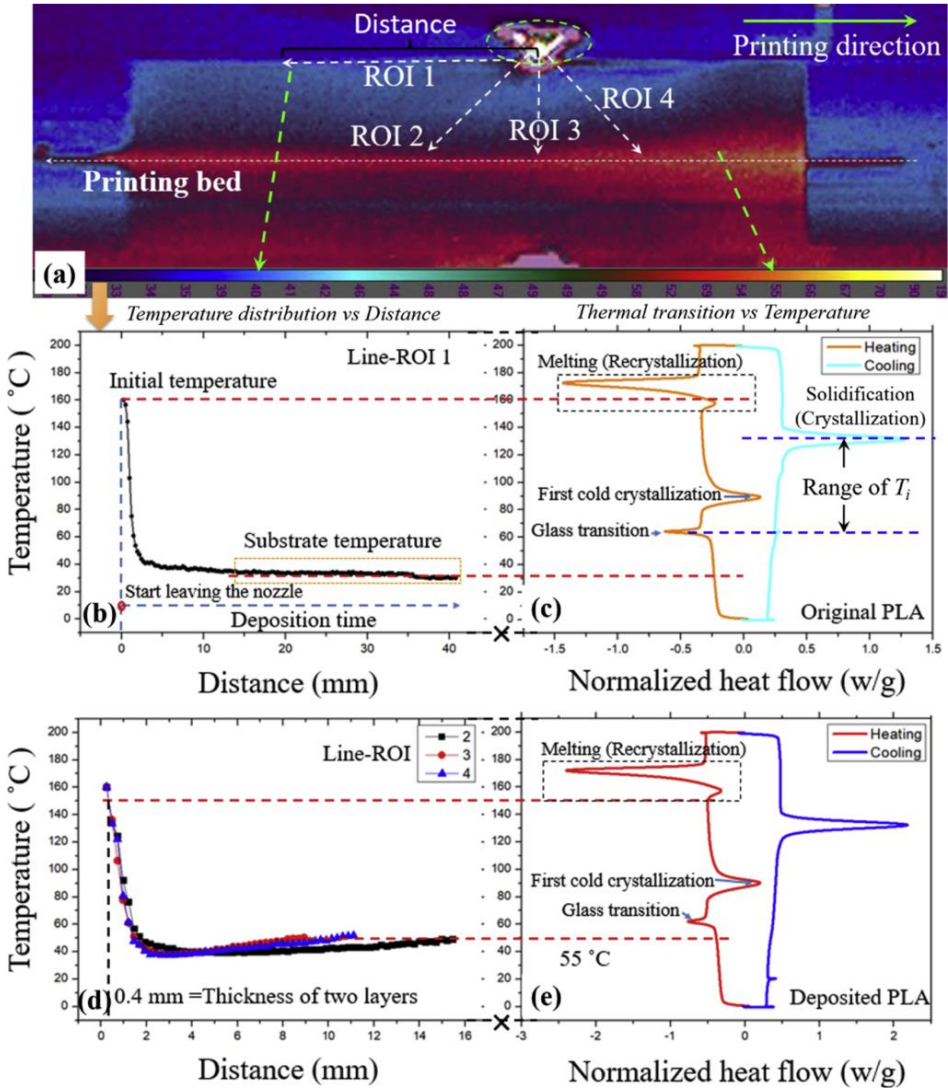


Figure 3-3. FLIR thermographs and temperature data from the 3-D printing embedding process, and corresponding DSC thermal transitions of the PLA material (original filament and deposited plastic), from Paper 1 [61].

Challenge 2: In order to obtain accurate optical fibre measurements, the coating material of the optical fibre should remain in the original state (i.e. glassy, not melt or degraded) during the integration process and a strong non-slipping bonding between the coating and the surrounding thermoplastic material is needed to transfer strain by a shearing motion.

Solution: The integrity of the OF and the bond between two polymer materials was investigated in Paper 1 [61]. Thermal transitions of the coating material, i.e. polyimide, and the matrix material PLA were characterized by the DSC. Temperature evolution of the extruded PLA during the OF embedding process was investigated using real-time thermography taken by a FLIR IR camera (Figure 3-3). It was confirmed that when the nozzle temperature was defined as 215 °C, which enables to fully melt the PLA matrix, the OF polyimide coating remains still in the glassy state during the embedding process. In a subsequent investigation, consistent optical fibre measurements were also achieved with a slightly higher temperature resin CF/PA6 (nozzle temperature = 290 °C - 300 °C) [83]. Regarding thermal resistance, consistent OF measurements and test results from the DSC confirmed the OF manufacturer data that the fibre can sustain 300 °C temperature environment for at least short periods of time [84].

A tensile test was carried out to investigate the OF/thermoplastic interface bonding properties by comparing the OF strain to strain from the cyanoacrylate surface-bonded strain gauges. Bonding between the optical fibre coating and the surrounding plastic is at least partially achieved by the shrinkage of plastic while it cools down. As shown in Figure 3-4, embedded OFs can be viewed as accurate and reliable distributed strain sensors inside the 3-D printed specimens.

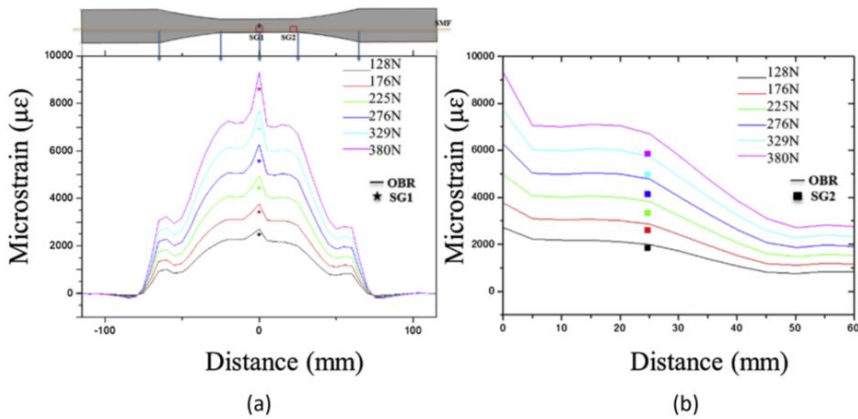


Figure 3-4. Strains from the embedded OF (lines, denoted OBR) and from electric strain gauges (point markers, SG1 and SG2) at different load levels during a tensile test, from Paper 1 [61].

3.2 ASSESSMENT OF THE ATTACHMENT QUALITY (RQ2)

3.2.1 *IN-SITU RESIDUAL STRAINS IN BLOCKS OF PLA*

Residual strain from 3-D printing of thermoplastic products is a compressive strain generated in fabrication due to high temperature effects from the production process. The crystallinity of thermoplastic material increases, and the physical volumetric shrinkage occurs when the hot material cools down to room temperature. During the optical fibre attachment process, residual strains are built into the host structure and they are partially responsible for clamping and fixing the optical fibre sensor to the surrounding polymer matrix. Residual strains and corresponding residual stresses remain 'frozen in' inside the component without any external mechanical loading.

In a fully infilled 3-D printed specimen, each section of the OF is encapsulated by analogous 3-D printed roads experiencing the same phase transformation and thermal cycles individually during the 3-D printing process. Thus, the residual strains measured from embedded OFs should display a uniform strain distribution. A sudden distortion in the central part of the residual strain profile (outside the ingress/egress regions) implies a bonding defect, damage or a large void. Thus, the attachment quality of the embedded OF can be assessed by using the residual strains on the OF. When measuring residual strains, the pre-attachment free fibre is taken as the reference state, and the load-free room temperature condition after the fibre integration as the measurement state. That is, strains relative to free-fibre are measured after the attachment process is finished.

Residual strains in 3-D printed polymers were first measured and discussed in Paper 1 [61]. As shown in Figure 3-5, an in-situ distributed measurement of residual strains was achieved. Experimental strain measurements showed that outliers were always present in the ingress and egress parts of the embedded OF, while the strains in the central region remained constant and uniform. Residual strain distributions in the horizontal and vertical directions inside a block of 3-D printed PLA, and the main mechanisms of residual strain creation were also discussed in Paper 1. The potential of in-situ OBR technology for detecting invisible manufacturing defects was demonstrated by a trial experiment in Paper 1, as shown in Figure 3-6.

Assessment of the attachment quality (RQ2)

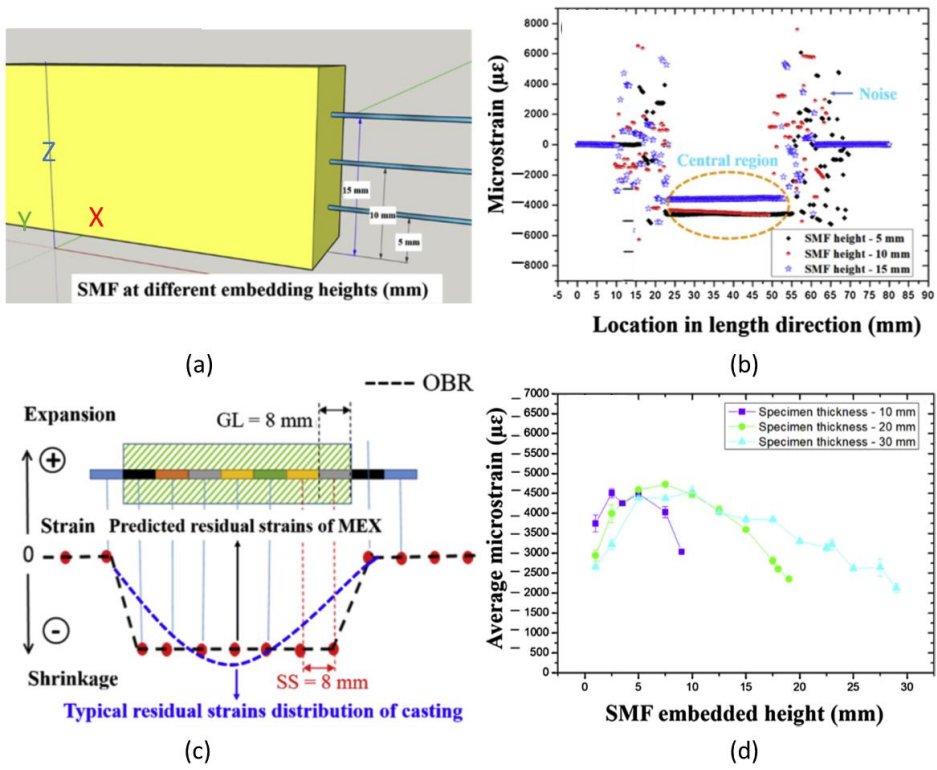


Figure 3-5. Distributed residual strains within a block of 3-D printed PLA [61].

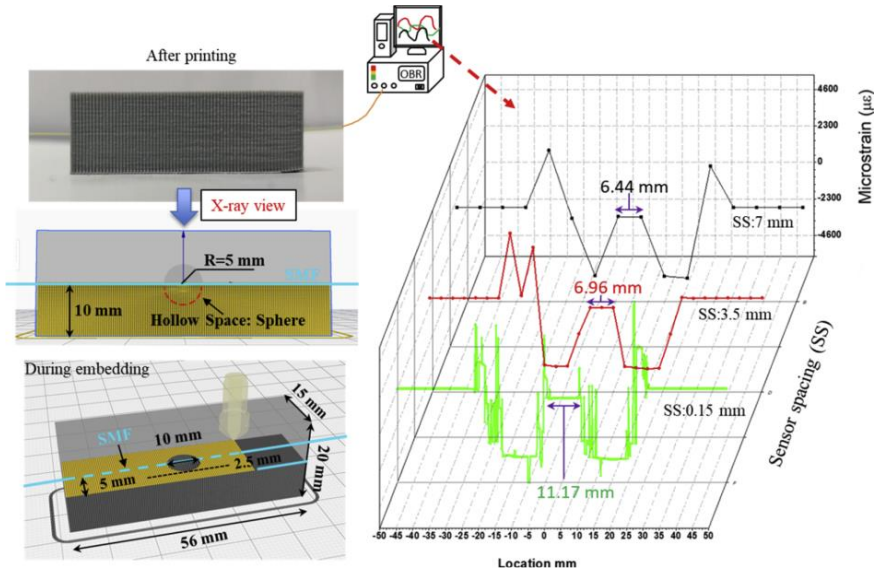


Figure 3-6. A schematic illustration of a spherical defect (void) detection by using residual strains, from Paper 1 [61].

3.2.2 *RESIDUAL STRAINS FROM VARIOUS OPTICAL FIBRE ATTACHMENT METHODS*

As discussed in the previous Section, residual strains can help to assess the quality of in-situ OF integration by 3-D printing. Paper 3 [42] compares residual strains from five different attachment methods for optical fibres on steel, GF/Epoxy, and PA6 substrates. That is, four additional surface-bonding attachment methods besides the 'Embedding' method by 3-D printing were employed in these experiments. As shown in Figure 3-7, the residual strains of 'Cyanoacrylate', 'Araldite', and 'Weld' attachments are strongly affected by local effects in the hand-controlled attachment process. It is suspected that curing (for 'Cyanoacrylate' and 'Araldite',) or cooling (for 'weld') process is locally variable. Thereby, residual strain distributions became very inconsistent. In contrast, the residual strains of the 'Epoxy' (epoxy film, oven cured) and especially the 3-D printed 'Embedding' attachments originate from a more uniform origin of strain. Imperfections in the adhesion layer, and a non-uniform bondline are also well-known quality issues. In addition to curing or cooling related inconsistencies, these may also produce noisy datapoints or local distortions in the measured OF strain profiles.

In Section 4 of Paper 3, a calculation of index S is proposed to investigate the correlation between residual strains and creep strains measured by the attached OFs. When the correlation is good index S displays values around 100%. As shown in Figure 3-8, clear correlations between residual strains and creep strains were only witnessed for 'Epoxy' (Figure 3-8 (c)) and 'Embedding' (Figure 3-8 (e)) attachments (two attachments with the most uniform residual strains) where index S gave close to 100% values for the central part of embedded length.

Assessment of the attachment quality (RQ2)

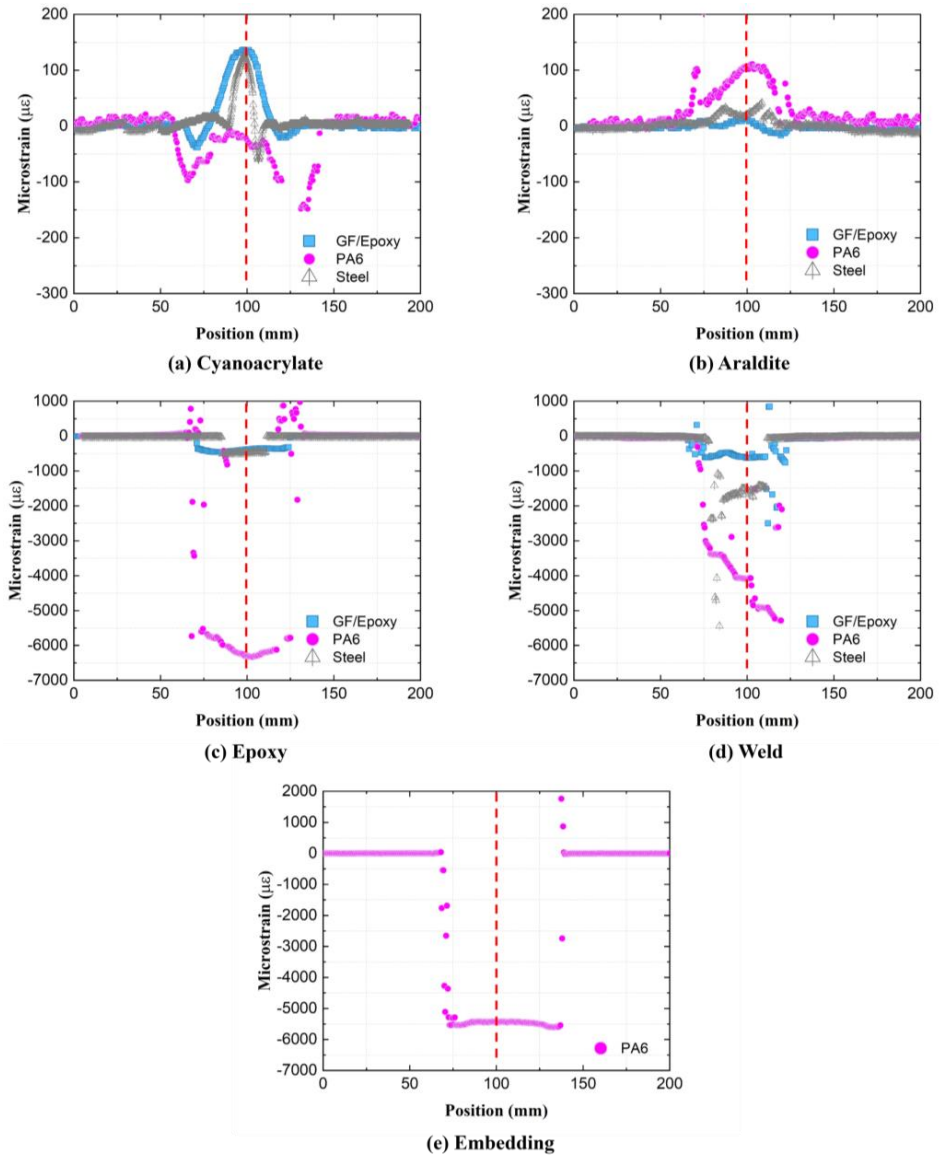


Figure 3-7. Residual strain profiles along the attached OFs created by using five different OF attachment methods in combination with three substrate materials (GF/Epoxy, PA6, Steel), from Paper 3 [42].

Assessment of the attachment quality (RQ2)

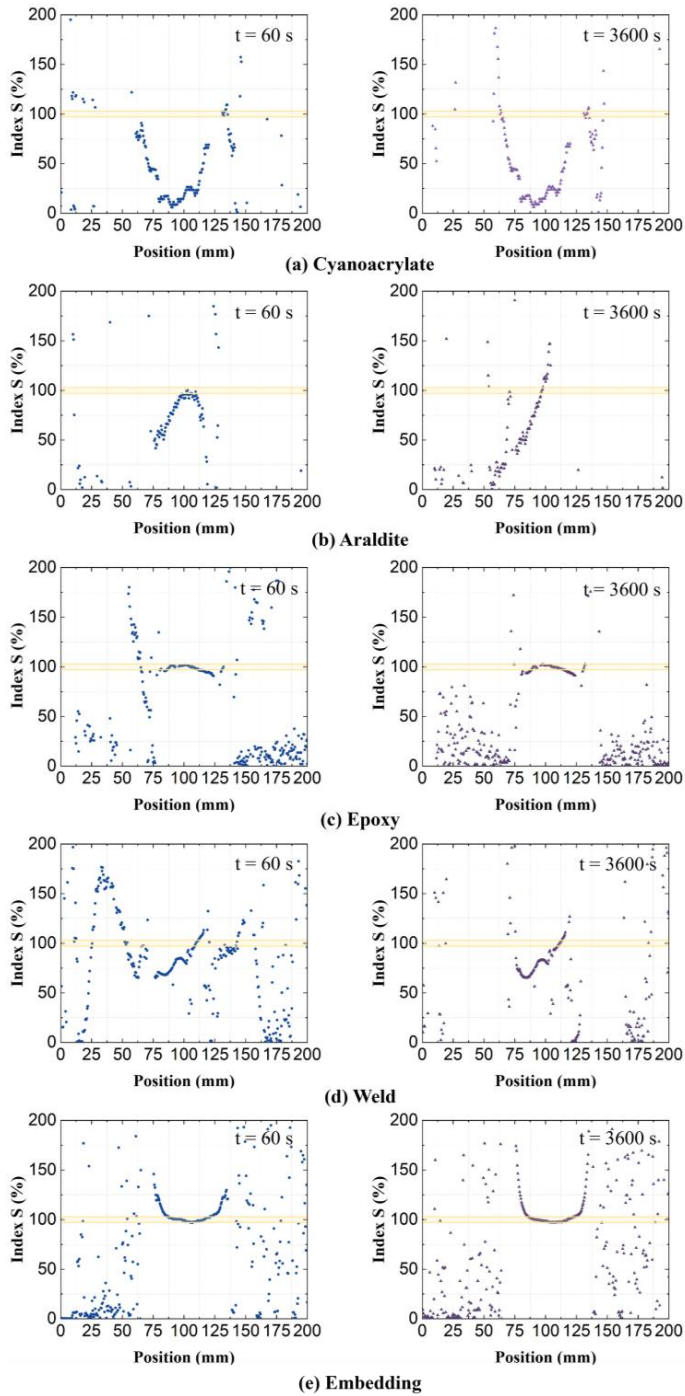


Figure 3-8. Index S calculated from residual strains and creep strains by using different attachment methods in a creep test (times $t = 60$ s, and $t = 3600$ s), from Paper 3 [42].

Assessment of the attachment quality (RQ2)

In summary, residual strains, as created by different attachment processes, are easily characterized by the self-recording measurements of optical fibres. Distributed residual strain can be a very useful quantitative metric for evaluating the attachment quality of integrated OFs. Furthermore, residual strains and their fluctuations along the sensor fibre appear to be correlated to the specific optical fibre attachment method.

3.3 AN ACCURATE CALCULATION MODEL (RQ3)

In previously discussed research, the DOFS has been realized as an embedded or surface bonded strain sensor. To avoid accounting for temperature effects, all DOFS measurements have been recorded at a constant room temperature. This points to an important issue however. One of the most significant limitations for using the DOFS today is their coupled sensitivity to both temperature and strain. This can introduce large errors for signal interpretation. For instance, when using OBR 4600, a 1 °C temperature variation along the sensing fibre will introduce errors for the strain measurement at a value of ca. 8.34 $\mu\epsilon$. Experiments have shown that linear calculation models for describing the relationship between strain and temperature (see Equation 2-1) were lacking in accuracy, especially when applied over a wide range of temperatures. Thus, providing a more accurate calculation model to distinguish between mechanical strain and temperature effects would be a useful improvement on the basic understanding of how the OF works. A series of temperature-controlled experiments and the corresponding data analysis in Paper 3 [79] was fully devoted for solving this task.

3.3.1 MECHANICAL LOADING EFFECT

As shown in Figure 3-9(a), a deformation controlled micro-positioner was used as the strain coefficient characterization setup. One end of the DOFS was fixed on a micro-positioner by a small drop of cyanoacrylate, while the other end was fixed on a stationary steel bracket. The strain was applied on the DOFS by a 1-D linear movement of the micro-positioner. After each measurement, the strain on the DOFS was increased by ca. 1000 $\mu\epsilon$. A total of seven measurements were recorded, going from 0 $\mu\epsilon$ to roughly 9000 $\mu\epsilon$.

The results in Figure 3-9 (b),(c) show a clear linear relationship between the RBS shift and the applied strain. This was expected. In the absence of temperature change, the mechanical strain on the DOFS can be written as:

$$\epsilon = -\frac{\bar{\lambda}}{cK_\epsilon} \Delta\nu_M \quad \text{(Equation 3-1)}$$

where K_ϵ is the strain coefficient, $\bar{\lambda}$ is the central wavelength of the incident light and c is the speed of light. Obtained experimental results agree that K_ϵ is a constant with a value of 0.787. Thus, Equation 3-1 yields the conversion factor ϵ

= $(-6.68 \mu\epsilon / \text{GHz}) \cdot \Delta v_M$ for our OBR system. Using this conversion factor, the linear fit of the RBS shift and strain, in Figure 3-9(c) is near perfect ($R^2=1$).

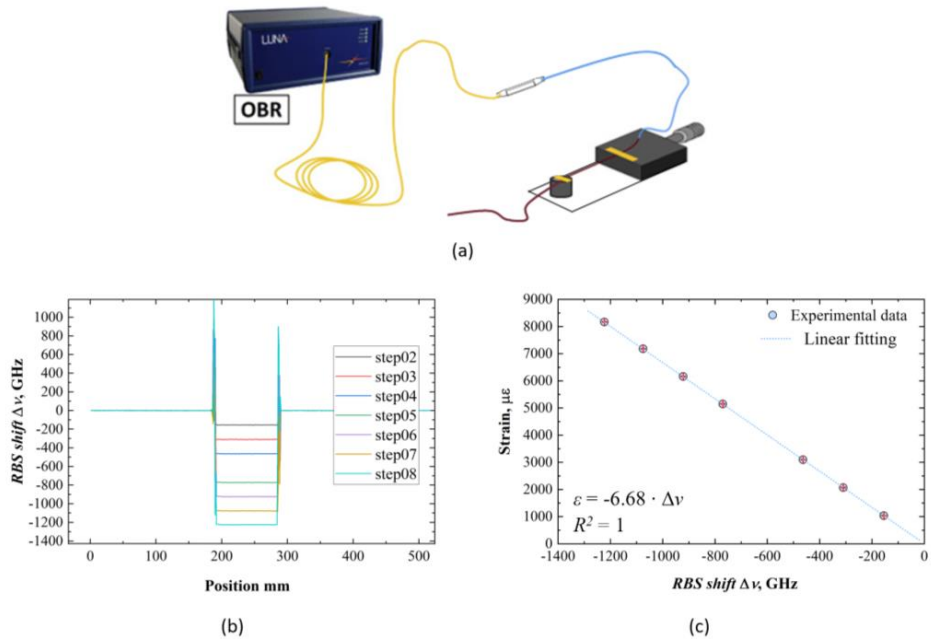


Figure 3-9.(a) Schematic of the strain coefficient characterization setup, (b) RBS shift obtained from mechanical strain, and (c) the linear fit of the measured RBS shift and strain.

3.3.2 COUPLED MECHANICAL AND THERMAL LOADING

In order to investigate the relationship between Rayleigh backscattering spectral (RBS) shift, strain and temperature, a series of DOFS measurements were carried out with naked optical fibres without any surrounding substrate structure beyond the PI coating. Optical fibres were exposed to loading environments where a constant mechanical loading was coupled with varying thermal loads (Figure 3-10(a)), and a constant thermal loading was coupled with varying mechanical loads (Figure 3-10(b)). When mechanical strain is constant, the mechanical loading induced RBS shift Δv_M (blue dotted line in Figure 3-10(a)) is achieved by subtracting Δv_T from $\Delta v_{T\&M}$. The Δv_M shows no variation with temperature and is equal to the Δv_{PM} , which is the RBS shift achieved by pure mechanical loading. Analogously, at constant temperature, the differences between $\Delta v_{T\&M}$ at different temperatures (empty and solid circles in Figure 3-10(b)) are constant and this difference remains independent from mechanical

loading. These results show that strain and temperature effects can be added/subtracted by superposing the RBS shifts under coupled loading conditions. This mechanical-thermal loading superposition model is the basis of strain and temperature effects decoupling for the DOFS.

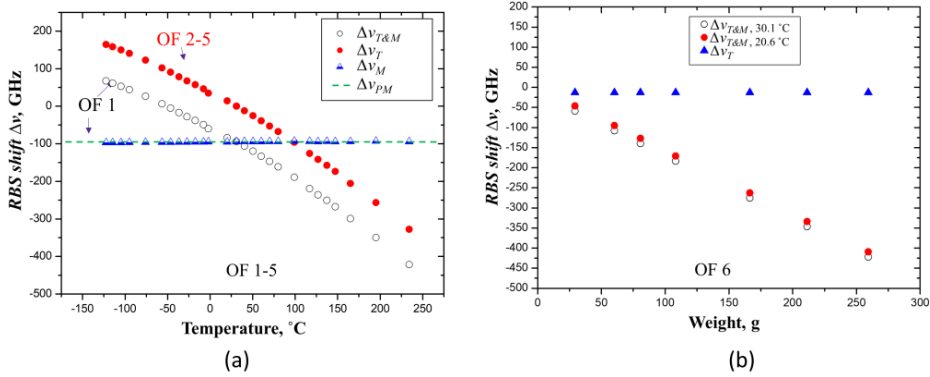


Figure 3-10. The RBS shifts of optical fibres under coupled mechanical and thermal loading conditions: (a) constant mechanical load, (b) constant temperature, from Paper 3 [79].

3.3.3 THE NOVEL POLYNOMIAL FORMULA

The relationship between temperature change $\Delta T = T_m - T_r$ and the corresponding RBS shift Δv_T is described for the general case as [79]:

$$\Delta v_T = -\frac{c}{\lambda} \cdot \int_{T_r}^{T_m} K_T(T) dT \quad (\text{Equation 3-2})$$

For germanosilicate core fibre, the coefficient $K_T = \alpha + \beta$, while the right-hand side corresponds to the coefficient of thermal expansion (CTE) of silica (α), and the second term corresponds to the thermo-optic coefficient of the fiber (β). K_T is often viewed as constant, i.e. not temperature dependent, with a value equal to $6.45 \cdot 10^{-6}/^\circ\text{C}$. The linear formula obtained from this is typically used to calculate temperature in the OBR measurement. However, experimentally measured relationship between temperature and RBS shift exhibits a clear non-linear behavior in a wider temperature range as can be seen in Figure 3-11(a). The reason for the temperature sensitivity of RBS spectrum arises from thermal expansion, and the refractive index change of the glass fibre. For silica optical fibre core, the value of thermal expansion coefficient α is constant at approximately $0.55 \cdot 10^{-6}/^\circ\text{C}$, while the refractive index n exhibits a significant temperature dependence [56,85–88]. The optical properties of materials

(including refractive index n) are modeled by coupling various types of oscillators to the electromagnetic radiation field. A single oscillator model for the refractive index n of silica is expressed by [86]:

$$\beta = \frac{dn}{dt} = \frac{n^2 - 1}{2n} (-3\alpha) - \frac{n^2 - 1}{2n} \left(\frac{1}{E_{eg}} \cdot \frac{dE_{eg}}{dT} \cdot \frac{E_{ig}^2}{E_{ig}^2 - E^2} \right) \quad (\text{Equation 3-3})$$

where, E is the photon energy, and E_{eg} is the excitonic band gap and E_{ig} is the isentropic band gap in the infrared region as shown in the energy level diagram in Figure 3-11(b).

It is evident from Equation 3-3, that the β is predominant by the temperature dependence of the Band-gap energy [89]. The temperature dependence of the energy band gap is closely linked to interactions between electrons/excitons and phonons [90, 91]. Both Bose-Einstein-type and Varshni-type functions are proven to provide an excellent description of the non-linear temperature dependence of the band-gap energy due to the electrons and phonons interaction [92]. While the Varshni function is certainly quite useful for quantitative characterization of the temperature dependence of Band-gap energy across various temperature ranges, thus, according to Ghosh [88], β is thereby simply expressed by a quadratic function of temperature as follows:

$$\beta = b_0 + b_1T + b_2T^2 \quad (\text{Equation 3-4})$$

where b_0 , b_1 and b_2 are constants. Deducing from underlying physics (Equations 3-2 and 3-4) the polynomial formula for accurate temperature RBS shift when using the DOFS was first proposed in Paper 3 [79] as:

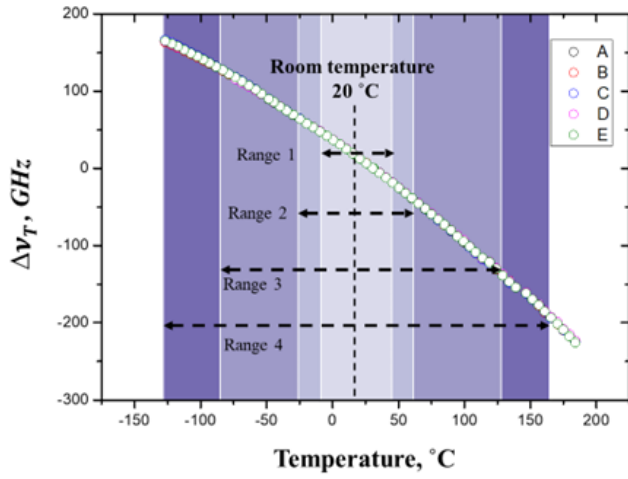
$$\Delta v_T = -\frac{c}{\lambda} \cdot \int_{T_r}^{T_m} K_T(T) dT = C_0(T_m - T_r) + C_1(T_m^2 - T_r^2) + C_2(T_m^3 - T_r^3) \quad (\text{Equation 3-5})$$

where C_0 , C_1 and C_2 are again constants and Δv_T is the RBS shift, T_m is the measurement temperature of the OBR measurement test and T_r is the temperature of the OBR reference test. Hence, this polynomial spectral shift formula, which is based on the electron-phonon interaction physical mechanism, enables high precision temperature measurements with the OBR.

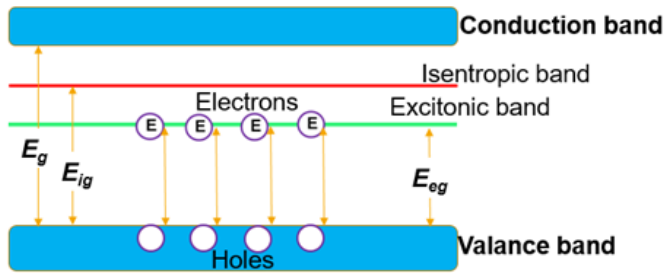
In order to compare the two approaches (linear and polynomial), the RBS shift - temperature curve was fitted by the usual linear model (Equation 3-2) and the

new non-linear model (Equation 3-5) separately. The goodness of fit of the two models was assessed by using the adjusted R-squared metric. The adjusted R-squared was calculated for four different temperature ranges (as in Figure 3-11(a)) and the results are shown in Figure 3-12 (a). The linear and non-linear fitting curves have very similar R^2 values for the narrow temperature Range 1. However, when the temperature range becomes wider, the polynomial formula shows a much better goodness-of-fit (higher R^2 value) compared to the linear formula. Figure 3-12 (b) shows an example with relative errors for the OBR temperature measurements (%error) when using the polynomial and linear formulas. When the temperature shift remains within Range 1, there is little difference between the errors of polynomial and linear formulas (mostly < 5%). When the temperature shift exceeds Range 1, the polynomial formula shows a much higher temperature measurement precision over the whole measured temperature range. This experiment clearly demonstrates how the polynomial formula improves the temperature measurement accuracy over an extended temperature range.

An accurate calculation model (RQ3)



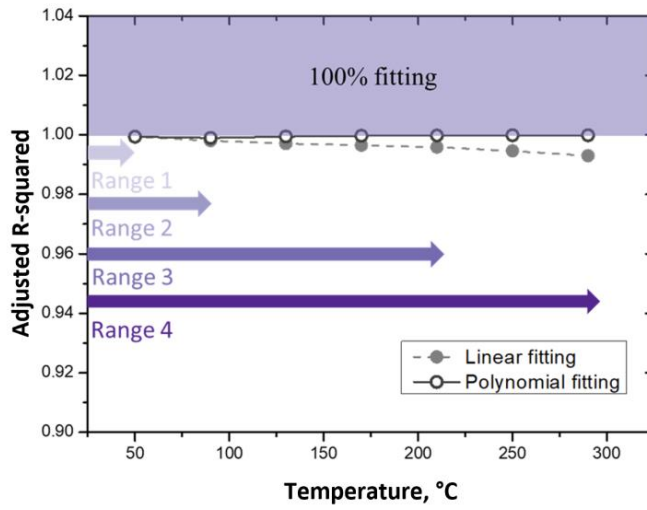
(a)



(b)

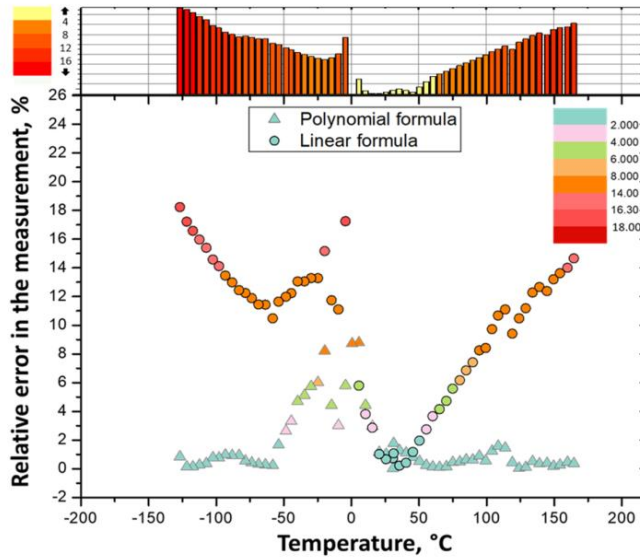
Figure 3-11. (a) Thermal loading induced RBS shifts measured by the OBR and (b) energy level diagram for silica glass, from Paper 3 [79].

An accurate calculation model (RQ3)



(a)

Difference between the relative error rate of Polynomial and Linear formula



(b)

Figure 3-12. The goodness of linear and polynomial fitting formulas with increasing temperature ranges: (a) the adjusted R-square metric, (b) relative error in the temperature measurement [79].

3.4 CREEP STRAIN MEASUREMENTS (RQ4)

In engineering applications, both the short-term and the long-term performance of a structure is important. Creep phenomenon describes the time dependent behavior where the material deforms with time under constant state of stress (typically much lower than the yielding stress or the fracture stress). Creep is regarded as an important life-limiting factor especially when polymeric structures are required to service for long periods of time [93]. At room temperature, creep is often neglected for metals. However, for polymers and polymer composites, creep is a critical phenomenon for their long-term service life already at room temperature, because of the visco-elastic nature of the material [94,95]. Even though long fibres in fibre reinforced polymer (FRP) composites can reduce creep, a significant increase of strain can be observed even in these materials [96]. Creep development is dependent on the interaction between loading parameters such as time, temperature and stress level in particular. The monitoring of creep behavior is important so that the actual status of the composite structure can be evaluated.

In previous research, the concepts of DOFS embedding methods by 3-D printing have been proposed and demonstrated. To the best of the authors knowledge, experimental work on comparing the DOFS attachment methods under time-dependent loading has been very limited. The effects of creep on the strain transfer behavior of the attached distributed optical fibre sensor have not been openly investigated. Both Paper 3 [79] and Paper 4 [83] were devoted for providing new knowledge on this matter.

3.4.1 REGION OF INTEREST (ROI)

The bathtub curves in Figure 3-13 display typical strains measurements from the surface attached DOFS sensor. When stretched uniformly along the embedding length (EL), the central region of the DOFS often shows quasi-constant strains. The transition between a free and an attached optical fibre, also called the ingress/egress of the optical fibre, often displays gradual tapering curves due to the employed post-processing algorithm (see Figure 2-3). Apart from these ingress/egress regions, the quasi-constant central region is hereby referred to as the region of interest (ROI). An average strain value on the DOFS needs to be extracted to interpret the measurements from the DOFS. Only the strains from the ROI of the DOFS should be averaged to discard the ingress/egress transition regions in distributed strains. The chosen length of the ROI can significantly

affect the averaged strain value and reducing the ROI length is a simple strategy to remove the ingress/egress regions effect. However, the quasi-constant central region, forming the ROI, can become shorter or even disappear with increasing the length of disturbed regions as illustrated in Figure 3-13 (b) and Figure 3-13 (c). This can for example occurs with excessive bondline thickness over a limited embedding length. When this happens, the peak value of the strain curve (Figure 3-13(c)) can be used as an alternative metric for interpreting the DOFS strains.

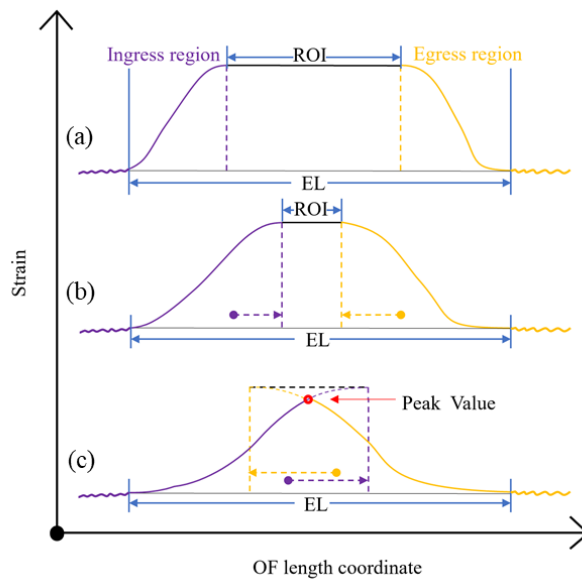


Figure 3-13. Illustration of embedding length (EL), region of interest (ROI) and peak value on the strain curves from DOFS, from Paper 4 [83].

3.4.2 COMPARISON OF DIFFERENT OF ATTACHMENT METHODS

Figure 3-14 shows spatial strain profiles obtained from the DOFS and strains from the contact extensometer on the same specimen at 60, 600, 1800, and 3600 s into the creep loading time. Initial short-term strains are omitted (i.e. reference is taken right after the creep load is applied) and only the creep strain development after the load application is presented. A similar structure can be observed in the strain curves of all DOFS attachments. The strains display a bath-tub shape with respect to the position and rise with increasing time. The strain values in the ROI of the 'Cyanoacrylate' and 'Embedding' (which is the 3-D printing integration method) attachments agree well to corresponding strains from the extensometer. Their strain profiles also show a more consistent flat

plateau than manually applied ‘Araldite’, ‘Epoxy’ and ‘Weld’ attachments strain curves, which fluctuate along the DOFS. Most of the strains from ‘Epoxy’ are clearly lower than extensometer strains, while the strains from ‘Araldite’ and ‘Weld’ attachments became locally higher after 600 s. The best agreement between the OBR and extensometer measurements is observed in the 3-D printed ‘Embedding’ attachment.

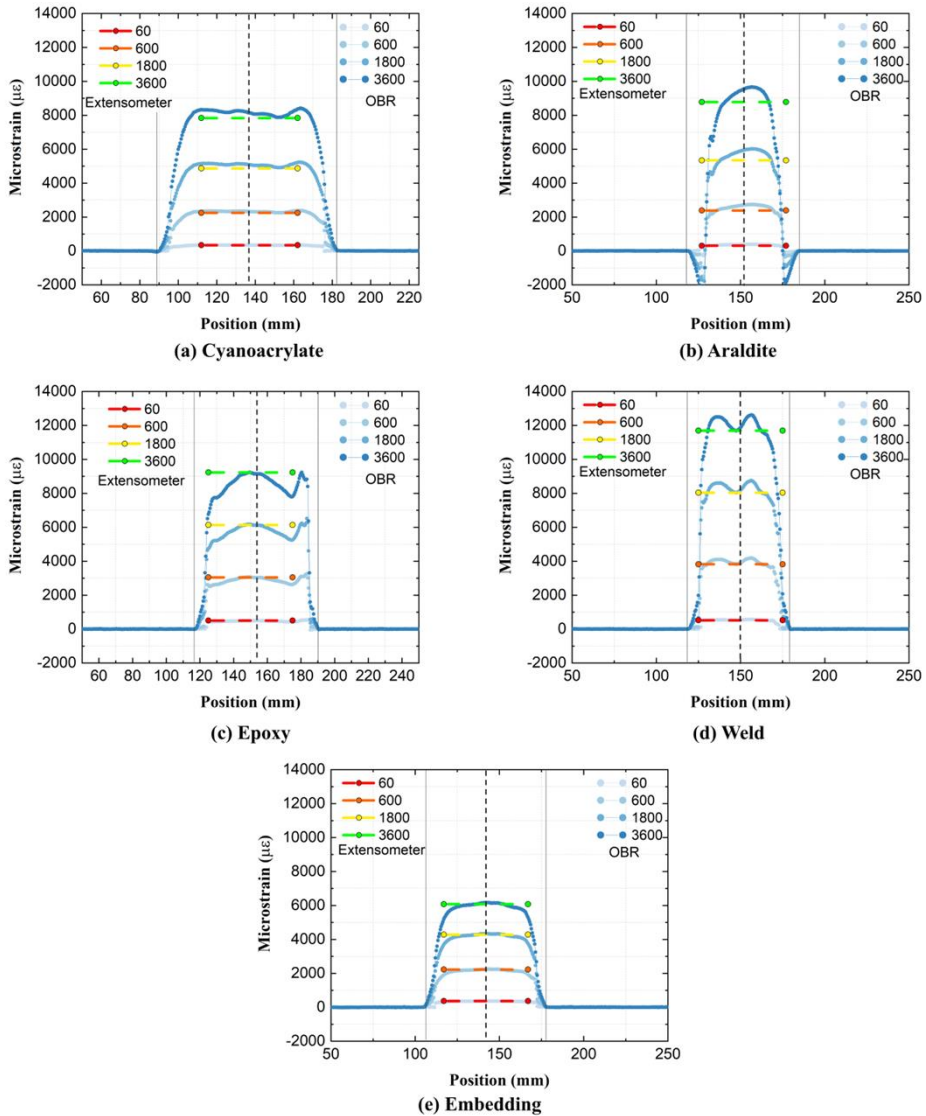


Figure 3-14. Spatial strain profiles along the attached DOFS (on a PA6 substrate) during creep, from Paper 3 [42].

In addition to the visual analysis of strain curves, statistical analysis can also be adopted to quantitatively compare the difference between these DOFS attachments as shown in Figure 3-15. The coefficient of variation (CV) is calculated from spatial DOFS strains as the metric of the bonding inconsistency along the ROI of the DOFS. A perfect attachment transfers 100% strain of the substrate to the attached optical fibre sensor. Thus, the difference between strains from the DOFS and strains from the contact extensometer helps to characterize the measurement accuracy of the DOFS attachment method. The differences between the DOFS strains and the extensometer strains are hereby defined by the absolute and relative difference coefficients C_A and C_R as follows:

$$C_A(t) = |\varepsilon_{OBR}(t) - \varepsilon_{EXT}(t)| \quad \text{(Equation 3-6)}$$

$$C_R(t) = \left| \frac{\varepsilon_{OBR}(t) - \varepsilon_{EXT}(t)}{\varepsilon_{EXT}(t)} \right| \times 100\% \quad \text{(Equation 3-7)}$$

where $\varepsilon_{OBR}(t)$ is the averaged OBR strain (ROI = 40 mm, in the center of curves in Figure 3-14) and $\varepsilon_{EXT}(t)$ is the strain from the extensometer during creep time t . These calculated coefficients CV , $C_A(t)$ and $C_R(t)$ are shown in Figure 3-15 for all types of attachments. Figure 3-15(c) shows how the 'Embedding' i.e. 3-D printing attachment enables the lowest strain variability compared to the other hand-controlled attachment methods. The lowest absolute and relative strain differences $C_A(t)$, $C_R(t)$ i.e. the strain transfer loss is observed in the 'Embedding' attachment (Figure 3-5 (a), (b)). All relative differences $C_R(t)$ between the extensometer and the OBR strains are observed to remain constant or slightly decrease with time. In summary, these results show that the 3-D printing attachment achieves a uniform bonding quality, a high measurement accuracy and the strain transfer coefficient remains nearly constant during 1 h of creep.

Creep strain measurements by optical fibres (RQ4)

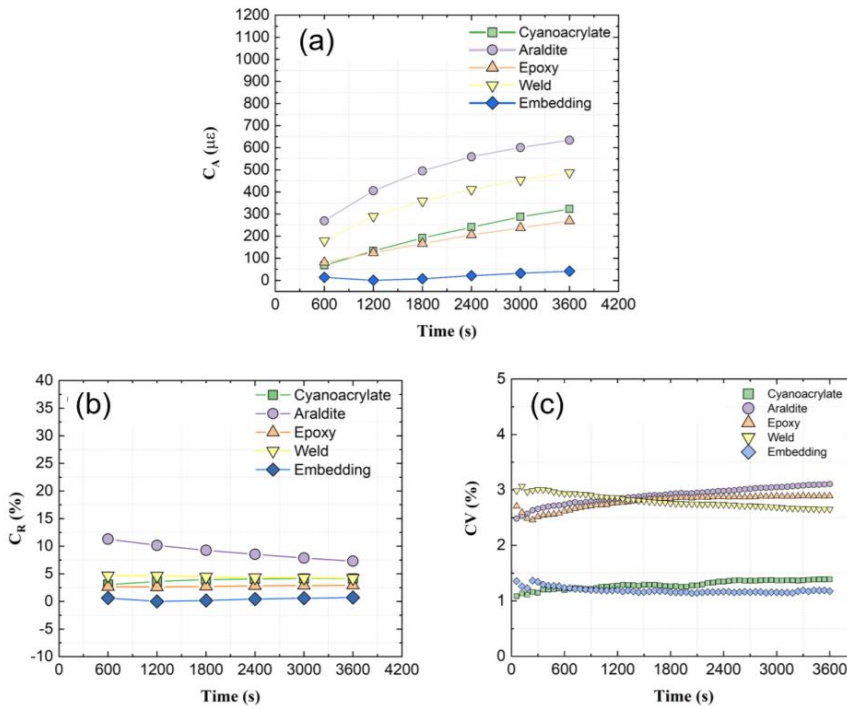


Figure 3-15. Statistical analysis of the difference between the strains from the DOFS and the corresponding contact extensometer, from Paper 4 [83].





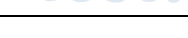
3.4.3 BOTTOM INTERLAYER THICKNESS EFFECTS

When using the 3-D printing integration method, many factors can significantly affect the strain transfer from the substrate to the attached optical fibres sensors [97–99]. For example, the bottom interlayer thickness (bondline thickness between the structure and the OF sensor), Young’s modulus of the attachment layer, and the attachment length of the OF sensor have all been shown to be influential parameters. However, only the bottom interlayer thickness has not been investigated experimentally, as the other parameters have [98–103]. The 3-D printing integration method can produce a consistent interlayer thickness with prescribed values, enabling to experimentally investigate the strain transfer behavior from the substrate to the DOFS for the first time. Detailed results of this investigation are presented in Paper 4 [83].

Figure 3-16 shows spatial strain profiles along the DOFS attached by 3-D printing with different bottom interlayer thicknesses (DOFS-0 to DOFS-8, see Table 3-1) and the corresponding statistical analysis of the difference between the DOFS strains and the extensometer (EXT) strains. Strains from the DOFS using a

traditional cyanoacrylate glue attachment (DOFS-C) are also plotted in the same diagram for comparison. The spatial strain profiles from different bottom thickness configurations (the first column in Figure 3-16) have distinctly different spatial distribution patterns for the same creep load. When the bottom interlayer thickness is thin (DOFS-0 and DOFS-2), spatial strain curves show a ‘bathtub’ shape. By increasing the bottom interlayer thickness (DOFS-4 and DOFS-8), the plateau shortens and finally converts into a peak. For 3-D printed attachments, all averaged DOFS strains (ROI= 50 mm) or the peak values of DOFS strains are smaller than the EXT strains and show an increasing trend of disagreement with the increase of the bottom interlayer thickness. The absolute difference $C_A(t)$ continues to increase with increasing of the creep time, while the relative difference $C_R(t)$ remains approximately constant with the creep time. In summary, the monotonically increasing disagreement between the DOFS strains and the EXT strains indicates an increasing strain transfer lag caused by a larger bottom interlayer thickness. No significant distortions were observed on the strain profiles during creep, indicating no cracking or delamination inside the attachment layers surrounding DOFS during the creep test.

Table 3-1. DOFS attachment configurations, from Paper 4 [83].

Attachment configuration	Bottom interlayer thickness T		Location of the optical fibre	Layup sequence of the 3-D printed embedding element
	No. of layers	Approximate thickness		
DOFS-0	0	< 0.1 mm		[OF 90,0]
DOFS-2	2	0.4 mm		[90,0 OF 90,0]
DOFS-4	4	0.8 mm		[90,0,90,0 OF 90,0]
DOFS-8	8	1.6 mm		[90,0,90,0,90,0,90,0 OF 90,0]
DOFS-C	N/A	N/A		‘Cyanoacrylate’

Creep strain measurements by optical fibres (RQ4)

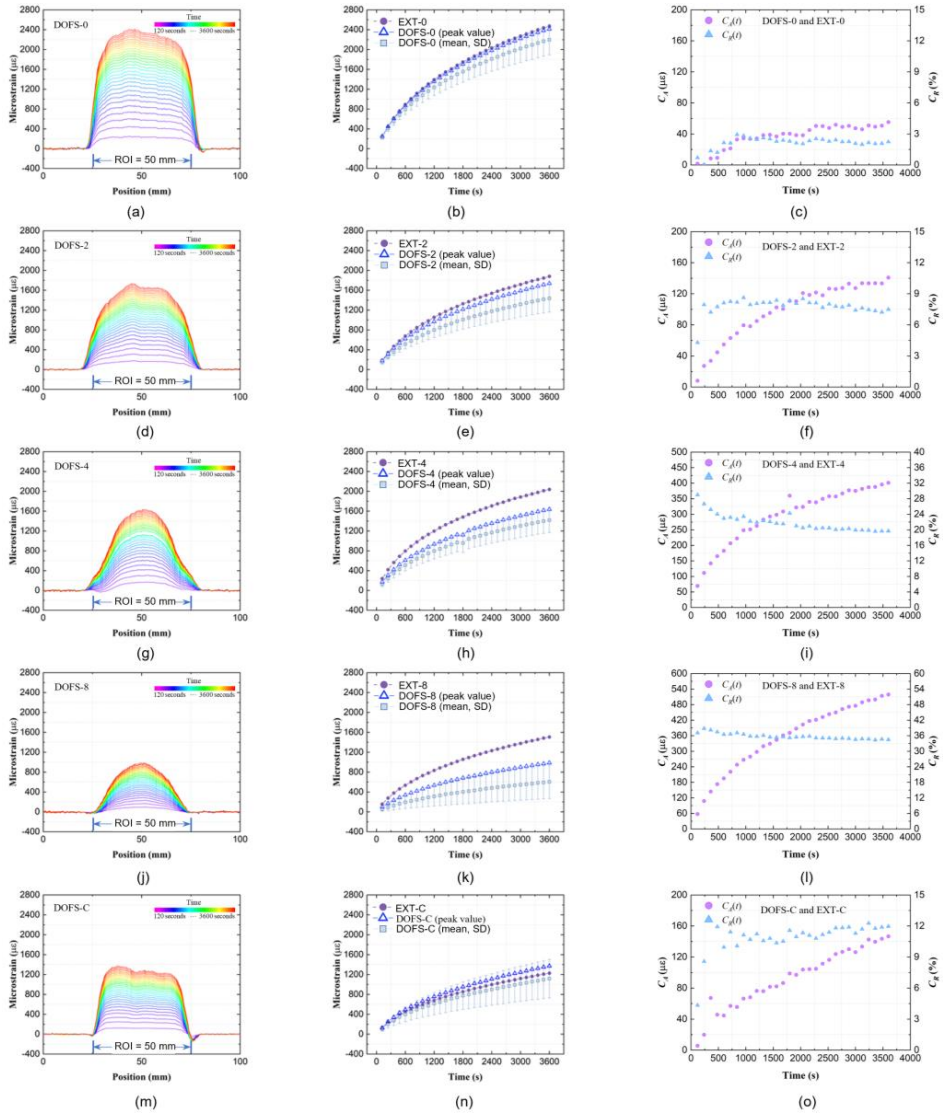


Figure 3-16. Comparison between creep strains from the DOFS and the contact extensometer strains with different 3-D printed attachment configurations (in Table 3-1), from Paper 4 [83].

3.4.4 SHEAR LAG CORRECTION

Experimental data in Figure 3-16 shows that bottom interlayer thickness T_{thk} has a significant influence on the strain transfer coefficients for optical fibre sensors. This shear lag needs to be understood and accounted for, to assure the measurement accuracy of the attached DOFS for engineering applications. Thus, a simple calculation method that accounts for the shear lag effect between the component and the optical fibre strains is hereby presented.

An average strain transfer coefficient K_M for FBG sensors has been generalized from known theoretical models [100–102,104–107]:

$$K_M(T_{thk}) = 1 - \frac{\sinh(\alpha)}{\alpha \cosh(\alpha)} \quad (\text{Equation 3-8})$$

where T_{thk} is bottom interlayer thickness, and parameter α is dominating the shear lag behavior between the substrate and the optical fibre sensor. Parameter α is normally expressed by complex analytical equations using different variables from material properties and geometrical properties of the optical fibre and the attachment layer [104]. When interlayer thickness T_{thk} is considered as the only non-constant variable, the strain transfer coefficient K_M can be simplified to:

$$K_M(T_{thk}) = 1 - \frac{\tanh\left(\sqrt{\frac{1}{T_{thk}S}}\right)}{\sqrt{\frac{1}{T_{thk}S}}} \quad (\text{Equation 3-9})$$

Parameter S is similar to α , but it is independent from thickness T_{thk} i.e. the thickness variable has been separated. Thus, in this work, parameter S is the same for all specimens with different bottom interlayer thicknesses. When both thickness T_{thk} and the strain transfer coefficient $K_M(T_{thk})$ are measured from a number of test configurations, a curve fitting procedure can be applied to obtain the missing constant S . As the relationship is established, the strain transfer coefficient $K_M(T_{thk})$ for DOFS with any unknown bottom thickness T_{thk} can be calculated. This method allows to semi-empirically predict the strain transfer coefficients for optical fibre surface attachments with arbitrary embedding interlayer thickness as shown in Figure 3-17. Because the precise value of bottom interlayer thickness T_{thk} and $K_M(T_{thk})$ are still difficult to know in practice,

a Monte-Carlo sampling method, using estimated uncertainty ranges for experimentally obtained T_{thk} and K_M , is adopted to predict strain transfer coefficients K_M in Figure 3-17.

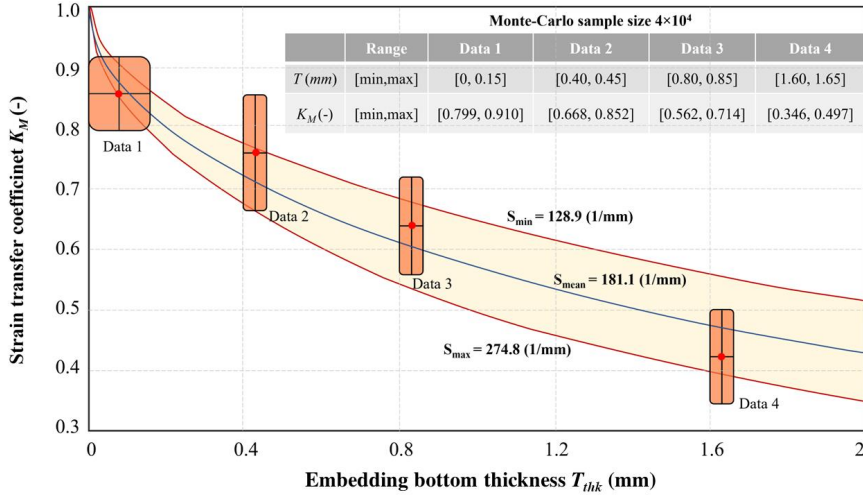


Figure 3-17. Strain transfer coefficient versus bottom interlayer thickness curve from the shear lag correction model, from Paper 4 [83].

CONCLUSIONS

This work has proposed a novel optical fibre (OF) sensor integration principle by material extrusion 3-D printing. Practical challenges, validity and the reliability of the developed method were hereby investigated. The improvements in current state-of-the-art, and the novel experimental results are documented below.

1. An optical fibre sensor embedding procedure was proposed. The developed approach was experimentally investigated using distributed optical fibre sensors.

A standard single mode optical fibre was embedded into the fused deposition modeling (FDM) fabricated specimen during the 3-D printing process. Microscopy observations showed the OF is well encapsulated by the thermoplastic material. Tensile testing showed that bonding between the OF and the PLA matrix is strong enough to enable the embedded OF working as a distributed strain sensor up to 10,000 $\mu\epsilon$. Strains from the embedded OF show fair agreement with strains from electrical strain gauges. It is noted that unreliable strain data occurs in the ingress and egress parts of the distributed optical fibre.

2. Residual strains are generated inside the substrate structure and thereby on the embedded the optical fibre sensor during the OF attachment process. Residual strains are however very uniform for the small-scale material extrusion i.e. 3-D printing process. A sudden distortion in the residual strain profile may imply a bonding defect, damage or a large void around the embedded OF.

Residual strain distribution in FDM fabricated specimens was in-situ measured and demonstrated in longitudinal and through-thickness direction for the first time by using the embedded DOFS. This strain is induced by material volumetric shrinkage from material cooling during after the 3-D printing process. It results

in a horizontally uniform distribution of residual strains. Strain curves from the center region of embedded OFs are constant and representative, whereas noisy data are always present in the egress and ingress parts of the OF attachment. A sudden drop of residual strains was observed when a hollow sphere was designed and realized inside the center of the specimen. This experiment demonstrates the possibility of identifying manufacturing defects by using residual strains from the embedded OFs

Residual strain can also be created when fixing the OFs on the surface of the specimens, before any external mechanical loading occurs. Residual strains of crosslinked structural adhesives such as the 'Cyanoacrylate', 'Araldite', and thermoplastic fusion-based method like hand-controlled 'Weld' attachments become very inconsistent, because they are strongly affected by the local nature of curing or cooling. In contrast, residual strains of oven cured 'Epoxy' attachment and surface attachment by 3-D printing originate from a more uniform source of strain on the specimens. This indicates that residual strain fluctuations along the DOFS length are caused by nonuniformities created in the fibre attachment process. Fluctuations in the residual strain profile refer to a non-uniform occurrence in the bondline in terms of thickness, small cracks, etc.

3. Coupled sensitivity to both thermal and mechanical loading effects hinders DOFS applications. A more accurate calculation model is hereby provided to distinguish between strain and temperature effects over an extended temperature range.

Pure mechanical loading effects (RBS shifts) are proven to be linear with strain, while the mechanical and thermal loading effects are shown to be independent and superposable with each other. Under coupled OBR measurement conditions, the mechanical strain can be obtained by subtracting the temperature effect from the coupled RBS shift and vice versa. Due to the relationship between thermo-optic coefficient and temperature, pure thermal loading effects are proven to be nonlinear with temperature. Thus, a polynomial formula for calculating temperature is deduced from physics-based models. The polynomial formula shows a higher temperature measurement accuracy than a linear formula over an extended temperature range. The proposed non-linear temperature effect calculation model is a useful improvement on the basic understanding of how the OF works.

4. Long-term performance of DOFS embedded by 3-D printing were investigated and quantitatively compared with other more traditional DOFS attachment methods.

Tested specimens gave a satisfactory agreement between the attached optical fibre sensors and contact extensometer strains in two sets of creep tests. Test results revealed that distributed strain transfer coefficients along the optical fibre sensors remain approximately constant with time. Relative difference between OF strains and contact extensometer strains either remained constant or converged towards slightly more similar values over time.

Strain fluctuations along the OF length are partially caused by nonuniformities created in the fibre attachment process. A machine-controlled attachment process (such as in situ 3-D printing) achieves a highly uniform bonding quality, and a high measurement accuracy. Creep strain measurement accuracy comparable to a cyanoacrylate glue attachment was achieved by optical fibres embedded at zero interlayer thickness. By increasing the bottom interlayer thickness, a disagreement between the OF strains and the extensometer strains increases monotonically, showing that a shear lag is introduced between the substrate and the OF sensor strains. A semi-empirical calculation method was proposed to correct the optical fibre strains for the shear lag effect at an arbitrary interlayer thickness.

FUTURE WORK

1. Optical fibre integration

A novel optical fibre (OF) sensor integration principle by material extrusion 3-D printing technology is proposed in this work for thermoplastic materials. At current stage, the adopted OF integration procedure has specialized fixtures to fix and align the OF during the 3-D printing process. Because of this reason, the OF is integrated only in a straight line. In SHM, it is required to monitor the status of different key points of structures, thus the OFs are expected to be placed along patterns with 3-D curvatures. It is necessary to integrate the OF with more degrees of freedom than available today. Future research can be conducted on 1) attaching new modified fixtures to the 3-D printer to enable automated OF integration during 3-D printing, and 2) pre-embedding the OF into a filament for the 3-D printer and constructing a modified printer head for this smart filament.

2. Live monitoring

In this thesis, the potential of in-situ OBR technology for detecting invisible manufacturing defects has been demonstrated. Optical fibres are a convenient tool for evaluating manufacturing quality. More future applications to assess the quality of different manufacturing processes by using optical fibres are certainly expected, such as filament winding and automated fibre placement technologies.

A live monitoring of any manufacturing process can significantly increase the value of this technique in the industry application. One of the problems is the coupled sensitivity of thermal and mechanical effects of OF sensors. With the technology development, the OF sensors will be able to solve this problem and sense the temperature and strain simultaneously for live monitoring of fabrication processes.

Bibliography

- [1] K. Schwab, *The Fourth Industrial Revolution*, Currency, 2017.
- [2] Gokhale, P., Bhat, O. and Bhat, S., 2018. Introduction to IOT. *International Advanced Research Journal in Science, Engineering and Technology*, 5(2018): 41-44.
- [3] S.G. Hegde, *Study of IoT: Understanding IoT Architecture, Applications, Issues and Challenges*, (n.d.) 7.
- [4] Y. Zhang, J. Yu, A Study on the Fire IOT Development Strategy, *Procedia Engineering*. 52 (2013) 314–319. <https://doi.org/10.1016/j.proeng.2013.02.146>.
- [5] D. Bandyopadhyay, J. Sen, Internet of Things: Applications and Challenges in Technology and Standardization, *Wireless Pers Commun*. 58 (2011) 49–69. <https://doi.org/10.1007/s11277-011-0288-5>.
- [6] Soumyalatha, S.G.H., 2016, May. Study of IoT: understanding IoT architecture, applications, issues and challenges. In 1st International Conference on Innovations in Computing & Net-working (ICICN16), CSE, RRCE. *International Journal of Advanced Networking & Applications* (Vol. 478).
- [7] E. Ozer, M.Q. Feng, 13 - Structural health monitoring, in: F. Pacheco-Torgal, E. Rasmussen, C.-G. Granqvist, V. Ivanov, A. Kaklauskas, S. Makonin (Eds.), *Start-Up Creation* (Second Edition), Woodhead Publishing, 2020: pp. 345–367. <https://doi.org/10.1016/B978-0-12-819946-6.00013-8>.
- [8] F. Lamonaca, P.F. Sciammarella, C. Scuro, D.L. Carni, R.S. Olivito, Internet of Things for Structural Health Monitoring, in: 2018 Workshop on Metrology for Industry 4.0 and IoT, 2018: pp. 95–100. <https://doi.org/10.1109/METROI4.2018.8439038>.
- [9] Z. Ding, C. Wang, K. Liu, J. Jiang, D. Yang, G. Pan, Z. Pu, T. Liu, Distributed Optical Fiber Sensors Based on Optical Frequency Domain Reflectometry: A review, *Sensors*. 18 (2018) 1072. <https://doi.org/10.3390/s18041072>.
- [10] S.T. Kreger, D.K. Gifford, M.E. Froggatt, B.J. Soller, M.S. Wolfe, High Resolution Distributed Strain or Temperature Measurements in Single- and Multi-Mode Fiber Using Swept-Wavelength Interferometry, in: *Optical Fiber Sensors*, OSA, Cancún, Mexico, 2006: p. ThE42. <https://doi.org/10.1364/OFS.2006.ThE42>.
- [11] A. Abdelgawad, K. Yelamarthi, Structural health monitoring: Internet of things application, in: 2016 IEEE 59th International Midwest Symposium on Circuits and Systems (MWSCAS), 2016: pp. 1–4. <https://doi.org/10.1109/MWSCAS.2016.7870118>.
- [12] P. Ferdinand, *The Evolution of Optical Fiber Sensors Technologies During the 35 Last Years and Their Applications in Structure Health Monitoring*, (2014) 17.
- [13] P. Lenke, M. Wendt, S. Liehr, K. Krebber, Distributed humidity sensing based on Rayleigh scattering in polymer optical fibers, in: J.L. Santos, B. Culshaw, J.M. López-Higuera, W.N. MacPherson (Eds.), *Porto, Portugal*, 2010: p. 76533X. <https://doi.org/10.1117/12.866279>.
- [14] X. Bao, L. Chen, Recent Progress in Distributed Fiber Optic Sensors, *Sensors*. 12 (2012) 8601–8639. <https://doi.org/10.3390/s120708601>.
- [15] *Internet of Things for Optical Sensors*, (n.d.). <https://ukdiss.com/examples/internet-of-things-for-optical-sensors.php> (accessed September 17, 2021).
- [16] X.W. Ye, Y.H. Su, J.P. Han, Structural Health Monitoring of Civil Infrastructure Using Optical Fiber Sensing Technology: A Comprehensive Review, *The Scientific World Journal*. 2014 (2014) e652329. <https://doi.org/10.1155/2014/652329>.
- [17] D.C. Sweeney, A.M. Schrell, C.M. Petrie, An Adaptive Reference Scheme to Extend the Functional Range of Optical Backscatter Reflectometry in Extreme Environments, *IEEE Sensors Journal*. 21 (2021) 498–509. <https://doi.org/10.1109/JSEN.2020.3013121>.

References

- [18] R.K. Palmer, T.E. Blue, Modulation Transfer Function for Distributed Temperature Measurements Using an Optical Fiber Sensor System, *IEEE Sensors Journal*. 18 (2018) 1911–1918. <https://doi.org/10.1109/JSEN.2017.2788895>.
- [19] M.S. Peixoto e Silva, T.H.C. de Barros, H.P. Alves, J.F. do Nascimento, J.F. Martins Filho, Evaluation of Fiber Optic Raman Scattering Distributed Temperature Sensor Between –196 and 400 °C, *IEEE Sensors J.* 21 (2021) 1527–1533. <https://doi.org/10.1109/JSEN.2020.3016322>.
- [20] A.D. Kersey, A Review of Recent Developments in Fiber Optic Sensor Technology, *Optical Fiber Technology*. 2 (1996) 291–317. <https://doi.org/10.1006/ofte.1996.0036>.
- [21] A. Güemes, A. Fernández-López, P. Díaz-Maroto, A. Lozano, J. Sierra-Perez, Structural Health Monitoring in Composite Structures by Fiber-Optic Sensors, *Sensors*. 18 (2018) 1094. <https://doi.org/10.3390/s18041094>.
- [22] Y. Muanenda, C.J. Oton, F. Di Pasquale, Application of Raman and Brillouin Scattering Phenomena in Distributed Optical Fiber Sensing, *Frontiers in Physics*. 7 (2019). <https://www.frontiersin.org/article/10.3389/fphy.2019.00155>.
- [23] H. Alemohammad, A. Azhari, R. Liang, Fiber optic sensors for distributed monitoring of soil and groundwater during in-situ thermal remediation, in: C.S. Baldwin, G. Pickrell, H.H. Du (Eds.), *Anaheim, California, United States, 2017*: p. 102080I. <https://doi.org/10.1117/12.2270033>.
- [24] X. Bao, Y. Wang, Recent Advancements in Rayleigh Scattering-Based Distributed Fiber Sensors, *Advanced Devices & Instrumentation*. 2021 (2021). <https://doi.org/10.34133/2021/8696571>.
- [25] G. Allwood, G. Wild, S. Hinckley, Fiber Bragg Grating Sensors for Mainstream Industrial Processes, *Electronics*. 6 (2017) 92. <https://doi.org/10.3390/electronics6040092>.
- [26] D. Sengupta, G. Rajan, *Introduction to Optical Fiber Sensors*, Routledge Handbooks Online, 2016. <https://doi.org/10.1201/9781315369815-4>.
- [27] Amira, Z., Bouyahi, M. and Ezzedine, T. Measurement of temperature through Raman scattering. *Procedia Computer Science*, 73 (2015): 350-357.
- [28] S. Adachi, Distributed optical fiber sensors and their applications, in: 2008 SICE Annual Conference, IEEE, Chofu, 2008: pp. 329–333. <https://doi.org/10.1109/SICE.2008.4654674>.
- [29] A. Signorini, S. Faralli, M.A. Soto, G. Sacchi, F. Baronti, R. Barsacchi, A. Lazzeri, R. Roncella, G. Bolognini, F.D. Pasquale, 40 km long-range Raman-based distributed temperature sensor with meter-scale spatial resolution, in: *Optical Fiber Communication Conference (2010), Paper OWL2*, Optica Publishing Group, 2010: p. OWL2. <https://doi.org/10.1364/OFC.2010.OWL2>.
- [30] N. Lalam, W.P. Ng, X. Dai, Q. Wu, Y.Q. Fu, Analysis of Brillouin Frequency Shift in Distributed Optical Fiber Sensor System for Strain and Temperature Monitoring, in: *Proceedings of the 4th International Conference on Photonics, Optics and Laser Technology*, SCITEPRESS - Science and Technology Publications, Rome, Italy, 2016: pp. 333–340. <https://doi.org/10.5220/0005842803330340>.
- [31] Y. Dong, X. Bao, L. Chen, 2-km-range and 2-cm-spatial-resolution Brillouin optical fiber sensor using a transient differential pulse pair, in: *Proceedings of 2011 International Conference on Electronics and Optoelectronics*, 2011: pp. V4-11-V4-14. <https://doi.org/10.1109/ICEOE.2011.6013412>.
- [32] Li, E., 2017, October. Rayleigh scattering based distributed optical fiber sensing. In *AOPC 2017: Fiber Optic Sensing and Optical Communications (Vol. 10464, pp. 381-387)*. SPIE.

References

- [33] Optical Backscatter Reflectometer 4600, User Guide, Luna, USA, chrome-extension://efaidnbmnnpbpcjpcglefindmkaj/https://lunainc.com/sites/default/files/assets/files/resource-library/OBR-4600-UG6_SW3.10.1.pdf. (accessed July 02, 2018).
- [34] X. Lu. Coherent Rayleigh time domain reflectometry: Novel applications for optical fibre sensing. PhD diss., Ecole Polytechnique Fédérale de Lausanne, 2016.
- [35] X. Lu, P.J. Thomas, J.O. Hellevang, A Review of Methods for Fibre-Optic Distributed Chemical Sensing, *Sensors*. 19 (2019) 2876. <https://doi.org/10.3390/s19132876>.
- [36] M.F. Bado, J.R. Casas, A Review of Recent Distributed Optical Fiber Sensors Applications for Civil Engineering Structural Health Monitoring, *Sensors*. 21 (2021) 1818. <https://doi.org/10.3390/s21051818>.
- [37] C. Liang, Q. Bai, M. Yan, Y. Wang, H. Zhang, B. Jin, A Comprehensive Study of Optical Frequency Domain Reflectometry, *IEEE Access*. 9 (2021) 41647–41668. <https://doi.org/10.1109/ACCESS.2021.3061250>.
- [38] A.K. Sang, Distributed Vibration Sensing using Rayleigh Backscatter in Optical Fibers, (2011). <https://vtechworks.lib.vt.edu/handle/10919/77274> (accessed April 8, 2022).
- [39] L. Chamoin, S. Farahbakhsh, M. Poncelet, An educational review on distributed optic fiber sensing based on Rayleigh backscattering for damage tracking and structural health monitoring, *Meas. Sci. Technol.* 33 (2022) 124008. <https://doi.org/10.1088/1361-6501/ac9152>.
- [40] C. Kralovec, M. Schagerl, Review of Structural Health Monitoring Methods Regarding a Multi-Sensor Approach for Damage Assessment of Metal and Composite Structures, *Sensors*. 20 (2020) 826. <https://doi.org/10.3390/s20030826>.
- [41] D.C. Betz, L. Staudigel, M.N. Trutzel, M. Kehlenbach, Structural Monitoring Using Fiber-Optic Bragg Grating Sensors, *Structural Health Monitoring*. 2 (2003) 145–152. <https://doi.org/10.1177/1475921703002002006>.
- [42] S. Wang, E. Sæter, K. Lasn, Comparison of DOFS Attachment Methods for Time-Dependent Strain Sensing, *Sensors*. 21 (2021) 6879. <https://doi.org/10.3390/s21206879>.
- [43] G. Rodriguez, J.R. Casas, S. Villalba, SHM by DOFS in civil engineering: a review, *Structural Monitoring and Maintenance*. 2 (2015) 357–382. <https://doi.org/10.12989/smm.2015.2.4.357>.
- [44] N.A. Houlst, O. Ekim, R. Regier, Damage/Deterioration Detection for Steel Structures Using Distributed Fiber Optic Strain Sensors, *Journal of Engineering Mechanics*. 140 (2014) 04014097. [https://doi.org/10.1061/\(ASCE\)EM.1943-7889.0000812](https://doi.org/10.1061/(ASCE)EM.1943-7889.0000812).
- [45] C. Davis, M. Knowles, N. Rajic, G. Swanton, Evaluation of a Distributed Fibre Optic Strain Sensing System for Full-Scale Fatigue Testing, *Procedia Structural Integrity*. 2 (2016) 3784–3791. <https://doi.org/10.1016/j.prostr.2016.06.471>.
- [46] J.V. Roosbroeck, E. Jacobs, E. Voet, J. Vlekken, Installation and test procedures of optical strain gauges for aeronautical applications, in: 20th International Conference on Optical Fibre Sensors, International Society for Optics and Photonics, 2009: p. 75037Q. <https://doi.org/10.1117/12.837542>.
- [47] Y.B. Lin, K.C. Chang, J.C. Chern, L.A. Wang, Packaging methods of fiber-Bragg grating sensors in civil structure applications, *IEEE Sensors Journal*. 5 (2005) 419–424. <https://doi.org/10.1109/JSEN.2005.844539>.
- [48] A. Sun, Study of simultaneous measurement of temperature and pressure using double fiber Bragg gratings with polymer package, *Opt. Eng.* 44 (2005) 034402. <https://doi.org/10.1117/1.1870493>.
- [49] J. Yang, L. Yuan, Package and installation of embeddable fiber optic sensors, *Optics and Lasers in Engineering*. 47 (2009) 1085–1090. <https://doi.org/10.1016/j.optlaseng.2009.05.002>.

References

- [50] L. Meng, L. Wang, Y. Hou, G. Yan, A Research on Low Modulus Distributed Fiber Optical Sensor for Pavement Material Strain Monitoring, *Sensors*. 17 (2017) 2386. <https://doi.org/10.3390/s17102386>.
- [51] R. Jockwer, P. Grönquist, A. Frangi, Long-term deformation behaviour of timber columns: Monitoring of a tall timber building in Switzerland, *Engineering Structures*. 234 (2021) 111855. <https://doi.org/10.1016/j.engstruct.2021.111855>.
- [52] J. Montesano, M. Selezneva, C. Poon, Z. Fawaz, K. Behdinan, Application of fiber optic sensors for elevated temperature testing of polymer matrix composite materials, *Science and Engineering of Composite Materials*. 18 (2011) 109–116. <https://doi.org/10.1515/SECM.2011.014>.
- [53] A. Iadicicco, D. Natale, P. Di Palma, F. Spinaci, A. Apicella, S. Campopiano, Strain Monitoring of a Composite Drag Strut in Aircraft Landing Gear by Fiber Bragg Grating Sensors, *Sensors (Basel)*. 19 (2019) 2239. <https://doi.org/10.3390/s19102239>.
- [54] P. Ferdinand, S. Magne, V. Dewynter-Marty, S. Rougeault, L. Maurin, Applications of Fiber Bragg Grating Sensors in the Composite Industry, *MRS Bull.* 27 (2002) 400–407. <https://doi.org/10.1557/mrs2002.126>.
- [55] E. Saeter, K. Lasn, F. Nony, A.T. Echtermeyer, Embedded optical fibres for monitoring pressurization and impact of filament wound cylinders, *Composite Structures*. 210 (2019) 608–617. <https://doi.org/10.1016/j.compstruct.2018.11.051>.
- [56] A. Wosniok, D. Skoczowsky, M. Schukar, S. Pötzsch, S. Pötschke, S. Krüger, Fiber optic sensors for high-temperature measurements on composite tanks in fire, *J Civil Struct Health Monit.* 9 (2019) 361–368. <https://doi.org/10.1007/s13349-019-00338-7>.
- [57] S. Goossens, B.D. Pauw, T. Geernaert, M.S. Salmanpour, Z.S. Khodaei, E. Karachalios, D. Saenz-Castillo, H. Thienpont, F. Berghmans, Aerospace-grade surface mounted optical fibre strain sensor for structural health monitoring on composite structures evaluated against in-flight conditions, *Smart Mater. Struct.* 28 (2019) 065008. <https://doi.org/10.1088/1361-665X/ab1458>.
- [58] M. Mulle, A. Yudhanto, G. Lubineau, R. Yaldiz, W. Schijve, N. Verghese, Internal strain assessment using FBGs in a thermoplastic composite subjected to quasi-static indentation and low-velocity impact, *Composite Structures*. 215 (2019) 305–316. <https://doi.org/10.1016/j.compstruct.2019.02.085>.
- [59] M. Arhant, N. Meek, D. Penumadu, P. Davies, N. Garg, Residual Strains using Integrated Continuous Fiber Optic Sensing in Thermoplastic Composites and Structural Health Monitoring, *Exp Mech.* 58 (2018) 167–176. <https://doi.org/10.1007/s11340-017-0339-2>.
- [60] E. Voet, G. Luyckx, I. De Baere, J. Degrieck, J. Vlekken, E. Jacobs, H. Bartelt, High Strain Monitoring during Fatigue Loading of Thermoplastic Composites Using Imbedded Draw Tower Fibre Bragg Grating Sensors, *AST*. 56 (2008) 441–446. <https://doi.org/10.4028/www.scientific.net/AST.56.441>.
- [61] S. Wang, K. Lasn, C.W. Elverum, D. Wan, A. Echtermeyer, Novel in-situ residual strain measurements in additive manufacturing specimens by using the Optical Backscatter Reflectometry, *Additive Manufacturing*. 32 (2020) 101040. <https://doi.org/10.1016/j.addma.2020.101040>.
- [62] A. Mirabedini, A. Ang, M. Nikzad, B. Fox, K.-T. Lau, N. Hameed, Evolving Strategies for Producing Multiscale Graphene-Enhanced Fiber-Reinforced Polymer Composites for Smart Structural Applications, *Advanced Science*. 7 (2020) 1903501. <https://doi.org/10.1002/advs.201903501>.
- [63] H.G.M. Doan, P. Mertiny, Creep Testing of Thermoplastic Fiber-Reinforced Polymer Composite Tubular Coupons, *Materials*. 13 (2020) 4637. <https://doi.org/10.3390/ma13204637>.

References

- [64] T. Tsukada, S. Minakuchi, N. Takeda, Assessing residual stress redistribution during annealing in thick thermoplastic composites using optical fiber sensors, *Journal of Thermoplastic Composite Materials*. 33 (2020) 53–68.
<https://doi.org/10.1177/0892705718804580>.
- [65] FS62, NVMS. (n.d.). <https://nvms.com.au/product/fs62-high-performance-fiber-bragg-grating-fbg-strain-sensors/> (accessed September 23, 2021).
- [66] DISTRIBUTED FIBER OPTIC SENSING LEADS THE WAY TO BETTER BONDING AND WELDING, (n.d.).
<http://ati.mydigitalpublication.co.uk/articles/distributed-fiber-optic-sensing-leads-the-way-to-better-bonding-and-welding> (accessed September 23, 2021).
- [67] K.S.C. Kuang, L. Zhang, W.J. Cantwell, I. Bennion, Process monitoring of aluminum-foam sandwich structures based on thermoplastic fibre–metal laminates using fibre Bragg gratings, *Composites Science and Technology*. 65 (2005) 669–676.
<https://doi.org/10.1016/j.compscitech.2004.09.005>.
- [68] E.A.Y.F. Corp Henkel, Adhesives for Fiber Optics Assembly: Making the Right Choice, (n.d.).
https://www.photonics.com/Articles/Adhesives_for_Fiber_Optics_Assembly_Making_the/a25147 (accessed June 24, 2021).
- [69] E. Marin, Y. Ouerdane, Dual-Fibre Bragg Grating Sensor for Simultaneous Temperature and Strain Sensing of Composite Materials Manufacturing, (2014) 10.
- [70] L. Reekie, J.P. Dakin, J.-L. Archambault, M.G. Xu, Discrimination between strain and temperature effects using dual-wavelength fibre grating sensors, *Electronics Letters*. 30 (1994) 1085–1087. <https://doi.org/10.1049/el:19940746>.
- [71] K. Kishida, Y. Yamauchi, A. Guzik, Study of optical fibers strain-temperature sensitivities using hybrid Brillouin-Rayleigh system, *Photonic Sens.* 4 (2014) 1–11.
<https://doi.org/10.1007/s13320-013-0136-1>.
- [72] D.-P. Zhou, W. Li, L. Chen, X. Bao, Distributed Temperature and Strain Discrimination with Stimulated Brillouin Scattering and Rayleigh Backscatter in an Optical Fiber, *Sensors*. 13 (2013) 1836–1845. <https://doi.org/10.3390/s130201836>.
- [73] Yang Du, Tiegeng Liu, Zhenyang Ding, Qun Han, Kun Liu, Junfeng Jiang, Qinnan Chen, Bowen Feng, Cryogenic Temperature Measurement Using Rayleigh Backscattering Spectra Shift by OFDR, *IEEE Photon. Technol. Lett.* 26 (2014) 1150–1153.
<https://doi.org/10.1109/LPT.2014.2317702>.
- [74] A. Faustov, A. Gussarov, M. Wuilpart, A.A. Fotiadi, L.B. Liokumovich, O.I. Kotov, I.O. Zolotovskiy, A.L. Tomashuk, T. Deschoutheete, P. Mégret, Distributed optical fibre temperature measurements in a low dose rate radiation environment based on Rayleigh backscattering, in: F. Berghmans, A.G. Mignani, P. De Moor (Eds.), Brussels, Belgium, 2012: p. 84390C. <https://doi.org/10.1117/12.922082>.
- [75] P. Stajanca, K. Hicke, K. Krebber, Distributed Fiberoptic Sensor for Simultaneous Humidity and Temperature Monitoring Based on Polyimide-Coated Optical Fibers, *Sensors*. 19 (2019) 5279. <https://doi.org/10.3390/s19235279>.
- [76] A. Güemes, A. Fernández-López, B. Soller, Optical Fiber Distributed Sensing - Physical Principles and Applications, *Structural Health Monitoring*. 9 (2010) 233–245.
<https://doi.org/10.1177/1475921710365263>.
- [77] A. Barrias, J.R. Casas, S. Villalba, SHM of Reinforced Concrete Elements by Rayleigh Backscattering DOFS, *Front. Built Environ.* 5 (2019) 30.
<https://doi.org/10.3389/fbuil.2019.00030>.
- [78] C.G. Berrocal, I. Fernandez, R. Rempling, Crack monitoring in reinforced concrete beams by distributed optical fiber sensors, *Structure and Infrastructure Engineering*. 17 (2021) 124–139. <https://doi.org/10.1080/15732479.2020.1731558>.

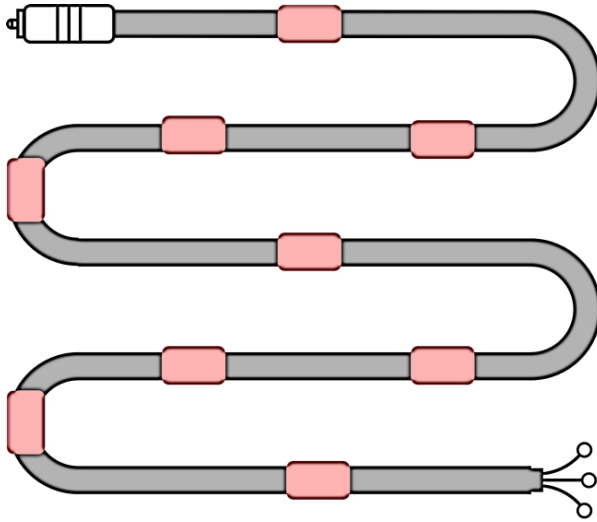
References

- [79] S. Wang, K. Lasn, Accurate non-linear calculation model for decoupling thermal and mechanical loading effects in the OBR measurements, *Opt. Express*. 29 (2021) 1532. <https://doi.org/10.1364/OE.410686>.
- [80] MANUFACTUR3D, The 7 Types of Additive Manufacturing Technologies, MANUFACTUR3D. (2018). <https://manufactur3dmag.com/7-types-additive-manufacturing-technologies/> (accessed October 9, 2021).
- [81] The 7 categories of Additive Manufacturing | Additive Manufacturing Research Group | Loughborough University, (n.d.). <https://www.lboro.ac.uk/research/amrg/about/the7categoriesofadditivemanufacturing/> (accessed October 9, 2021).
- [82] D. Pranzo, P. Larizza, D. Filippini, G. Percoco, Extrusion-Based 3D Printing of Microfluidic Devices for Chemical and Biomedical Applications: A Topical Review, *Micromachines*. 9 (2018) 374. <https://doi.org/10.3390/mi9080374>.
- [83] K.L. Shaoquan Wang, Integration of optical fibre sensors by material extrusion 3-D printing – the effect of bottom interlayer thickness, Submitted. (2022).
- [84] ClearLite® POLY 1550 17 Photonic Fibers, (n.d.). <https://fiber-optic-catalog.ofsoptics.com/SMB-E1550H-FIBER-716762> (accessed March 16, 2022).
- [85] W. Wang, Y. Yu, Y. Geng, X. Li, Measurements of thermo-optic coefficient of standard single mode fiber in large temperature range, in: X. Zhang, D. Erickson, X. Fan, Z. Chen (Eds.), Beijing, China, 2015: p. 96200Y. <https://doi.org/10.1117/12.2193091>.
- [86] F.G. Della Corte, M. Esposito Montefusco, L. Moretti, I. Rendina, G. Cocorullo, Temperature dependence analysis of the thermo-optic effect in silicon by single and double oscillator models, *Journal of Applied Physics*. 88 (2000) 7115–7119. <https://doi.org/10.1063/1.1328062>.
- [87] G. Ghosh, Sellmeier coefficients and dispersion of thermo-optic coefficients for some optical glasses, *Appl. Opt.*, AO. 36 (1997) 1540–1546. <https://doi.org/10.1364/AO.36.001540>.
- [88] G. Ghosh, Model for the thermo-optic coefficients of some standard optical glasses, *Journal of Non-Crystalline Solids*. 189 (1995) 191–196. [https://doi.org/10.1016/0022-3093\(95\)00247-2](https://doi.org/10.1016/0022-3093(95)00247-2).
- [89] A. Rivero, M. Quintero, Ch. Power, J. Gonzalez, R. Tovar, J. Ruiz, Temperature variation of optical energy gap values of the compound CuGaTe₂, *Journal of Elec Materi*. 26 (1997) 1428–1432. <https://doi.org/10.1007/s11664-997-0062-3>.
- [90] P.K. Sarswat, M.L. Free, A Study of Energy Band Gap Temperature Relationships for Cu₂ZnSnS₄ Thin Films, (n.d.).
- [91] O. Kopylov, J. Lee, I. Han, W.J. Choi, J.D. Song, I. Yeo, Temperature dependence of the excitonic energy band gap in In(Ga)As nanostructures, *Journal of the Korean Physical Society*. 60 (2012) 1828–1832. <https://doi.org/10.3938/jkps.60.1828>.
- [92] B. Pejova, B. Abay, I. Bineva, Temperature Dependence of the Band-Gap Energy and Sub-Band-Gap Absorption Tails in Strongly Quantized ZnSe Nanocrystals Deposited as Thin Films, *J. Phys. Chem. C*. 114 (2010) 15280–15291. <https://doi.org/10.1021/jp102773z>.
- [93] M. Katouzian, S. Vlase, Creep Response of Carbon-Fiber-Reinforced Composite Using Homogenization Method, *Polymers (Basel)*. 13 (2021) 867. <https://doi.org/10.3390/polym13060867>.
- [94] Y.-Y. Zhang, Z. Sun, Y.-Q. Li, P. Huang, Q. Chen, S.-Y. Fu, Tensile creep behavior of short-carbon-fiber reinforced polyetherimide composites, *Composites Part B: Engineering*. 212 (2021) 108717. <https://doi.org/10.1016/j.compositesb.2021.108717>.
- [95] W.K. Goertzen, M.R. Kessler, Creep behavior of carbon fiber/epoxy matrix composites, *Materials Science and Engineering: A*. 421 (2006) 217–225. <https://doi.org/10.1016/j.msea.2006.01.063>.

References

- [96] P. Dasappa, P. Lee-Sullivan, X. Xiao, P.H. Foss, Tensile creep of a long-fiber glass mat thermoplastic composite. I. Short-term tests, *Polymer Composites*. 30 (2009) 1146–1157. <https://doi.org/10.1002/pc.20671>.
- [97] C.-C. Cheng, Y.-L. Lo, B.S. Pun, Y.M. Chang, W.Y. Li, An Investigation of Bonding-Layer Characteristics of Substrate-Bonded Fiber Bragg Grating, *JOURNAL OF LIGHTWAVE TECHNOLOGY*. 23 (2005) 9.
- [98] W. Zhang, W. Chen, Y. Shu, X. Lei, X. Liu, Effects of bonding layer on the available strain measuring range of fiber Bragg gratings, *Appl. Opt.*, AO. 53 (2014) 885–891. <https://doi.org/10.1364/AO.53.000885>.
- [99] S.-C. Her, C.-Y. Tsai, Strain measurement of fiber optic sensor surface bonding on host material, *Transactions of Nonferrous Metals Society of China*. 19 (2009) s143–s149. [https://doi.org/10.1016/S1003-6326\(10\)60262-2](https://doi.org/10.1016/S1003-6326(10)60262-2).
- [100] G. Zhou, H. Li, L. Ren, D. Li, Influencing parameters analysis of strain transfer in optic fiber Bragg grating sensors, in: N. Meyendorf, G.Y. Baaklini, B. Michel (Eds.), San Diego, CA, 2006: p. 61790R. <https://doi.org/10.1117/12.661858>.
- [101] M. Liang, N. Chen, X. Fang, G. Wu, Strain transferring mechanism analysis of the surface-bonded FBG sensor, *Appl. Opt.* 57 (2018) 5837. <https://doi.org/10.1364/AO.57.005837>.
- [102] G. Xue, X. Fang, X. Hu, L. Gong, Measurement accuracy of FBG used as a surface-bonded strain sensor installed by adhesive, *Appl. Opt.* 57 (2018) 2939. <https://doi.org/10.1364/AO.57.002939>.
- [103] S.-C. Her, C.-Y. Huang, The Effects of Adhesive and Bonding Length on the Strain Transfer of Optical Fiber Sensors, *Applied Sciences*. 6 (2016) 13. <https://doi.org/10.3390/app6010013>.
- [104] H. Zhao, Q. Wang, Y. Qiu, J. Chen, Y. Wang, Z. Fan, Strain transfer of surface-bonded fiber Bragg grating sensors for airship envelope structural health monitoring, *J. Zhejiang Univ. Sci. A*. 13 (2012) 538–545. <https://doi.org/10.1631/jzus.A1100336>.
- [105] J. Li, Z. Zhou, J. Ou, Interface strain transfer mechanism and error modification for adhered FBG strain sensor, in: Y.N. Kulchin, O.B. Vitrik, V.I. Stroganov (Eds.), Khabrovsk, 2005: pp. 278–287. <https://doi.org/10.1117/12.634066>.
- [106] S.-C. Her, C.-Y. Huang, Effect of Coating on the Strain Transfer of Optical Fiber Sensors, *Sensors*. 11 (2011) 6926–6941. <https://doi.org/10.3390/s110706926>.
- [107] N. Perogamvros, P. Motwani, A. Murphy, S. Taylor, Investigation of Surface Strain Fields of Thermoplastic Composites Using Fibre Optic Sensors, (n.d.) 2.

PART 2: APPENDICES



Paper I



Full Length Article

Novel in-situ residual strain measurements in additive manufacturing specimens by using the Optical Backscatter Reflectometry



Shaoquan Wang^{*}, Kaspar Lasn, Christer Westum Elverum, Di Wan, Andreas Echtermeyer

Department of Mechanical and Industrial Engineering, Norwegian University of Science and Technology (NTNU), Richard Birkelands vei 2B, 7491, Trondheim, Norway

ARTICLE INFO

Keywords:

Material extrusion
Residual strain
Manufacturing defect
Optical fiber
Optical Backscatter Reflectometry

ABSTRACT

Material extrusion (MEX) is a well established production method in additive manufacturing. However, internal residual strains are accumulated during the layer-by-layer fabrication process. They bring about shape distortions and a degradation of mechanical properties. In this paper, an in-situ distributed measurement of residual strains in MEX fabricated thermoplastic specimens is achieved for the first time. This innovative measuring system consists of an Optical Backscatter Reflectometry (OBR) interrogation unit connected to a distributed fiber optic strain sensor which is embedded during the MEX process. The characteristic residual strain distribution inside 3D printed components is revealed and numerically validated. The main mechanisms of residual strain creation and the sensing principles of in-situ OBR are described. A minimum measuring range of 4 mm and a spatial resolution of 0.15 mm were experimentally demonstrated. The potential of in-situ OBR technology for detecting invisible manufacturing defects was shown by a trial experiment.

1. Introduction

Material extrusion (MEX) is the most conventional additive manufacturing technology for plastics, also known as 3D printing. It offers great benefits to rapid prototyping and manufacturing applications [1]. MEX technology shows good potential in the automotive, aerospace, design and biomedical industries, due to its low cost, simplicity and environmental friendliness. Currently, it has already captured half of the 3D printing market [2]. The printer builds one layer at a time, with each subsequent layer being built directly on the previous. A wide variety of thermoplastic materials are available. However, a common negative characteristic is always recognized: accumulation of residual stress and strain during the material build up [3]. More specifically, the feedstock thermoplastic experiences a melting and rapid cooling cycle and a consequent phase transformation from molten to solid state during the deposition of each layer. Residual stress mainly arises from the shrinkage of the thermoplastic during the phase transformation and accumulates during the layer-by-layer build up process in MEX [4]. Residual stresses can significantly affect the dimensional accuracy, cause warping, interlayer delamination, cracking, decrease of mechanical properties and even interrupt the printing procedure when the specimen detaches from the printing bed. This kind of disadvantage, innate to layer-by-layer build-up hinders the application of the MEX.

An experimental research study was carried out by Dao et al. [5] to

evaluate the dimensional accuracy of models made by MEX. The results show that the dimensional inaccuracy of the MEX production is mainly induced by the material shrinkage after experiencing a phase transformation from a semiliquid to a solid state during the melting and cooling cycles. As reported by Casavola et al. [6], accumulation of residual stress due to the rapid heating and cooling cycles of thermoplastic can seriously affect the shape and the final dimensions of the parts. A FEA model was developed by Zhang and Chou [7] to simulate the shape distortion from the MEX process. The results show that part distortions are related to the stress accumulation during the deposition. Es-Said et al. [8] concluded that volumetric shrinkage, induced by phase transformation during solidification, caused weak interlayer bonding and high porosity resulting in reduced mechanical properties. Wang et al. [9] showed that decreasing the glass-transition temperature and linear shrinkage rate of the feedstock material is helpful for the reduction of inner stresses responsible for warp deformation. These results indicate that the contraction of thermoplastics during MEX processing is believed to be the main cause of distortions, interlayer delamination and degradation of mechanical properties. Hence, for eliminating these negative effects, processing optimization aiming at reducing residual strains can improve the strength and the shaping precision. It is regarded as an important issue for successful industrial application of the MEX technology.

Evaluating residual strain distribution is essential for MEX

^{*} Corresponding author.

E-mail address: shaoquan.wang@ntnu.no (S. Wang).

<https://doi.org/10.1016/j.addma.2020.101040>

Received 11 September 2019; Received in revised form 17 December 2019; Accepted 2 January 2020

Available online 03 January 2020

2214-8604/© 2020 The Authors. Published by Elsevier B.V. This is an open access article under the CC BY license (<http://creativecommons.org/licenses/by/4.0/>).

parameter optimization [10]. Unfortunately, it is quite challenging to measure residual strains during MEX by using traditional measurement technologies. To the best of the authors' knowledge, only one series of promising works in this field was reported by Kantaros et al. and Kousiatza et al. over the recent years [10,11]. In this research, an in-situ point strain measurement was performed through one Fiber Bragg Grating (FBG). A short FBG was embedded at the midplane of the samples. The residual strain at the centroid of the specimen, where the grating was located, was viewed as the average residual strain of the whole specimen. However, point sensors present serious limitations in application. For instance, the measured strain value from FBG can be distorted, when the grating of the FBG fiber passes through a manufacturing defect, like an under/over-filled region or distorted part of the structure. Additionally, the number of point sensors necessary to obtain a global strain monitoring, becomes impractically high for large specimens. The lack of reliable in-situ and distributed measurement approaches for residual strains impedes the development of the MEX technology.

In this study, a novel approach for measuring the solidification-induced residual strain distribution in MEX fabricated specimens was achieved for the first time. The measuring system consists of an Optical Backscatter Reflectometry (OBR) interrogation unit connected to a standard single mode optical fiber embedded in the component during the MEX process. Based on Rayleigh backscattering, distributed strain sensing is achieved along the axis of the optical fiber. A non-invasive embedding procedure is presented and validated from micro to macro scale. A comparison between the in-situ OBR and the electrical strain gauge validates the reliability of the new approach. A characteristic horizontal residual strain distribution and the vertical average residual strain distribution were revealed inside MEX fabricated specimens. A simplified description is presented that captures key mechanisms of residual strain creation in MEX. The molecular behavior of the feed-stock material induced by temperature evolution during the MEX process was characterized by a differential scanning calorimetry (DSC) instrument and by an infrared camera. The effects of the OBR post-processing parameters and specimen dimensions on the measurement results were analyzed. Moreover, the possibility of detecting manufacturing defects by this innovative method was also demonstrated.

2. Materials and methods

2.1. OBR instrument and the optical fiber strain sensor

As shown in Fig. 1 (a), the distributed optical fiber strain sensor (DOFS) is SMB-E1550H fiber from OFS Fitel, LLC. It is a silica/silica/polyimide fiber with a core diameter of 6.5 μm , a clad diameter of 125 μm and a coating diameter of 155 μm . It is a single mode fiber (SMF) with an operating wavelength of 1550 nm. The polyimide coating enables working temperatures between -65 °C and +300 °C. The SMF is spliced to a secondary coated optical fiber (SCOF), whose end is a connector port for transmitting the sensing signal to the interrogator. An "OBR 4600" reflectometer from Luna Instruments (Luna Innovations Incorporated, Virginia, USA) is used as the interrogator device as shown in Fig.1 (b).

2.2. Specimen preparation

The MEX printed test specimens were built on a PRUSA I3 MK2S 3D printer (Fig.1 (c)). A 1.75 mm PLA filament (3DNet) was selected for this research. PLA is the most common and representative thermoplastics for MEX printing, very popular in application and also preferred as an environmentally-friendly material. In principle, similar experiments could be carried out with any common 3D printing materials. The alignment holders (Fig.2 (a)) were printed from 1.75 mm ABS filament (3DNet), because it enables sufficient thermal stability on the heating bed during printing. Cura software is used to control the

printing process. The printing parameters are summarized in Table 1. All specimens were infilled by PLA roads at 90° with respect to the X direction of the specimen, as shown in Fig. 1 (d). The X-Y-Z coordinates defined in Fig. 1 (d) will also be used in the following sections.

In order to investigate the effects of specimen geometry on the in-situ OBR measurement results, eight sets of samples were printed as shown in Table 2. The length of X axis of the specimens of group 1 (G11 ~ G15) increases from 15 mm to 80 mm, while both the width (Y axis) and height (Z axis) remain at 15 mm and 20 mm respectively. The specimens of Group 2 (G21 ~ G23) have different widths as the unique variable parameter.

2.3. Sensor embedment

In order to achieve in-situ measurements of residual strains, the SMF part of the sensor needs to be embedded into the MEX fabricated specimen. A schematic illustration of the SMF embedding procedure as well as the final printed specimen after embedding are shown in Fig. 2. Prior to the experiment, the G-code was rewritten to pause the 3D printer at a self-defined deposition layer, and resumed the printing process after a self-defined time period. A methodology for SMF integration during the building procedure is briefly described below:

(1) Alignment holder assembly

An alignment holder was designed to assist the placement of the SMF during printing. The alignment holder contains plug-in component blocks with different thickness (Fig.2). Each component has a groove covered by a soft double-face tape to fix the SMF. By assembling blocks, two holders are able to support the optical fiber and assure the sensors' positioning at a specific height.

(2) SMF embedding

When the layer where the optical fibre should be implemented was reached, the 3D printer was paused automatically for 15 s. The SMF was then hand placed on the surface of the last deposited layer along the X axis and fixed by tapes on the holders as shown in Fig.2. Subsequently, the printing process was resumed. A new layer was built on the previous, and the SMF became encapsulated by extruded thermoplastic.

(3) Replacement and cooling

Each printed specimen was detached from the build platform right after finishing the print. Measurements were taken after the specimen had gradually cooled down to room temperature.

2.4. Optical Backscatter Reflectometry

2.4.1. OBR working principles

Optical Backscatter Reflectometry (OBR) is an optical frequency-domain method that measures Rayleigh backscatter over the length of the optical fiber. Rayleigh scattering happens when a photon penetrates a medium composed of particles whose sizes are much smaller than the incident photon wavelength. In this scattering process, the energy of the incident photon is conserved but its direction is changed randomly. In an optical fibre, silica molecules moved randomly in the molten state and froze in place during fabrication, leading to random fluctuations of the refractive index, on a scale smaller than the optical wavelength. In the OBR system, a laser source sends the incident light through the optical fiber. Rayleigh backscattering happens along the entire fiber length and its pattern acts as a unique fingerprint for each fiber. The Rayleigh backscattering in an optical fiber has similarities with fiber Bragg gratings (FBG): changes in physical length induce a frequency shift of the reflected spectrum [12–14]. These Rayleigh backscattering spectral shifts (RBS) are measured and scaled to give distributed

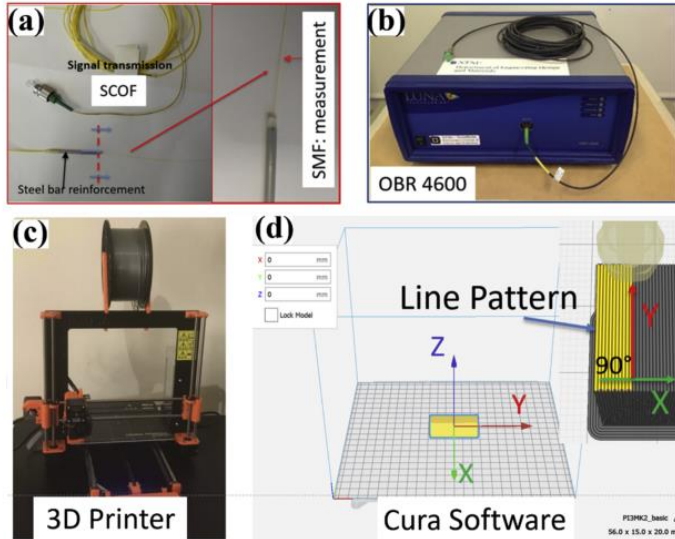


Fig. 1. Measurement and manufacturing devices: (a) Distributed optical fiber strain sensor, (b) LUNA OBR 4600 interrogator apparatus, (c) Prusa 3D printer, (d) Infill control software.

temperature or strain measurements with a high sensitivity and spatial resolution. The OBR has been applied successfully in distributed optical fiber sensor (DOFS) systems for monitoring of strain and temperature in different materials [15–20]. Heinze et al. [15] reported a new experimental method based on OBR to measure strains due to cure shrinkage in large volumes of hardening epoxy. In the study of Billon et al. [16], OBR was used as a truly distributed sensing system to monitor the strain of a concrete structural element tested in four-point bending. OBR was also adopted by Villalba et al. in detecting and monitoring the presence of damage-induced cracks in concrete structures [17]. Under ideal conditions, the DOFS based on OBR have a spatial resolution of under 1 mm and the strain resolution can be as good as 0.001 % [15,18,19]. This enables approximately thousand sensing points for every meter length of the optical fiber. Thus, the OBR system can be used to map strain distributions of a structure rather than a rough extrapolation from a few point measurements [20].

2.4.2. OBR signal demodulation

The RBS ($\Delta\nu$) between the spectra of free and loaded SMF are demodulated using the OBR Desktop v3.13.0 software. Identical to the response of an FBG, the $\Delta\nu$ of the spectrum induced by environmental perturbation can be given as [18]:

$$-\frac{\Delta\nu}{\nu} = K_T \Delta T + K_\epsilon \epsilon \tag{1}$$

Where ν is the mean optical frequency, and K_T and K_ϵ are the temperature and strain coefficients, respectively.

$$K_T = \alpha + \xi \tag{2}$$

$$K_\epsilon = 1 - \frac{n_{eff}^2}{2} (p_{12} - \mu(p_{11} + p_{12})) \tag{3}$$

K_T is a sum of the thermal expansion coefficient $\alpha = (1/\Lambda)(\partial\Lambda/\partial T)$, Λ is the volume of the optical fiber, and the thermo-optic coefficient $\xi = (1/$

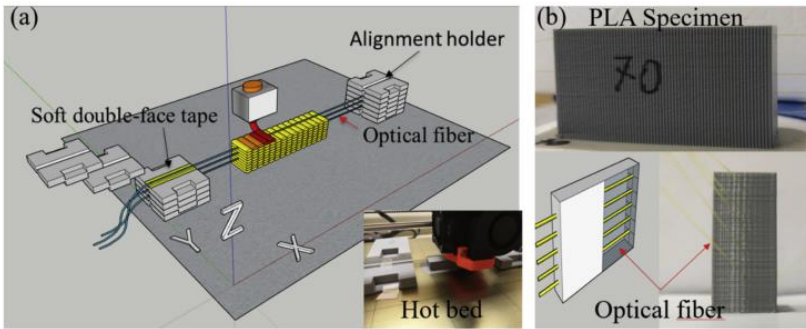


Fig. 2. A schematic illustration of the SMF embedding procedure (a) and a MEX fabricated specimen with the SMF ingressing and egressing at several locations (b).

Table 1
Printing parameters.

Layer height	Print speed	Print temperature	Build Plate temperature	Infill pattern	Infill direction	Build plate adhesion	Fan cooling
0.2 mm	30 mm/min	205 °C	60 °C	Lines	90°	Brim	Open

Table 2
MEX Specimen dimensions.

Specimen No.	Length (mm)	Width (mm)	Height (mm)	Infill density
G11	15	15	20	100 %
G12	25	15	20	100 %
G13	40	15	20	100 %
G14	56	15	20	100 %
G15	80	15	20	100 %
G21	56	15	20	100 %
G22	56	25	20	100 %
G23	56	50	20	100 %

$n(\partial n/\partial T)$, with typical values of $0.55 \times 10^{-6} \text{ }^\circ\text{C}^{-1}$ and $6.1 \times 10^{-6} \text{ }^\circ\text{C}^{-1}$ for Germanium-doped silica core fibers. K_r is a function of the group index n ; the components of the strain-optic tensor, p_{ij} ; and Poisson's ratio μ . Typical values for germanium-doped silica are reported in [18]: $K_r = 0.78$, and $K_T = 6.45 \times 10^{-6} \text{ }^\circ\text{C}^{-1}$.

2.4.3. Residual strain sensing by in-situ OBR technology

Since the SMF is embedded into a substrate material, the generalized demodulation equation is modified to account for residual strains in MEX. Before embedding, the optical fiber (without any mechanical loading, at room temperature) is connected to the OBR interrogator and the reference spectrum is recorded. In the next step, the SMF is embedded into the specimen during MEX. After printing, the specimen is removed from the hot bed and cooled down to room temperature, and a measurement spectrum was recorded from the specimen after cooling. In general, thermally induced strains are applied to the SMF as a result of the mismatch in the coefficients of thermal expansion (CTE) between the SMF (α_f) and the matrix material (α_m). Eq.(1) is modified as [10]:

$$-\Delta v|_v = K_r(\epsilon_{res} + (\alpha_m - \alpha_f)\Delta T) + K_T \Delta T \quad (4)$$

ϵ_{res} accounts for the solidification-induced residual strains during MEX and ΔT is the temperature difference between the initial reference and the final measurement. In this research, the temperature of the reference and measurement test is the same T_{room} i.e. $\Delta T = 0$ and Eq. (4) reduces to:

$$-\Delta v|_v = K_r \epsilon_{res} \quad (5)$$

Eq.(5) can be further converted to:

$$\epsilon_{res} = -\frac{\bar{\lambda}}{CK_r} \Delta v \quad (6)$$

where $\bar{\lambda}$ is the center wavelength of the scan and C is the speed of light inside the fiber. The scan center wavelength is 1550 nm. The constant K_r of 0.780 can be substituted to yield the following conversion factor:

$$\epsilon_{res} = -6.67(\mu\text{E}/\text{GHz}) * \Delta v. \quad (7)$$

By using this conversion factor, the solidification induced residual strain ϵ_{res} in MEX along the axis of embedded SMF can be calculated from RBS (Δv).

2.5. Temperature profile measurement and the DSC

The temperature evolution during the MEX was measured using a FLIR A655sc IR camera at 50 frames per second at full frame 640×480 resolution. The approximate distance from the lens to the target was

500 mm.

In order to fully understand the mechanisms of residual strain creation and ensure the strain transfer effectiveness of the SMF/PLA interface, the thermal transition and corresponding molecular behavior of PLA and SMF coating material during the MEX process were investigated by DSC. More details will be discussed in subsection 3.1 and 3.3. DSC samples were prepared from chopped feedstock PLA filament before printing and G14 specimen separately. Chopped SMF was used as the optical fiber coating DSC sample. Measurements were performed on a DSC-250 instrument (TA instruments, New Castle, DE) from 0 °C up to 300 °C, at a heating rate of 10 °C/min, and kept at isothermal state for 10 min, then cooled down to 0 °C at a cooling rate of 10 °C/min. Nitrogen atmosphere was employed during the experiment, using a 50 ml/min flow rate.

2.6. Micro-characterization

All sample cross-sections were prepared from a G14 specimen by polishing in Meta 250 autopolisher (Buehler Inc, USA) using low speed and water cooling. A RH-2000 digital microscope (Hirox, Ltd, France) and a FEG Quanta 650 Environmental scanning electron microscope ESEM (Thermo Fisher Scientific Inc., USA) were used to observe possible manufacturing flaws induced by SMF embedding.

3. Results and discussion

The in-situ OBR has never before been adopted for MEX fabricated thermoplastic components according to the best of this author's knowledge. Prior to measuring residual strains, preliminary tests were conducted to validate the in-situ OBR measurement approach. Subsequently the MEX fabricated specimens will be measured in both horizontal and vertical directions. The effects of specimen dimensions on the measurement results are discussed. Combined with the results of DSC and infrared camera testing, the key mechanisms of residual strain creation in MEX are investigated and a simplified description for the residual strain creation is presented. Finally, the possibility of detecting manufacturing defects by this innovative method will be presented.

3.1. Validation of in-situ OBR technology applied in MEX

3.1.1. Practical challenges and countermeasures

The practical challenges related to the use of in-situ OBR technology in MEX are mainly twofold: the first one is that the SMF embedding procedure is expected to be non-invasive with little disturbance to the MEX process. Another concern is related to the strain transfer effectiveness between the sensor and the surrounding material.

The SMF is expected to be straight during embedding. Nevertheless, the moving nozzle may displace the SMF during deposition, leading to damage or bending of the optical fiber. A broken optical fiber can not transfer a sensing signal, and bending of the optical fiber can induce noise into the data. These hidden dangers were mitigated by selecting an appropriate layer thickness of 0.2 mm, slightly larger than the diameter of the SMF. Fig.3 shows the micrographs taken from three cross-section planes of the embedded SMF. As shown in cross-section 1 in Fig.3 (b), the SMF is entirely encapsulated by the PLA material through the surfaces in both the substrate and embedding layers without pinching. In cross-sections 2 and 3 in Fig.3 (c) and (d), the embedded SMF appears straight without bending or visible damage. In SEM

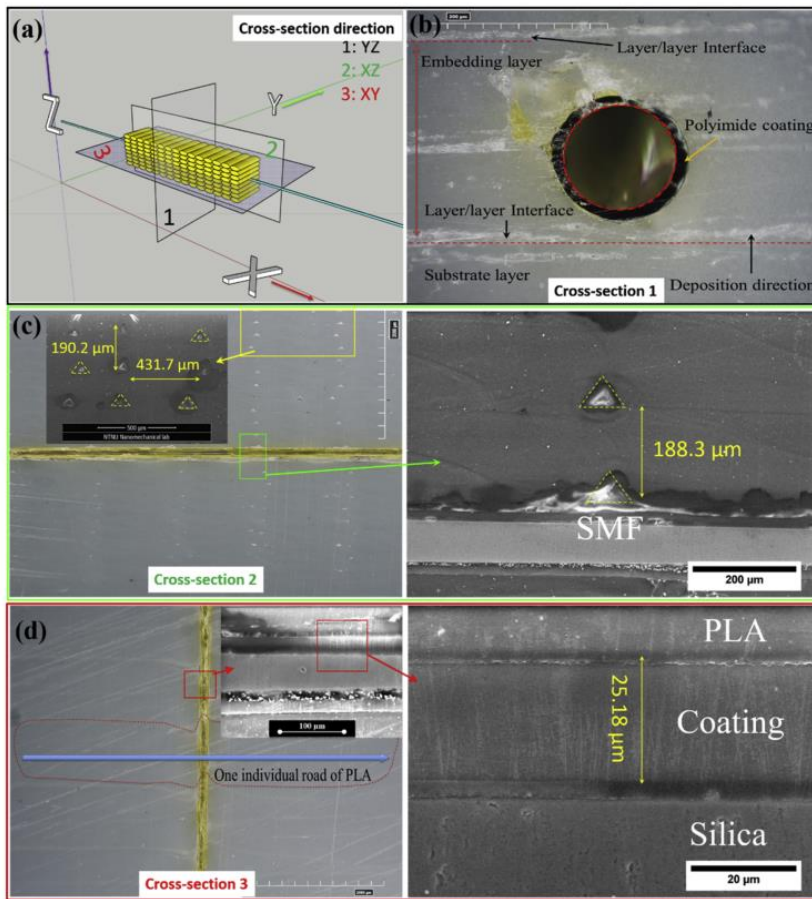


Fig. 3. Micrograph analysis of embedded SMF:(a) Illustration of sampling position in specimen, (b) Optical micrograph of cross-section 1, (c) Optical and electron micrograph in cross-section 2, (d) Optical and electron micrograph in cross-section 3.

images of Fig.3 (c), there are no voids surrounding the optical fiber. The special patterns of near triangular voids are proved to be intrinsic to the MEX, as the vertical and horizontal distances between two adjacent voids are corresponding to the layer thickness and nozzle diameter separately [23]. The SMF/PLA interface and Coating/Silica interface of SMF are well bonded in SEM images of Fig.3 (d). There are no delaminations or cracks generated by the SMF embedment. In conclusion, the embedment process brings no disturbance on the MEX process and no visible damage on the SMF itself.

When the SMF is used as a strain sensor, the strain of the surrounding material needs to be transferred into the optical fiber by the PLA/ SMF interface. As mentioned by Grave [18], when the coating material of the SMF becomes soft, the strain of its surroundings can not be transferred into the fiber by shear accurately. Thus, the interface compliance will affect the accuracy of the measurement. In the present work, the PLA/SMF interface is mainly composed of the polyimide coating on the SMF. In order to assure the strain transfer effectiveness, the polyimide coating needs to remain in the glassy state during the

MEX process. Thus, thermal transitions of polyimide are important physical characteristics for the application of the OBR technology. Specifically, the frozen molecular motions of thermoplastics are activated during glass transition, hence the brittle and glassy polymer becomes soft and flexible. In this case, the polyimide coated SMF is no longer suitable for strain measurements. Fig. 4 shows the DSC heating-cooling thermograms for the polyimide coating of the SMF. No endothermic or exothermic peaks emerged in the DSC curve up to 300 °C. The polyimide coating remains in the glassy state during printing, with sufficient stiffness to transfer residual strains from the MEX process to the silica of the optical fiber.

3.1.2. OBR based strain sensing compared to electrical strain gauges

As a distributed strain sensing system, the entire embedded SMF is required to be evenly bonded with the surrounding matrix to enable continuous strain field measurements. Thus, an initial proof of concept tensile test was carried out to investigate the SMF/PLA interfacial bonding. The strain values were measured by the OBR and electrical

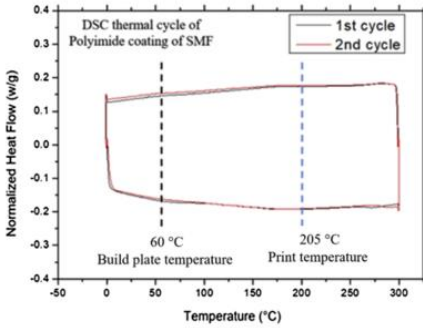


Fig. 4. DSC curve of the SMF polyimide coating.

strain gauges (SG) simultaneously to compare the strains from this OBR method with a traditional method. The SMF was embedded in a 3D printed dog-bone specimen (220 mm × 25 mm × 2 mm), while two SGs were bonded on the surface by cyanoacrylate. A hole ($\varnothing = 2$ mm) was built in the middle of the tensile specimen to investigate the measurement capability of the OBR technology near sharp strain gradients. The MEX-fabricated specimens were infilled in a line pattern perpendicular to the long axis of the specimen. The SMF was applied in the mid-plane of the specimen with a distance 1 mm from the hole and the SGs were bonded 0 mm and 25 mm from the hole, as shown in Fig. 5 (a). The tensile test was conducted in an Instron 5 kN test machine and the strain measurements were taken by in-situ OBR technology and SGs (FLAB-6-17, 6 mm × 2.2 mm, 120 Ω , Tokyo Measuring Instruments Laboratory Co., Ltd.) at the same time instance.

Fig. 5 shows the strain measurements from the OBR and two electric strain gauges. A continuous strain field along the specimen length was successfully obtained through the OBR method. A gradual strain increase over the gauge length of the specimen was exhibited in the strain field. The highest values were obtained at the equator of the hole, which coincides with the expected strain concentration location. A general agreement can be seen between the results of SGs and the in-situ OBR technology, but there are small deviations. The SG1 and SG2 showed tensile strains of similar magnitude, but always less than the OBR results. The difference between OBR and SG values at higher stresses (225 N ~ 380 N) is 14 %, while it is smaller at lower stresses (0 N ~ 225 N). This phenomenon arises from the intrinsic characteristic of applying SGs. The SMF is more accurate, as it measures strains over a

very narrow width (155 μm). The SG measures an average over its width (2200 μm), where the lower strains dominate. The averaging effect over a spatially changing strain field is most likely the main cause for the strain discrepancy. Secondly, the mislocation between the SMF and SG is inevitable. The whole SG area is more offset from the hole edge (stress concentration region) compared to the SMF, naturally leading to lower peak strains than SMF. Additionally, the strain may not always be transmitted to the SG completely due to the possible partial debonding between SG and specimen surface during tension. In conclusion, the embedded SMF seems evenly and well connected with PLA and no PLA/SMF interfacial debonding happens before 10,000 $\mu\epsilon$. The embedded SMF can be viewed as a reliable distributed strain sensor in the MEX fabricated specimen. Especially, when a steep variation exists in the strain field, applying the in-situ OBR method can measure strains more accurately than by using single-point SGs.

3.2. Experimental measurement results

3.2.1. Residual strain distribution

The data from the SMF were measured by OBR interrogator and analyzed by the OBR Desktop v3.13.0 software. In post-processing, the software defines many virtual strain gauges along the length of the SMF. All virtual strain gauges have the same gauge length (GL) and sensor spacing (SS) between them as shown in Fig.6 (a). After comparing the reference and measurement spectrum, strain of each virtual sensor is calculated from an average RBS on the corresponding GL part. One SMF is embedded in the midplane of a specimen (56 mm × 15 mm × 20 mm) in the X direction during the MEX process. When GL and SS parameters are both set to 8 mm, the embedded SMF can be viewed as an array of 7 virtual strain gauge sensors placed back-to-back along the axis of SMF. Each measurement point corresponds to one virtual strain sensor, which shows the average strain of the GL = 8 mm long section of the SMF. As shown in Fig.6 (b), the MEX induced residual strain value on each virtual strain sensor is negative, which indicates shrinkage strain. In the horizontal direction, experimental measurement results show similar negative values inside the specimen, except for the two points from the egress parts of the embedded SMF. The strain differences in the egress parts may be induced by the signal outliers in the measurement, which will be briefly discussed in subsection 3.2.2. Contrary to traditional casting and injection moulding where the residual strains increase from the exterior to the interior and lead to a symmetric tapered distribution [15,21], the MEX shows a horizontally uniform distribution of residual strains as shown in Fig.6 (c).

In order to characterize the residual strain distribution in both

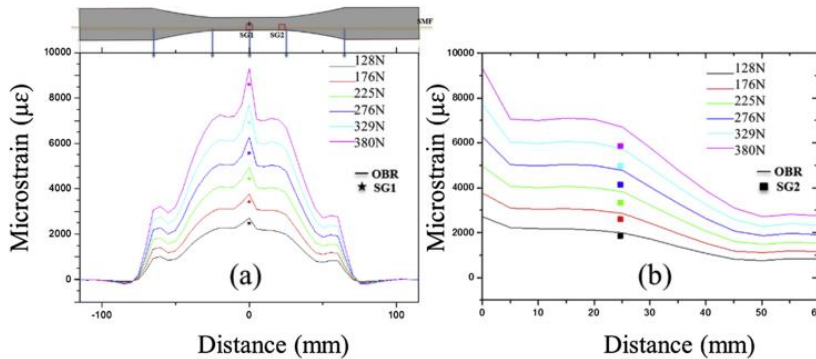


Fig. 5. Strain measurements from the OBR and electric strain gauges during a tensile test.

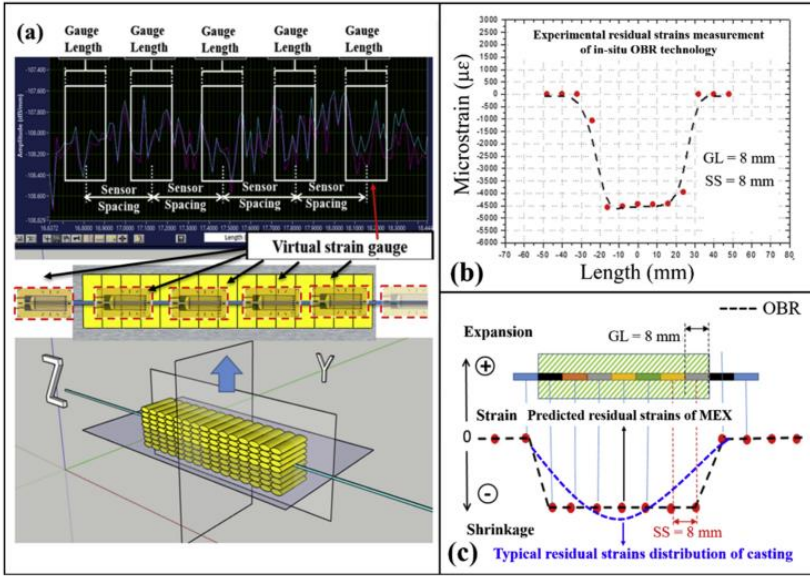


Fig. 6. Schematic illustration of post-processing parameters (a), experimental measurement of residual strains in MEX (b) and comparison between the residual strain distribution in casting and MEX (c).

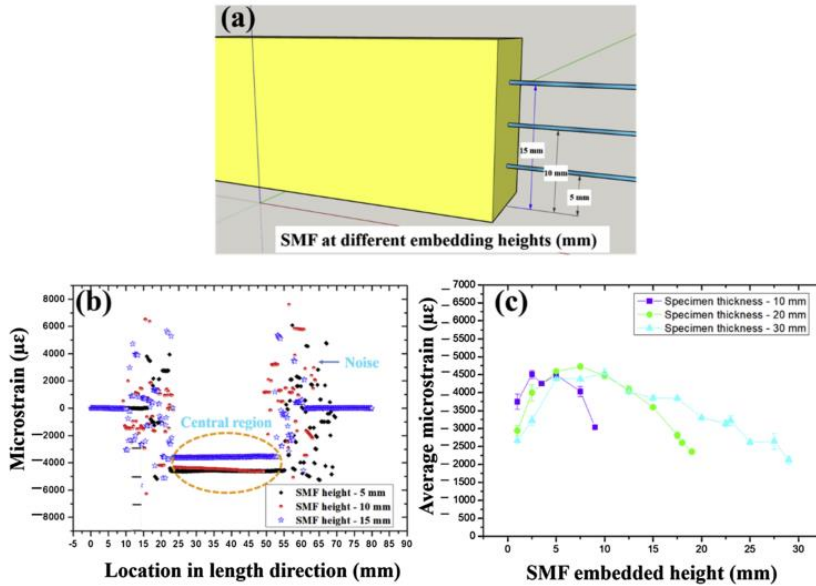


Fig. 7. Residual strain distribution in specimens: (a) Illustration of multiple SMF embedding, (b) Measurement of residual strain distribution in length direction at different heights in 20 mm thick G14 specimen, (c) Calculated average residual strain distributions in thickness direction of specimens with thickness of 10 mm, 20 mm and 30 mm.

length (horizontal) and thickness (vertical) directions, the SMFs were embedded in the midplane at different heights (in Z direction) along the length (in X direction) of the specimen (56 mm × 15 mm × 20 mm) as shown in Fig.7 (a). The adopted OBR parameters here are 4 mm GL and 0.15 mm SS, enabling high resolution measurements. A short overview about the effects of post-processing parameters on the measured strains is given in Appendix A. As shown in Fig.7 (b), no regular and continuous data can be observed in the ingress and egress parts of embedded SMF, however the data measured in the central region of embedded SMF are constant. The scattered outliers are viewed as noise while the constant values in the central region are believed to be representative of the residual strain in the MEX fabricated specimen. More details related to measurement noise will be discussed in chapter 3.2.2 and 3.4. In the length direction of G14 specimen, the residual strains in the bottom, middle and top layers all show a uniform distribution simultaneously. In this research, the mean value of the central region from the embedded SMF is used as the average residual strain of the layer where the SMF is in. As shown in Fig. 7 (c), the variation of average residual strain values shows a well-defined height dependency. The average residual strain increases from the bottom to about one third of specimen thickness and then starts to decrease until the top of the specimen. Such 'parabolic trend' of average residual strains in thickness direction of MEX fabricated PLA has never been reported before. Two additional specimens with a lower thickness (56 mm × 15 mm × 10 mm) and a higher thickness (56 mm × 15 mm × 30 mm) were measured to verify the repeatability of the parabolic trend in average residual strains. As shown in Fig.7 (c), the specimens with different thicknesses all show similar parabolic distribution of average residual strains in the thickness direction. The most extreme residual strains develop inside the specimen, at ca. 1/3 height from the build plate.

3.2.2. Effect of specimen dimensions

The in-situ OBR technique may be applied to MEX-fabricated specimens of different dimensions. It is therefore of interest to investigate how the geometrical size of specimens affects the OBR measurement. One SMF was embedded within the midplane of the specimen built as shown in Table 2. As shown in Fig.8 (a), the obtained data is scattered along the embedded SMF randomly, and no constant and continuous data can be observed in the short G11 specimen. For G12, the embedding length of the SMF increased to 25 mm and the outliers are still apparent in the ingress and egress parts of embedded SMF, however the data became stable in the central region. In this region, the strains measured by OBR are constant and representative of the residual strain in the MEX fabricated specimen. In measurement of G14, the length of stable strain section was again longer than that of G12, meanwhile the scattered outliers remain in the ingress and egress parts of the SMF. Again, with increasing the specimen length, a similar trend was observed in G15. In conclusion, when the specimen length is too small, the measurement data are mostly noise, making it challenging to pick out true values from the outliers. After increasing the specimen length, noise still exists in the ingress and egress parts of the embedded SMF, but the data in the central region becomes constant and representative. The residual strain values of the central section of embedded SMF do not change with further increasing the specimen length.

A specific filter program can be developed to remove the outliers. The outliers always exist and have highly inconsistent values. The SMF here experiences a large strain gradient (from 0 $\mu\epsilon$ to ca. -5000 $\mu\epsilon$) from the free part (outside the specimen) to the embedded part (inside the specimen) in the edges of specimens. The appearance of outliers or noises in strain gradient region of optical fibers during the OBR test have also been reported by previous researchers [15]. Considering practical applications, ignoring the data of the erratic end sections is suggested as a simple alternative to developing a specific filter program. In this way, the average strain of the central stable section is used as the representative residual strain in MEX. For each specimen size, 4

specimens were tested to verify the repeatability of test data. As seen from Fig.9 (a) and (b), the residual strains of specimens with different widths and lengths are all approximately -4450 $\mu\epsilon$. The specimen length and width have little effect on the residual strains, besides the erratic end regions. The data from ingress and egress parts of the embedded SMF includes a number of outliers. A certain length of embedded SMF is required to distinguish true values from the outliers at the ends. Experience shows that when the specimen length exceeds 25 mm and the width exceeds 5 mm, the in-situ OBR technology can measure residual strains of specimens generated during the MEX process without much difficulty.

3.3. A simplified description for residual strain creation

Based on the specimen temperature history during MEX and corresponding molecular behavior, a simplified description is presented that captures the key mechanisms of residual strain creation.

3.3.1. Temperature profile and corresponding thermal transitions

The temperature evolution of PLA material during MEX and SMF embedding process was investigated using real-time thermography taken by a FLIR IR camera. In the thermograph of Fig. 10 (a), four white lines, i.e. regions of interest (ROI), were placed from the nozzle tip to the current depositing layer and the adjacent previous deposited layers, respectively. The temperature versus distance of ROI 1 shows the temperature evolution of PLA from leaving the nozzle horizontally, along the length of current layer deposition. The temperatures in ROI 2, 3 and 4 show the temperature evolution of the PLA in the thickness direction, toward the previously deposited layers during MEX. Fig. 10 (c) and (e) shows the DSC heating-cooling thermograms of PLA. No obvious differences can be seen between the DSC curves of original filament and extruded i.e. once solidified PLA. The peaks in DSC curves are related to the glass transition, first cold crystallization, interaction between recrystallization and melting of PLA, respectively. As shown in Fig. 10 (b), the temperature in ROI 1 shows a rapid decline from 160 °C to 56 °C, then decreases slowly to a constant temperature of ca. 30 °C (substrate temperature), with the increasing distance to the nozzle. The original far field PLA filament first melts in the heating chamber, changes from the solid state into the viscous flow and then is extruded off the nozzle. Molten PLA is required to ensure layer to layer adhesion and sufficient wetting of the strain sensor during embedding. The temperature finally drops to constant substrate temperature (below glass transition) during the solidification of PLA, before the hot nozzle approaches this area again during the next MEX process cycle. This thermal cycling experienced by the PLA filament during the MEX process is called melting and rapid cooling cycling [22]. When a new layer is built on this layer, the temperature distributions on ROIs 2, 3 and 4 in Fig.10 (d) showed a very similar trend. The results show that the already solidified plastic, i.e. extruded PLA, will be partially melted again and cooled down to a constant temperature with the increase of distance to the nozzle. Only the adjoining material of substrate layers less than 0.4 mm to the nozzle, two times of layer thickness, experience partial remelting and cooling cycles. In conclusion, the PLA material first experiences a melting and rapid cooling cycling after being squeezed out from the nozzle, and then encounters repeated remelting and cooling cycles in the heat affect zone within ca. 0.4 mm thickness (ca. two deposited layers deep) during the following process.

3.3.2. Description for the residual strain creation

Based on the discussion above, a simplified description for the residual strain creation reflected by embedded SMF is shown in Fig. 11. In the MEX process, the embedded SMF and surrounding PLA material experience two kinds of thermal cycles:

- i melting and rapid cooling during the printing of the current layer.
- ii remelting and cooling during the printing of subsequent layers.

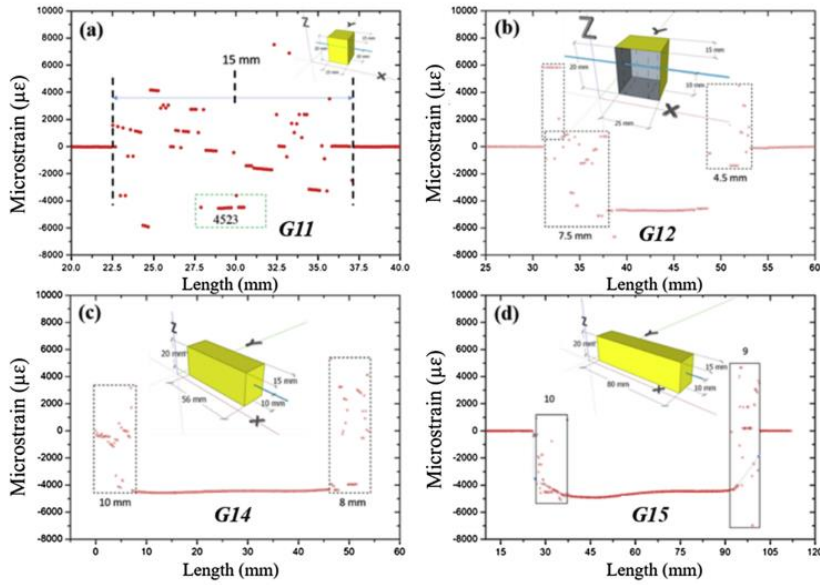


Fig. 8. In-situ OBR measurements of residual strains in MEX specimens with different lengths: (a) 15 mm, (b) 25 mm, (c) 56 mm, (d) 80 mm.

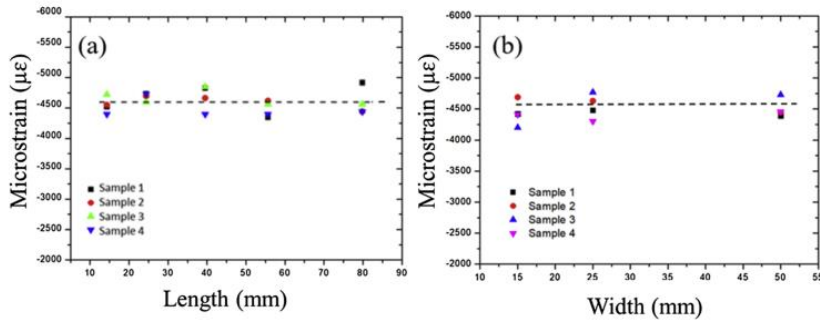


Fig. 9. Average residual strains of MEX fabricated specimens with different lengths (a) and widths (b), data from the central region.

In step 1, before embedding SMF, the PLA is first melted in the heating chamber and extruded out from the nozzle to form the substrate layer. The state of the PLA changes from a semi-molten state to solid during the first melting and rapid cooling. The SMF is placed on the solidified substrate layer before the deposition of a new layer on it. At this moment, the SMF is free from any external strain loading. During step 2, a new layer is built on the solidified substrate PLA layer, where the SMF is laid on. The substrate material in the heat affected zone will remelt. A neck is formed on the interface between the substrate and the new layer, wetting the SMF at the same time. On a molecular level, molecules diffuse, forming an interfacial zone that encapsulates the SMF, and/or forms chemical bonding across the PLA/PLA interface [22]. The bonding between the PLA and polyimide coating is of secondary/physical (i.e. non-covalent) type. The new layer, the substrate layers below, and the SMF in the middle are welded together during the cooling of the interface layer. Residual strain is generated due to the

phase transformation of deposited layers. In step 3 and subsequent steps, the next new layers will be built on the layer encapsulating the SMF. The sensing region will be shortly influenced by the remelting and cooling cycles until it is outside of the heat affected zone. Before removing from the hotbed, the specimen is continuously heated by the hot bed/nozzle and cooled by ambient cold air, resulting in non-uniform thermal gradients inside the 3-D printed structure. Finally, the whole specimen integrated with SMF is detached from the hotbed and cools down to room temperature. The contraction of embedded SMF is only induced by the filament material volumetric shrinkage due to its cooling during MEX. The fabrication induced residual strain is a compressive strain mainly determined by phase transformation and thermal cycles during the MEX process. In a 100 % infilled specimen, each section of SMF is encapsulated by the same amount of PLA roads with the same mesostructure (i.e. contacting surface area and air gap) within the same layer. Because of the characteristic manufacturing of MEX, the

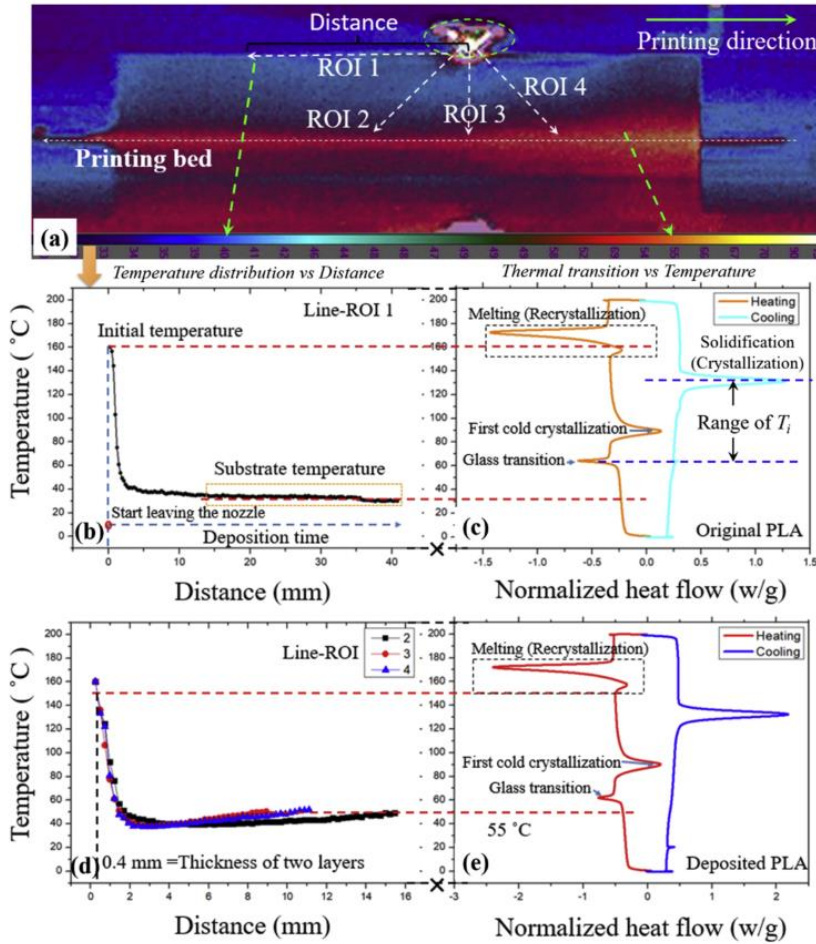


Fig. 10. Thermograph of the specimen during the MEX process (a), temperature distributions and corresponding DSC thermal transitions of original PLA (b)-(c) and deposited PLA (d)-(e).

PLA roads in the same layer experience almost the same phase transformation and thermal cycles individually, resulting in a horizontally uniform distribution of residual strains.

3.3.3. Numerical validation

The OBR measurement results should ideally be validated by comparing the results with the state of the art, but no similar experiments have been reported. Thus, a numerical validation by Monte Carlo sampling of the experimental test results in this research was adopted. As discussed above, the residual strains measured by SMF are mainly induced by the PLA volumetric shrinkage during the MEX process. A theoretically reasonable value range of the residual strain can be approximated by the coefficient of thermal expansion (CTE) of the material. The PLA surrounding the SMF is assumed as an isotropic material, then the volumetric CTE is three times the linear CTE in one

direction since the SMF is believed to be inert to the radial strain. Thus, the residual strain measured ϵ_{OBR} by SMF can be estimated by the following formula:

$$\epsilon_{OBR} = \frac{\Delta V}{3V} = \frac{\Delta L}{L} = \int_{T_i}^{T_f} \alpha_L(T) dT \quad (8)$$

Where α_L is the linear CTE, T_i and T_f are the initial and final temperatures respectively.

The T_f , i.e. room temperature, is already known as 20 °C, while the initial temperature T_i depends on when the effective connection between the SMF and PLA is established. The accurate value of T_i is highly process specific and unknown. According to Fig. 10 (b)-(c), the T_i should exist between solidification and glass transition temperatures, i.e. 130 °C to 60 °C. The α_L value can be estimated between 30×10^{-6} to 85×10^{-6} m/m/K from 3D printing material suppliers in the market. Fig.12 (a) shows 100,000 possible residual strain values calculated

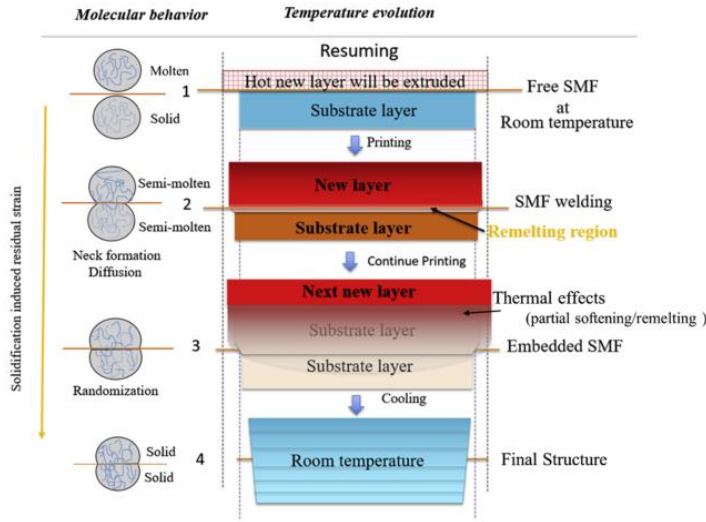


Fig. 11. Simplified description of residual strains creation in MEX and its measurement by in-situ OBR technology.

using Eq. (8) by Monte Carlo sampling. The values of T_i and α_L were selected uniformly from their regions as shown in Fig.12 (b) and (c). The OBR measurement residual strain values (from Fig. 9) were included in the region of numerically calculated values. Fig. 12 (d) shows the distribution statistics of the numerically calculated residual strains, while the OBR measurement values are close to the bar of maximum

number of results.

3.4. Manufacturing defect detection

One of the advantages of in-situ OBR measurements is the ability of detecting internal defects during the MEX process. By internal

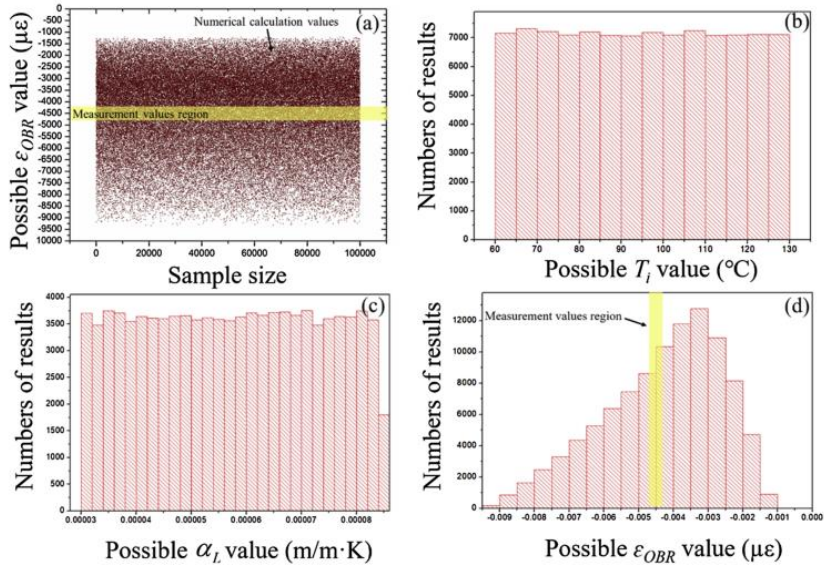


Fig. 12. Numerical predictions vs. OBR measurement results of residual strains: (a) Numerically calculated values, (b) Distribution statistics of T_i , (c) Distribution statistics of α_L , (d) Distribution statistics of the Monte Carlo sampling results.

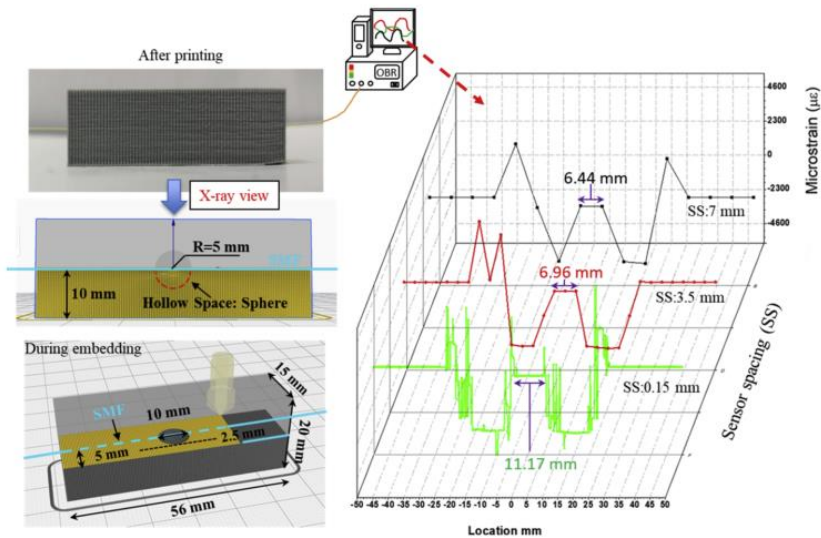


Fig. 13. A schematic illustration of a pre-designed defect inside the specimen and corresponding measurement results from the OBR.

manufacturing defects we hereby mean voids in 100 % infill specimens. The reference residual strain distribution in a MEX fabricated specimen (without defects) can be obtained from previous results. By comparing it with the measurement results of specimens with a void defect, the location and the size of the void can be identified non-destructively with in-situ OBR technology.

In this study, one specimen was pre-designed with a hollow sphere void ($\varnothing = 10$ mm) in the specimen center to mimic a manufacturing defect. A SMF fiber was embedded in the midplane of the printed block as shown in Fig. 13(left). After printing, the residual strains in the specimen were processed with $GL = 7$ mm and SS values at 7 mm, 3.5 mm and 0.15 mm, respectively. The result is shown in Fig.13 (right). Different to the usual residual strain distribution, a sudden reduction in strains appears in the center of the specimen. The strain curve drops close to zero and then keeps flat for 6 mm–10 mm before restoration. The length and position of the distorted section coincides with the pre-designed defect. With the decrease of SS , the location of the defect didn't change, but the length became more exact, showing higher spatial resolution. Notably, the measurement noise appears nearby the two sides of defect regions. This is consistent with previous test results regarding the ingress and egress parts of the embedded SMF. Thus the experiment here demonstrates the possibility of identifying manufacturing defects by this new OBR approach. Measuring fine scale abrupt local changes in strains with OBR can become difficult due to noise problems.

4. Conclusions

In this work, a novel approach for in-situ measurements of the solidification induced residual strain distribution in MEX fabricated specimens was demonstrated for the first time. Optical backscatter reflectometry (OBR) based fiber-optic sensing system was embedded to measure distributed residual strains. The practical challenges, validity and reliability of the developed approach were investigated. The experimental OBR measurement results are summarized as follows:

- 1 The microscopy observations and DSC testing showed that the SMF

is well encapsulated by the PLA and the presented embedding procedure is non-invasive in both micro- and macro-scale. The tensile test showed that the SMF/matrix interface is uniform and enables the SMF to work as a reliable distributed strain sensor at least up to 10,000 $\mu\epsilon$. The in-situ OBR strain data shows fair agreement with point measurement from electrical strain gauges.

- 2 The horizontal inplane size (length and width) of the sample brings minor effects on the measurement results. A noise region is always present in the egress and ingress part of the embedded SMF, whereas the signals from the center region are constant and representative. The OBR can be adopted as a reliable in-situ measurement method for residual strains, when the embedding length of SMF is longer than 25 mm.
- 3 The temperature evolution, measured by the IR camera, showed that the PLA material experiences several melting and rapid cooling cycles after leaving the nozzle. The residual strains in MEX are mainly created by the contraction of thermoplastics during phase transformation induced by thermal cycles. Because of the special manufacturing method of MEX, the residual strain value in each point of the same layer is almost the same, resulting in a horizontally uniform distribution of residual strains. In the vertical direction (height), the average residual strain values show a parabolic trend. Largest residual strain occurs inside the bulk of the specimen at ca. 1/3 height from the heat bed.
- 4 A hollow sphere located in the center of the 100 % infill specimen was pre-designed to mimic a manufacturing defect i.e. a large void. The in-situ OBR technology was able to detect this manufacturing defect successfully. The method shows a good potential for future applications in production property assessment from 3D printing.

Funding

This research did not receive any specific grant from funding agencies in the public, commercial, or not-for-profit sectors.

CRedit authorship contribution statement

Shaoquan Wang: Conceptualization, Data curation, Formal analysis, Investigation, Methodology, Software, Validation, Visualization, Writing - original draft, Writing - review & editing. **Kaspar Lasn:** Project administration, Resources, Supervision, Funding acquisition, Writing - original draft, Formal analysis. **Christer Westum Elverum:** Writing - original draft, Writing - review & editing, Supervision. **Di**

Wan: Writing - review & editing, Investigation. **Andreas Echtermeyer:** Writing - original draft, Writing - review & editing, Resources, Supervision.

Declaration of Competing Interest

None.

Appendix A. Post-processing parameters effects on strain measurements

In OBR, two parameters, i.e. gauge length (GL) and sensor spacing (SS) need to be defined for the post processing program. To analyze the influence of post-processing parameters, the same measurement data was processed with different GL and SS values. When SS was set to a constant 5 mm, the strain values with different GL from 4 mm to 50 mm show a similar pattern and an average value at about -4444 $\mu\epsilon$ as seen in Table A1. But the sensing length, which was the distance between the start point and end point of the bathtub, decreases slightly with increasing GL (see in Fig. A1 (a)). When the GL is set to 4 mm, the sensing length is closest to the real length of the specimen. The spatial resolution of the strain measurement is mainly influenced by SS. A constant GL of 4 mm interacting with five SS values were also tested: 4 mm, 2 mm, 1 mm, 0.5 mm, and 0.15 mm, thus representing 14, 28, 56, 112 and 374 measuring points, respectively. As shown in Fig. A1 (b), using a smaller SS, a strain map with higher spatial resolution is achieved, however more noise peaks also emerge in the results. The strain values from different SS sets are analyzed statistically and presented in Table A2. All mean strains were ca.1000 $\mu\epsilon$ smaller than the average strains in Table A1. It is notable that calculated standard deviations of each set were very large compared with the mean strain. The obvious distortion of the measured data is due to the relatively erratic measurements in the ingress and egress part of the embedded SMF, i.e. the ends of the bathtub. After removing the data from the ingress and egress part from the consideration, the mean strain became again very close to -4444 $\mu\epsilon$, while the standard deviations of the reintegrated data of different sets are very small as shown in second half of Table A2. Therefore, it is concluded that a very high spatial resolution at mm level can be accomplished by selecting appropriate GL and SS. The disadvantage of a high spatial resolution mode is the presence of the noise. Noisy data should be identified - here at the ingress/egress locations - and removed from further consideration. Based on the obtained results, the minimum SS, i.e. spatial resolution, and GL for the in-situ OBR system adopted in this research are 0.15 mm and 4 mm, respectively.

Table A1
Residual strain values from different GL (SS = 5 mm = Const.), at the bathtub bottom.

GL (mm)	4	16	30	50
Average strain ($\mu\epsilon$)	-4429	-4458	-4457	-4432
Standard deviations ($\mu\epsilon$)	93	59	56	8
Sensing length (mm)	60	55	44	34

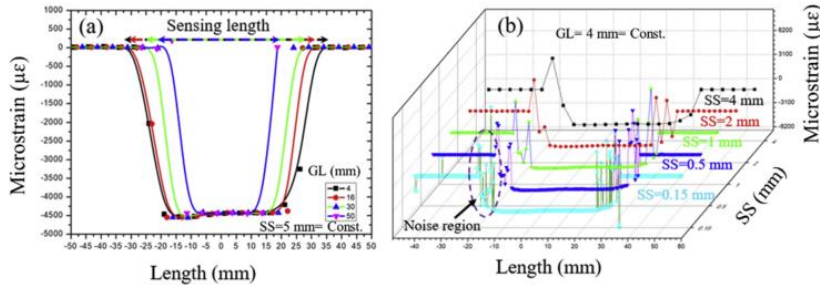


Fig. A1. Residual strain distribution in MEX fabricated specimens: (a) Influence of GL parameter on the results, (b) Influence of SS parameter on the results.

Table A2
Residual strain values from different SS (GL = 4 mm = Const.), at the bathtub bottom.

Statistical property	SS (mm)	4	2	1	0.5	0.15
Original	Average strain ($\mu\epsilon$)	-3561	-3487	-3601	-3546	-3623
	Standard deviations ($\mu\epsilon$)	2294	2233	2225	2286	2110
Disregarding noise regions	SS (mm)	4	2	1	0.5	0.15
	Average strain ($\mu\epsilon$)	-4473	-4477	-4479	-4481	-4483
	Standard deviations ($\mu\epsilon$)	53	56	56	54	55

References

- [1] H. Bikas, Panagiotis Stavropoulos, George Chrysolouris, Additive manufacturing methods and modelling approaches: a critical review, *Int. J. Adv. Manuf. Technol.* 83 (1-4) (2016) 389–405.
- [2] Pedram Parandoush, Dong Lin, A review on additive manufacturing of polymer-fiber composites, *Compos. Struct.* 182 (2017) 36–53.
- [3] Hongbin Li, Taiyong Wang, Qing Li, Zhiqiang Yu, Wang Na, A quantitative investigation of distortion of poly(lactic acid/PLA) part in MEX from the point of interface residual stress, *Int. J. Adv. Manuf. Technol.* 94 (1-4) (2018) 381–395.
- [4] C. Kousiatza, D. Karalekas, In-situ monitoring of strain and temperature distributions during fused deposition modeling process, *Mater. Des.* 97 (2016) 400–406, <https://doi.org/10.1016/j.matdes.2016.02.099>.
- [5] Q. Dao, J.C. Frimodig, Li X.-Z. Le HN, S.B. Putnam, K. Golda, et al., Calculation of shrinkage compensation factors for rapid prototyping (MEX 1650), *Comput. Appl. Eng. Educ.* 7 (1999) 186–195, [https://doi.org/10.1002/\(SICI\)1099-0542\(1999\)7:3<186::AID-CAE7>3.0.CO;2-Q](https://doi.org/10.1002/(SICI)1099-0542(1999)7:3<186::AID-CAE7>3.0.CO;2-Q).
- [6] Caterina Casavola, Alberto Cazzato, Vincenzo Moramarco, Giovanni Pappaletta, Residual stress measurement in Fused Deposition Modelling parts, *Polym. Test.* 58 (2017) 249–255.
- [7] Y. Zhang, K. Chou, A parametric study of part distortions in fused deposition modelling using three-dimensional finite element analysis, *Proc. Inst. Mech. Eng. Part B J. Eng. Manuf.* 222 (2008) 959–968, <https://doi.org/10.1243/09544054JEM990>.
- [8] O.S. Es-Said, J. Foyos, R. Noorani, Mel Mendelson, R. Marloth, B.A. Pregger, Effect of layer orientation on mechanical properties of rapid prototyped samples, *Mater. Manuf. Process.* 15 (1) (2000) 107–122.
- [9] Tian-Ming Wang, Jun-Tong Xi, Jin Ye, A model research for prototype warp deformation in the MEX process, *Int. J. Adv. Manuf. Technol.* 33 (11-12) (2007) 1087–1096.
- [10] A. Kantaros, D. Karalekas, Fiber Bragg grating based investigation of residual strains in ABS parts fabricated by fused deposition modeling process, *Mater. Des.* 50 (2013) 44–50, <https://doi.org/10.1016/j.matdes.2013.02.067>.
- [11] C. Kousiatza, D. Tzetzis, D. Karalekas, In-situ characterization of 3D printed continuous fiber reinforced composites: a methodological study using fiber Bragg grating sensors, *Compos. Sci. Technol.* 174 (2019) 134–141, <https://doi.org/10.1016/j.compscitech.2019.02.008>.
- [12] M. Froggatt, J. Moore, High-spatial-resolution distributed strain measurement in optical fiber with Rayleigh scatter, *Appl. Opt.* 37 (1998) 1735–1740, <https://doi.org/10.1364/AO.37.001735>.
- [13] C.K.Y. Leung, K.T. Wan, D. Inaudi, X. Bao, W. Habel, Z. Zhou, J. Ou, M. Ghandehari, H.C. Wu, M. Imai, Review: Optical fiber sensors for civil engineering applications, *Mater. Struct.* 48 (2013) 871–906, <https://doi.org/10.1617/s11527-013-0201-7>.
- [14] J.-M. Henault, G. Moreau, S. Blairon, J. Salin, J.-R. Courivaud, F. Taillade, E. Merliot, J.-P. Dubois, J. Bertrand, S. Buschaert, et al., Truly distributed optical fiber sensors for structural health monitoring: from the telecommunication optical fiber feedstocking tower to water leakage detection in dikes and concrete structure strain monitoring, *Adv. Civ. Eng. Mater.* 2010 (2010), <https://doi.org/10.1155/2010/930796>.
- [15] S.øren Heinze, Andreas Echtermeyer, In-situ strain measurements in large volumes of hardening epoxy using Optical Backscatter Reflectometry, *Appl. Sci.* 8 (7) (2018) 1141.
- [16] Astrid Billon, Jean-Marie Henault, Marc Quiertant, Frédéric Taillade, Aghiad Khadour, Renaud-Pierre Martin, Karim Benzarti, Quantitative strain measurement with distributed fiber optic systems: qualification of a sensing cable bonded to the surface of a concrete structure, In EWSHM-7th European Workshop on Structural Health Monitoring (2014).
- [17] V. Villalba, J.R. Casas, S. Villalba, Application of OBR fiber optic technology in structural health monitoring of Can Fatjó Viaduct (Cerdanyola de Vallès-Spain), Proceedings of the VI International Conference on Bridge Maintenance, Safety and Management, Lake Maggiore, Italy, 8–12 July, 2012.
- [18] Jon Grave, L. Harald, Magnus L. Håheim, Andreas T. Echtermeyer, Measuring changing strain fields in composites with distributed Fiber-Optic sensing using the optical backscatter reflectometer, *Compos. Part B Eng.* 74 (2015) 138–146.
- [19] Stephen T. Kreger, Dawn K. Gifford, Mark E. Froggatt, Brian J. Soller, Matthew S. Wolfe, High resolution distributed strain or temperature measurements in single- and multi-mode fiber using swept-wavelength interferometry, *Optical Fiber Sensors*, p. The42, Optical Society of America, 2006.
- [20] Erik Saeter, Kaspar Lasa, Fabien Nony, Andreas T. Echtermeyer, Embedded optical fibres for monitoring pressurization and impact of filament wound cylinders, *Compos. Struct.* 210 (2019) 608–617.
- [21] Taylan Örs, Fanny Gouraud, René Guinebretière, Marc Huger, Vincent Michel, Olivier Castelnaud, Neutron diffraction measurements of residual stress distribution in large zirconia based refractory bricks produced by electro-fusion and casting, *J. Eur. Ceram. Soc.* 37 (5) (2017) 2295–2302.
- [22] Lourens G. Blok, Marco L. Longana, H. Yu, Ben K.S. Woods, An investigation into 3D printing of fibre reinforced thermoplastic composites, *Addit. Manuf.* 22 (2018) 176–186.
- [23] Sigmund A. Tronvoll, Nils Petter Vedvik, Christer W. Elverum, Torgeir Welo, A new method for assessing anisotropy in fused deposition modeled parts using computed tomography data, *Int. J. Adv. Manuf. Technol.* 105 (1-4) (2019) 47–65.

Paper II



Accurate non-linear calculation model for decoupling thermal and mechanical loading effects in the OBR measurements

SHAOQUAN WANG^{*} AND KASPAR LASN

Department of Mechanical and Industrial Engineering (MTP), Norwegian University of Science and Technology (NTNU), Richard Birkelands vei 2B, 7491, Trondheim, Norway

^{*}shaoquan.wang@ntnu.no

Abstract: Fiber optic sensors are increasingly used in several fast-growing industries. Aerospace, energy storage, and the medical sector consider new implementations of optical fibers mainly for condition monitoring purposes. Applications using optical fibers entail measurements of distributed strains and temperatures. However, the spectral shifts of transmitted and reflected light are simultaneously sensitive to both of these influences. This coupled sensitivity can introduce large errors for signal interpretation. An accurate calculation model for signal decoupling is necessary to distinguish pure mechanical strains from pure thermal loading. Approaches where the spectral shift is assumed to vary linearly with temperature give large errors when the temperature variation is high. This investigation derives and validates a new temperature formula that is used for high precision strain and temperature discrimination. The non-linear temperature formula is deduced from physics-based models and is validated with Rayleigh backscattering based OBR measurements. Our calculation approach demonstrates improved accuracy over an extended temperature range. The relationship between strain and temperature effects in the coupled mechanical and thermal loading environment is further studied in detail.

© 2021 Optical Society of America under the terms of the OSA Open Access Publishing Agreement

1. Introduction

More than 60 different optical fiber sensor types have been developed as future sensors in previous decades [1,2]. Compared to conventional electrical sensors, optical fibers have several distinguishing advantages: (i) immunity to electromagnetic interference and environmental corrosion; (ii) small size and insignificant disturbance for the integrity of the structure; (iii) high temperature resistance; (iv) a lifetime exceeding 25 years [3–5]. In addition, optical fibers can multiplex a large number of sensors along a single fiber and set up a distributed optical fiber sensors (DOFS) network. By measuring the intrinsic backscattering variation in the fiber caused by external perturbations, the DOFS techniques based on multi fiber Bragg grating (FBG), Raman, Brillouin, and Rayleigh backscattering have been developed successfully. Nowadays, the DOFS are used for structural health monitoring in industrial infrastructure, in aerospace components, in architectural structures, and in human health applications.

Today, one of the most significant limitations for using the DOFS is their coupled sensitivity to both temperature and strain. For instance, temperature variations along the sensing fiber will introduce errors for the strain measurement. The ability to distinguish between strain and temperature effects is critical for the large-scale success of DOFS applications. Rayleigh backscattering spectrum has been adopted in DOFS to determine strain and temperature along the entire length of an optical fiber. Modeled as a weak FBG with a random period, changes in the refractive index or in the physical optical fiber length cause the Rayleigh backscattering spectral (RBS) shift in frequency. The RBS shift shows a cross-sensitivity to both strain and temperature similar to FBGs. In the field of DOFS techniques based on FBGs, different approaches have been proposed to discriminate strain and temperature [6–9]. These methods utilize well-designed

optical fiber sensor systems which have different temperature and strain sensitivities. Once the temperature and strain coefficients of the optical fiber are known, the temperature and strain variation can be determined by using the inverse of the coefficients' matrix. Most recent strain/temperature discrimination methods in Rayleigh backscattering based DOFS are analogous to the decoupling techniques of FBGs [10–14]. One solution utilizes the spectral shifts of the fast and slow modes of birefringence by autocorrelation and by cross-correlation of RBS shifts in the polarization maintaining fiber (PMF) [10,11]. The distributed autocorrelations of the Rayleigh spectral signature are strongly related to thermal effects on the fiber, while distributed cross-correlations of the Rayleigh spectral signature are related to both thermal and strain effects. Another method uses stimulated Brillouin scattering and Rayleigh backscattering in a single-mode fiber (SMF) to discriminate between the temperature and strain changes [12,13]. The Brillouin frequency shift and the distributed RBS shift were induced by strain and temperature variations. Although both methods are sensitive to temperature and strain, their sensitivities are different and independent from each other; therefore, a complete temperature and strain discrimination can be realized by measuring a pair of spectral shifts along the PMF sensor. Although the methods above conveniently utilize a single fiber for dual-measurements of strain and temperature, they are also complicated and costly. Measuring Brillouin scattering and Rayleigh backscattering in a PMF requires two systems of measurement techniques. PMF is also more expensive compared to single-mode optical fibers for large applications. A simple way to achieve discrimination utilizes a SMF and a reduced-cladding SMF [14], because the temperature and strain coefficients of the two optical fibers are different. However, two types of SMFs must be attached closely side by side, and two interferometers are needed for measurements when using this system.

All previous strain/temperature discrimination methods for DOFS based on Rayleigh backscattering (developing from the techniques of FBGs) assume that strain- and thermally-induced effects are both linear with respect to RBS shifts. The superposition of strain and temperature induced spectral changes has also been found to apply well for FBGs. Rayleigh scattering-based DOFS have been successfully used to perform temperature measurements under thermal conditions [15,16], and coupled with irradiation [17], or humidity [18]. In these investigations, RBS shifts are modeled using linear relations to temperature with good accuracy within temperature ranges from ca. 0 °C to ca. 75 °C. However, obvious measurement errors occur for linear fitting at high temperatures (> 80 °C) and at cryogenic low temperatures (< -73 °C). Additionally, the temperature induced RBS shifts are shown to be humidity and low dose radiation independent. The review of existing literature for Rayleigh scattering-based DOFS shows clearly that superposition/decoupling of strain and temperature induced spectral changes has not been addressed with sufficient rigor thus far, especially for thermal conditions beyond typical inside and outside temperatures.

In this paper, a simple and effective calculation model is realized for strain and temperature discrimination by using the OBR, a high resolution DOFS technology based on Rayleigh backscattering. Identical physically separated optical fibers are used to compensate for temperature effects. During the procedure, the measurement fiber experiences a coupled mechanical and thermal loading while the compensation fiber only the thermal loading. The temperature effect for the OBR is shown to be nonlinear due to the thermo-optic coefficient and its relationship with temperature. Improving state of the art, a polynomial temperature calculation formula is deduced from a physics-based model. High precision temperature measurements over an extended temperature range are carried out by using a customized test set-up where OBR measurements are taken inside the temperature chamber of a DMTA (dynamic mechanical thermal analysis) test instrument. The relationship between strain and temperature effects is studied in the coupled mechanical and thermal loading environment. A novel high-precision calculation model is applied to subtract temperature effects from the coupled measurement data.

2. Experimental setup

2.1. Interrogator devices and sensors

As shown in Fig. 1(a), a reflectometer OBR 4600 from Luna Instruments is used as the interrogator device for the DOFS measurements. The optical fiber SMB-E1550H from OFS Fitel with a silica/silica/polyimide structure and a core diameter 6.5 μm , a cladding diameter 125 μm , and a coating of 155 μm diameter is used for sensing strain and temperature. The independent temperature measuring system in the experiment consists of an electronic temperature sensor with accompanying data acquisition equipment. The temperature sensor is a special K-type wire thermocouple SRTC-TT-KI-40-1M and the data is read and stored by a DP9800-TC digital thermometer from OMEGA Engineering.

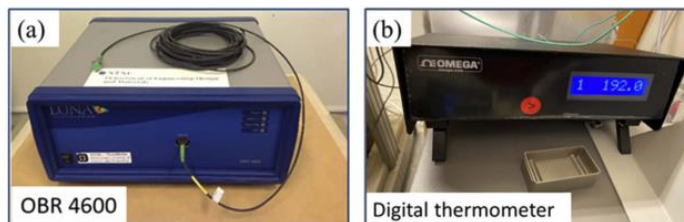


Fig. 1. (a) Interrogator apparatus LUNA OBR 4600, (b) Thermometer DP9800-TC.

2.2. Mechanical and thermal loading set-up

A customized experimental set-up is used to investigate the combined loading effect from strain and temperature on the OBR RBS shift measurements. The set-up assembly (Fig. 2) consists of a temperature chamber, a clamper, a perforated tube, and a dead weight system. The temperature chamber from a NETZSCH Eplexor DMTA machine is used to control the temperature around the optical fibers. The chamber has capacity from -150 $^{\circ}\text{C}$ to 500 $^{\circ}\text{C}$. However, a smaller range from -130 $^{\circ}\text{C}$ to 240 $^{\circ}\text{C}$ is used for this investigation. The clamper is attached to the ceiling of the chamber to fix the top of the optical fiber. The optical fiber then passes through a perforated tube which protects it from vibrations induced by the cooling fan. The mechanical loading on the fibers is created by a system of dead weights. One thermocouple is plugged into the perforated tube to provide accurate and independent temperature information about the optical fiber measurement region. By these small modifications to the DMTA temperature chamber, a controlled thermal and mechanical loading can be applied to individual fibers, or groups of optical fibers simultaneously.

2.3. Measurement procedure

Before each OBR measurement, the DMTA chamber temperature is maintained for two minutes to fully heat or cool down the optical fiber sensor and the measurement system around it. During the testing procedure the optical fibers are heated from room temperature to the highest temperature first and then cooled down to the lowest temperature of the range. The signals from the optical fibers and the K-type sensors are recorded simultaneously over ca. 5 seconds period at each temperature measurement. The average RBS shift over the measurement zone of the optical fiber is recorded, while the mean temperature of the K-type sensor is used as an independent temperature measurement. The K-type sensor data is used for the temperature values on the

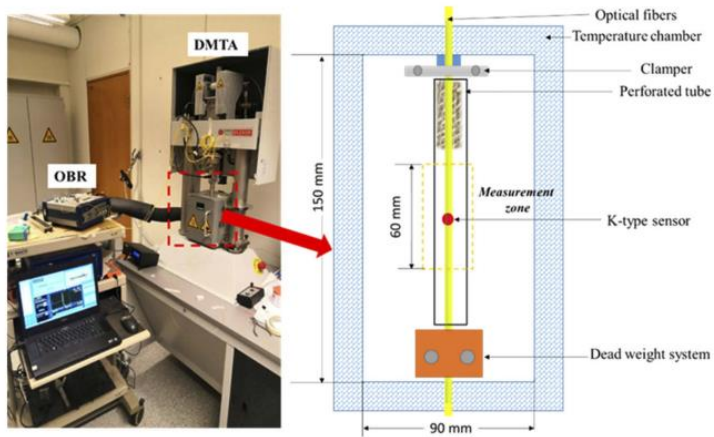


Fig. 2. Mechanical and thermal loading instrument with the OBR system.

x-axes of figures shown in the following Sections. The instrumentation parameters for OBR 4600 and DP9800-TC digital thermometer are shown in Table 1.

Table 1. Equipment parameters.

OBR 4600					
Incident light	Sensor diameter	Scan mode	Sensing range	Gauge length	Sensor spacing
$\lambda = 1550 \text{ nm}$	155 μm	Single scan-standard	60 mm	10 mm	4 mm
Digital thermometer					
Sensor type		Sensor diameter	Limits of error		
K-type (SRTC-TT-KI-40-1M)		190 μm	0.75% above 0 °C and 2.0% below 0 °C		

3. Results and discussion

3.1. Thermal loading effects

In this Section, a polynomial formula is first deduced from the underlying physics. Thereafter it is applied for precise temperature measurements with the OBR. The non-linear formula is compared to the usual linear formula under pure thermal loading conditions over four temperature ranges. It has to be pointed out that FBGs are outside of the experimental scope of current investigation. However, the analyses approach described below is also applicable to these optical fiber sensors.

3.1.1. Polynomial temperature formula

As described by Wang [19], the distributed Rayleigh backscattering along the length of the optical fiber can be modeled as a weak FBG with a random period. Thus the RBS shifts induced by the temperature change are identical to FBGs, expressed by [20]:

$$\frac{\Delta\nu(T)}{\bar{\nu}} = -\frac{\Delta\lambda(T)}{\bar{\lambda}} = -\left(\frac{1}{\Lambda}\Delta\Lambda(T) + \frac{1}{n}\Delta n(T)\right) \quad (1)$$

where $\bar{\nu}$ and $\bar{\lambda}$ are the mean optical frequency and the mean wavelength of the scan, $\Delta\nu(T)$ is the measured spectral shift of the light, n is the effective refractive index and Λ is the grating period. The temperature sensitivity of the spectrum arises from the thermal expansion, and the refractive index change of the glass fiber. The first term on the right-hand side corresponds to the coefficient of thermal expansion (CTE) of silica (α), and the second term corresponds to the thermo-optic coefficient of the fiber (β). Thus, Eq. (1) transforms into [21]:

$$\frac{\Delta\nu(T)}{\bar{\nu}} = -\left(\int \alpha(T)dT + \int \beta(T)dT\right) = -\int K_T(T)dT \quad (2)$$

where the temperature conversion factor is defined as $K_T(T) = \alpha + \beta$. Thus, the temperature induced RBS shift $\Delta\nu_T$ between the OBR reference scan (fiber temperature $T = T_r$) and the OBR measurement scan (fiber temperature $T = T_m$) in the Rayleigh scattering-based DOFS is calculated by Eq. (3), where c is the speed of light and $\bar{\lambda}$ is the center wavelength of the scan (1550 nm for the current device):

$$\Delta\nu_T = -\frac{c}{\bar{\lambda}} \cdot \int_{T_r}^{T_m} K_T(T)dT \quad (3)$$

In the single mode silica optical fiber, the value of α is approximately $0.55 \cdot 10^{-6}/^\circ\text{C}$, while the value of β is from 10^{-8} to $8.5 \cdot 10^{-6}/^\circ\text{C}$ [22]. Simplifying the values of α and β as constants, coefficient K_T becomes equal to $6.45 \cdot 10^{-6}/^\circ\text{C}$ for the germanosilicate core fiber used in this research. The relationship between the temperature change $\Delta T = T_m - T_r$ and the temperature change induced RBS shift $\Delta\nu_T$ for this OBR measurement set-up is sometimes described in even simpler form, using C_T as the constant equal to $-1.248 \text{ GHz}/^\circ\text{C}$, in:

$$\Delta\nu_T = C_T \cdot \Delta T \quad (4)$$

However, in the infrared wavelength region adopted by the OBR system, the β of silica glass has also been found to be strongly dependent of temperature [23–26]. The relationship between temperature and refractive index n exhibits a non-linear behavior at high temperatures [16]. The optical properties of materials (including refractive index n) are determined by coupling various types of oscillators to the electromagnetic radiation field. Corte et al. [24] uses a single oscillator model to obtain the refractive index n of silica by:

$$n^2 = 1 + \frac{E_p^2}{E_g^2 - E^2} \quad (5)$$

where E_p is electronic plasma energy, E the photon energy, and E_g is the optical band gap average energy. The E_p is inversely proportional to the volume, and the E_g is dependent on the temperature. In order to show the temperature dependence of the refractive index, a physically meaningful model from Gorachand Ghosh [25,26] is hereby applied. In this model, $E_{ig}^2 = E_g E_{eg}$, where E_{eg} is the excitonic band gap and E_{ig} is the isentropic band gap in the infrared region as shown in the energy level diagram (Fig. 3). As shown in Eq. (6), the model of Ghosh [25] includes the first right-hand term which is related to the CTE (α), and the second right-hand term related to optical band gap temperature coefficients E_{eg} and E_{ig} . The isentropic band gap E_{ig} is considered invariant with temperature, thus the temperature shift of excitonic band gap E_{eg}

controls the quantitative behavior of dn/dT [25]. A simple model for β is now expressed by Eq. (7).

$$\beta = \frac{dn}{dT} = \frac{n^2 - 1}{2n}(-3\alpha) - \frac{n^2 - 1}{2n} \left(\frac{1}{E_{eg}} \cdot \frac{dE_{eg}}{dT} \cdot \frac{E_{ig}^2}{E_{ig}^2 - E^2} \right) \quad (6)$$

$$\beta = A(T) + B(T) \quad (7)$$

where thermo-optic coefficient β is controlled by two factors $A(T)$ and $B(T)$. It is assumed that the first factor $A(T)$ represents the contribution from the CTE (α), and the second term, $B(T)$ represents the contribution of the excitonic band gap (E_{eg}). According to Ghosh [25], $A(T)$ has only a minor contribution to the temperature dependence of the refractive index compared to $B(T)$, and is viewed as constant a_0 in Eq. (8), while a quadratic function of temperature is used to express the contribution of $B(T)$ as shown in Eq. (9) [25].

$$\beta = a_0 + B(T) \quad (8)$$

$$B(T) = b_0 + b_1T + b_2T^2 \quad (9)$$

Thereby, K_T also becomes expressed as a quadratic function of temperature:

$$K_T(T) = \alpha + \beta = \alpha + a_0 + B(T) = H_0 + H_1T + H_2T^2 \quad (10)$$

Finally, inserting Eq. (10) into Eq. (3), the latter can be rewritten and rearranged as:

$$\Delta\nu_T = -\frac{c}{\lambda} \cdot \int_{T_r}^{T_m} K_T(T)dT = C_0(T_m - T_r) + C_1(T_m^2 - T_r^2) + C_2(T_m^3 - T_r^3) \quad (11)$$

where the temperature difference and the RBS shift between the reference test and the measurement test become related by the polynomial temperature formula. This formula is physics-based and enables high precision temperature measurements with the OBR. Based on analogy the formula is also applicable for the FBGs.

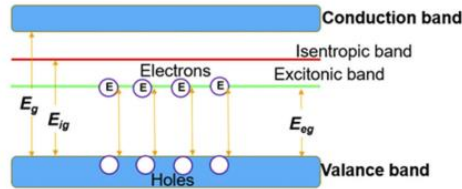


Fig. 3. Energy level diagram for silica glass.

3.1.2. Comparison between linear and polynomial formulas

A reference OBR test was implemented at $T_r = 30.6$ °C, and then a series of measurements were performed over a temperature range from -130 °C to 200 °C. Five independent optical fibers (A, B, C, D and E) were positioned simultaneously in the temperature chamber (see Fig. 2) without any mechanical loading. The measured RBS shift was fitted by the usual linear model and the new non-linear model separately to compare the difference between the two approaches. The measured data and the parameters of linear and non-linear curve fits are shown in Fig. 4 and in

Table 2, respectively. The linear model is described by $\Delta v_T = a + bT_m$, where Δv_T is the RBS shift induced by thermal loading, T_m is the temperature of the measurement scan, $b = -\frac{c}{\lambda}K_T$, and a has the value of Δv_T when $T_m = 0$ °C. The non-linear model is expressed by Eq. (11), where $T_r = 30.6$ °C (reference temperature). By using the linear curve fitting formula, the value of $b = -1.225$ GHz/°C was obtained, similar to $-\frac{c}{\lambda}K_T = -1.248$ GHz/°C predicted previously in Section 3.1.1. The results in [15–18,27] show that linear fitting is reasonable within a small temperature range, however the discrepancies of using a linear formula become evident with temperatures far away from the reference temperature. The measurement data and the fitting curves of four different ranges symmetric to room temperature (see Fig. 4) are shown in Fig. 5 for visual comparison. In the smallest Range 1 (from -5 °C to 45 °C), both the linear and polynomial fitting curves agree with the measurement data, almost overlapping each other. With the expansion of the temperature range, the linear and polynomial fitting curves start to diverge from each other as shown for Range 2 (from -25 °C to 65 °C) and for Range 3 (from -85 °C to 125 °C). In the widest Range 4 (from -125 °C to 165 °C) only the non-linear curve is still acceptable for representing the measurement data.

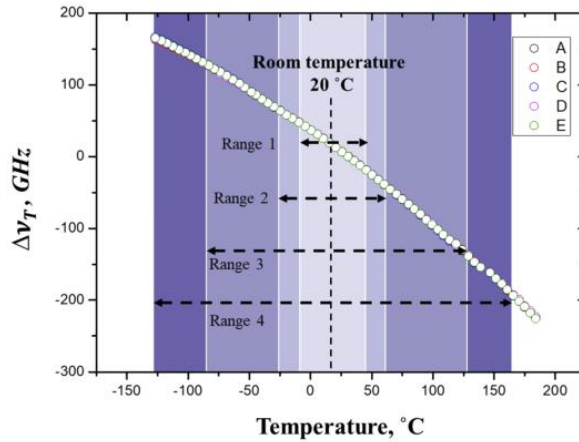


Fig. 4. Thermal loading induced RBS shifts measured by the OBR.

Table 2. Parameters obtained for linear and non-linear curve fitting models.

Linear fitting formula	$\Delta v_T = a + bT_m$
a (GHz)	37.76
b (GHz/°C)	-1.22
Polynomial fitting formula	$\Delta v_T = C_0(T_m - T_r) + C_1(T_m^2 - T_r^2) + C_2(T_m^3 - T_r^3)$
T_r (°C)	30.6
C_0 (GHz/°C)	1.18
C_1 (GHz/°C ²)	$1.35 \cdot 10^{-3}$
C_2 (GHz/°C ³)	$2.56 \cdot 10^{-7}$

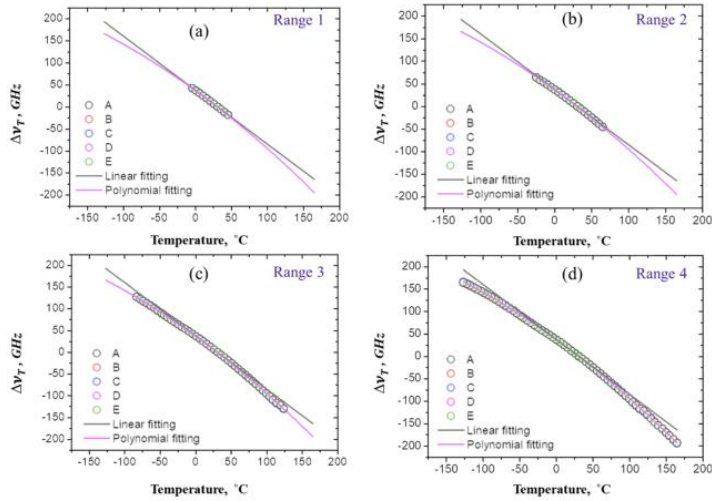


Fig. 5. The RBS shifts from the OBR and two alternative fitting curves when expanding the temperature range.

The adjusted R-squared metric is a modified version of the R-squared that is often used to evaluate the goodness-of-fit. High adjusted R-squared ≤ 1 indicates a good fit for the model. The adjusted R-squared is calculated for different temperature ranges and the results are shown in Fig. 6(a). The linear and non-linear fitting curves have very similar R^2 values for Range 1. When the temperature range becomes wider, as expected, the polynomial formula shows a greatly improved goodness-of-fit compared to the linear formula. Figure 6(b) displays the relative errors for the OBR temperature measurements (%error) when using the polynomial and the linear formulas:

$$\%error = \frac{|T_K - T_{OBR}|}{T_K} \cdot 100\% \quad (12)$$

where T_K is the temperature measured by the K-type thermocouple (Fig. 2) and T_{OBR} is the temperature measured by the OBR using the optical fiber. When the temperature remains within Range 1, there is little difference between the errors of polynomial and linear formulas (mostly < 5%). When the temperature exceeds Range 1, the polynomial formula shows a better temperature measurement precision over the whole measured temperature range. This experiment clearly demonstrates how the polynomial formula deduced from physics-based models improves the temperature measurement accuracy over an extended temperature range.

3.2. Mechanical loading effects

In the absence of temperature change, the mechanical strain relationship to the RBS shift can be written as [19]:

$$\varepsilon = -\frac{\bar{\lambda}}{c \cdot K_E} \Delta\nu_M \quad (13)$$

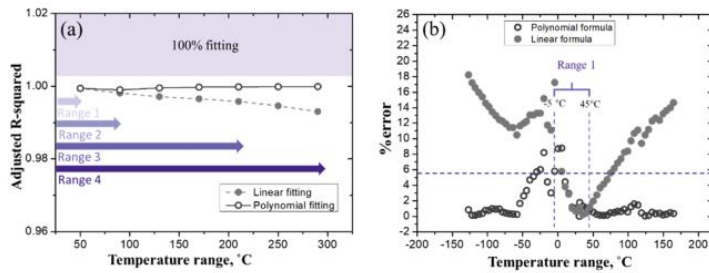


Fig. 6. The goodness of linear and polynomial fitting formulas with increasing temperature range: (a) Adjusted R-squared metric, (b) Relative error in the temperature measurement.

where K_ε is the strain coefficient and c is the speed of light. Previous research in our group has shown that K_ε is a constant with a value of 0.787 [28]. Thus, Eq. (13) yields the conversion factor: $\varepsilon = (-6.67 \mu\text{e} / \text{GHz}) \Delta v_M$ for this OBR system.

3.3. Decoupling of mechanical and thermal loading effects

In this Section, the optical fibers are exposed to loading environments where a constant mechanical loading is coupled with varying thermal loads, and a constant thermal loading is coupled with varying mechanical loads. The relationship between strain and temperature effects for the RBS shift is experimentally investigated. Both, the linear and the non-linear (polynomial) formulas are applied for decoupling the mechanical and thermal loading effects. The relative errors of the two methods are compared.

3.3.1. Coupled mechanical and thermal loading

The optical fiber (OF1) was measured before and after it was loaded by a dead weight (60.23 g) at room temperature. This measurement gives the pure mechanical loading induced RBS shift (Δv_{PM}). The mean value of Δv_{PM} over the measurement zone (Fig. 2) was calculated -95 GHz, shown by a green dashed line in Fig. 7(a). Subsequently, four additional independent optical fibers (OF2, OF3, OF4 and OF5) were placed into the temperature chamber. The measurement temperature of the chamber was varied from -125 °C to 240 °C. The RBS shift of OF1 ($\Delta v_{T\&M}$) was induced by coupled mechanical and thermal loading, while the other four fibers sensed only the same thermal loading without any mechanical loading. The Δv_T is the average RBS shift of four optical fibers over their measurement zones. The $\Delta v_{T\&M}$ from OF1 shows the same nonlinear trend as Δv_T but at values uniformly shifted below from Δv_T . The mechanical loading induced RBS shift Δv_M (blue dotted line) is achieved by subtracting Δv_T from $\Delta v_{T\&M}$. As evident from Fig. 7(a), the Δv_M shows almost no variation with temperature and is in excellent agreement with Δv_{PM} .

Finally, another optical fiber (OF6) was subjected to a changing mechanical load by using different dead weights at 20.6 °C and at 30.1 °C separately. Figure 7(b) shows the $\Delta v_{T\&M}$ of OF6 at these two different temperatures while increasing the dead weight. The temperature difference induced Δv_T is calculated by subtracting $\Delta v_{T\&M}$ at 20.6 °C from $\Delta v_{T\&M}$ at 30.1 °C at the same weight. Figure 7(b) shows that, at constant temperature, the mechanical loading affects the RBS shifts in the OBR linearly with applied dead weight (i.e., mechanical strain). The constant small difference between $\Delta v_{T\&M}$ (empty and solid circles) comes from the small temperature difference. The Δv_T remains mechanical loading independent. These results show

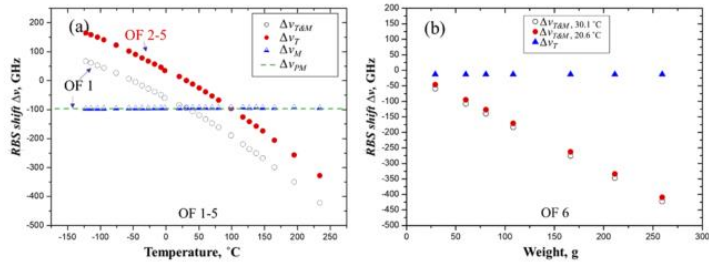


Fig. 7. The RBS shifts of optical fibers under coupled mechanical and thermal loading conditions, measured by the OBR.

that mechanical and thermally-induced effects can be considered independent from each other in the OBR measurements. Thus, the strain and the temperature effects can be added/subtracted by superposing the RBS shifts under coupled loading conditions.

3.3.2. Application of the polynomial formula

Mechanical loading is typically of main concern in the analysis of structures. That means the strain measurements are usually considered as the primary outputs from optical fiber sensors in engineering applications. The environmental temperatures can be obtained from separate thermal sensors and the influence of temperature is then subtracted from the overall loading effect. The linear and polynomial formulas are hereby applied to obtain pure mechanical strains from the coupled loading on the optical fiber. A new optical fiber (OF7) is loaded by using a dead weight of 29.32 g. The temperature data is obtained from an independent K-type thermal sensor. The pure Δv_M is decoupled by the same subtraction of OBR measurements as seen in Fig. 7(a) and as described in Section 3.3.1. Figure 8 shows the $\Delta v_{T&M}$ of OF7 while changing the surrounding temperature from -100 °C to 240 °C. The pure mechanical loading induced RBS shift Δv_{RM} of OF7 was measured by the OBR at reference temperature (31.4 °C) before and after loading by the dead weight. The Δv_{M-p} is the mechanical loading induced RBS shift when subtracting the Δv_T calculated by the polynomial formula (Table 2) from $\Delta v_{T&M}$, while the Δv_{M-L} uses the linear formula (Table 2). As shown in Fig. 9(a), both the values of Δv_{M-p} and Δv_{M-L} are in very good agreement with the Δv_{RM} from 0 °C to 50 °C. The difference between the Δv_{M-p} and Δv_{M-L} increases rapidly when the temperature is higher than 60 °C or lower than 0 °C.

The relative error (%error) between linear and polynomial formulas is also compared in Fig. 9(b):

$$\%error = \frac{|\Delta v_{RM} - \Delta v_M|}{\Delta v_{RM}} \cdot 100\% \quad (14)$$

where Δv_M can be Δv_{M-p} or Δv_{M-L} based on the formula applied. When the temperature shift is small (e.g., as in Range 1 in Figs. 4–6), there is little practical difference between the measuring errors of the polynomial and the linear formulas (< 3%). When the temperatures exceed the range from ca. -25 °C to 75 °C, the linear model becomes poorly suited for decoupling mechanical and thermal loading effects in the OBR measurement. The polynomial model works well over the whole temperature range. Thus, the polynomial formula is a more accurate model to account for thermal loading effects. It enables to decouple RBS shifts with a higher precision over a wider range of temperatures.

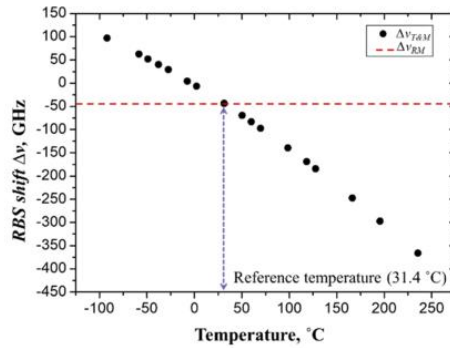


Fig. 8. The $\Delta\nu_{RM}$ and the $\Delta\nu_{T\&M}$ of OF7 with a constant mechanical loading.

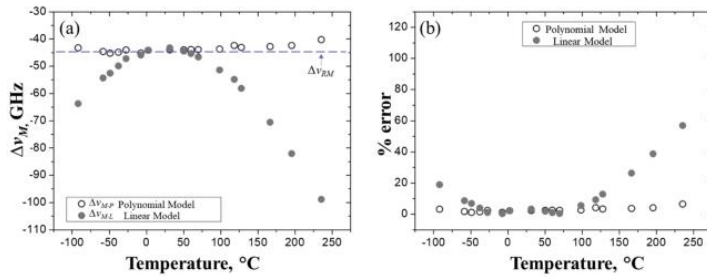


Fig. 9. A comparison between linear and polynomial models for an engineering application: (a) decoupled mechanical loading RBS shifts, (b) relative errors of RBS shift measurements.

4. Conclusions

1. Thermal loading induced RBS shifts of the OBR measurements are proven to be non-linear with temperature due to the relationship between the thermo-optic coefficient and temperature.
2. A polynomial formula is deduced from physics-based models for accurate temperature measurements with the OBR. The polynomial formula shows a higher temperature measurement precision than a linear formula over an extended temperature range.
3. Pure mechanical loading induced RBS shifts are shown to be linear with strain. Under coupled OBR measurement conditions, the mechanical and thermal loading effects are shown to be independent from each other. Pure mechanical strains can be obtained by subtracting the temperature effect (e.g. modelled by the polynomial formula) from the coupled RBS shift.

Funding

European Union's Horizon 2020 research and innovation programme and Hydrogen Europe and Hydrogen Europe Research (Grant ID: 826262).

Acknowledgments

This project has received funding from the Fuel Cells and Hydrogen 2 Joint Undertaking under grant agreement No. 826262, <https://thor-fch2.eu/>.

Disclosures

The authors declare no conflicts of interest.

References

1. L. Palmieri, "Distributed Optical Fiber Sensing Based on Rayleigh Scattering," *The Open Opt. J.* **7**(1), 104–127 (2013).
2. X. Bao and L. Chen, "Recent Progress in Distributed Fiber Optic Sensors," *Sensors* **12**(7), 8601–8639 (2012).
3. M. Froggatt and J. Moore, "High-spatial-resolution distributed strain measurement in optical fiber with Rayleigh scatter," *Appl. Opt.* **37**(10), 1735 (1998).
4. Z. Ding, C. Wang, K. Liu, J. Jiang, D. Yang, G. Pan, Z. Pu, and T. Liu, "Distributed Optical Fiber Sensors Based on Optical Frequency Domain Reflectometry: A review," *Sensors* **18**(4), 1072 (2018).
5. S. Kreger, D. Gifford, M. Froggatt, B. Soller, and M. Wolfe, "High Resolution Distributed Strain or Temperature Measurements in Single- and Multi-Mode Fiber Using Swept-Wavelength Interferometry," in *Optical Fiber Sensors, OSA Technical Digest (CD)* (Optical Society of America, 2006), paper ThE42.
6. M. Xu, L. Reekie, J. Dakin, and J. Archambault, "Discrimination between strain and temperature effects using dual-wavelength fibre grating sensors," *Electron. Lett.* **30**(13), 1085–1087 (1994).
7. M. Emmanuel and Y. Ouerdane, "Dual-Fibre Bragg Grating Sensor for Simultaneous Temperature and Strain Sensing of Composite Materials Manufacturing," in *proceeding of EWSHM - 7th European Workshop on Structural Health Monitoring*, L. Cam, ed. (Academic, Nantes, France, 2014), pp. 946–953.
8. S. Mondal, U. Tiwari, G. Poddar, V. Mishra, N. Singh, S. Jain, S. Sarkar, K. Chattopadhyaya, and P. Kapur, "Single fiber Bragg grating sensor with two sections of different diameters for longitudinal strain and temperature discrimination with enhanced strain sensitivity," *Rev. Sci. Instrum.* **80**(10), 103106 (2009).
9. S. Oh, W. Han, U. Paek, and Y. Chung, "Discrimination of temperature and strain with a single FBG based on the birefringence effect," *Opt. Express* **12**(4), 724 (2004).
10. X. Lu, M.A. Soto, and L. Thévenaz, "Discrimination of temperature and strain by combined refractive index and birefringence measurements using coherent Rayleigh sensing," in *proceeding of IEEE Conference on Optical Fiber* (Institute of Electrical and Electronics Engineers, Jeju Island, 2017), pp. 1–4.
11. W. Li, L. Chen, and X. Bao, "Compensation of temperature and strain coefficients due to local birefringence using optical frequency domain reflectometry," *Opt. Commun.* **311**, 26–32 (2013).
12. K. Kinzo, Y. Yamauchi, and A. Guzik, "Study of optical fibers strain-temperature sensitivities using hybrid Brillouin-Rayleigh System," *Photonic Sens.* **4**(11), 1–11 (2014).
13. D. Zhou, W. Li, L. Chen, and X. Bao, "Distributed Temperature and Strain Discrimination with Stimulated Brillouin Scattering and Rayleigh Backscatter in an Optical Fiber," *Sensors* **13**(2), 1836–1845 (2013).
14. Z. Ding, D. Yang, Y. Du, K. Liu, Y. Zhou, R. Zhang, Z. Xu, J. Jiang, and T. Liu, "Distributed strain and temperature discrimination using two types of fiber in OFDR," *IEEE Photonics J.* **8**(5), 1–8 (2016).
15. D. Yang, T. Liu, Z. Ding, Q. Han, K. Liu, J. Jiang, Q. Chen, and B. Feng, "Cryogenic temperature measurement using Rayleigh backscattering spectra shift by OFDR," *IEEE Photonics Technol. Lett.* **26**(11), 1150–1153 (2014).
16. A. Wosniok, D. Skoczowski, M. Schukar, S. Pöttsch, S. Pötschke, and S. Krüger, "Fiber optic sensors for high-temperature measurements on composite tanks in fire," *J. Civ. Struct. Health Monit.* **9**(3), 361–368 (2019).
17. A. Faustov, A. Gussarov, M. Wuilpart, A. A. Fotiadi, L. B. Liokumovich, O. I. Kotov, I. O. Zolotovskiy, A. L. Tomashuk, T. Deschoutheete, and P. Mégret, "Distributed optical fibre temperature measurements in a low dose rate radiation environment based on Rayleigh backscattering," *Proc. SPIE* **8439**, 84390C (2012).
18. S. Pavol, K. Hicke, and K. Kriebber, "Distributed Fiberoptic Sensor for Simultaneous Humidity and Temperature Monitoring Based on Polyimide-Coated Optical Fibers," *Sensors* **19**(23), 5279 (2019).
19. S. Wang, K. Lasn, C. Elverum, D. Wan, and A. Echtermeyer, "Novel in-situ residual strain measurements in additive manufacturing specimens by using the Optical Backscatter Reflectometry," *Addit. Manuf.* **32**, 101040 (2020).
20. P. A. Kisaka, E. M. Beres-Pawlik, J. Wojcik, and W. Wojcik, "Fiber Bragg grating sensors for temperature measurement," *Proc. SPIE* **5576**, 270–276 (2004).
21. R. Rajnikumar, K. G. Narayankhedkar, G. Krieg, M. Suber, A. Nyilas, and K. P. Weiss, "Fiber Bragg gratings for sensing temperature and stress in super conducting coils," *IEEE Trans. Appl. Supercond.* **16**(2), 1737–1740 (2006).

22. J. Komma, C. Schwarz, G. Hofmann, D. Heinert, and R. Nawrodt, "Thermo-optic coefficient of silicon at 1550 nm and cryogenic temperatures," *Appl. Phys. Lett.* **101**(4), 041905 (2012).
23. W. Wang, Y. Yu, Y. Geng, and X. Li, "Measurements of thermo-optic coefficient of standard single mode fiber in large temperature range," In *proceeding of Optical Instruments and Technology: Optical Sensors and Applications*, (Academic, Beijing, 2015), pp. 96200.
24. F. Della Corte, M. Esposito Montefusco, L. Moretti, I. Rendina, and G. Cocorullo, "Temperature dependence analysis of the thermo-optic effect in silicon by single and double oscillator models," *J. Appl. Phys.* **88**(12), 7115–7119 (2000).
25. G. Gosh, "Sellmeier coefficients and dispersion of thermo-optic coefficients for some optical glasses," *Appl. Opt.* **36**(7), 1540–1546 (1997).
26. G. Ghosh, "Model for the thermo-optic coefficients of some standard optical glasses," *J. Non-Cryst. Solids* **189**(1-2), 191–196 (1995).
27. K. Lasn, E. Sæter, and A. Echtermeyer, "Sensing of Structural Damage with OBR Based Fibre-Optic Networks," (STO-Meeting Proceedings Paper, 2018), <https://ntnuopen.ntnu.no/ntnu-xmlui/handle/11250/2587611>.
28. H. M. Lund, "Health monitoring of composites using optical fibres," (Master's thesis, NTNU, 2012), <https://ntnuopen.ntnu.no/ntnu-xmlui/handle/11250/241661>.

Paper III

Article

Comparison of DOFS Attachment Methods for Time-Dependent Strain Sensing

Shaoquan Wang *, Erik Sæter and Kaspar Lasn *

Department of Mechanical and Industrial Engineering, Norwegian University of Science and Technology (NTNU), Richard Birkelands vei 2B, 7491 Trondheim, Norway
 * Correspondence: shaoquan.wang@ntnu.no (S.W.); kaspar.lasn@ntnu.no (K.L.)

Abstract: Structural health monitoring (SHM) is a challenge for many industries. Over the last decade, novel strain monitoring methods using optical fibers have been implemented for SHM in aerospace, energy storage, marine, and civil engineering structures. However, the practical attachment of optical fibers (OFs) to the component is still problematic. While monitoring, the amount of substrate strain lost by the OF attachment is often unclear, and difficult to predict under long-term loads. This investigation clarifies how different attachment methods perform under time-dependent loading. Optical fibers are attached on metal, thermoset composite, and thermoplastic substrates for distributed strain sensing. Strains along distributed optical fiber sensors (DOFS) are measured by optical backscatter reflectometry (OBR) and compared to contact extensometer strains under tensile creep loading. The quality of the bondline and its influence on the strain transfer is analyzed. Residual strains and strain fluctuations along the sensor fiber are correlated to the fiber attachment method. Results show that a machine-controlled attachment process (such as in situ 3-D printing) holds great promise for the future as it achieves a highly uniform bondline and provides accurate strain measurements.

Keywords: structural health monitoring; optical fiber; attachment methods; 3-D printing; distributed strain sensing



Citation: Wang, S.; Sæter, E.; Lasn, K. Comparison of DOFS Attachment Methods for Time-Dependent Strain Sensing. *Sensors* **2021**, *21*, 6879. <https://doi.org/10.3390/s21206879>

Academic Editor: Nicolas Riesen

Received: 14 September 2021

Accepted: 13 October 2021

Published: 17 October 2021

Publisher's Note: MDPI stays neutral with regard to jurisdictional claims in published maps and institutional affiliations.



Copyright: © 2021 by the authors. Licensee MDPI, Basel, Switzerland. This article is an open access article distributed under the terms and conditions of the Creative Commons Attribution (CC BY) license (<https://creativecommons.org/licenses/by/4.0/>).

1. Introduction

Maintaining the integrity of structural components and infrastructures over years of service is a considerable challenge, and many structural health monitoring (SHM) systems have been developed for this purpose. Among those, distributed optical fiber sensors (DOFSs), or optical fiber (OF) sensors in short, hold many advantages over traditional SHM technologies. Notably, the OF measures directly on the component, it has a long service life, a good corrosion resistance, a small size, and it is immune to electromagnetic interference.

However, the integration of OF sensors inside the component, or attaching them on the component surface, is still a challenge for many practical applications [1]. A limited scope literature review identifies basic types of attachment methods [2–15] for fixing the optical fibers, as shown in Table 1. Structural engineering applications (concrete, timber, and steel) tend to adhere the OF directly on the surface by a rigid glue [2], pre-embed the OF in a package filled with rigid glue or soft rubber [5–7], or attach specialized optical cables to the component [8]. Similar methods are adopted for polymers and polymer composites [9,10]. In addition, the OF can be embedded directly inside the polymer or composite components during the manufacturing process [11–15]. Polymer matrix surrounding the OF enables the strain transfer and protects the sensor. When the OF is attached on the surface, the geometry and the mechanical properties of the bondline will affect the accuracy of strain measurements. Thin and rigid bonding is necessary for accurate transfer of strain. Non-appropriate attachments can decrease the strain transfer coefficient, add noise, and give false measurements [16]. Adhesives, such as epoxy, cyanoacrylate, polyester, and quartz glue, are used quite arbitrarily on many substrate materials. The low surface energy,

however, becomes a challenge for reliable bonding on thermoplastics with these standard adhesives [17].

Table 1. An overview of optical fiber attachment concepts.

Substrate	Attachment Method	Adhesives	Application Case
Concrete, steel, and timber	Surface mounting	Cyanoacrylate, epoxy, quartz glue, polyester	Strain, cracking, and vibration [2–4]
	Pre-embedded bar	Epoxy, silicone, rubber	Strain [5–7]
	Specialized optical cables	Epoxy	Creep strains and temperature [8]
Thermosets and thermoset composites	Surface mounting	Cyanoacrylate	Stiffness degradation and strain [9]
	Embedding	Epoxy resin	Impact damage [10,11]
Thermoplastics and thermoplastic composites	Surface mounting	Cyanoacrylate	Strain [12]
	Embedding (Hand-layup)	Inside the composite	Residual strains [13]
	Embedding (Hot-pressing)	Partially fixed with epoxy	Relaxation [14]
	In situ embedding (3-D printing)	Inside the polymer	Residual strains and defects [15]

To date, the experimental work on attachment methods of distributed OF sensors has been very limited. This is the first investigation where attachments for DOFS are compared under time-dependent loading. Spatially and temporally varying strain profiles are compared along the OF attachment bondline. Practical solutions for fixing the OF on metals, thermoset composites, and thermoplastics are experimentally compared. Both crosslinked structural adhesives and un-crosslinked melting/fusion-based attachments are employed for the sensor attachment process. All attachments remain intact throughout the creep test, so any glue-line durability aspects are out of the scope of this investigation.

Experimental strains from optical fibers revealed distinct regions of strain disturbances at the ingress/egress parts of the DOFS. These regions are present for all OF attachments, affecting distributed strain analysis, especially if the attachment lengths are short. Practical analysis methods are suggested for estimating the lengths of the disturbed regions. Moreover, residual strains, as created by the attachment process, were easily characterized by the optical fiber self-recording measurements. Strain fluctuations along the OF length were related to specific fiber attachment processes. A novel optical fiber attachment method based on polymer extrusion additive manufacturing showed good performance, achieving uniform and accurate OF strain measurements.

2. Materials and Methods

2.1. Materials

Three material systems were employed as substrate specimens carrying OFs for tensile creep experiments: a glass fiber epoxy composite, a 3-D-printed PA6 thermoplastic (unreinforced), and a generic mild steel. Between them, a wide range of material behaviors are covered. Structural steel, when loaded within the elastic range, gives negligible time-dependent strains. Unreinforced PA6, on the other hand, creeps extensively already at low loads at room temperature. The GF/Epoxy composite response to creep depends on the lay-up but is somewhere between the previous two materials. Test specimens from all substrate materials were prepared in dogbone shapes, with nominal dimensions adopted from ASTM E8 [18] and ASTM D638 [19] standards, as described in Figure 1 and Table 2.

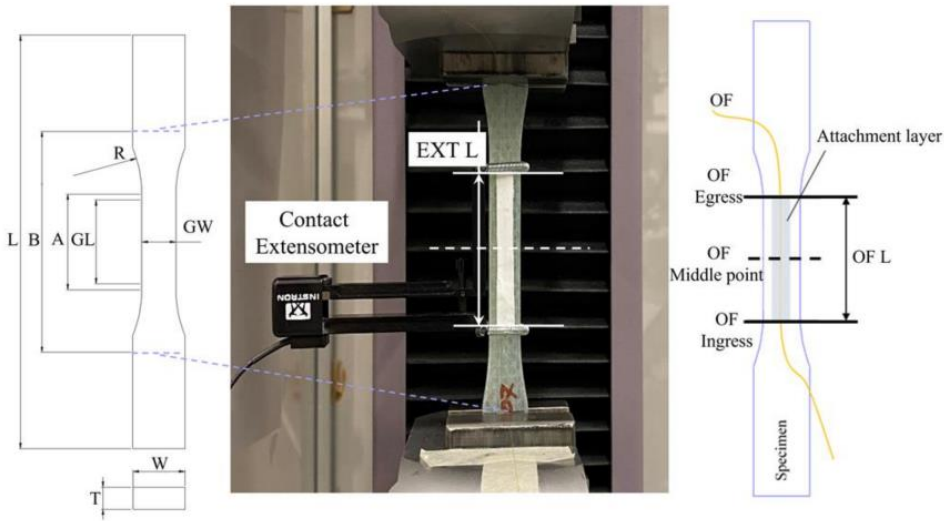


Figure 1. The geometry of specimens and the positioning of the optical fiber (OF).

Table 2. Dogbone specimen dimensions (mm), after ASTM E8 [18] and ASTM D638 [19], with reference to Figure 1.

Dimensions	PA6	GF/Epoxy	Steel
GL—Gauge length	50	50	25
GW—Width	13	13	6
T—Thickness	6.4	7	3
R—Radius of fillet	76	76	6
L—Overall length	165	165	100
A—Length of reduced parallel section	57	57	32
B—Distance between grips	115	115	40
W—Width of grip section	19	19	10
OF L—Attached optical fiber length	50	50	25
EXT L—Extensometer gauge length	50	50	25

Steel and GF/Epoxy dogbones were extracted from plates with a water jet cutting system. Steel specimens were cut from a 3-mm-thick plate. The GF/Epoxy plate (7 mm thick) was made by vacuum-assisted resin infusion using 8 layers of 1200 gsm unidirectional 3B HiPer-tex fabric in a quasi-isotropic $[90, 45, 0, -45]_s$ layup sequence. The epoxy was mixed from EPIKOTE MGS RIMR 135 and EPIKURE curing agent MGS RIMH 137. PA6 dogbones were built on a PRUSA I3 MK2S 3-D printer from natural Ultrafuse 1.75 mm filaments. The polyamide specimens were also infilled by a $[90, 45, 0, -45]_{4s}$ layup using a 0.2 mm layer height.

All specimens received the same basic surface preparation by cleaning with acetone, abrading with the 120 grit sanding paper, and re-cleaning with acetone, before attaching the OFs. The optical fiber sensor is SMB-E1550H from OFS Fitel. It is a silica/silica/polyimide fiber with a core diameter of 6.5 μm , a cladding diameter of 125 μm , and a coating diameter of 155 μm . Altogether, five attachment methods were used for fixing the optical fibers as summarized in Table 3. These attachment methods were chosen based on previous projects in our lab: a regular cyanoacrylate glue, two types of epoxies (one cold/rapid curing and one hot-curing epoxy film), and two thermoplastic fusion-based attachments (one manual welding and one 3-D printing-based welding). The ‘Embedding’ method

by 3-D printing was only employed for PA6 specimens, after being built on the same 3-D printer. All specimens had a single OF installed along the centerline of the specimen, as shown in Figure 1.

Table 3. Investigated optical fiber attachment methods.

Attachment Denotation	Shorthand Name	Method	Details ¹
a	‘Cyanoacrylate’	Cyanoacrylate adhesive	Standard adhesive for strain gauges.
b	‘Araldite’	Araldite Rapid adhesive	Two component rapid curing epoxy.
c	‘Epoxy’	Epoxy film adhesive	Adhesive film (Gurit SA 80) is placed over the OF, and cured for 12 h at 80 °C under vacuum.
d	‘Weld’	OF is manually fused/glued on the substrate by a filament of thermoplastic material	A PA6 filament (1.75 mm, natural, Ultrafuse) is melted and extruded with a Leister Triac hot-air tool.
e	‘Embedding’	The OF is 3-D printed under a cuboid volume (64 mm × 10 mm × 0.4 mm) embedding it directly on the surface of the PA6 specimen.	PA6 (1.75 mm filament, natural, Ultrafuse).

¹ Room temperature varied between 19 and 25 °C and relative humidity between 15 and 35% during the attachment and testing procedures.

2.2. Creep Testing

Mechanical testing was performed on a 5 kN MTS Model 42 universal testing machine. An illustration of the applied creep load–time curve can be seen in Figure 2. At the beginning of the test (time t_1), all specimens were initially loaded to the same preload (15 N), and then further until the defined creep load using a high cross-head speed (100 mm/min for GF/Epoxy and PA6, and 10 mm/min for steel). The small load overshoot before time t_2 is an artifact of control-loop programming. The load adjusted quickly (<40 s) and it was maintained constant with less than 1 N variation during the one-hour creep test. Time t_2 is defined as the start of the creep load, which was kept on until $t_n = 3600$ s.

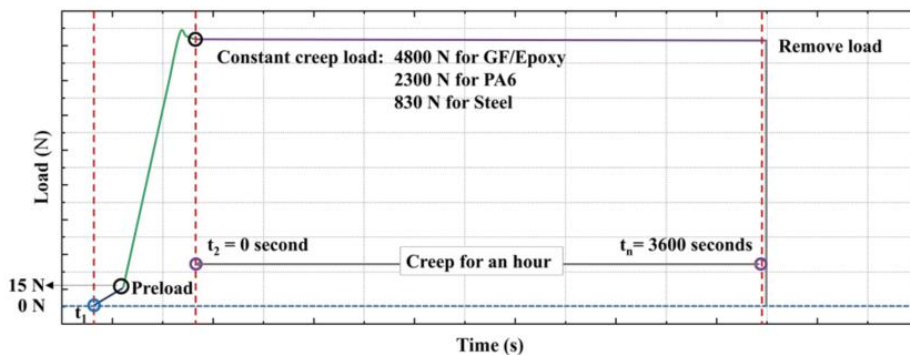


Figure 2. The creep loading procedure.

2.3. Strain Measurements

A contact extensometer Instron 2620-601 with the same gauge length as the OF attachment length OF L in Figure 1, was adopted for independent strain measurements. Extensometer strains are compared to the averaged OF strains of the same specimen.

Reflectometer OBR 4600 from Luna Instruments was used as the OF interrogator device. Technical details about the entire distributed strain measurement system can be found in Appendix A. To obtain any strain measurement, two light spectra, one from the reference scan and one from the measurement scan, are analyzed in the software. In the program, the OF becomes divided into many virtual strain gauges along the sensing length of the fiber. Each gauge works as a separate virtual strain sensor. All virtual sensors have the same gauge length and spacing between them as shown in Figure 3a. In our work, a sensor spacing of 0.5 mm and a gauge length of 10 mm were selected. This gives overlapping virtual strain gauges. Based on previous experience, this configuration is a good compromise between high spatial resolution and unwanted noise occurrences. Strains are calculated from the frequency shifts of the measured spectrum and averaged along the length of each virtual sensor. Thus, some strains from the ingress and egress parts of the OF can be artificially smaller than the natural strain in the surrounding material. The OBR measured/calculated strain curve in the ingress and egress parts tapers gradually as shown in Figure 3b. The disturbed region l contains a gradually increasing curve in the ingress region and a gradually decreasing curve in the egress region. It would seem reasonable to assume that l should be equal to the chosen virtual gauge length value. However, the OBR system uses a cross-correlation algorithm to compare the spectra before and after loading. When only a small part of the virtual strain gauge exceeds the attachment length, the calculated strain will not decrease just yet. The disturbed region l therefore turns out to be slightly smaller than the gauge length [20]. Avoiding inaccurate ingress/egress regions l , only strains from the central region of the attached fiber can be used to calculate the average OF strain. This quasi-constant central region is referred to as the region of interest (ROI) as indicated in Figure 3b.

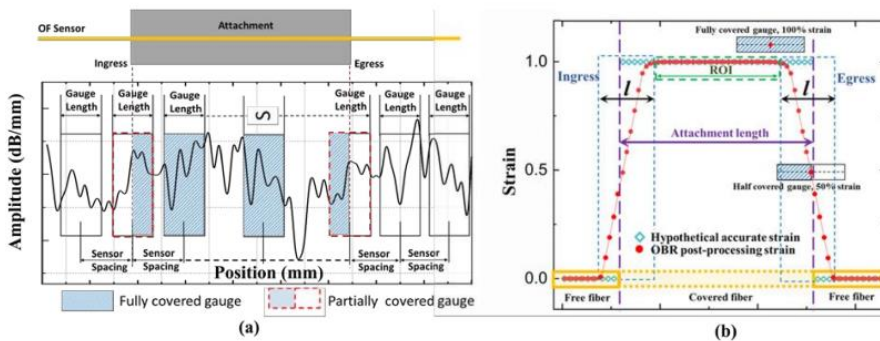


Figure 3. Illustration of OBR post processing parameters (a) and strains at the disturbed region l at the ingress/egress of the OF (b).

The OBR measurements were recorded every 60 s throughout the 1 h creep test. In order to calculate strain, three kinds of reference measurements were used. References taken before the OFs were attached on the specimens (i.e., free OFs) are hereby denoted as free-fiber references. Strains calculated by comparing to the free-fiber reference are called *relative free-fiber strains*. Two kinds of references were taken at times t_x of the creep test, where $x=1, 2$, as seen in Figure 2. The strains obtained by comparison to the reference at t_x are called *relative- t_x strains*. Relative- t_2 strains represent the time-dependent strain

development during tensile creep. Relative- t_1 strains are similar, but additionally include the strain from the load ramp-up procedure.

3. Results

Tensile creep testing was carried out on GF/Epoxy, PA6, and steel specimens. Creep loads were applied as 4800, 2300, and 830 N, which acting on 91, 83.2, and 18 mm² cross-section areas, gave approximately 2500, 18000, and 250 $\mu\epsilon$ initial (short-term) strains, respectively.

In the current Section 3, raw data from the tests is displayed as follows: (i) experimental strain measurements from three types of substrate specimens are presented by different OF attachment methods, separately; and (ii) spatial and temporal strain curves are accompanied by a coarse analysis of presented data. A more detailed analysis is carried out later in Section 4.

3.1. GF/Epoxy Composite

Figure 4 shows the relative- t_2 spatial strain profiles obtained by the OBR at 60, 600, 1800, and 3600 s after t_2 . Analogous relative- t_2 strains from the contact extensometer, constant within the EXT L gauge length, are also plotted on the same figure. The midpoints and the start/end points of the OF attachments are indicated by vertical dashed and solid lines, respectively. These positions correspond to the same markings in Figure 1. The OF attachment length (OF L) is nominally the same as EXT L of the extensometer; however, some adhesives flowed during the curing process, leading to a longer actual OF L for these attachments. The ROI was defined as 40 mm in the center of the OF L to calculate the average relative- t_2 OF strains shown in Figure 5. The error bars in Figure 5 show ± 1 standard deviation for the OF strain profiles within the ROI.

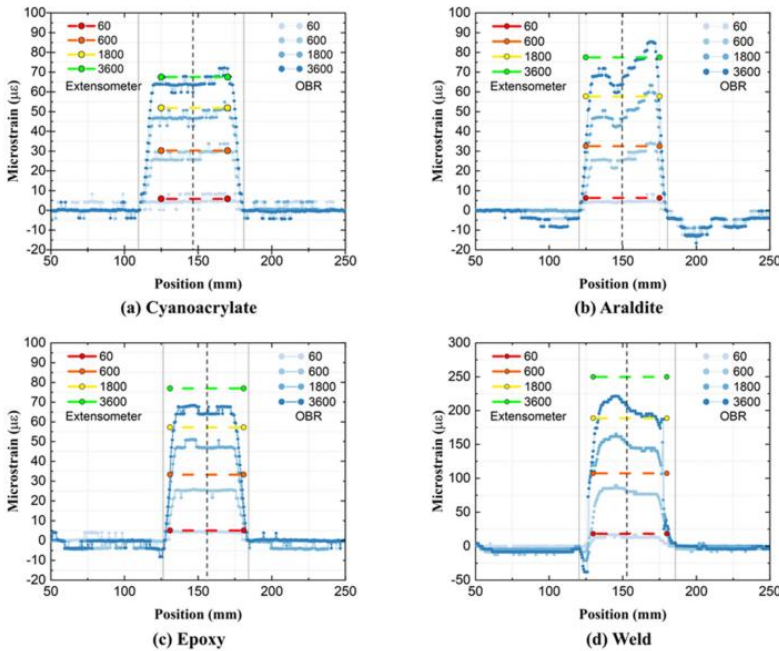


Figure 4. Relative- t_2 spatial strain profiles on GF/Epoxy specimens.

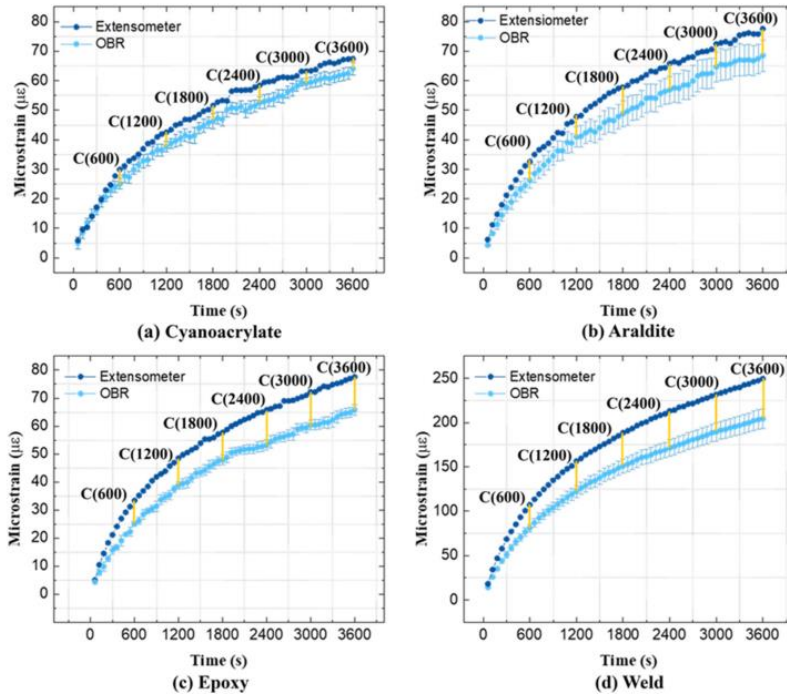


Figure 5. Average relative- t_2 strains of GF/Epoxy specimens measured throughout the creep test.

In Figure 4, all OF attachments are seen to behave qualitatively in a similar fashion. The OFs display positive strains in reverse bath-tub profiles, which increase with time during creep loading, as expected. Strains from the ‘Cyanoacrylate’ and ‘Epoxy’ film attachments show a more consistent flat plateau than from the manually applied ‘Araldite’ and ‘Weld’ attachments. However, even the biggest strain fluctuation, e.g., in ‘Araldite’ (ca. $25 \mu\epsilon$) is small compared to the initial strain from loading the GF/Epoxy specimen (ca. $2500 \mu\epsilon$). Only the OF strain profile of the ‘Cyanoacrylate’ attachment compares well to corresponding strains from the extensometer. The OF strains from ‘Araldite’, ‘Epoxy’, and especially the ‘Weld’ attachments, are clearly lower than the corresponding extensometer strains.

A detailed temporal comparison of average relative- t_2 strains from the OBR and the extensometer is shown in Figure 5. All strains increase with time, while the slope of the curve decreases. Relative- t_2 extensometer strains behave generally in the same manner as the averaged OF strains during creep. The relative- t_2 strain increase for the ‘Weld’ attachment is ca. $200 \mu\epsilon$ after 3600 s, while it is only around $80 \mu\epsilon$ for all other attachments. Since both the OBR and the extensometer show similarly high values for the ‘Weld’ attachment, this inconsistency must arise from an unknown variability in the specimen production/preparation. Throughout all creep testing, the strains from the OBR are consistently smaller than strains from the extensometer. The difference between the OBR and extensometer strains is smallest for the ‘Cyanoacrylate’ attachment compared to the other three attachments. The yellow markings with coefficients C (time) in Figure 5 are clarified and discussed later in Section 4.

3.2. Thermoplastic PA6

The PA6 specimens were initially loaded to very high strains of ca. 18000 $\mu\epsilon$. Thereafter, Figure 6 shows how relative- t_2 strains along the OFs compare to the corresponding strain profiles from the extensometer. As relative- t_2 strains exceed 6000–12000 $\mu\epsilon$ after 1 h of creep, overall strains approaching 3% are hereby measured on PA6 dogbones. Regardless of the high strain values, all attachments display strain curves that are qualitatively similar to the GF/Epoxy specimen curves previously. Strains fluctuate with respect to position and rise with increasing time. The new attachment ‘Embedding’ by 3-D printing also shows similar characteristics to other attachments. Notably, the strain profiles of the ‘Embedding’ attachment are very consistent and uniform. The profiles of ‘Cyanoacrylate’ and ‘Embedding’ attachments compare best to corresponding strains from the extensometer. OF strains from ‘Araldite’ and ‘Weld’ attachments are higher than the corresponding extensometer strains, while OF strains from ‘Epoxy’ are lower. The temporal development of average relative- t_2 strains on the PA6 specimens in Figure 7 was calculated using the same ROI = 40 mm as for GF/Epoxy specimens. For GF/Epoxy, the strains from the OBR were consistently smaller than strains from the extensometer. This relationship is more complex for PA6, as shown in Figure 7, where the OBR strains are now measured larger for ‘Cyanoacrylate’, ‘Araldite’, and ‘Weld’ attachments. For the ‘Embedding’ attachment, excellent agreement between OBR and extensometer strains can be noted.

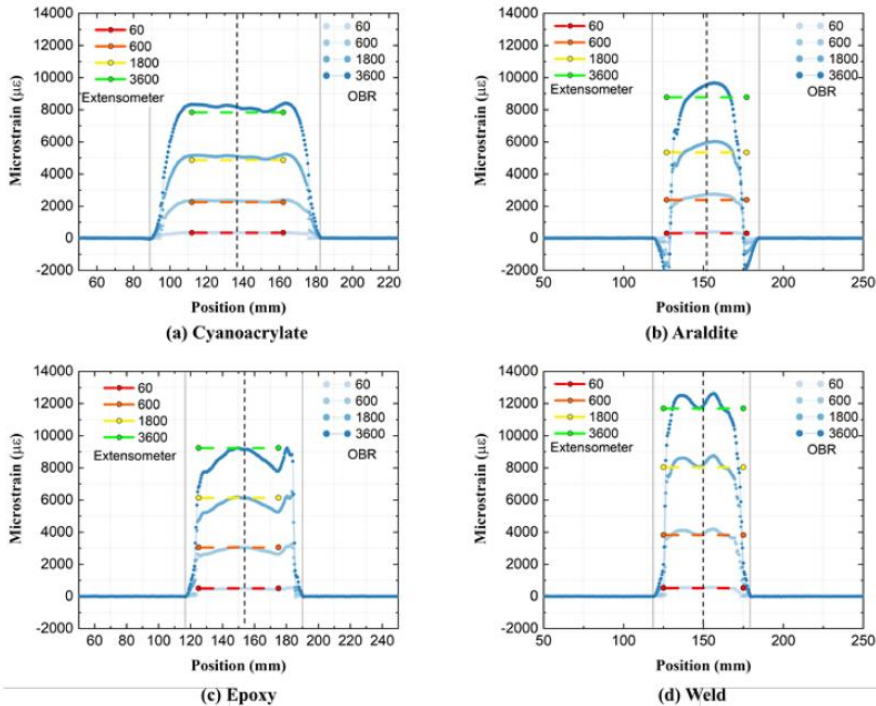


Figure 6. Cont.

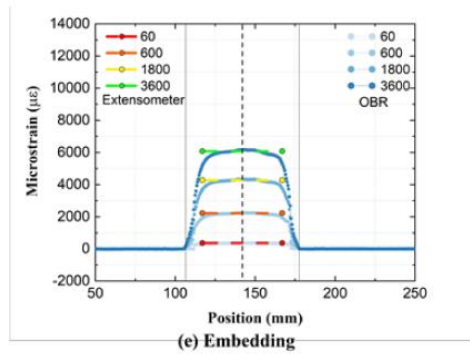


Figure 6. Relative- t_2 spatial strain profiles on PA6 specimens.

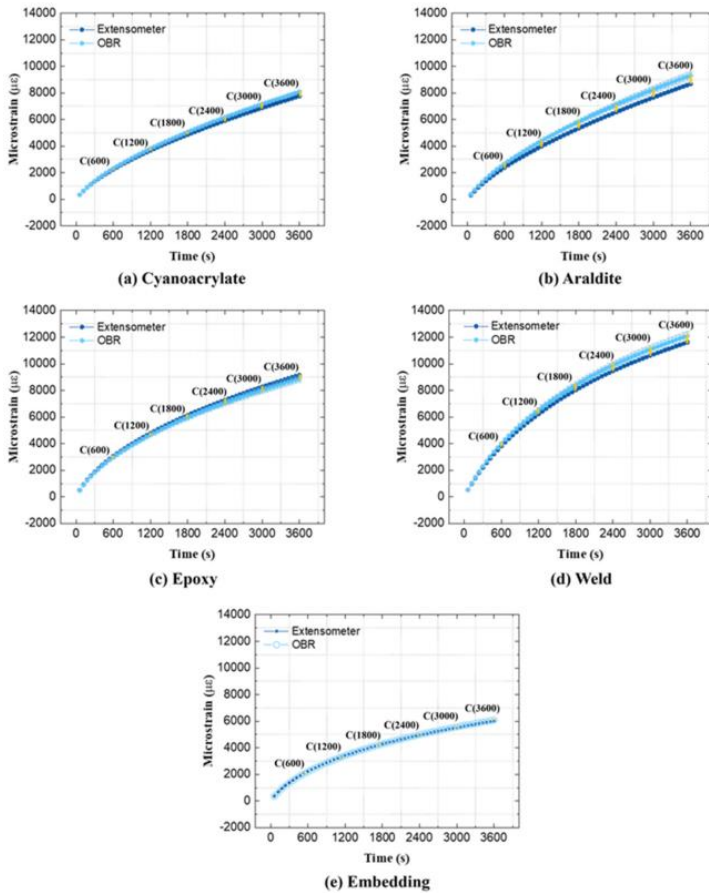


Figure 7. Average relative- t_2 strains of PA6 specimens measured throughout the creep test.

3.3. Steel

Creep strains are very small for steel specimens at room temperature. Therefore, relative- t_1 strains, i.e., using reference measurements from unloaded specimens, were chosen for the spatial strain data analysis. Relative- t_1 strain profiles from the OBR and from the extensometer are compared in Figure 8. All strain profiles from the OBR (except for the ‘Weld’) show high variability along the attachment length. This can be caused by the small size of the steel specimen, which negatively affects the practical attachment procedure. It proved difficult to manually handle OFs over short attachment lengths, and to fix them uniformly onto small-sized steel specimens. Expectedly, the OBR strains did not change much during creep loading. However, the extensometer strains appear to increase with time by ca. 20–35 $\mu\epsilon$. This was unexpected; however, it was witnessed from all experiments in Figure 8. In order to clarify how strains from the OBR and the extensometer diverge during creep, average relative- t_2 strain developments (using ROI = 15 mm) are shown in Figure 9. All strain–time curves measured by the OBR fluctuate around zero. Contrary to the OBR, the extensometer shows increasing strain–time curves before ca. 1500–1800 s and then the curves remain flat. This behavior was seen on all specimens consistently, and it is likely related to the warmup drift of the extensometer. Potential issues that can affect contact extensometer strains are briefly summarized in Appendix B.

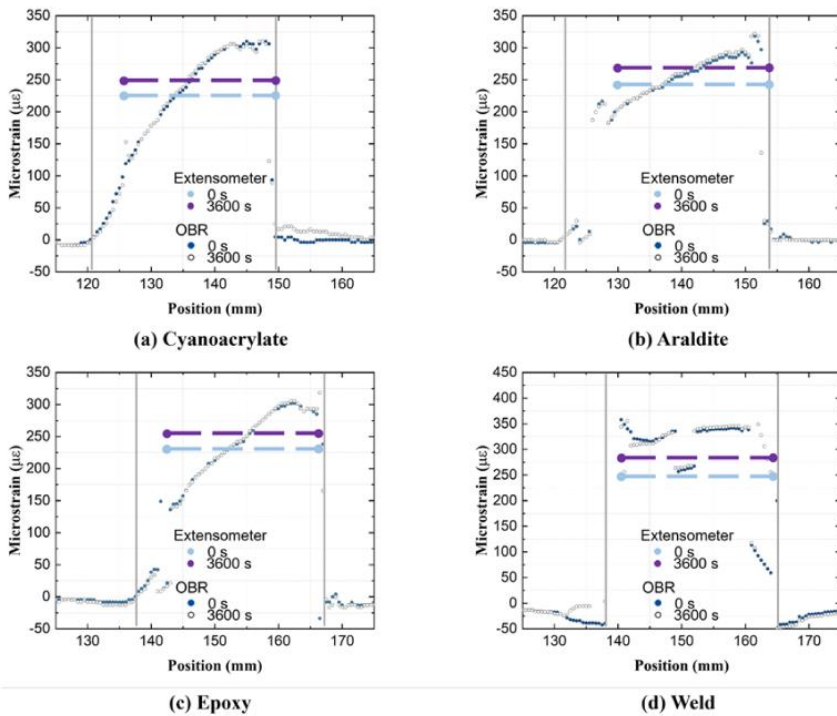


Figure 8. Relative- t_1 spatial strain profiles on steel specimens.

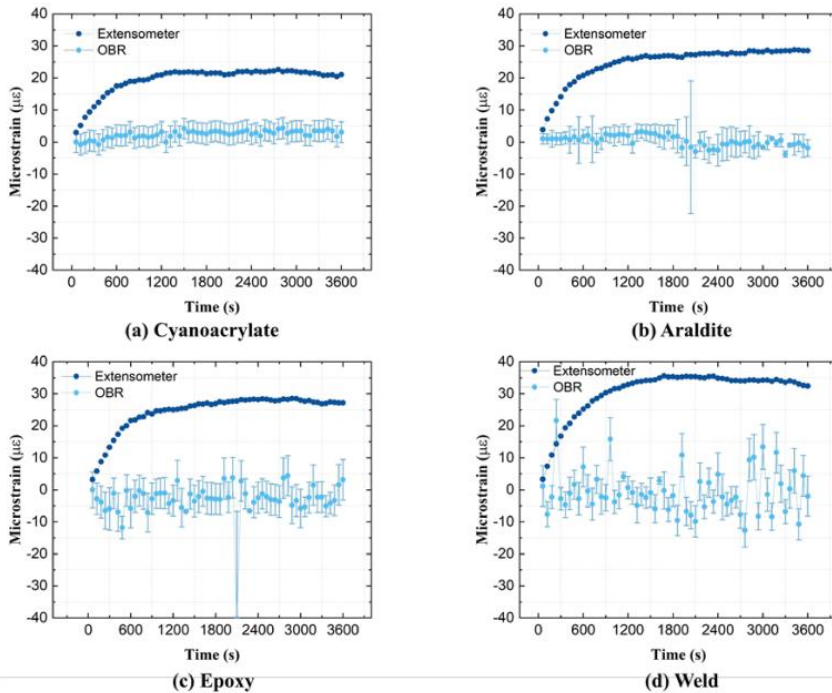


Figure 9. Average relative- t_2 strains of steel specimens measured throughout the creep test.

4. Discussion

Based on the raw data from Section 3, the differences between the adopted attachment methods are further analyzed and discussed in detail. In addition, residual strains are presented, and their creation mechanisms are discussed. Correlations between attachment methods and strain data are also emphasized.

4.1. The OF Attachment Process

As seen from Figures 4 and 6, different OF attachment methods produce different shapes of spatial strain profiles. Not only are the mean values different, but the strain profile variability along the OF is clearly different. The OF attachment process appears to affect the strain profile variability. Well-controlled attachment methods ('Cyanoacrylate', 'Epoxy', 'Embedding') tend to produce more uniform strain profiles compared to less-controlled methods ('Araldite', 'Weld'). Small imperfections, such as small cracks, thickness variations in the adhesion layer, and misalignment of the attached OF, are well-known quality issues. These imperfections are created in the attachment process, producing noisy datapoints or local distortions in the strain profile.

4.1.1. Residual Strains

Residual strains are created in the attachment process when fixing the OFs to the substrate, before any external mechanical loading occurs. These residual strains are not trivial to predict or measure by conventional means. However, they can be characterized directly, since the OF works as a strain sensor throughout the attachment process. To this end, the pre-attachment free fiber is taken as the reference state, and the load-free condition

after the attachment (without any external loading) as the measurement state. Figure 10 shows residual strains from all five attachments on steel, GF/Epoxy, and PA6 substrates. The centerlines of substrate specimens are shifted to a common generic 100 mm coordinate, marked by a vertical dashed line.

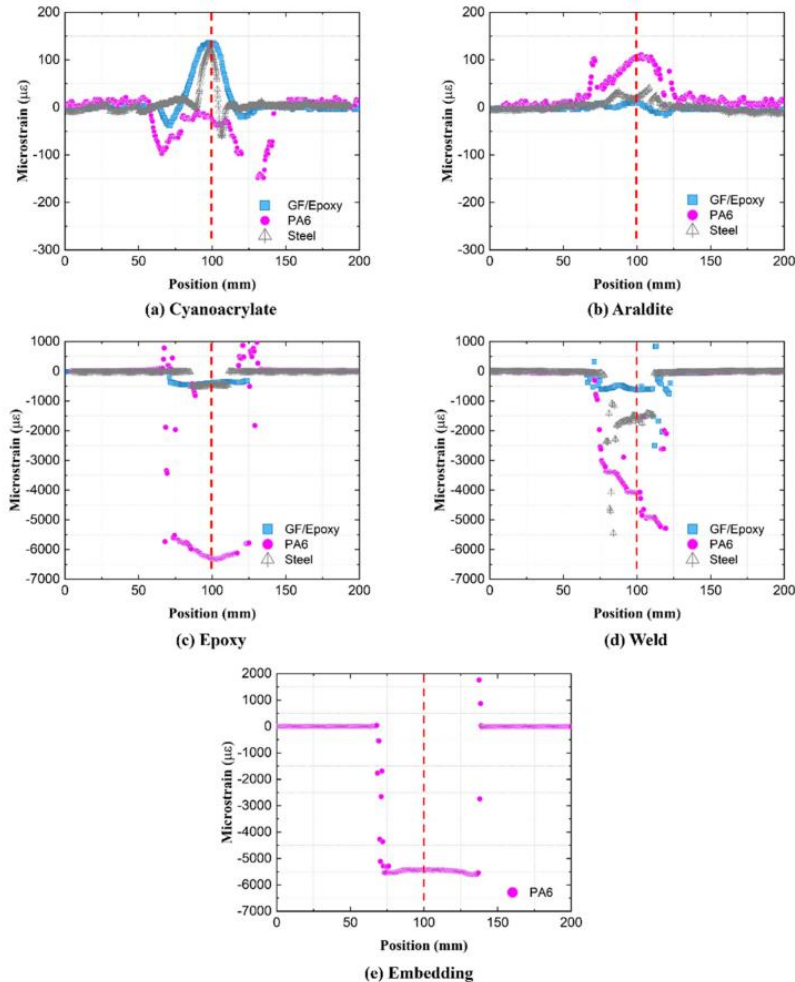
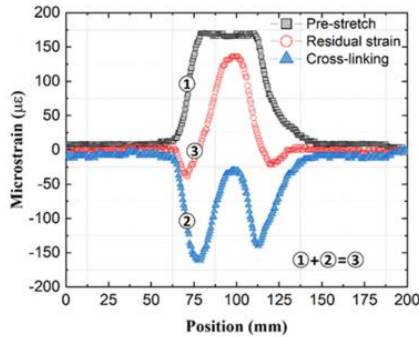


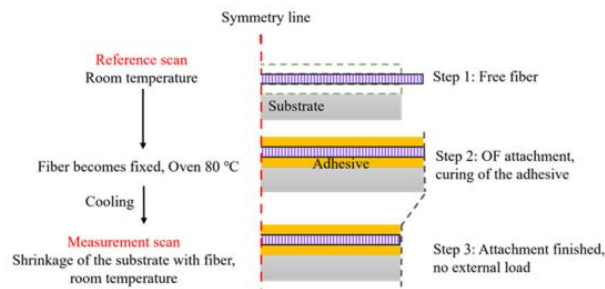
Figure 10. Residual strain profiles along the attached OFs.

Residual strains from cold curing ‘Cyanoacrylate’ and ‘Araldite’ attachments from Figure 10a,b are small (below $\pm 150 \mu\epsilon$) on all substrates. They are created by a combination of compressive shrinkage and a small tensile pre-stretch, applied by hand on the optical fiber. In room-temperature curing, compressive strains are generated from chemical volumetric shrinkage during crosslinking. At the same time, during the installation process, the OF was slightly stretched (using two tapes outside the gauge area) to align it with the specimen. This pre-stretch was hand-controlled, and thus the magnitude of tensile strain

varied over different specimens. Figure 11a illustrates in detail how in these cold-curing cases the overall residual strain consists of the pre-stretch (measured during the attachment process) and from the curing shrinkage (calculated by subtracting the pre-stretch from the overall residual strain).



(a) Cold curing ('Cyanoacrylate', GF/Epoxy)



(b) Hot curing ('Epoxy')

Figure 11. Residual strain formation for cold and hot curing OF attachments.

For the 'Epoxy' attachment in Figure 10c, residual strains on all specimens are predominantly compressive and much larger than residual strains from the cold curing 'Cyanoacrylate' and 'Araldite' attachments previously. During the fiber attachment, the specimens were heated in an oven for 12 h at 80 °C to cross-link the epoxy film and then cooled back down to room temperature. In addition to chemical volumetric shrinkage of epoxy from curing, the residual strains of the 'Epoxy' attachment originate from the physical volumetric shrinkage of substrates during the cooling process. This process is illustrated in Figure 11b. The temperature change for all three specimens is ca. 60 °C, while the CTE of PA6 (80–90 $\mu\text{m}/(\text{m}^\circ\text{C})$) is much larger than CTE of steel (9–17 $\mu\text{m}/(\text{m}^\circ\text{C})$), and CTE of quasi-isotropic GF/Epoxy (12–20 $\mu\text{m}/(\text{m}^\circ\text{C})$). Thus, residual strains on PA6 became much larger (ca. $-6000 \mu\epsilon$) than residual strains on GF/Epoxy and steel specimens (ca. $-500 \mu\epsilon$).

Residual strains for the manually applied 'Weld' attachment in Figure 10d appear less uniform. The mechanism of residual strain creation becomes rather complex, as the strain value is affected by the local shrinkage of PA6 filament (after hot-air welding), and similarly, local contraction of substrates during cooling. Because of locally inconsistent

temperatures from the hand-controlled weld process, uneven distributions of residual strains along the OFs are created.

The residual strains of in situ ‘Embedding’ (Figure 10e) originate from the shrinkage of cooling from the deposited PA6 filament during the 3-D printing process [15]. Printing parameters, such as the temperature, extrusion speed, and printing speed, are automatically well controlled, resulting in a high but very uniform residual strain distribution along the attached OF.

In summary, the residual strains of ‘Cyanoacrylate’, ‘Araldite’, and ‘Weld’ attachments are strongly affected by local effects in the attachments process. Thereby, residual strain becomes very inconsistent. In contrast, the residual strains of the ‘Epoxy’ and ‘Embedding’ attachments originate from a global and more uniform source of strain on the specimens. Fluctuations in the residual strain profile refer to a non-uniform occurrence in the bondline in terms of thickness, small cracks, etc. The nonuniform cooling process of the specimen (even for ‘Epoxy’ when taken out of the oven) may also contribute to some variations in residual strains.

4.1.2. Correlation between Residual Strains and Creep Strains

During data analysis, correlations between the residual strains and creep strains were noted for some attachment methods. To visualize these correlations, residual strains and relative- t_2 OF strains (at 60 and 3600 s) were first normalized by the peak values of strain curves within the ROI. Then, correlations between the normalized residual strain and normalized relative- t_2 strain were visualized by calculating an index S :

$$S(t) = \left| \frac{\varepsilon_R^N(t)}{\varepsilon_{t_2}^N(t)} \right| \times 100\% \tag{1}$$

where ε_R^N is the normalized residual strain and $\varepsilon_{t_2}^N$ is the normalized relative- t_2 strain. Figure 12 shows the calculated indices $S(t)$, for all attachment types on PA6 specimens, at $t = 60$ s and $t = 3600$ s. Specifically, from Figure 12c,e, it is easy to see excellent, nearly one to one correlation between the normalized ‘Epoxy’ and ‘Embedding’ strains between 80 mm and 130 mm position along the attachment length, while the S index varies randomly elsewhere. This correlation shows how creep strains that develop later in life are affected by the specific (imperfect) attachment process.

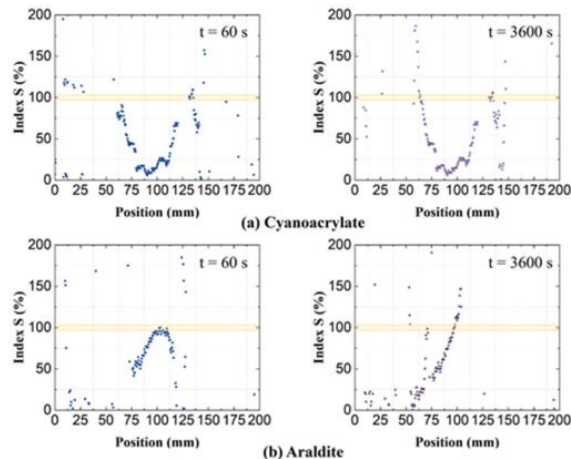


Figure 12. Cont.

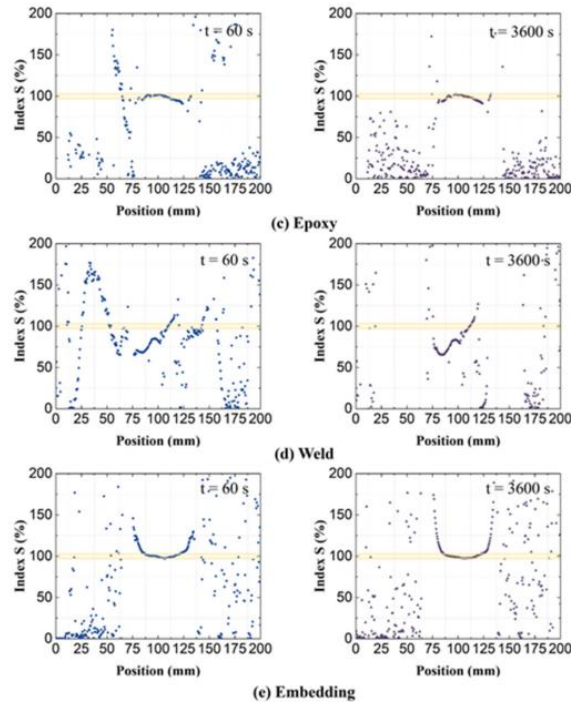


Figure 12. Index S , the quotient of normalized residual strains and normalized relative- t_2 creep strains, on PA6 substrates.

Clear correlations between residual strains and creep strains were only witnessed for the ‘Epoxy’ and ‘Embedding’ attachments. As discussed in Section 4.1.1, the residual strains of ‘Cyanoacrylate’, ‘Araldite’, and ‘Weld’ attachments are heavily affected by local (thermal) effects in the attachment process. Fluctuations in their residual strain profiles are more random due to these local variations.

4.1.3. Variability of Creep Strains

As seen from the strain data presented in Section 3, all fiber attachment methods produce somewhat nonuniform spatial strains along the OF sensor length. A nonuniform bondline induces fluctuations in the profiles of the measured strains. Figure 13 compares the coefficient of variation (CV) from different attachment methods. These CVs are calculated from spatial relative- t_2 OF strains (SD can be seen as error bars in Figures 5 and 7). Well-controlled attachment methods (e.g., ‘Cyanoacrylate’, by virtue of low viscosity) show lower variability than hand-controlled and more viscous attachments (‘Araldite’ and ‘Weld’). Machine-controlled 3-D printed ‘Embedding’ attachment has the lowest strain variability. The initial CV of GF/Epoxy in Figure 13a shows very large values compared to the CV obtained later in the creep test. As a ratio (SD divided by the mean), CV is affected by the variations in SD as well as in the average value. Specifically, when the average value is very small, a situation similar to division by zero is approached. As seen in Figures 5 and 7, the initial average strain of the GF/Epoxy specimens is ca. $5 \mu\epsilon$, while it is ca. $340 \mu\epsilon$ in PA6 specimens. Apart from these initial high CV values, Figure 13a,b show that CV of the OF spatial strain profile remains nearly constant through the 1 h creep

test. This means, SD increases in constant proportion to the mean for all tested attachment types.

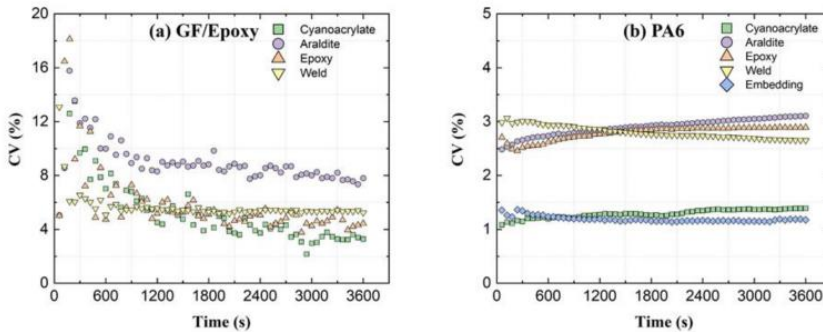


Figure 13. OF strain variability expressed by the coefficient of variation (CV) vs. time for different attachment methods.

4.2. The Accuracy of OBR Strains

4.2.1. The Choice of ROI (and Disturbed End Regions)

In practical SHM applications, the strain value from the OF sensor is used to assess the strain state of the host component. However, disturbed strain regions at the ingress/egress of the optical fiber attachment have to be excluded from the strain analysis. These disturbed regions are present at every transition between a free and an attached or embedded optical fiber (including when OF passes through a void inside the structure). Only the middle of the fiber contains ROI suitable for interpreting substrate strains. Thus, especially for short OF attachment lengths, the selection of ROI (or alternatively, the ingress/egress lengths) becomes important for accurate strain analyses. The choice of ROI defines how much of the attachment ends are discarded. It filters out inaccurate ingress and egress regions of the attached OF. Throughout previous analyses, the ROI was defined as the central 40 mm for GF/Epoxy and PA6 specimens. This choice is hereby scrutinized. The influence of the ROI length on averaged relative- t_2 OF strains is shown in Figure 14 for GF/Epoxy and in Figure 15 for PA6 substrates. Average strains at 60 and 3600 s were calculated using different ROIs. Average strains first increase with decreasing ROI, and then remain constant on a plateau when the disturbed ends become fully excluded. As evident, previously selected ROIs of 40 mm are positioned at the beginning of the plateaus and were indeed a good choice to achieve accurate average strain values for both the GF/Epoxy and PA6 specimens.

Disturbances in the ingress and egress regions are partially caused by averaging errors from the OBR post-processing, as discussed in Section 2.3. Experience with OBR strain measurements shows that steep strain gradients tend to produce more measurement noise and thereby also play a role in the size of these disturbed regions. The most accurate way to identify disturbed regions from experimental data is by parametric analysis, similar to Figures 14 and 15. Alternatively, disturbed lengths l (Figure 3b) can be identified manually/visually directly from strain profiles. Using this manual approach, disturbed region lengths l were read from relative- t_2 strain profiles at 3600 s as shown in Table 4. For GF/Epoxy, lengths l varied around 10 mm, when the gauge length (GL) for the virtual OBR sensor was selected as 10 mm. When the gauge length GL was set to 20 mm, the disturbed region lengths also doubled. For PA6, the disturbed region length l was much less predictable, typically exceeding the selected gauge length GL. The strain profiles of the PA6 specimens were inconsistent and fluctuations on the strain profiles make an accurate length l difficult to extract. It shows that the disturbed region length l cannot be simply

defined equal to the OBR gauge length. Additionally, a more thorough analysis without human inspection would be preferred.

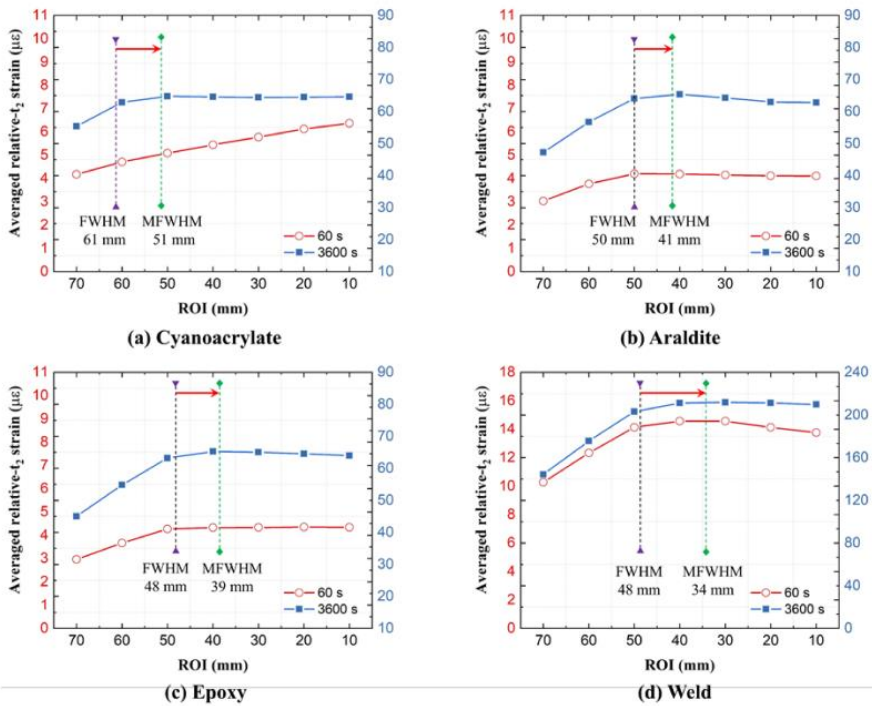


Figure 14. Average relative- t_2 OF strains as a function of the region of interest (ROI) length on GF/Epoxy specimens.

Table 4. The influence of the OBR virtual gauge length (GL) on disturbed region lengths l , at $t = 3600$ s (all dimension in mm).

Specimen, Attachment Method	Actual OF Attachment Length	Disturbed Ingress Region l		Disturbed Egress Region l	
		OBR	OBR	OBR	OBR
		GL = 10	GL = 20	GL = 10	GL = 20
GF/Epoxy, Cyanoacrylate	70	9.0	17.5	8.0	19.0
GF/Epoxy, Araldite	51	9.5	16.5	9.0	16.5
GF/Epoxy, Epoxy	53	8.0	17.5	11.5	22.0
GF/Epoxy, Weld	55	14.5	16.5	9.0	19.0
PA6, Cyanoacrylate	77	22.0	29.5	18.5	30.5
PA6, Araldite	54	15.0	23.5	28.0	30.5
PA6, Epoxy	58	11.0	25.0	10.0	24.0
PA6, Weld	59	16.0	16.5	14.0	16.5
PA6, Embedding	64	24.0	31.5	13.0	25.0

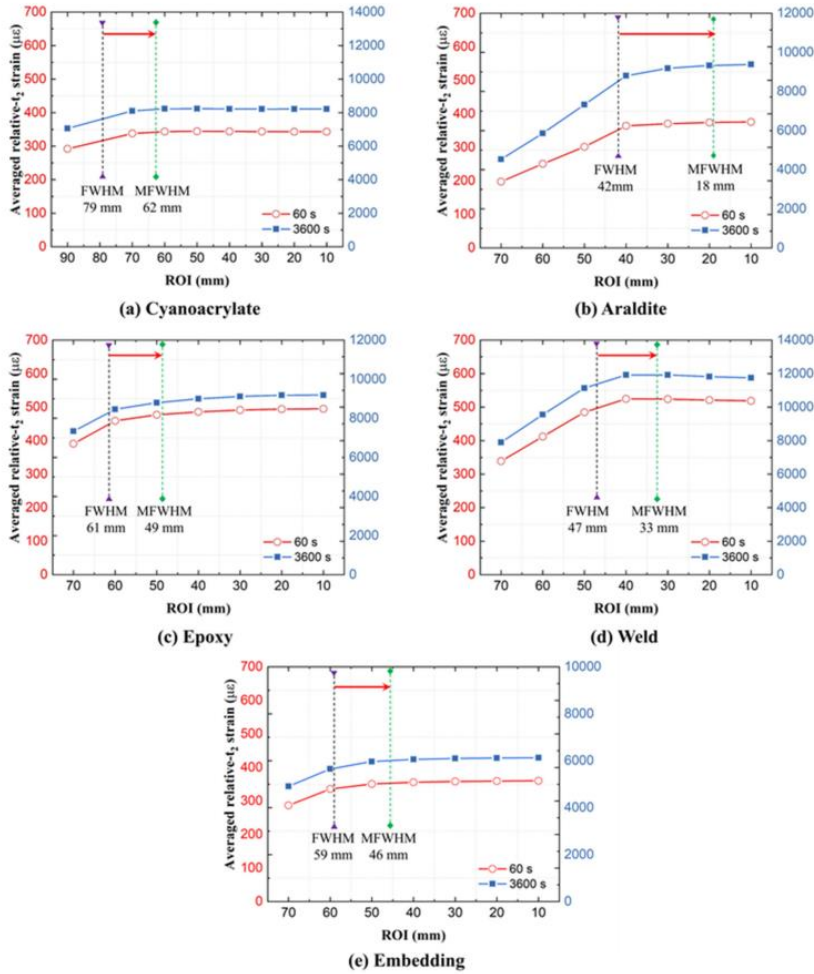


Figure 15. Average relative-t₂ OF strains as a function of the region of interest (ROI) length on PA6 specimens.

Automated ROI definition can be devised based on the full width half maximum (FWHM) concept for the spatial strain curve as shown in Figure 16. FWHM is the width of the strain curve measured between two strain points, which are at half of the maximum peak value. FWHM calculation is easy to automate. As shown in Figures 14 and 15, a gap still exists between the FWHM-based ROI and the plateau of the strain-ROI curve. So, the FWHM, when used directly as ROI, is inaccurate. As described in Figure 16, the modified FWHM (MFWHM)-based automated ROI can be more accurate, defined by:

$$ROI = EL - 4 \times I_1 \tag{2}$$

where EL is the embedding length of DOFS and I_1 is the gap between the EL and FWHM at one end of the curve. Hereby, EL is defined as the length of the strain curve measured

between the two strain points where the strain first exceeds $10 \mu\epsilon$. In this method, the length difference between the automated ROI (i.e., MFWHM) and the regular FWHM is assumed to be $2l_1$. As shown in Figures 14 and 15, using MFWHM provides a fairly accurate alternative for the ROI selection.

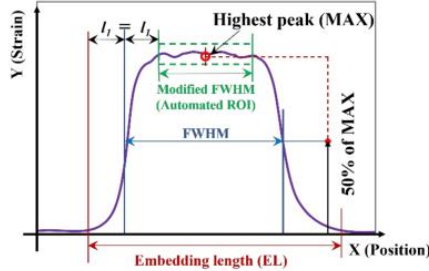


Figure 16. Automated ROI definition using regular and modified FWHM.

4.2.2. The Difference between OBR and Contact Extensometer Strains

The strain measurement accuracy of the attached OF can be determined by comparing averaged OBR strains to contact extensometer strains along the same specimen length. The difference between OBR and extensometer strains can be defined by two sets of coefficients $C(t)$:

$$C_A(t) = |\epsilon_{OBR}(t) - \epsilon_{EXT}(t)| \tag{3}$$

$$C_R(t) = \left| \frac{\epsilon_{OBR}(t) - \epsilon_{EXT}(t)}{\epsilon_{EXT}(t)} \right| \times 100\% \tag{4}$$

where coefficients C_A and C_R denote absolute and relative differences, respectively. Coefficient C_R is similar to the strain transfer coefficient from the substrate to the OF, provided that the contact extensometer strain is equal to the substrate strain. Variables $\epsilon_{OBR}(t)$ and $\epsilon_{EXT}(t)$ are relative- t_2 strains from the OBR and extensometer as shown in Figures 5 and 7 at times $t = 600, 1200, 1800, 2400, 3000,$ and 3600 s, respectively. The calculated coefficients $C(t)$ for all attachments on the GF/Epoxy and PA6 substrates are shown in Figure 17.

For GF/Epoxy specimens, only very low absolute strain differences (ca. $3\text{--}12 \mu\epsilon$) are reported in Figure 17a. Since Equation (3) is the numerator for Equation (4), and its value remains nearly constant while the denominator increases with creep, the relative difference C_R as a consequence shows a decreasing trend for GF/Epoxy in Figure 17c. The low-viscosity ‘Cyanoacrylate’ attachment gave the smallest difference coefficients C , and thereby the best agreement between OBR and extensometer strains. The manually applied ‘Weld’ attachment, on the other hand, showed the largest difference between the OBR and extensometer strains.

For PA6 substrates, much higher absolute strain differences C_A (between 13 and $650 \mu\epsilon$) can be noted from Figure 17b. The absolute strain difference increases similar to the measured strains themselves, as seen in Figure 7. This causes a nearly constant relative strain difference C_R as calculated in Figure 17d. The ‘Embedding’ attachment displays excellent agreement and nearly identical values from two strain measurement methods. Again, the manually applied ‘Araldite’ attachment gives the largest difference between the OBR and extensometer strains.

In summary, all relative differences C_R between the extensometer and OBR strains are observed to either remain constant or decrease with time. The best agreement between the OBR and extensometer strains is achieved by the automated ‘Embedding’ and low-viscosity ‘Cyanoacrylate’ attachments. The worst agreement of strains is obtained for the manually controlled ‘Araldite’ and ‘Weld’ attachments.

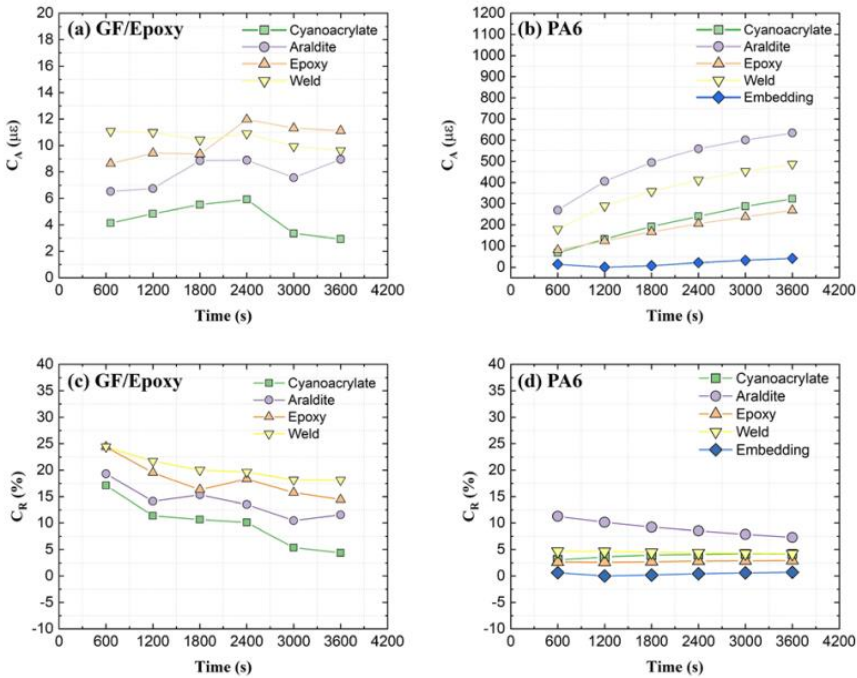


Figure 17. Difference coefficients $C(t)$ between OBR and extensometer strains.

5. Conclusions

1. As experimentally demonstrated, optical fiber sensors can be used to measure residual strains created by their own attachment process. The mechanisms of residual strain creation were briefly discussed. Correlations between residual strain and creep strains were observed for 'Epoxy' and 'Embedding' attachment methods.
2. Creep strains up to 3% were measured from OFs fixed with five different attachment methods on three types of substrate specimens.
 - Unreinforced PA6 and GF/Epoxy substrates gave a satisfactory agreement between the optical fiber and contact extensometer strains. The relative difference between OF strains and contact extensometer strains either remained constant or converged towards more similar values over time.
 - Negligible creep strains of steel specimens were accurately measured only by OFs, as the contact extensometer displayed artificial warmup drift.
3. Problem areas for using DOFS over short attachment lengths are identified as follows.
 - Unreliable strain data occurs in the ingress and egress regions of the fiber.
 - Strain fluctuations along the OF length are caused by nonuniformities created in the fiber attachment process.
4. Optical fiber attachment methods were compared from the aspects of residual strains and creep strain development. The main takeaways from the experiments are summarized in Table 5. The best performing attachments were 'Cyanoacrylate' and 'Embedding'. Concluding from these qualitative observations, an optimal optical fiber attachment method:

- Is machine-controlled, e.g., utilizes an attachment process, such as 3-D printing, to achieve a uniform residual strain profile and a high strain transfer coefficient;
 - Uses a low-viscosity adhesive, such as cyanoacrylate, for the same reasons as previous;
 - Aims to minimize residual strains, e.g., by using room temperature curing or annealing.
5. Practical and easily automated approaches can be devised for defining the disturbed ingress/egress region lengths for strain measurement. For example, the modified FWHM approach gives fairly accurate estimations.

Table 5. Qualitative comparison of DOFS attachment methods on three different substrates.

Attachment Method	Substrate	Residual Strain (Figure 10)	Creep Strain Variability (Figure 13)	Creep Strain Accuracy (Figure 17)	Attachment Process
'Cyanoacrylate'	GF/Epoxy	Low/Nonuniform	Low	High	Manual
	PA6	Low/Nonuniform	Low	Medium	Manual
	Steel	Low/Nonuniform	-	-	Manual
'Araldite'	GF/Epoxy	Low/Nonuniform	High	Medium	Manual
	PA6	Low/Nonuniform	High	Low	Manual
	Steel	Low/Nonuniform	-	-	Manual
'Epoxy'	GF/Epoxy	Medium/Uniform	Low	Low	Manual
	PA6	High/Uniform	High	Medium	Manual
	Steel	Medium/Uniform	-	-	Manual
'Weld'	GF/Epoxy	Medium/Nonuniform	Low	Low	Manual
	PA6	High/Nonuniform	High	Medium	Manual
	Steel	Medium/Nonuniform	-	-	Manual
'Embedding'	GF/Epoxy	-	-	-	-
	PA6	High/Uniform	Low	High	Automated
	Steel	-	-	-	-

Author Contributions: Conceptualization, S.W. and K.L.; methodology, S.W., E.S. and K.L.; validation, S.W.; formal analysis, S.W.; investigation, S.W.; resources, K.L.; writing—original draft preparation, S.W.; writing—review and editing, E.S. and K.L.; visualization, S.W.; supervision, K.L.; project administration, K.L.; funding acquisition, K.L. All authors have read and agreed to the published version of the manuscript.

Funding: This project was partially funded by the Fuel Cells and Hydrogen 2 Joint Undertaking under grant agreement No. 826262, <https://thor-fch2.eu/> (accessed on 1 October 2021).

Data Availability Statement: Regarding raw data availability, please contact the authors.

Conflicts of Interest: The authors declare no conflict of interest.

Appendix A. Distributed Strain Sensing System

As shown in Figure A1, the distributed strain sensing system consists of a distributed optical fiber sensor (DOFS), a PC, an optical fiber switch, and an interrogator device. The DOFS is obtained by splicing a data transfer cable to a sensing optical fiber. The sensing fiber section is a 1-m-long single mode fiber with an operating wavelength of 1550 nm. The fiber SMB-E1550H was purchased from OFS Fitel. It is a silica/silica/polyimide fiber with a core diameter of 6.5 μm , a cladding diameter of 125 μm , and a coating diameter of 155 μm . The data cable is 1.5 m long, reinforced with a rubber jacket, and ends with a pigtail. All DOFS are first connected to an optical fiber switch and then to the Optical Backscattering Reflectometer OBR 4600 from Luna Instruments. OBR 4600 measures Rayleigh backscatter over the full length of the DOFS. Detailed technical parameters of the OBR 4600 device are listed in Table A1. During the measurement procedure, a laser source sends the incident light through the OF, and subsequently Rayleigh backscattering

occurs along the entire fiber. Changes on the fiber, such as strain and temperature, induce a frequency shift to the reflected light spectrum. These Rayleigh backscattering spectral shifts are measured and scaled to give distributed temperature or strain measurements with a high spatial resolution.

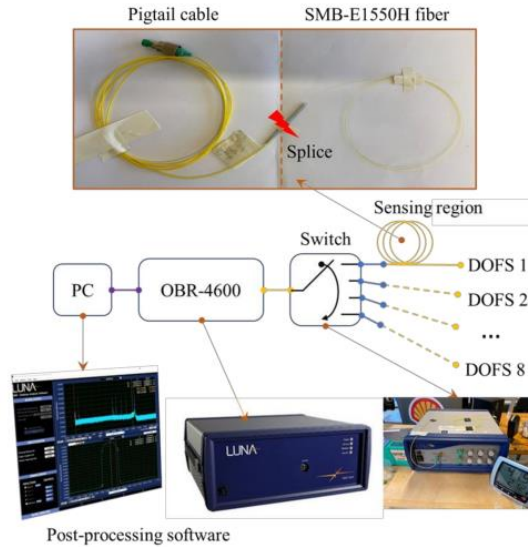


Figure A1. Distributed strain sensing system.

Table A1. Specifications of the OBR 4600 device.

Laser	Tunable Laser Source (TLS)
Wavelength Range	1525–1610 nm
Internal laser module maximum rated output power	10.0 mW
Standard mode	30 m/70 m
Extended mode	2000 m
Scan time (30 m mode)	3 s
Sensitivity	−130 dB
Dynamic range	80 dB
Spatial resolution (30 m mode)	20 μm
Strain resolution	±1.0 με
Temperature resolution	±0.1 °C

Appendix B. Uncertainties of Contact Extensometer Strains

A small load was applied on steel specimens. Uniform stress in the gauge region of the steel dogbone was estimated as 46 MPa, much smaller than its yield strength of 250 MPa. Thus, the measurement should display linear elastic behavior and no rise in strain during one hour of room temperature creep. As evident from Figure 9, all strain-time curves measured by the OBR fluctuate around zero. The extensometer, however, showed increasing strains before ca. 1500 s, which then remained flat after 1800 s. This deviation of extensometer strains from linear elastic behavior (i.e., near-zero strain values) was unexpected.

One possible reason is the warmup drift [21]. When the extensometer is first powered, the flow of current generates heat. This heat produces a small artificial strain drift. After the temperature of the extensometer stabilizes, the warmup drift will also stabilize. The

process is affected by time, excitation voltage, and room temperature. The warmup drift effect was replicated for the used extensometer in additional proof-of-concept experiments, e.g., as shown in Figure A2. This warmup drift also probably contributed to the small but consistent strain difference between the OBR and extensometer strains for the GF/Epoxy specimens (Figures 4 and 5). The presence of warmup drift is much less consequential for PA6 specimens since their strain values in Figures 6 and 7 were orders of magnitude higher.

Figure A3 suggests a few other reasons that can potentially induce measurement errors for the contact extensometer. The trapezoid cross-sectional profile of the steel specimen was created by water jet cutting. The knife-edges were positioned on the canted and rough edge surfaces and then fixed by rubber bands. During the test, the extensometer might rotate slightly on the edge of the specimen. Local yielding may also happen at the contact points of the knife-edges. Attaching the contact extensometer knives on the canted and narrow edges of the steel specimens is not the best measurement practice.

A stringent reasoning of why small creep strains were measured by the contact extensometer, as witnessed in in Figure 9, cannot unfortunately be provided after the testing was finished. Warmup drift is likely the biggest contributing factor. Possible misalignment and contact imperfections at the knife-edges can also contribute to measurement uncertainties. However, these effects should rather reduce the measured strain values. For the steel specimens of this creep experiment, the OFs clearly provide more accurate strain data (in agreement with expectation) compared to the contact extensometer strains.

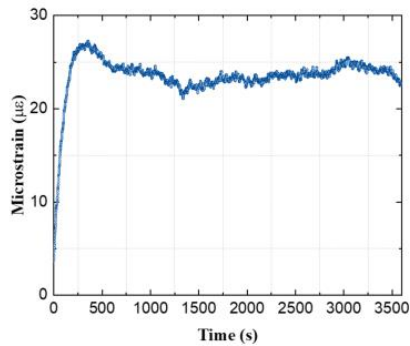


Figure A2. Strain from the contact extensometer on a steel specimen (unloaded, hanging by a hook) at room temperature.

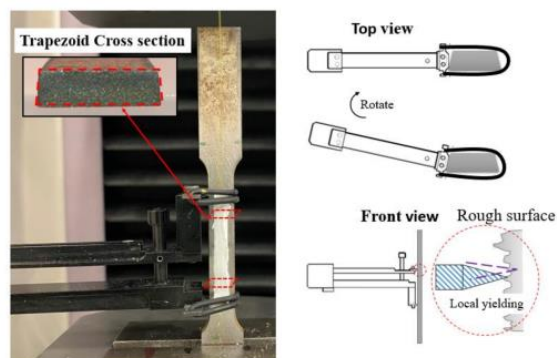
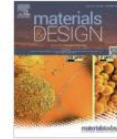


Figure A3. Other possible causes for measurement errors for the contact extensometer.

References

- Betz, D.C.; Staudigel, L.; Trutzel, M.N.; Kehlenbach, M. Structural monitoring using fiber-optic Bragg grating sensors. *Struct. Health Monit.* **2003**, *2*, 145–152. [CrossRef]
- Rodriguez, G.; Casas, J.R.; Villalba, S. SHM by DOFS in civil engineering: A review. *Struct. Monit. Maint.* **2015**, *2*, 357–382. [CrossRef]
- Hoult, N.A.; Ekim, O.; Regier, R. Damage/Deterioration Detection for Steel Structures Using Distributed Fiber Optic Strain Sensors. *J. Eng. Mech.* **2014**, *140*, 04014097. [CrossRef]
- Bin Lin, Y.; Chang, K.C.; Chern, J.C.; Wang, L. Packaging methods of fiber-Bragg grating sensors in civil structure applications. *IEEE Sens. J.* **2005**, *5*, 419–424. [CrossRef]
- Yang, J.; Yuan, L. Package and installation of embeddable fiber optic sensors. *Opt. Lasers Eng.* **2009**, *47*, 1085–1090. [CrossRef]
- Meng, L.; Wang, L.; Hou, Y.; Yan, G. A Research on Low Modulus Distributed Fiber Optical Sensor for Pavement Material Strain Monitoring. *Sensors* **2017**, *17*, 2386. [CrossRef] [PubMed]
- Sun, A.; Qiao, X.G.; Jia, Z.A.; Li, M.; Zhao, D.Z. Study of simultaneous measurement of temperature and pressure using double fiber Bragg gratings with polymer package. *Opt. Eng.* **2005**, *44*, 034402. [CrossRef]
- Jockwer, R.; Grönquist, P.; Frangi, A. Long-term deformation behaviour of timber columns: Monitoring of a tall timber building in Switzerland. *Eng. Struct.* **2021**, *234*, 111855. [CrossRef]
- Montesano, J.; Selezneva, M.; Poon, C.; Fawaz, Z.; Behdinan, K. Application of fiber optic sensors for elevated temperature testing of polymer matrix composite materials. *Sci. Eng. Compos. Mater.* **2011**, *18*, 109–116. [CrossRef]
- Li, W.; Cheng, C.; Lo, Y. Investigation of strain transmission of surface-bonded FBGs used as strain sensors. *Sens. Actuators A Phys.* **2009**, *149*, 201–207. [CrossRef]
- Saeter, E.; Lasn, K.; Nony, F.; Echtermeyer, A.T. Embedded optical fibres for monitoring pressurization and impact of filament wound cylinders. *Compos. Struct.* **2019**, *210*, 608–617. [CrossRef]
- Wosniok, A.; Skoczowsky, D.; Schukar, M.; Pöttsch, S.; Pöttschke, S.; Krüger, S. Fiber optic sensors for high-temperature measurements on composite tanks in fire. *J. Civ. Struct. Health Monit.* **2019**, *9*, 361–368. [CrossRef]
- Tsukada, T.; Minakuchi, S.; Takeda, N. Assessing residual stress redistribution during annealing in thick thermoplastic composites using optical fiber sensors. *J. Thermoplast. Compos. Mater.* **2018**, *33*, 53–68. [CrossRef]
- Arhant, M.; MEEK, N.; Penumadu, D.; Davies, P.; Garg, N. Residual Strains using Integrated Continuous Fiber Optic Sensing in Thermoplastic Composites and Structural Health Monitoring. *Exp. Mech.* **2017**, *58*, 167–176. [CrossRef]
- Wang, S.; Lasn, K.; Elverum, C.W.; Wan, D.; Echtermeyer, A. Novel in-situ residual strain measurements in additive manufacturing specimens by using the Optical Backscatter Reflectometry. *Addit. Manuf.* **2020**, *32*, 101040. [CrossRef]
- Biswas, P.; Bandyopadhyay, S.; Kesavan, K.; Parivallal, S.; Sundaram, B.A.; Ravisankar, K.; Dasgupta, K. Investigation on packages of fiber Bragg grating for use as embeddable strain sensor in concrete structure. *Sens. Actuators A Phys.* **2010**, *157*, 77–83. [CrossRef]
- Zhang, J.; de Souza, M.; Creighton, C.; Varley, R. New approaches to bonding thermoplastic and thermoset polymer composites. *Compos. Part A Appl. Sci. Manuf.* **2020**, *133*, 105870. [CrossRef]
- ASTM E8. *Standard Test Methods for Tension Testing of Metallic Materials*; ASTM International: West Conshohocken, PA, UAS, 2016.
- ASTM D638. *Standard Test Method for Tensile Properties of Plastics*; ASTM International: West Conshohocken, PA, UAS, 2010.
- Luna Technologies Inc. *User Guide: Optical Backscatter Reflectometer Model OBR 4600*; Luna Technologies Inc.: Roanoke, VA, USA, 2006; Available online: https://lunainc.com/sites/default/files/assets/files/resource-library/OBR-4600-UG6_SW3.10.1.pdf (accessed on 1 October 2018).
- Epsilon Technologies Corp. *User Guide*. Available online: <https://www.epsilontech.com/understanding-extensometer-warmup-drift/> (accessed on 1 July 2021).

Paper IV



Integration of optical fibre sensors by material extrusion 3-D printing – The effect of bottom interlayer thickness

Shaoquan Wang^{*}, Kaspar Lasn

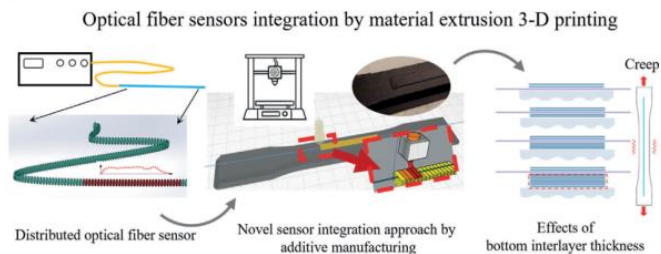
Department of Mechanical and Industrial Engineering, Norwegian University of Science and Technology (NTNU), Richard Birkelands vei 2B, 7491 Trondheim, Norway



HIGHLIGHTS

- A novel 3-D printing based solution for integrating optical fiber sensors into thermoplastic composite structures is proposed.
- A critical variable in this fiber attachment process (and for surface bonding in general) is the bottom interlayer thickness, which was in-situ investigated for the first time.
- Experimentally measured strain transfer coefficients along the optical fiber sensors remained constant under creep loading.
- A simple calculation method that enables to predict the shear lag effect for optical fibre sensors was derived and validated.

GRAPHICAL ABSTRACT



ARTICLE INFO

Article history:

Received 17 February 2022
 Revised 29 June 2022
 Accepted 30 June 2022
 Available online 2 July 2022

Keywords:

Thermoplastic composite
 Optical fibre
 3-D printing
 Structural health monitoring
 Semi-automation

ABSTRACT

Thermoplastic composites are becoming the materials of choice for lightweight structures. Distributed optical fibre sensors can be valuable for structural health monitoring of thermoplastic composites, improving safety against damage and extending the operational life of composite components. However, the practical integration of optical fibres into thermoplastic composites remains still to be solved. To this end, a novel sensor integration approach by 3-D printing is proposed, and mechanical testing is conducted to test its performance. Optical fibres were placed inside thermoplastic embedding elements at controlled interlayer thicknesses (0 to 1.6 mm) from the substrate surface. Self-sensing experiments by optical fibres identified a uniform level of residual strains at $-1600 \mu\epsilon$ from the 3-D printing attachment process. Furthermore, tensile creep testing (up to ca. 1% strain) revealed that distributed strain transfer coefficients for optical fibre sensors remain constant with time. A simple calculation method that accounts for the shear lag effect between the component and optical fibre strains was derived from previous analytical work. This method enables the empirical prediction of strain transfer coefficients for optical fibre surface attachments with arbitrary embedding interlayer thickness.

© 2022 The Authors. Published by Elsevier Ltd. This is an open access article under the CC BY license (<http://creativecommons.org/licenses/by/4.0/>).

1. Introduction

Fibre reinforced thermoplastic composites are becoming more popular over the entire spectrum of industrial and commercial applications. Their success over thermoset composites is attributed

^{*} Corresponding author.

E-mail address: shaoquan.wang@ntnu.no (S. Wang).

<https://doi.org/10.1016/j.matdes.2022.110914>

0264-1275/© 2022 The Authors. Published by Elsevier Ltd.

This is an open access article under the CC BY license (<http://creativecommons.org/licenses/by/4.0/>).

to better recyclability, lower manufacturing cost, and a good impact resistance [1]. Meanwhile, accurate and robust structural health monitoring (SHM) techniques are needed to ensure a safe operational life of thermoplastic composite components. Onboard sensor systems enable online monitoring, early detection of damage, and allow to extend the lifetimes of components based on their actual mechanical performances [2]. Compared to single-point or quasi-distributed fibre optic sensors such as Fibre Bragg Gratings (FBGs), distributed optical fibre sensors (DOFS) are preferred for high spatial resolution SHM of composite structures [3–6].

Any optical fibre (OF) strain sensor needs to be integrated into the composite material so that it deforms together with the component [7]. Thus, the OF performance depends to a large degree on the integration/attachment technique [8–10]. For example, optical fibres can be placed directly inside the composite material, between layers of thermoplastic tapes during the layup, which are then fused together with embedded OFs inside [11]. By using this method, strain from the component is directly transferred to the OF while the surrounding material protects the fibre sensor from the hostile environment [12–14]. However, there are also disadvantages to using this embedding method for OF integration. Voids or resin pockets are sometimes created around the embedded optical fibre which can locally affect the strength of the composite [15]. Embedded optical fibre becomes invisible to the eye and its accurate positioning within the structure is difficult to assess. Furthermore, optical fibres can encounter a high loss in transmitted/reflected signal power from bending at the edges of the laminate, or within the fabric structure which can induce micro-bending. High shrinkage of matrix material brings a birefringence effect to the OFs, leading to distortions of the measured signal spectrum instead of peak shifting [13]. Finally, the OF placement cannot usually be chosen with great flexibility during embedding, e.g. the intended ingress and egress regions may not be compatible with the manufacturing process.

Alternatively to embedding, OFs can also be bonded on the surface of a composite component after completing the manufacturing process [16–18]. Surface-bonding allows for more flexibility in attaching the OFs. It gives better opportunities for retrofitting existing structures with sensors, and for replacing damaged OFs with new ones. A thin bonding element on the surface can be removed or added without affecting the internal structure of the component if broken OFs are to be replaced. Admittedly, the surface-bonding solution has also some disadvantages that impair its suitability for lifetime monitoring of thermoplastic composites. Most structural adhesives are thermosetting polymers, and thermoplastics have poor adhesion with them due to their inherently low reactivity, surface energy and insufficient diffusion between the two materials [19–21]. Thermoset adhesives such as cyanoacrylate are also sensitive to the environment, they can have poor temperature or humidity resistance. Some adhesives need to be cured at a high temperature which is inconvenient and introduces heat into the host structure. Excessive amount of adhesive can induce a non-uniform bonding thickness and thereby a non-uniform strain transfer from the substrate to the surface-bonded sensor [22].

The attachment of optical fibres continues to be a manual process, thereby requiring careful working procedures and highly skilled assemblers. Automated solutions for bonding optical fibre sensors to thermoplastic composite materials have not yet become widespread [14,23]. For example, a semi-automated OF integration method during the braiding process of thermoset composites has been reported [23]. The optical fibre is placed between dry carbon fibre layers, and the bonding of the optical fibre to the composite is achieved later in the resin infusion process. However, this method cannot be directly used for thermoplastic composites. Automated methods are often developed for particular applications, resulting

in lower flexibility in terms of product variety [24]. At the same time automated solutions help to improve product quality and consistency, adding the possibility of producing larger components, reducing material waste, and enabling easier in-process monitoring.

Out of all other alternatives, thermoplastic fusion bonding is perhaps the most practical solution for attaching optical fibre sensors to thermoplastic composites [25]. Additive manufacturing is popular for fabricating small-volume structures with complex structural geometries. Recently, the integration of OFs by 3-D printing has attracted the attention of several researchers. For example, point sensing FBGs have been embedded into metals during fused additive manufacturing (FDM) [26–28]. FBGs have also been embedded into 3-D printed polymer components again by using FDM, as reported by Karalekas et al. [29–31], Leal-Junior et al. [32,33], Manzo et al. [34], Nascimento et al. [28] and Falcetelli et al. [35]. Distributed OF sensors were embedded in titanium parts by Zhou et al. [36] using laser powder bed fusion. Inspired by this work, Wang et al. developed the embedding strategy for distributed OF sensors by in-situ FDM [37]. The most recent investigation by Wang et al. [38] compared different optical fibre surface attachment methods including the in-situ FDM process. Sensor integration attempts by 3-D printing are still in an early stage of research and only a few reference works are available. For embedded optical fibres, the difficulty of strain measurements with low infilling densities has been a typical research topic [32] along with some interest about residual strain measurements [37].

Ideally, strains from the surface bonded OFs should be equal to strains of the host structure. However, strain transfer errors through the attachment layer cannot be fully avoided. Previous researchers have numerically investigated important factors that affect the strain transfer coefficients from the substrate to the adhered FBGs [9,39,40]. The results show that thickness of the interlayer (i.e. bondline thickness between the structure and the OF sensor) is a very important parameter, along with the length of the FBG sensor and the Young's modulus of the attachment layer [39–48]. Correlation between the geometrical parameters of the attachment layer and the strain transfer to the surface-bonded FBGs has been investigated by using analytical models and the FEM [40–45]. On this topic, experimental investigations and the validation of numerical models are much more rare. The influence of bottom interlayer thickness has only been analyzed by numerical simulations thus far, unlike the effects from the Young's modulus and the bonding length, which have also been experimentally investigated [39,40,43,46–48]. The most likely reason is that a consistent OF attachment thickness with prescribed values is difficult to produce by conventional hand-controlled surface bonding methods.

This research proposes a novel solution for semi-automated integration of distributed OF sensors on the surface of thermoplastic composite structures. Single mode optical fibres are in-situ embedded by material extrusion 3-D printing into block-shaped embedding elements on the surfaces of dogbone specimens. Short-fibre reinforced thermoplastic composite is extruded over the OF sensor at a controlled interlayer thickness. Distributed strain sensing system is achieved by using Rayleigh backscattering. Strain measurements by optical fibres are compared to contact extensometer strains in a tensile creep test. An experimental investigation on how the bottom interlayer thickness affects the strain transfer behavior of the DOFS has been carried out.

2. Materials and methods

Before mechanical testing, short carbon fibre reinforced polyamide (CF/PAG) specimens were prepared for the sensor integration

process. These specimens were produced by 3-D printing and the additive manufacturing process was thereafter continued for the OF integration on their surfaces. Optical fibres were placed inside small blocks of extruded thermoplastic called embedding elements, at a controlled thickness from the substrate surface.

2.1. Specimen preparation

Fused Filament Fabrication (FFF) i.e. small scale material extrusion is the most widely used manufacturing process within thermoplastic additive manufacturing. This method is also used by the PRUSA I3 MK3S 3-D printer, which was first employed to build the test specimens, and later for sensor integration purposes. Nylon 6 based composite filament (CF/PA6) from PolyMide (20 wt% chopped carbon fibres) and the dogbone specimen geometry were selected to build the test structure. Dogbone shape is very convenient for realizing a uniform tensile creep loading. A line pattern with 100% infill density and a quasi-isotropic layup sequence [90,45,0,-45]_{4s}, where 0° angle denotes the longitudinal direction of the specimen, were employed to print the test specimens. Remaining printing parameters are detailed in Table 1.

Nylon 6 is known for good mechanical properties and its resistance to non-polar solvents [49]. Still, pure thermoplastic materials are rarely used for load-bearing components, due to their limited stiffness and strength. Composite components typically contain long fibre reinforcements along the main loading directions, which add stiffness, strength, and significantly reduce creep. Today, continuous fibre 3-D printing remains still technically challenging, and short-fibre reinforcements are much more popular with basic FFF printers, producing short-fibre reinforced polymer composites [50]. Creep strains in short-fibre reinforced composites are much higher than in any realistic long fibre reinforced composite laminates. In addition, the simple dogbone geometry allows to easily choose appropriate load levels for accelerated creep strain development compared to typical real-life composite structures. Therefore, compared to practical long-fibre reinforced composite structures, the specimen and the test set-up in this research provide larger/accelerated creep strain values for studying strain transfer from the component to the optical fibre sensor. In principle, similar 3-D printed OF attachments as used here can be realized with any type of thermoplastic composite provided that the matrix material and the resin of the embedding element are able to fuse and form a durable bond. In this sense, the choice of CF/PA6 composite material for this investigation is generic and arbitrary.

2.2. Sensor integration

As shown in Fig. 1, instrumenting the dogbone specimen occurs by means of embedding the optical fibre sensor into a specifically designed block-shaped embedding element. This embedding element is fabricated by the same printer and the same filament material on the surface of the specimen. The integration process is semi-automated and printing parameters are well-controlled. As previous work has showed, 3-D printing based integration process gives a more consistent bondline and promotes good measurement accuracy compared to other practical alternatives [38].

During operation, the 3-D printer is controlled by a modified G-code, which pauses printing after finishing a specific build layer where the optical fibre is integrated, and then resumes printing after a short delay. The OF attachment process (Fig. 1) follows a carefully planned procedure which can be summarized as follows.

- (1) Preparation of two alignment holders with the same height as the finished layer.
- (2) Placing the holders near the two ends of the specimen and placing the fibre on the last layer surface.
- (3) Straightening the OF and fixing it on the alignment holders. Slight tension keeps the OF straight and controls its location on the specimen.
- (4) Finishing the printing process and waiting for the system to cool down.
- (5) Removing the alignment holders and detaching the instrumented specimen from the printing platform.

In order to investigate how the bottom thickness of the attachment layer affects measured strains, four different embedding configurations and a reference attachment with cyanoacrylate glue were realized. Dogbone test specimen is detailed in Fig. 2 and the specifics of embedding elements are further described in Table 2. For DOFS-0 configuration, the optical fibre sensor was placed directly on the surface of the dogbone specimen while the embedding element was printed from two layers of extruded composite. The first layer at 90° and the subsequent layer at 0°, each ca. 0.2 mm thick, were built directly on top of the optical fibre sensor. When the nozzle moves in zigzag motion at 90° relative to the OF, it 'sews' the sensor fibre to the substrate. The fibre becomes fully encapsulated after the 0° layer on top is finished. For DOFS-2 configuration, the fibre was embedded in the middle of the embedding element with two layers below and two layers above the fibre. For DOFS-4, the sensor had four layers below and two layers above it. For DOFS-8, the number of layers under the fibre grew to eight, while still only two layers were printed above the sensor. It must be emphasized that embedding elements DOFS-0 to DOFS-8 were kept identical in other aspects besides the bottom thickness T which varies between different attachment configurations. The influence of bottom interlayer thickness on the strain transfer from the host structure to the DOFS is experimentally investigated. Cyanoacrylate glue attachment DOFS-C was also introduced to this investigation representing the best performing 'traditional' surface attachment for distributed optical fibre sensors [38]. Due to the embedding element, the dogbone specimens were not symmetrical in the thickness direction as shown in Fig. 2. This non-symmetry can introduce additional strain for the tensile experiment, however its effect was assumed small and it was not studied further in this investigation.

2.3. Distributed strain sensing system

Distributed strain sensing system (Fig. 3) consists of an OBR 4600 device, a switch, a DOFS, and a laptop computer for running the hardware and storing the data. The optical fibre interrogator OBR 4600 (Luna Instruments) measures spectral shifts as a function of position along the optical fibre length. It utilizes Rayleigh backscattering to obtain distributed strain measurements. As the

Table 1
3-D printing parameters for CF/PA6 specimens.

Element	Material	Nozzle temperature	Build plate temperature	Printing speed	Cooling	Build- adhesion	Layer height
Dogbone	CF/PA6	290 °C	45 °C	50 mm/s	OFF	Brim	0.2 mm
Embedding element	CF/PA6	300 °C	45 °C	25 mm/s	OFF	None	0.2 mm

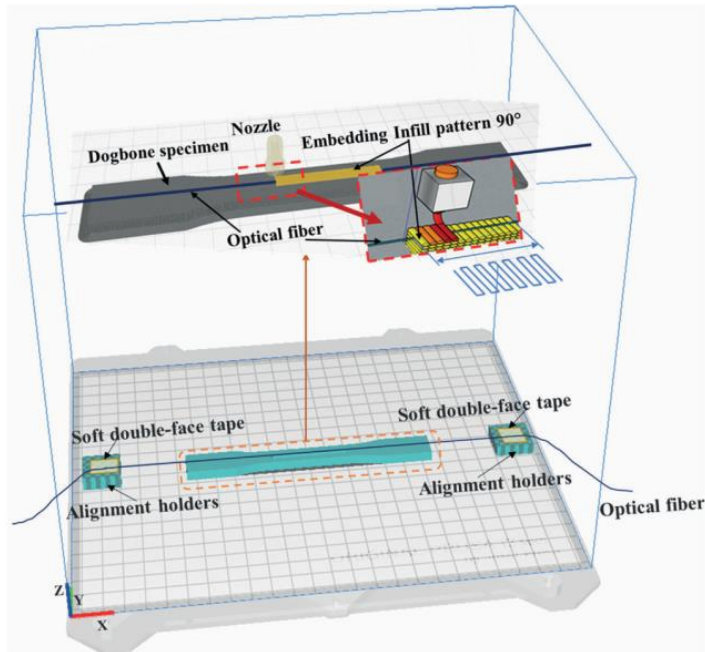


Fig. 1. Illustration of the optical fibre integration procedure.

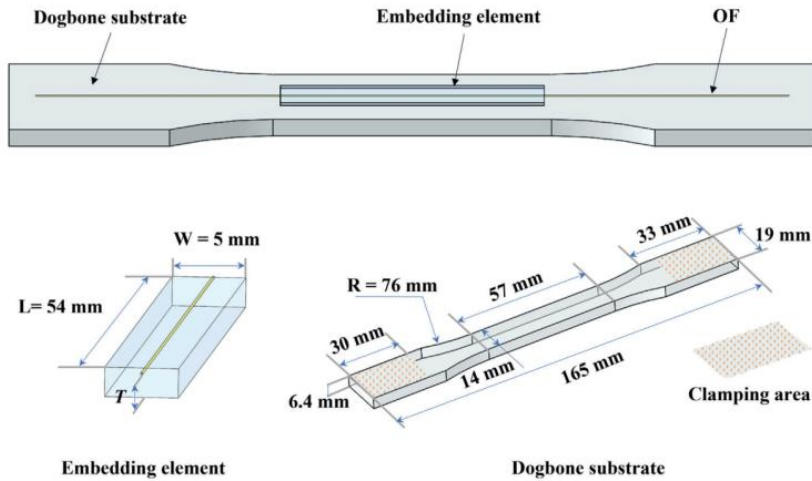


Fig. 2. Prescribed geometrical features of the dogbone specimen and the embedding element. The embedding element is placed symmetrically in the length and width directions, on one side of the dogbone.

optical fibre is mechanically strained, small changes in local Rayleigh backscattering spectra are calculated from the intrinsic variations reflected by the sensor fibre. These spectral shifts

change proportionally to the amplitude of strain. In general, Rayleigh spectral shifts are affected by both strain and temperature. However, all measurements in this investigation are taken

Table 2
Optical fibre attachment configurations.

Attachment configuration	Bottom thickness T		Location of the optical fibre	Layup sequence of the embedding element
	No. of layers	Approximate thickness		
DOFS-0	0	less than 0.1 mm		[OF 90,0]
DOFS-2	2	0.4 mm		[90,0 OF 90,0]
DOFS-4	4	0.8 mm		[90,0,90,0 OF 90,0]
DOFS-8	8	1.6 mm		[90,0,90,0,90,0,90,0 OF 90,0]
DOFS-C	N/A	N/A		'Cyanocrylate'

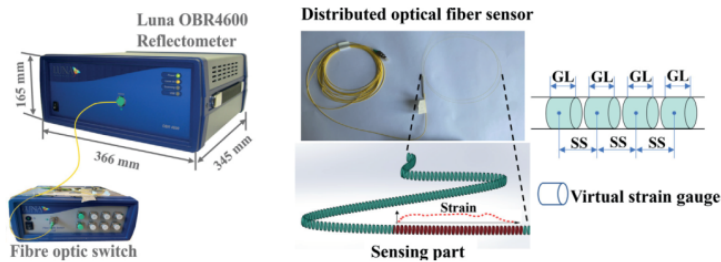


Fig. 3. OBR 4600 interrogator system and the distributed optical fibre sensor (DOFS).

at constant room temperature, so the temperature effects are assumed negligible for all practical purposes.

A single mode fibre SMB-E1550H from OFS Fitel is employed as the distributed optical fibre sensor. The diameters of the core, the cladding, and the coating of this silica/silica/polyimide fibre are $6.5 \mu\text{m}$, $125 \mu\text{m}$ and $155 \mu\text{m}$, respectively. The laser in the OBR 4600 device sends light pulses through the optical fibre, and reflected Rayleigh backscattering spectra are measured by the same interrogator and stored in the computer memory. By comparing the spectra before and after mechanical loading, strains along the optical fibre are calculated. The measurement system offers practical spatial resolutions below 1 cm, a strain resolution of $1 \mu\epsilon$, and a sensing length of ca. 50–70 m [51]. The post-processing configuration with sensor spacing $SS = 0.5 \text{ mm}$, and gauge length of $GL = 5 \text{ mm}$ was chosen as a compromise between high spatial resolution and unwanted noise occurrences. By choosing this 5 mm gauge length value, each virtual strain sensor along the optical fibre has been assigned the typical dimension of a physical strain gauge. Much shorter sensor spacing indicates that virtual strain sensors on the DOFS are overlapping. These two parameters were selected based on quick trials with the test data, and on previous experiences from similar measurements.

2.4. Creep testing

Mechanical testing of dogbone specimens was performed on a MTS Model 42 universal testing machine. The test set-up is shown in Fig. 4(a). Test machine fixtures clamp the ends of the dogbone specimens at a length of 30 mm as seen in Fig. 2. The creep load-time curve is presented in Fig. 4(b). All specimens were initially loaded up to a small pre-load of 15 N, and then further until 1800 N using a cross-head speed of 100 mm/min. This loading produced initial (short-term) strains of approximately $8000 \mu\epsilon$. A short adjustment period of less than 40 s was necessary due to

the control-loop programming before the load settled to a constant value at time t_2 . Creep loading was maintained constant with less than 1 N variation and the test was stopped at 1 h after t_2 .

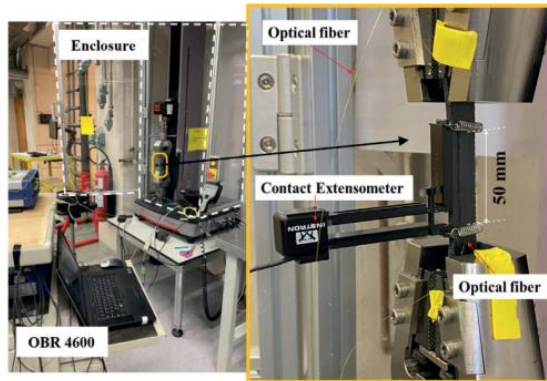
Strains were recorded every 120 s from time t_2 until the end of the experiment. Strain of the dogbone was simultaneously monitored by the DOFS system and the contact extensometer (EXT) set-up, as shown in Fig. 4(a). Extensometer Instron 2620–601 has a gauge length of 50 mm. Its knife edges were mounted on the side of the composite specimen to measure averaged strain along the same region where the DOFS was attached.

Two different baseline references were used to calculate both the DOFS and the contact extensometer (EXT) strains. References taken before the DOFS were fixed on the specimens (i.e. when the fibres were free) are hereby denoted as free-fibre references. Accordingly, strains calculated by comparing to the free-fibre reference are called *relative free-fibre strains*. Another reference was taken at time t_2 of the creep test. Similarly, strains obtained by comparing to the reference at t_2 are called *relative- t_2 strains*. As evident from the load-time curve in Fig. 4(b), relative- t_2 strain represents only the time-dependent portion of strain development during tensile creep, excluding short-term strain from the load ramp-up procedure.

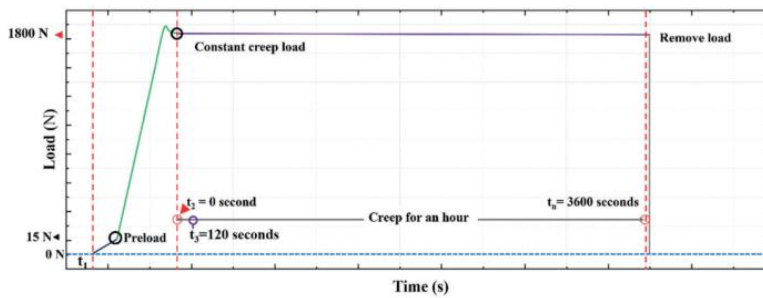
Although only one specimen for each configuration (Table 2) is reported in this paper, two additional specimens were internally fabricated and tested for each configuration. These two additional tests yielded very repeatable results. Therefore, for the sake of clarity in the figures and to reduce the volume of the paper, only one specimen for each test configuration is hereby reported.

3. Results and discussion

As previous investigation has demonstrated [38], the bondline consistency of optical fibre surface attachments varies a lot



(a) Two strain measurement systems



(b) Load-time curve

Fig. 4. Experimental test set-up.

between different attachment methods. Imperfections such as small cracks and the misalignment of the OF can cause noisy data-points and local distortions in the DOFS strain profile. Bottom interlayer thickness between the optical fibre and the substrate surface also holds a high degree of uncertainty. This interlayer thickness is difficult to control in hand-operated optical fibre integration processes. Furthermore, since high-resolution computed tomography equipment is not widespread, measuring the bottom thickness is typically a destructive process that involves cutting, polishing, and optical microscopy. On the other hand, the bottom thickness value can be easily prescribed for a machine-controlled attachment process, e.g. when using the 3-D printing principle. The effect of bottom interlayer thickness on distributed optical fibre strains has not been experimentally investigated until now.

In the following, residual strains and creep strains from varied bottom interlayer thickness optical fibre placements are experimentally compared. Strain curves obtained from 3-D printed OF sensor attachments are also compared to a typical high-accuracy attachment method using cyanoacrylate glue. In addition, OF strains are compared to contact extensometer strains within the same dogbone specimen gauge length.

3.1. Embedded length (EL), region of interest (ROI) and peak value

Along both, load free fibres and strain-loaded optical fibres, a fluctuation of strains within ca. $\pm 5 \mu\epsilon$ is considered a normal level

of noise. It is present everywhere on the DOFS and these small strain variations are usually ignored in the measurement [52]. By measuring the length of the region where strains exceed this normal level of noise, the true embedded length of the fibre (denoted as EL in Fig. 5) can be obtained. The Table in Fig. 5 shows true DOFS embedded lengths (ELs) obtained by measuring where the strain exceeds $\pm 5 \mu\epsilon$ of signal noise, from Fig. 6 (a)-(d). The ELs for DOFS-0 to DOFS-8 were all prescribed for 3-D printing as 55 mm. The ELs obtained from residual strain values vary within 53.0 ± 5 mm and 58.5 ± 5 mm. Considering the size of the extrusion bead, the tolerances of the specific printer, and the virtual DOFS gauge length of 5 mm (which is assumed to govern the error [38]), this is a good agreement between the design aim and the actual realized embedded length of the optical fibre sensor.

As Fig. 6 and further strain graphs show, in practical OBR measurements, the strains in the DOFS ingress and egress transition regions are observed to be highly variable. Thus, in order to meaningfully compare mean strains from the OBR measurements to averaged values of extensometer strains, these highly variable disturbed strains at the transition regions must be excluded from the analysis [38,53]. This way, only strains from the central region of the DOFS attachment, with relatively even strain distribution, are averaged to assess the strain state of the host component. This quasi-constant central region symmetric with respect to the length of the specimen, is referred to as region of interest (ROI). As shown in Fig. 5, disturbed regions located at the ingress/egress of the opti-

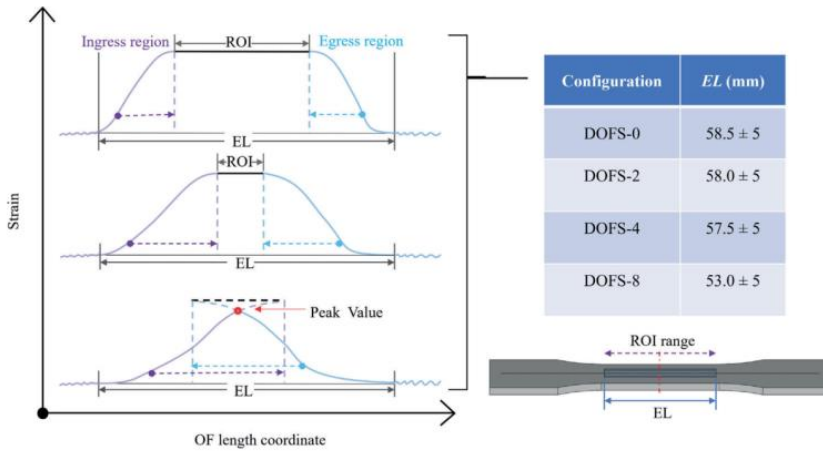


Fig. 5. Illustration of EL, ROI and Peak Value on simplified DOFS strain curves. The EL values in the Table are obtained from residual strain curves after 3-D printing (Fig. 6).

cal fibre attachment, define a transition between a free and an attached optical fibre. In the usual analysis, strains from the ROI are averaged when interpreting spatial strain curves from the DOFS. However, as illustrated in Fig. 5 and exemplified with measured strain curves later, with increasing the length of disturbed regions, which occurs with increasing bottom interlayer thickness, the central region forming the ROI becomes shorter or even disappears. In this case, the Peak Value can be used as an alternative characteristic or metric for DOFS strains.

3.2. Residual strains from the attachment process

During the optical fibre attachment process, residual strains can be built into the host structure of the optical fibre sensor. Residual strains are created from changes in the material constitution (such as cure shrinkage of thermosets and changes in crystallinity of thermoplastics), and from physical volumetric shrinkage when the hot material cools down to room temperature. Residual strains and corresponding residual stresses remain 'frozen in' inside the component without any external mechanical loading. When measuring residual strains with optical fibres, the pre-attachment free fibre is taken as the reference state, and the load free room temperature condition after the fibre integration as the measurement state. That is, relative free-fibre strain is measured after the attachment process is finished.

As defined in Table 2, the DOFS were attached according to four embedding configurations and were also bonded by a cyanoacrylate glue as the control specimen. Residual strain distributions from the DOFS integrated with these five configurations are shown in Fig. 6. The profiles from 3-D printed attachments in Fig. 6(a)-(d) display very similar bathtub shapes with occasional outliers in the ingress/egress regions. In contrast, residual strains from the cold-curing cyanoacrylate attachment DOFS-C (Fig. 6(e)) are much smaller and drift up and down chaotically along the embedded DOFS length. Fig. 6(f) compares the mean values, standard deviations (SD) and the coefficient of variation (CV) for attachments DOFS-0 to DOFS-8. Mean values and SDs are calculated from spatial residual strains within the ROI = 40 mm as shown in Fig. 6(a)-(d). CV is the ratio of SD to the absolute value of the mean. The mean values of residual strains for DOFS-0 to DOFS-8 vary within 1500

$\mu\epsilon$ and 1750 $\mu\epsilon$ in compression and the CVs range from ca. 2.0% to 5.5%. No monotonic trend with increasing embedding bottom thickness was observed for different attachment configurations. The mean values of residual strains turn out to be independent of the small variation in embedding bottom thickness.

In summary, all 3-D printed attachment configurations produced nearly uniform compressive residual strains of ca. 1600 $\mu\epsilon$ along the OF sensor length. These strains are created by the cooling shrinkage of the polymer melt together with a few layers of re-heated substrate material. In comparison, the tiny residual strains from the cyanoacrylate glue (between $\pm 70 \mu\epsilon$) were created in a fully room-temperature process, by a combination of locally variable compressive shrinkage of the glue and a small tensile pre-stretch applied by hand, when aligning the fibre during the attachment process [38]. This resulted with a random variation of small strains along the optical fibre length.

3.3. Creep strain analysis

Many structural components are monitored under long-term loading conditions. To understand time-dependent strain transfer from the host structure to the surface bonded optical fibre better, uniaxial tensile creep testing was carried out with dogbone specimens. Throughout creep loading, strains within the specimen gauge region were measured with the attached DOFS and the contact extensometer (EXT) simultaneously. This investigation focuses on time-dependent strain development, thereby discarding the initial short-term strains. Relative- t_2 strains of the DOFS and the extensometer were recorded. The influences of time and embedding bottom thickness T on distributed strain development were experimentally investigated.

3.3.1. Relative- t_2 creep strains

Fig. 7(a), (d), (g), (j) show relative- t_2 spatial strains from the DOFS attached by 3-D printing with different embedding bottom thicknesses. For comparison, Fig. 7(m) shows relative- t_2 strains when using the traditional cyanoacrylate glue attachment. Note that the vertical axis range is the same for all strain curves on Fig. 7. Relative- t_2 strains from different bottom thickness configurations show distinctly different spatial distribution patterns. For

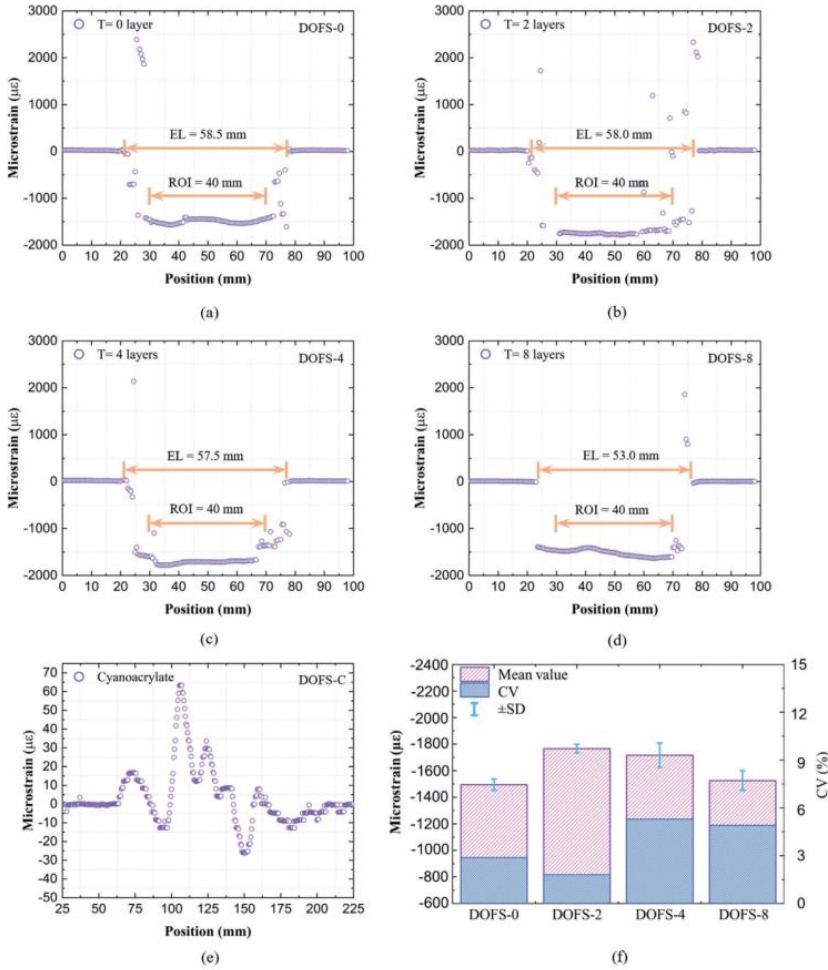


Fig. 6. DOFS measured residual strains for different attachment configurations.

example, DOFS-0 and DOFS-C show a spatial strain distribution again similar to a 'bathtub'. Strain values increase gradually in the ingress region, decrease gradually in the egress region, and hold a nearly constant plateau value in the middle. By increasing the embedding bottom thickness, the length of the plateau however shortens (DOFS-2) and finally disappears (DOFS-4 and DOFS-8). The shape of the spatial strain curve begins to display a peak where the plateau used to be. With the creep time increasing, relative- t_2 strains of the DOFS also keep on increasing. At first sight, no significant distortions emerge on the strain profiles, indicating no cracking or delamination in the specimen or at the optical fibre/matrix interface during creep.

Fig. 7(b), (e), (h), (k), (n) show temporal average relative- t_2 strains and peak value strains from all attachments, using the data

over the gauge length of the contact extensometer, i.e. ROI = 50 mm. As seen from the spatial strain plots, this ROI includes transition regions at the ingress/egress of the optical fibre for all types of attachments. Strain measurements from the attached DOFS are compared to the EXT strains from the contact extensometer. The difference between DOFS strains and EXT strains is further elaborated in Fig. 8(c), (f), (i), (l), (o) by calculating absolute differences $C_A(t)$ and relative differences $C_R(t)$, as defined by Eqs. (1) and (2).

$$C_A(t) = |e_{DOFS}(t) - e_{EXT}(t)| \quad (1)$$

$$C_R(t) = \left| \frac{e_{DOFS}(t) - e_{EXT}(t)}{e_{EXT}(t)} \right| \times 100\% \quad (2)$$

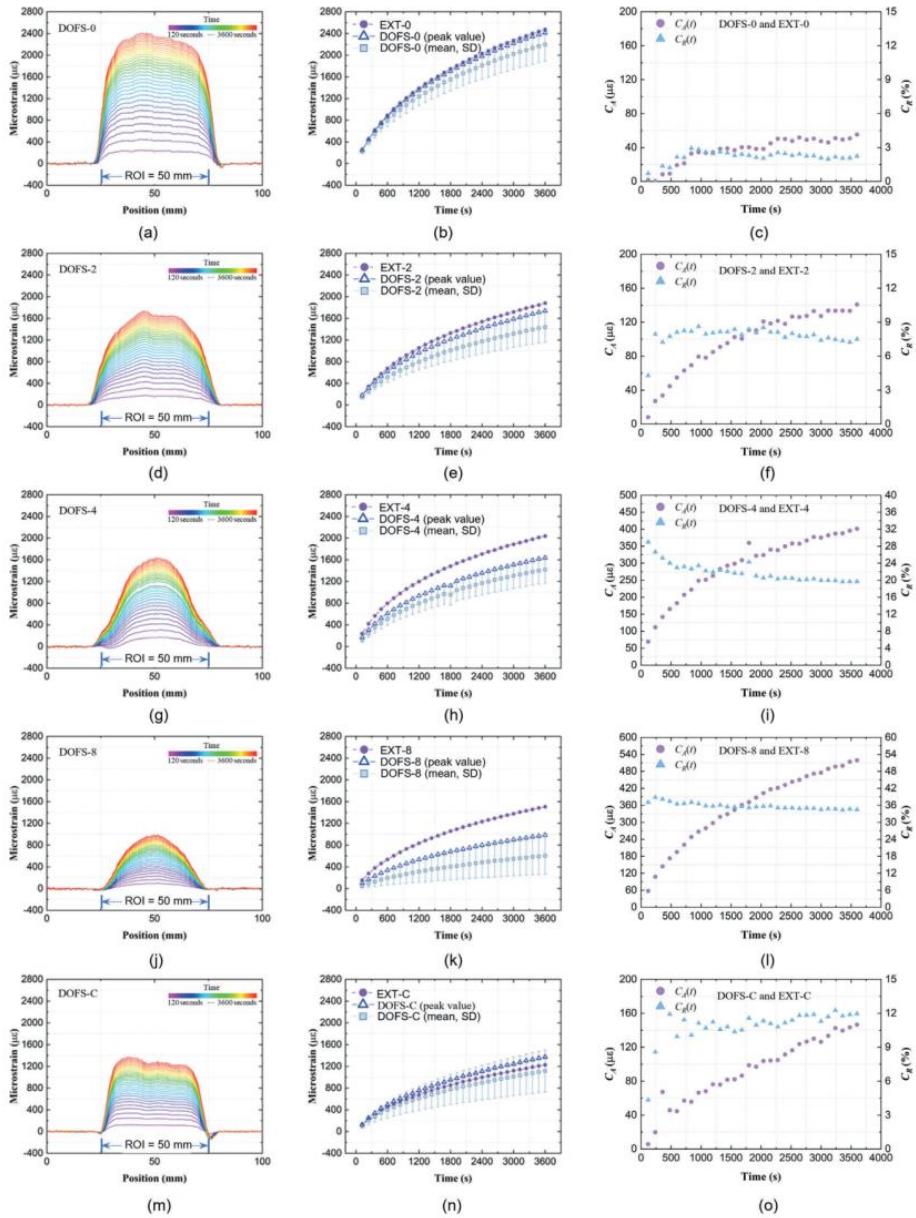


Fig. 7. Relative- t_2 creep strains from the DOFS and the contact extensometer (EXT).

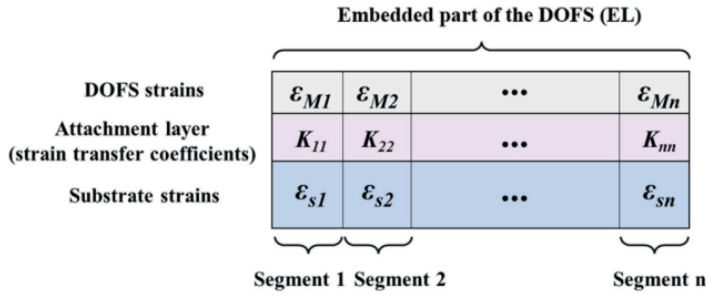


Fig. 8. Discretization of the substrate/attachment/DOFS structure.

In these Equations, $\epsilon_{EXT}(t)$ denotes relative- t_2 strains from the extensometer, while $\epsilon_{DOFS}(t)$ are defined as the peak values of the DOFS strain curves within the ROI.

The thinnest 3-D printed attachment DOFS-0 and the cyanoacrylate glue display the best agreement between extensometer strains and peak relative- t_2 strains from the optical fibres. The peak values and the extensometer strains are also very close for the slightly thicker DOFS-2 attachment. For all attachments, the absolute difference $C_A(t)$ continues to increase with increasing of the creep time, while the relative difference $C_R(t)$ flattens out after initial transient and then remains almost constant.

From specimens DOFS-0 to DOFS-8, the differences between average relative- t_2 strains and EXT strains quickly increase with the increase of the bottom interlayer thickness. Meanwhile, as the plateau region shortens to zero, average strains within any length of ROI, let alone ROI = 50 mm, are not suitable for interpreting the strain curves anymore. The plateau region simply ceases to exist. Alternatively, the peak values of DOFS strains can be used as a strain characteristic. However, the peak values are still smaller than EXT strains and the $C_A(t)$ shows an increasing trend of growth with both the increase of bottom interlayer thickness and with elapsed time. The relative difference $C_R(t)$ on the other hand remains nearly constant with time, increasing rapidly from 2.5% to 36% with only ca. 1.6 mm increase of bottom interlayer thickness. This monotonically increasing disagreement between DOFS strains and EXT strains indicates an increasing strain transfer lag in the embedding element caused by a larger bottom interlayer thickness.

Main highlights of the experimental data are summarized as follows. Strain measurement accuracy of DOFS-0 is comparable to using a high-accuracy cyanoacrylate attachment. However, a strain transfer lag develops quickly when increasing the bottom interlayer thickness. And finally, the relative difference $C_R(t)$ between extensometer and optical fibre strains remains approximately constant under creep loading conditions, for all tested configurations of DOFS attachments. This confirms similar findings first noted in [38].

3.3.2. The effect of time on strain transfer coefficients

Strain transfer coefficients of DOFS which are attached by low-creep thermoset adhesives, e.g., to CFRP laminates or to steel, are often viewed as constant in time. Meanwhile, the viscoelastic mechanical behavior of CF/PA6 thermoplastic composite causes much larger time-dependent deformations in creep; thus, it is essential to understand if and how does time play a role in the strain transfer process. The challenge lies in that both the substrate and the attachment layer are built from the same polymer composite material with highly time dependent mechanical properties.

As illustrated in Fig. 8, the substrate/attachment/DOFS structure can be discretized into n segments along the length of the DOFS-substrate adhesive joint. It is assumed that no slip occurs in the attachment. Using this framework, the strain distribution along the attached DOFS can be expressed by using a diagonal strain transfer matrix K_{ii} , as follows:

$$\begin{Bmatrix} \epsilon_{M1} \\ \epsilon_{M2} \\ \epsilon_{M3} \\ \vdots \\ \epsilon_{Mn} \end{Bmatrix} = \begin{bmatrix} K_{11} & 0 & \cdots & \cdots & 0 \\ 0 & K_{21} & 0 & \cdots & 0 \\ \vdots & 0 & K_{33} & 0 & \vdots \\ \vdots & \vdots & 0 & \ddots & 0 \\ 0 & 0 & \cdots & 0 & K_{nn} \end{bmatrix} \begin{Bmatrix} \epsilon_{s1} \\ \epsilon_{s2} \\ \epsilon_{s3} \\ \vdots \\ \epsilon_{sn} \end{Bmatrix} \quad (3)$$

where K_{ii} are the strain transfer coefficients between substrate strains ϵ_{si} and DOFS strains ϵ_{Mi} for the i th attachment segment. The initial set of coefficients K_{ii} can be calculated by adopting DOFS strains and EXT strains at $t_3 = 120$ s, as illustrated in Fig. 4(b). Extensometer strains represent substrate strains ϵ_{si} , which are considered equal/constant at every segment i along the length of the OF attachment. The DOFS strains ϵ_{Mi} are obtained from the embedded length (EL) of spatial strain curves in Fig. 7 and each segment i corresponds to one virtual strain gauge on the optical fibre. Initial strain transfer coefficients K_{ii} are calculated by using $K_{ii} = \epsilon_{Mi}/\epsilon_{si}$ from Equation (3), and plugging in the measurement data ϵ_{Mi} (DOFS) and ϵ_{si} (EXT) from the first time point $t_3 = t_2 + 120$ s. The choice of initial time point t_3 is arbitrary and a very similar analysis to what follows is produced by selecting e.g. $t_2 + 240$ s or $t_2 + 360$ s as the initial point in time.

As a first approximation, it is assumed that strain transfer coefficients K_{ii} remain constant in time. In this case, the DOFS strain profiles at a later time $t = t_n$ can also be predicted by Equation (3) by using the initial transfer matrix K_{ii} times extensometer strains ϵ_{si} at $t = t_n$. In this way, the DOFS strain profiles at $t_n = 960$ s, 1800 s and 3600 s are predicted and compared to actual measured DOFS strains in Fig. 9. For DOFS-0, DOFS-2 and DOFS-8, predicted strains match well with experimentally measured strains, all along the DOFS length, and all throughout the creep process. These results support the hypothesis that temporal variation does not affect the strain transfer coefficients K_{ii} .

It can be observed from Fig. 9(c), that predicted strain values of DOFS-4 were noticeably smaller than measured strains, and their distribution patterns had also changed at the ends of the embedded DOFS. For DOFS-4, the creep strains had developed faster than anticipated. One possible interpretation is that some imperfections (micro-cracks, local yielding) had developed at both ends of the DOFS early during the creep loading process. All other things equal, imperfections or damage are expected to appear at the ends of the bondline where stress concentrations are the highest. Looking

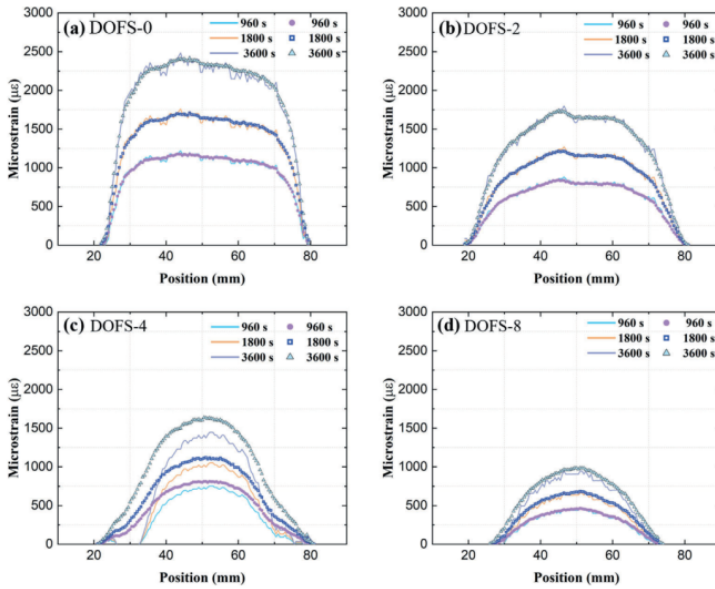


Fig. 9. Comparison between predicted (line) and measured (markers) relative- t_2 strains along the embedded DOFS at three distinct time points (Markers appear like a thick line).

back, the existence of possible imperfections at the ends of DOFS-4 was vaguely implied from early on, in the residual strain profile in Fig. 6(c).

3.3.3. The influence of bottom interlayer thickness

As the strain graphs in Fig. 7 showed, the thickness of bottom interlayer T affects the strain transfer behavior significantly. By increasing bottom interlayer thickness, the quasi-constant strain plateau in the middle of the attachment becomes contracted. Furthermore, the peak values of strain curves are also increasingly lower.

It is well known that specimens made by extrusion based 3-D printing still suffer from inconsistencies from the production process. This may cause a higher dispersion in material properties, compared to other more established manufacturing methods. To account for specimen-to-specimen variability, the DOFS strains of Fig. 7 are normalized by their corresponding EXT strain values in Fig. 10. This Figure shows normalized relative- t_2 DOFS strain profiles from specimens DOFS-0 to DOFS-8 at the beginning ($t = 120$ s) and at the end ($t = 3600$ s) of the creep test. Strains from the contact extensometer, constant at 100%, are also shown on the same Figure by horizontal red lines. The midpoints as well as the start/end points of the EXT gauge area are indicated by vertical dashed lines.

It is easy to recognize that normalized DOFS strain curves now display the strain transfer coefficients visually. Along the optical fibre, most of the DOFS strains are smaller than substrate strains (EXT strains) depending on the bottom thickness T of the embedding element. The left and the right columns of the Figure are nearly identical, confirming again that time does not significantly affect the strain transfer coefficients. However, by increasing the bottom thickness T , difference between DOFS strains and EXT

strains increases monotonically. Both the normalized strain magnitude and the shape of the strain curve change simultaneously. As Fig. 10 shows, by increasing the bottom interlayer thickness, the height of strain curve decreases, and the width of the curve contracts. The plateau shortens from DOFS-0 to DOFS-2 and transfers into a peak in DOFS-4. By further increasing the bottom thickness T in DOFS-8, the curves become narrower, and the peak sharpens. It can be concluded that bottom interlayer thickness T affects the DOFS strains in two ways: i) by increasing T the length of the ingress/egress, i.e. the strain gradient regions increases, and ii) by increasing T the peak values of DOFS strain curves decrease. The most likely reason is the 'shear lag' effect from the attachment layer. Similarly, this 'shear lag' effect has been shown to induce monotonically increasing/decreasing strain gradients for the FBG strain sensors in a number of earlier studies [41–47].

3.4. Shear lag correction

Both Fig. 7 and Fig. 10 have clearly demonstrated how distributed optical fibre strains do not agree with the extensometer, i.e. structural component strains, already when the embedding bottom thickness reaches 0.4 mm (DOFS-2) or larger. Any strain analysis that employs the bathtub curve from the DOFS sensor needs to account for this shear lag error. That is, DOFS strain curves must be interpreted to compare them with the uniform strain of the substrate that is measured by the extensometer. Reducing the length of the ROI (Fig. 5) is a simple practical method for discarding the ingress/egress regions of distributed strains [38]. However, as the experimental strain curves in Fig. 10 show, reducing the ROI alone is not sufficient to calculate strains from the DOFS measurement which are equal to the sub-

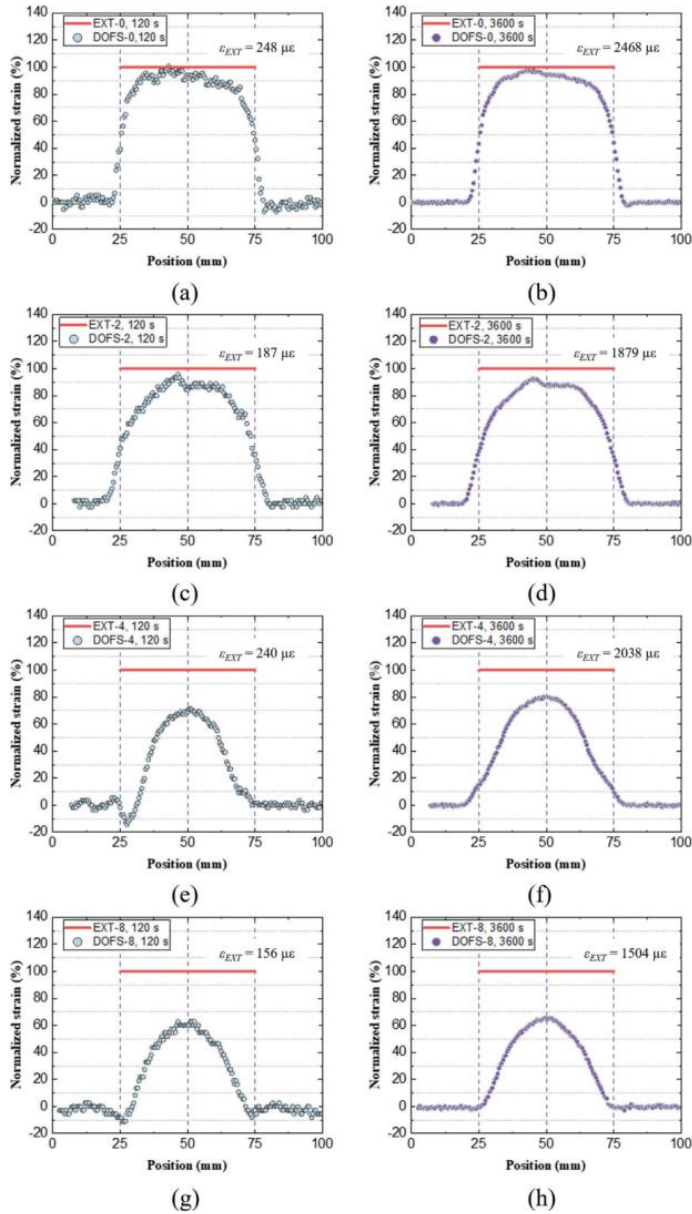


Fig. 10. Normalized relative- t_2 strains during tensile creep (at $t = 120$ s, $t = 3600$ s).

strate component strains (EXT strains). Experimental data shows that embedding bottom thickness T has a basic underlying influence on the DOFS strains. If accurate component strains are to be

measured by optical fibres, the shear lag needs to be corrected, besides accounting for tapered strains at the ingress/egress transition regions.

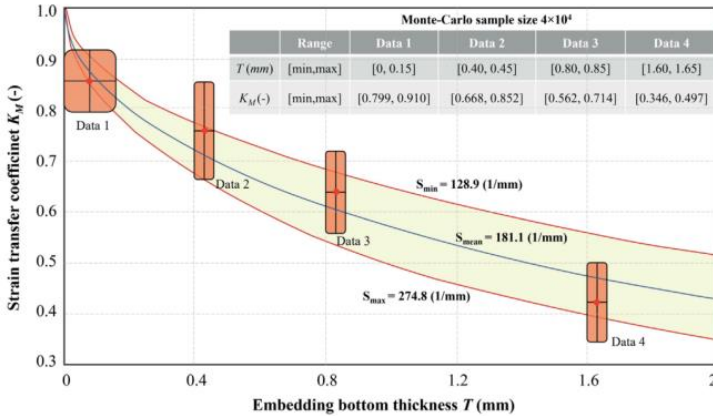


Fig. 11. Curve fitted strain transfer coefficients calculated from experimental data using the shear lag correction model.

As known from theoretical models of surface-bonded FBGs [41–47], the average strain transfer coefficient K_M for the FBG sensor can be expressed as:

$$K_M(T) = 1 - \frac{\sinh(\alpha)}{\alpha \cosh(\alpha)} \quad (4)$$

where T is the bottom thickness of the attachment layer (the same as in this investigation), and α is a 'hybrid' coefficient dominating the shear lag behavior between the substrate and the optical fibre sensor. This coefficient α combines material and geometrical properties of the optical fibre and the attachment layer. Although α can be expressed by complex equations using different variables in the analytical models [41], when bottom interlayer thickness T is considered as the only non-constant variable, it can be simplified as follows:

$$\alpha = \sqrt{\frac{1}{TS}} \quad (5)$$

Here, parameter S is a constant, independent from thickness T , and determined by the diameter and the modulus of the naked optical fibre, fibre coating, width of the bondline, etc. In this work, parameter S is considered as constant for all specimens with different embedding bottom thicknesses. Now, by substituting Eq. (5) into Eq. (4), the strain transfer coefficient is expressed as:

$$K_M(T) = 1 - \frac{\tanh(\sqrt{\frac{1}{TS}})}{\sqrt{\frac{1}{TS}}} \quad (6)$$

Consequently, when both thickness T and strain transfer coefficient $K_M(T)$ are known from several test configurations (of one or more), a curve fitting procedure can be applied to obtain the missing constant S . Then, by inserting the obtained S value back into Eq. (6), any unknown strain transfer coefficient for DOFS with arbitrary bottom interlayer thickness T can be calculated.

Unfortunately, in this investigation the bottom interlayer thickness T can not be known precisely, even if the number of 3-D printed attachment layers under the DOFS are prescribed. During embedding, the optical fibre ($\varnothing = 0.15$ mm) is encapsulated within one 0.2 mm layer of melt, on top of previously 3-D printed and solidified layers of thermoplastic composite. To account for this

vertical placement uncertainty, the value of bottom interlayer thickness is hereby estimated between the nominal bottom thickness T (Table 2) and $T + (0.2 - \varnothing)$ mm, that is, in the range $[T, T + 0.05]$ mm. The experimental strain transfer coefficients $K_M(T)$ corresponding to aforementioned bottom interlayer thicknesses T have to be obtained similarly as ranges of values. As shown in Fig. 10, strain transfer coefficients of embedded DOFS vary along the optical fibre length. From these curves, a conservative estimate for the limits of the coefficient range is obtained by using ROI = 5 mm (captures the highest peak in the middle of the curve) and by averaging the entire curve by using ROI = 50 mm (which includes tapered/lower end regions). Based on these [min, max] ranges for the experimental values of T and K_M , a range of parameters S can be calculated by using Monte-Carlo sampling. The input data was generated uniformly over the range [min, max] for each test configuration, as shown in Fig. 11. An obvious characteristic relationship can now be observed for all calculated curves of K_M as a function of bottom interlayer thickness T . Strain transfer coefficients K_M are especially sensitive to the variation of T when T is small, e.g., less than 0.4 mm (DOFS-0, DOFS-2). This explains why varied strain data are often obtained from optical fibres when using hand-controlled attachment methods, even though only a thin bottom layer of glue exists between the optical fibre and the substrate. The method presented here enables to predict the value of strain transfer coefficient K_M for any unknown thickness T . By using the shear lag correction method, a more accurate substrate strain measurement can now be realized even when optical fibres are attached through a thick intermediate layer of material.

4. Conclusions

1. A novel 3-D printing based embedding method was presented for attaching optical fibre sensors on the surface of thermoplastic composite components.
2. Residual strains from 3-D printing based attachment process reached ca. $-1600 \mu\epsilon$ for short-fibre reinforced CF/PA6 composite used in this study. All residual strain curves remained constant along the attachment length and were independent of the bottom interlayer thickness.

3. Creep strain measurement accuracy that is comparable to cyanoacrylate glue was achieved by optical fibres embedded at zero interlayer thickness. However, by increasing the bottom interlayer thickness, a shear lag effect is quickly introduced between the substrate and the OF sensor strains.
4. Strain transfer coefficients along the attached optical fibres remain constant with elapsed creep loading time. Departure from constant values implies that some forms of imperfections (cracks, local yielding) are occurring at these locations of sensor attachments. However, any such stiffness degradation mechanism needs more experimental confirmation.
5. A simple semi-empirical calculation method was proposed for correcting optical fibre strains for the shear lag effect at an arbitrary interlayer thickness T .
6. For future experiments of the same type, a few recommendations are suggested for better experimental control. The embedding elements are suggested for both sides of the dogbone specimen (one dummy if necessary), and they should remain in the same volume for all test configurations. Also, live temperature measurements are recommended on the test specimen to confirm that no excessive heating occurs when applying the load.

Declaration of Competing Interest

The authors declare that they have no known competing financial interests or personal relationships that could have appeared to influence the work reported in this paper.

Acknowledgment

This work was partially supported by the European Union's Horizon 2020 research and innovation programme and Hydrogen Europe and Hydrogen Europe Research (Grant ID: 826262).

References

- [1] H. Ning, N. Lu, A.A. Hassen, K. Chawla, M. Selim, S. Pillay, A review of Long fibre thermoplastic (LFT) composites, *Int. Mater. Rev.* 65 (2020) 164–188, <https://doi.org/10.1080/09506608.2019.1585004>.
- [2] M. Amafibia, D. Montalvão, O. David-West, G. Haritos, A Review of Structural Health Monitoring Techniques as Applied to Composite Structures, *Struct. Durab. Health Monit.* (1970). <http://www.techscience.com/sdhm/v11n2/35277> (accessed February 26, 2022).
- [3] H.-N. Li, T.-H. Yi, L. Ren, D.-S. Li, L.-S. Huo, Reviews on innovations and applications in structural health monitoring for infrastructures, *Struct. Monit. Maint.* 1 (2014) 1–45. <https://doi.org/10.12989/SMM.2014.1.1.001>.
- [4] E.J. Friebele, C.G. Askins, A.B. Bosse, A.D. Kersey, H.J. Patrick, W.R. Pogue, M.A. Putnam, W.R. Simon, F.A. Tasker, W.S. Vincent, S.T. Vohra, Optical fiber sensors for spacecraft applications, *Smart Mater. Struct.* 8 (1999) 813–838, <https://doi.org/10.1088/0964-1726/8/6/310>.
- [5] E. Saeter, K. Lasn, F. Nony, A.T. Echtermeyer, Embedded optical fibres for monitoring pressurization and impact of filament wound cylinders, *Compos. Struct.* 210 (2019) 608–617, <https://doi.org/10.1016/j.compstruct.2018.11.051>.
- [6] Z.-C. Zhu, C.-W. Chu, H.-T. Bian, J.-C. Jiang, An integration method using distributed optical fiber sensor and Auto-Encoder based deep learning for detecting sulfonized rust self-heating of crude oil tanks, *J. Loss Prev. Process Ind.* 74 (2022), <https://doi.org/10.1016/j.jlp.2021.104623> 104623.
- [7] S. Hassani, M. Mousavi, A.H. Gandomi, Structural Health Monitoring in Composite Structures: A Comprehensive Review, *Sensors* 22 (2022) 153, <https://doi.org/10.3390/s22010153>.
- [8] C. Kralovec, M. Schagerl, Review of Structural Health Monitoring Methods Regarding a Multi-Sensor Approach for Damage Assessment of Metal and Composite Structures, *Sensors* 20 (2020) 826, <https://doi.org/10.3390/s20030826>.
- [9] C.-C. Cheng, Y.-L. Lo, B.S. Pun, Y.M. Chang, W.Y. Li, An Investigation of Bonding-Layer Characteristics of Substrate-Bonded Fiber Bragg Grating, *J. Light. Technol.* 23 (2005) 9.
- [10] M.F. Bado, J.R. Casas, A. Dey, C.G. Berrocal, Distributed Optical Fiber Sensing Bonding Techniques Performance for Embedment inside Reinforced Concrete Structures, *Sensors* 20 (2020) 5788, <https://doi.org/10.3390/s20205788>.
- [11] C. Miguel Giraldo, J. Zúñiga Sagredo, J. Sánchez Gómez, P. Corredra, Demonstration and Methodology of Structural Monitoring of Stringer Rens out Composite Areas by Embedded Optical Fiber Sensors and Connectors Integrated during Production in a Composite Plant, *Sensors* 17 (2017) 1683, <https://doi.org/10.3390/s17071683>.
- [12] M. Mülle, A. Yudhanto, G. Lubineau, R. Yaldiz, W. Schijve, N. Verghese, Internal strain assessment using FBGs in a thermoplastic composite subjected to quasi-static indentation and low-velocity impact, *Compos. Struct.* 215 (2019) 305–316, <https://doi.org/10.1016/j.compstruct.2019.02.085>.
- [13] E. Voet, G. Luyckx, I. De Baere, J. Degrieck, J. Vlekken, E. Jacobs, H. Bartelt, High Strain Monitoring during Fatigue Loading of Thermoplastic Composites Using Imbedded Draw Tower Fibre Bragg Grating Sensors, *Adv. Sci. Technol.* 56 (2008) 441–446, <https://doi.org/10.4028/www.scientific.net/AST.56.441>.
- [14] S. Goossens, B.D. Pauw, T. Geernaert, M.S. Salmanpour, Z.S. Khodaei, E. Karachalios, D. Saenz-Castillo, H. Thienpont, F. Berghmans, Aerospace-grade surface mounted optical fiber strain sensor for structural health monitoring on composite structures evaluated against in-flight conditions, *Smart Mater. Struct.* 28 (2019) 065008, <https://doi.org/10.1088/1361-665X/ab1458>.
- [15] B. Glisic, D. Inaudi, Integration of long-gage fiber optic sensor into a fiber-reinforced composite sensing tape, in: D. Inaudi, E. Udd (Eds.), *San Diego, CA*, 2003 179, <https://doi.org/10.1117/12.484262>.
- [16] K.S.C. Kuang, L. Zhang, W.J. Cantwell, I. Bennon, Process monitoring of aluminum-foam sandwich structures based on thermoplastic fibre-metal laminates using fibre Bragg gratings, *Compos. Sci. Technol.* 65 (2005) 669–676, <https://doi.org/10.1016/j.compotech.2004.09.005>.
- [17] C. Davis, M. Knowles, N. Rajic, G. Swanton, Evaluation of a Distributed Fiber Optic Strain Sensing System for Full-Scale Fatigue Testing, *Procedia Struct. Integr.* 2 (2016) 3784–3791, <https://doi.org/10.1016/j.prostr.2016.06.471>.
- [18] J.V. Roosbroeck, E. Jacobs, E. Voet, J. Vlekken, Installation and test procedures of optical strain gauges for aeronautical applications, in: 20th Int. Conf. Opt. Fibre Sens., International Society for Optics and Photonics, 2009: p. 75037Q, <https://doi.org/10.1117/12.837542>.
- [19] J. Zhang, M. de Souza, C. Creighton, R.J. Varley, New approaches to bonding thermoplastic and thermoset polymer composites, *Compos. Part Appl. Sci. Manuf.* 133 (2020), <https://doi.org/10.1016/j.compositesa.2020.105870> 105870.
- [20] R.C. Don, J.W.G. Jr, S.H. McKnight, Bonding techniques for high performance thermoplastic composites, US5643390A, 1997, <https://patents.google.com/patent/US5643390A/en> (accessed May 13, 2022).
- [21] Surface treatment for adhesive bonding: Thermoset vs. thermoplastic composites, (n.d.), <https://www.compositesworld.com/articles/surface-treatment-for-adhesive-bonding-thermoset-vs-thermoplastic-composites> (accessed May 13, 2022).
- [22] E.A.Y.F. Corp Henkel, Adhesives for Fiber Optics Assembly: Making the Right Choice, (n.d.), https://www.photonics.com/Articles/Adhesives_for_Fiber_Optics_Assembly_Making_the/a25147 (accessed June 24, 2021).
- [23] W. Hufenbach, M. Gude, A. Czulak, M. Kretschmann, Development and implementation of an automatic integration system for fibre optic sensors in the braiding process with the objective of online-monitoring of composite structures, in: J.P. Lynch, K.-W. Wang, H. Sohn (Eds.), *San Diego, California, USA*, 2014 906134, <https://doi.org/10.1117/12.2035613>.
- [24] G. Dell'Anno, I. Partridge, D. Cartié, A. Hamlyn, E. Chehura, S. James, R. Tatam, Automated manufacture of 3D reinforced aerospace composite structures, *Int. J. Struct. Integr.* 3 (2012) 22–40, <https://doi.org/10.1108/17579861211209975>.
- [25] A. Yousefpour, M. Hojjati, J.-P. Immarigeon, Fusion Bonding/Welding of Thermoplastic Composites, *J. Thermoplast. Compos. Mater.* 17 (2004) 303–341, <https://doi.org/10.1177/08927705704045187>.
- [26] H. Li, L. Zhu, M. Dong, X. Lou, Y. Guo, Analysis on strain transfer of surface-bonding FBG on Al 7075-T6 alloy host, *Optik* 127 (2016) 1233–1236, <https://doi.org/10.1016/j.ijleo.2015.10.227>.
- [27] A. Hehr, M. Norfolk, J. Wenning, J. Sheridan, P. Leser, P. Leser, J.A. Newman, Integrating Fiber Optic Strain Sensors into Metal Using Ultrasonic Additive Manufacturing, *JOM* 70 (2018) 315–320, <https://doi.org/10.1007/s11837-017-2709-8>.
- [28] M. Nascimento, P. Inácio, T. Paixão, E. Camacho, S. Novais, T.G. Santos, F.M.B. Fernandes, J.L. Pinto, Embedded Fiber Sensors to Monitor Temperature and Strain of Polymeric Parts Fabricated by Additive Manufacturing and Reinforced with NiTi Wires, *Sensors* 20 (2020) 1122, <https://doi.org/10.3390/s20041122>.
- [29] A. Kantaros, D. Karalekas, Fiber Bragg grating based investigation of residual strains in ABS parts fabricated by fused deposition modeling process, *Mater. Des.* 50 (2013) 44–50, <https://doi.org/10.1016/j.matdes.2013.02.067>.
- [30] S.N. Economidou, D. Karalekas, Optical sensor-based measurements of thermal expansion coefficient in additive manufacturing, *Polym. Test.* 51 (2016) 117–121, <https://doi.org/10.1016/j.polymertesting.2016.03.001>.
- [31] C. Kousiatza, D. Karalekas, In-situ monitoring of strain and temperature distributions during fused deposition modeling process, *Mater. Des.* 97 (2016) 400–406, <https://doi.org/10.1016/j.matdes.2016.02.099>.
- [32] A.G. Leal-Junior, C. Marques, M.R.N. Ribeiro, M.J. Pontes, A. Frizzera, FBG-Embedded 3-D Printed ABS Sensing Pads: The Impact of Infill Density on Sensitivity and Dynamic Range in Force Sensors, *IEEE Sens. J.* 18 (2018) 8381–8388, <https://doi.org/10.1109/JSEN.2018.2866689>.
- [33] A. Leal-Junior, A. Theodosiou, C. Diaz, C. Marques, M. Pontes, K. Kalli, A. Frizzera-Neto, Fiber Bragg Gratings in CYTOP Fibers Embedded in a 3D-Printed Flexible Support for Assessment of Human-Robot Interaction Forces, *Materials* 11 (2018) 2305, <https://doi.org/10.3390/ma11112305>.

- [34] N. Reggiani Manzo, G.T. Callado, C.M.B. Cordeiro, L.C.M. Vieira Jr., Embedding optical Fiber Bragg Grating (FBG) sensors in 3D printed casings, *Opt. Fiber Technol.* 53 (2019), <https://doi.org/10.1016/j.yofte.2019.102015> 102015.
- [35] F. Falcietelli, R. Di Sante, E. Troiani, Strategies for Embedding Optical Fiber Sensors in Additive Manufacturing Structures, in: P. Rizzo, A. Milazzo (Eds.), *Eur. Workshop Struct. Health Monit.*, Springer International Publishing, Cham, 2021, pp. 362–371, https://doi.org/10.1007/978-3-030-64908-1_34.
- [36] R. Zou, R. Cao, M.A.S. Zaghoul, A. Yan, R. Chen, P. Ohodnicki, M. Buric, D. Crandall, X. Liang, A. To, K. Chen, Optical Fiber Sensor-Fused Additive Manufacturing and Its Applications in Residual Stress Measurements in Titanium Parts, in: *Asia Pac. Opt. Sens. Conf. 2016 Pap. Th1A7*, Optica Publishing Group, 2016 Th1A.7, <https://doi.org/10.1364/APOS.2016.Th1A.7>.
- [37] S. Wang, K. Lasn, C.W. Elverum, D. Wan, A. Echtermeyer, Novel in-situ residual strain measurements in additive manufacturing specimens by using the Optical Backscatter Reflectometry, *Addit. Manuf.* 32 (2020) 101040.
- [38] S. Wang, E. Sæter, K. Lasn, Comparison of DOFS Attachment Methods for Time-Dependent Strain Sensing, *Sensors*. 21 (2021) 6879, <https://doi.org/10.3390/s21206879>.
- [39] W. Zhang, W. Chen, Y. Shu, X. Lei, X. Liu, Effects of bonding layer on the available strain measuring range of fiber Bragg gratings, *Appl. Opt.* 53 (2014) 885–891, <https://doi.org/10.1364/AO.53.000885>.
- [40] S.-C. Her, C.-Y. Tsai, Strain measurement of fiber optic sensor surface bonding on host material, *Trans. Nonferrous Met. Soc. China*. 19 (2009) 143–149, [https://doi.org/10.1016/S1003-6326\(10\)60262-2](https://doi.org/10.1016/S1003-6326(10)60262-2).
- [41] H. Zhao, Q. Wang, Y. Qiu, J. Chen, Y. Wang, Z. Fan, Strain transfer of surface-bonded fiber Bragg grating sensors for airship envelope structural health monitoring, *J. Zhejiang Univ. Sci. A*. 13 (2012) 538–545, <https://doi.org/10.1631/jzus.A1100336>.
- [42] J. Li, Z. Zhou, J. Ou, Interface strain transfer mechanism and error modification for adhered FBG strain sensor, in: Y.N. Kulchin, O.B. Vitrik, V.I. Stroganov (Eds.), *Khabrovsk*, 2005 278–287, <https://doi.org/10.1117/12.634066>.
- [43] G. Zhou, H. Li, L. Ren, D. Li, Influencing parameters analysis of strain transfer in optic fiber Bragg grating sensors, in: N. Meyendorf, G.Y. Baaklini, B. Michel (Eds.), San Diego, CA, 2006 61790R, <https://doi.org/10.1117/12.661858>.
- [44] S.-C. Her, C.-Y. Huang, Effect of Coating on the Strain Transfer of Optical Fiber Sensors, *Sensors*. 11 (2011) 6926–6941, <https://doi.org/10.3390/s110706926>.
- [45] N. Perogamvros, P. Motwani, A. Murphy, S. Taylor, Investigation of Surface Strain Fields of Thermoplastic Composites Using Fibre Optic Sensors, In *BSSM 14th International Conference on Advances in Experimental Mechanics: Friction and wear*, 2019.
- [46] M. Liang, N. Chen, X. Fang, G. Wu, Strain transferring mechanism analysis of the surface-bonded FBG sensor, *Appl. Opt.* 57 (2018) 5837, <https://doi.org/10.1364/AO.57.005837>.
- [47] G. Xue, X. Fang, X. Hu, L. Gong, Measurement accuracy of FBG used as a surface-bonded strain sensor installed by adhesive, *Appl. Opt.* 57 (2018) 2939, <https://doi.org/10.1364/AO.57.002939>.
- [48] S.-C. Her, C.-Y. Huang, The Effects of Adhesive and Bonding Length on the Strain Transfer of Optical Fiber Sensors, *Appl. Sci.* 6 (2016) 13, <https://doi.org/10.3390/app6010013>.
- [49] K.S. Kumar, A.C. Reddy, Study on Reinforcement Materials for Nylon Matrix Composites - A Review, *Int J Sci Eng Res* 7 (2016) 156–160.
- [50] F. Ning, W. Cong, J. Qiu, J. Wei, S. Wang, Additive manufacturing of carbon fiber reinforced thermoplastic composites using fused deposition modeling, *Compos. Part B Eng.* 80 (2015) 369–378, <https://doi.org/10.1016/j.compositesb.2015.06.013>.
- [51] A. Barrias, J.R. Casas, S. Villalba, A Review of Distributed Optical Fiber Sensors for Civil Engineering Applications, *Sensors*. 16 (2016) 748, <https://doi.org/10.3390/s16050748>.
- [52] R. Chen, Z. Peng, M. Wang, A. Yan, S. Li, S. Huang, M.-J. Li, K.P. Chen, Spatially resolved fibre cavity ring down spectroscopy, *Sci. Rep.* 10 (2020) 20167, <https://doi.org/10.1038/s41598-020-76721-y>.
- [53] A. Iadicicco, D. Natale, P. Di Palma, F. Spinaci, A. Apicella, S. Campopiano, Strain Monitoring of a Composite Drag Strut in Aircraft Landing Gear by Fiber Bragg Grating Sensors, *Sensors*. 19 (2019) 2239, <https://doi.org/10.3390/s19102239>.

ISBN 978-82-326-5864-0 (printed ver.)
ISBN 978-82-326-6284-5 (electronic ver.)
ISSN 1503-8181 (printed ver.)
ISSN 2703-8084 (online ver.)



NTNU

Norwegian University of
Science and Technology